Investigating extracellular vesicle release from human coronary artery vascular smooth muscle cells in atherosclerosis

Eleni Charla

MRes, MSc, BSc

Submitted in fulfilment of the requirements for the degree of Doctor of Philosophy to the School of Cardiovascular and Metabolic Health, University of Glasgow.

Research conducted at the British Heart Foundation Glasgow Cardiovascular Research Centre, School of Cardiovascular and Metabolic Heath, College of Medical, Veterinary and Life Sciences, University of Glasgow, UK

September 2023

Author's Declaration

I declare that I, Eleni Charla, have written this thesis entirely by myself and this thesis is a record of the work performed by me with some exceptions as detailed below. Transmission electron microscopy was carried out by Mrs. Margaret Mullin based in the School of Life Sciences, University of Glasgow, UK. cDNA library preparation, small RNA sequencing and analysis of RNAseq data were carried out at Glasgow Polyomics (University of Glasgow, UK). I would like to thank Dr Graham Hamilton (University of Glasgow, UK) who performed the analysis of RNAseq data. Dr Simon Fisher (University of Glasgow, UK) re-analysed RNAseq data using a different approach. APOE KO mice were gifted from Professor Pasquale Maffia (University of Glasgow, UK). Dr Danila Gurgone (University of Glasgow, UK) and Dr Lucy McShane (University of Glasgow, UK) helped with Schedule 1 procedure. Antoniya Pashova (University of Glasgow, UK) optimised cel-miR-39-3p loading into EVs. This thesis has not been submitted previously for a higher degree. The work included in this thesis was completed at the University of Glasgow Cardiovascular Research Centre in the School of Cardiovascular and Metabolic Health under the supervision of Professor Stuart A. Nicklin, Dr John Mercer and Professor Pasquale Maffia.

Eleni Charla

2023

Acknowledgements

Firstly, I would like to express my infinite gratitude to my supervisors Professor Stuart Nicklin, Dr John Mercer and Professor Pasquale Maffia for being great supervisors all these years, supporting me and encouraging me. I am grateful for the opportunity to complete my PhD thesis in this amazing group. It was a wonderful journey filled with new experiences. A special thanks to Dr Lorraine Work for always helping with endless EV questions. I would also like to thank the British Heart Foundation and the University of Glasgow for their financial support all these years ad during the Covid-19 pandemic.

A huge thanks to members (past and present) of our group: Lisa, Ahmad, Julien, Antoniya and Josie who was there during my final experiments lifting my spirits. I would also like to thank Dr Danila Gurgone and Dr Lucy McShane from the Maffia group for helping with the animal study. Thanks to Professor Maffia for providing animals for the completion of the animal study. Thanks to Dr John McClure for his valuable advice regarding statistical analysis. Many thanks to everyone in the Level 4 lab, especially Nic for always being there to help with my TC problems. A special thanks to Wai for all your Nanosight troubleshooting support.

I met amazing people during my time in Glasgow, and they deserve a special thanks. Thank you, Rebecca for the EV chat, Erin, Sonya, Arun, Gabbi, Daniel, Talha, Kayle and Philip. A special thanks to our former amazing student rep, Alice Main for helping me with my PhD extension. Huge thanks to my PhD family, Antoniya, and Simon, for their friendship, the laughs, and hard times we shared together. Thanks to Simon for the science chats and his help all these years. Thanks to Antoniya for our endless talks and the support (emotional and scientific). You were the best office mates I could have asked for!

I want to thank my family who have supported me all these years. A special thanks to my mother for her unconditional love and support throughout all my life. Thanks to my little sister, Anthi, for always believing in me. I would also like to thank my pharmacist friends, Pinelopi, Mary, Elena and Fani for taking me mind off science from time to time.

Finally, my biggest thanks go my other half, Mark. Words cannot describe how grateful I am for your encouragement and support. Thank you for listening to me,

your understanding, putting up with all my moans, and standing by my side all times.

Table of Contents

List of Figures

List of Tables

List of Publications, awards

Journal article

Charla, E., Mercer, J., Maffia, P., Nicklin, SA. 2020. Extracellular vesicle signalling in atherosclerosis. *Cell Signal*, 75:109751. doi: 10.1016/j.cellsig.2020.109751. Epub 2020 Aug 26. PMID: 32860954; PMCID: PMC7534042.

Published Abstract

Charla, E., Mercer, J., Maffia, P., Nicklin, SA (2021) Characterising extracellular vesicle release from human coronary artery vascular smooth muscle cells exposed to oxidised LDL, Journal of Extracellular Vesicles, 10 (Supplement 1): PS25.12

Presentations

Profiling the small RNA cargo in extracellular vesicles derived from oxidised low-density lipoprotein-stimulated vascular smooth muscle cells. International Society for Extracellular Vesicles Annual meeting 2022, Lyon, France [Poster communication]

Characterising extracellular vesicle release from human coronary artery vascular smooth muscle cells exposed to oxidised LDL. International Society for Extracellular Vesicles Annual meeting 2021, Virtual meeting [Poster communication].

Investigating the effects of oxidised LDL treatment-treatment on extracellular vesicle release from human coronary artery vascular smooth muscle cells. UK Extracellular Vesicle Forum Annual meeting 2020, Virtual meeting [Oral communication, Young Investigator award finalist]

Awards

Conference Support Award, University of Glasgow College of MVLS, May 2022

Wellcome Institutional Strategic Support Fund (ISSF) Feasibility Award, November 2019

BSCR meeting travel grant, July 2019

Abbreviations

AAV	adeno associated virus
ABCA1	ATP binding cassette subfamily A member 1
ACACB	acetyl-CoA carboxylase 2
ACS	acute coronary syndrome
AFC	automatic fraction collector
AGO	argonaute
AKT2	AKT serine/threonine kinase 2
ALK	anaplastic lymphoma kinase
ANOVA	analysis of variance
APOE	apolipoprotein E
ARF6	ADP-ribosylation factor 6
ARRDC1	arrestin domain-containing protein 1
ASC	human adipose tissue-derived mesenchymal stromal cells
ASOs	antisense oligonucleotides
ATF3	activating transcription factor 3
ATP1B1	ATPase Na+/K+ Transporting Subunit Beta 1
ATP9A	ATPase Phospholipid Transporting 9A
AURKA	aurora kinase A
BCA	bicinchoninic acid
BCL2	B-cell lymphoma 2
BCL2L11	Bcl-2-like protein 11
BMDMs	bone-marrow derived macrophages
BM-hMSC	human bone marrow derived mesenchymal stromal cells
BMP-2	bone morphogenetic protein 2
BMSC	bone marrow mesenchymal stem cells
BrdU	bromodeoxyuridine
BSA	bovine serum albumin
CABG	coronary artery bypass grafting
CAD	coronary artery disease
CANTOS	Canakinumab Anti-inflammatory Thrombosis Outcome Study
CCL2	chemokine (C-C motif) ligand 2
CCL5	chemokine (C-C motif) ligand 5

CCM	conditioned cultured media
CD31	cluster of differentiation 31
CD68	cluster of differentiation 68
CDC42EP2	CDC42 Effector Protein 2
CDC6	cell division control protein 6
CDKN1B	cyclin-dependent kinase inhibitor 1B
CDKN1C	cyclin-dependent kinase inhibitor 1C
CDKN2A	cycle inhibitors cyclin dependent kinase inhibitor 2A
cDNA	complementary DNA
CDS	coding domain sequence
Cells/mL	cells per millilitre
CO_2	carbon dioxide
COLCOT	Colchicine Cardiovascular Outcomes Trial
COX-2	cyclooxygenase-2
COX5B	cytochrome c oxidase subunit 5b
COX7A2	cytochrome c oxidase subunit 7A
CPT1A	carnitine palmitoyltransferase 1A
CRP	c-reactive protein
Ct	cycle threshold
CT	computerised tomography
CVD	cardiovascular disease
DAPI	4′,6-Diamidine-2′-phenylindole dihydrochloride
DAVID	Database for Annotation, Visualization and Integrated Discovery
ddH2O	double distilled H_2O
DGCR8	diGeorge syndrome critical region 8
dH2O	distilled H_2O
DLK1	delta like non-canonical Notch ligand 1
DMEM	Dulbecco's modified eagle medium
DMSO	dimethyl sulphoxide
DNA	deoxyribonucleic acid
DNase	treated deoxyribonuclease
DPBS	Dulbecco’s phosphate buffered saline
ECs	endothelial cells

EDHF	endothelium-derived hyperpolarizing factor
EDTA	ethylenediamine tetra-acetic acid
EGFR	epidermal growth factor receptor
ELK1	ETS transcription factor
EndMT	endothelial-to-mesenchymal transition
EPCs	endothelial progenitor cells
ERBB2	erb-b2 receptor tyrosine kinase 2
ERK	extracellular signal-regulated kinase
ESCRT	endosomal sorting complex required for transport
ESE	early-sorting endosome
EVs	extracellular vesicles
EXP5	exportin 5
FCS	fetal calf serum
g	gravitational force
GAPDH	glyceraldehyde 3-phosphate dehydrogenase
GPL	General Public License
GO	gene ontology
GW4869	N,N′-Bis[4-(4,5-dihydro-1H-imidazol-2-yl)phenyl]-3,3′-p-phenylene-bis-acrylamide dihydrochloride
GWAS	genome-wide association studies
H/E	haematoxylin/eosin
H/R	hypoxia followed by reoxygenation
HAVSMCs	human aortic vascular smooth muscle cells
HBP1	HMG-Box Transcription Factor 1
HCAEC	human coronary artery endothelial cell
HCASMC	human coronary artery smooth muscle cell
HDAC4	histone deacetylase 4
HFD	high fat diet
HMC-1	human mast cells
HMG-CoA	3-hydroxy 3-methyl glutaryl CoA
HMGCR	3-hydroxy-3-methylglutaryl-CoA reductase
HPMECs	human placental microvascular ECs
hs-CRP	high-sensitivity C-reactive protein
HSP7C	heat shock cognate 71 kDa protein

HSP90a	heat-shock protein 90 alpha
HSPA8	heat shock protein 8
HSPCs	hematopoietic stem and progenitor cells
HUVECs	human umbilical vein endothelial cells
ICAM-1	intercellular adhesion molecule-1
IFN-γ	interferon gamma
IGV	integrative genomics viewer
IL-1ß	interleukin-1 beta
IL-6	interleukin-6
ILVs	intraluminal vesicles
IPA	ingenuity pathway analysis
IRAK-1	interleukin-1 receptor-associated kinase 1
IRS1	insulin receptor substrate 1
ISEV	International Society of Extracellular vesicles
JUPITER	Justification for the Use of Statins in Primary Prevention: an Intervention Trial Evaluating Rosuvastatin
kb	kilobase
kDa	kilodalton
KIT	KIT proto-oncogene receptor tyrosine kinase
KLF2	kruppel-like factor 2
KLF4	kruppel-like factor 4
KLF5	kruppel-like factor 5
KO	knockout
LCA	left carotid artery
LDHB	L-lactate dehydrogenase B chain
LDL	low-density lipoprotein
LDL-C	LDL-Cholesterol
LDLR	low-density lipoprotein receptor
lin− BMCs	lineage-negative bone marrow cells
LPS	lipopolysaccharide
LSEs	late-sorting endosomes
LV	lentiviral vector
m/lEVs	medium/large EVs
MCP-1	monocyte chemotactic protein-1

MESA	multi-ethnic study of atherosclerosis
MI	myocardial infarction
miRNA	microRNA
MISEV2018	Minimal Information for Studies of Extracellular Vesicles 2018
mL	millilitre
MLCK	myosin light-chain kinase
MMPs	matrix metalloproteases
mRNA	messenger RNA
MSCs	mesenchymal stem cells
mt	mitochondrial
MTOR	mechanistic target of rapamycin kinase
mTORC1	mechanistic target of rapamycin complex 1
MT-RNR1	mitochondrially encoded 12S RNA
MVBs	multivesicular bodies
MYOCD	myocardin
NF-κB	nuclear factor kappa B
ng/mL	nanogram per millilitre
NGS	next generation sequencing
NO	nitric oxide
NTA	nanoparticle tracking analysis
^{o}C	degrees Celsius
OCT	optimum cutting temperature
oxLDL	oxidised LDL
PAD	peripheral arterial disease
PARP1	poly(ADP-Ribose) Polymerase 1
PASMCs	pulmonary artery SMCs
PC	pancreatic cancer
PCA	principal component analysis
PCSK-9	proprotein convertase subtilisin/kexin type-9
PDGF	platelet derived growth factor
PFA	paraformaldehyde
PHACTR1	phosphatase and actin regulating protein 1
PIK3CA	phosphatidylinositol-4,5-bisphosphate 3-kinase catalytic subunit alpha

PK	proteinase K
PLA2	phospholipase A2
PLK2	polo like kinase 2
PMVK	phosphomevalonate kinase
pre-miRNA	precursor miRNA
pri-miRNA	primary miRNA
PTEN	phosphatase and tensin homolog
PVAT	perivascular adipose tissue
RAI14	Retinoic Acid Induced 14
RECK	reversion-inducing-cysteine-rich protein with kazal motifs
RISC	RNA-induced silencing complex
RM	repeated measures
RNA	ribonucleic acid
RNAi	RNA interference
RNYs	Ro-associated non-coding RNAs
rpm	revolution per minute
RQ	relative quantification
RT	reverse transcription
RT-PCR	reverse transcription polymerase chain reaction
RT-qPCR	reverse transcription quantitative real-time polymerase chain reaction
scaRNAs	small Cajal body-specific RNAs
SEC	size exclusion chromatography
SEM	standard error of the mean
sEVs	small EVs
SF	serum starvation/serum free
SIK1	salt inducible kinase 1
siRNAs	small interfering RNAs
SIRT1	silent information regulator 1
SM22α	smooth muscle protein 22α
SMCs	smooth muscle cells
snoRNA	small nucleolar RNAs
snRNAs	small nuclear RNAs
SP1	specificity protein 1

SPIRE	Studies of PCSK9 Inhibition and the Reduction of Vascular Events
SRAI/II	scavenger Receptor Class A type I and II
SR-BI	scavenger Receptor Class B, type I
SREBP-1	sterol regulatory element-binding protein 1
SREBP-2	sterol regulatory element-binding protein 2
sRNA	small RNA
SRSF1	serine/arginine splicing factor 1
TACE	metalloprotease TNF-α converting enzyme
TBS	tris-buffered saline
TBST	tris buffered saline containing 0.05% Tween 20
TE	tris-EDTA
TEM	transmission electron microscopy
TGFβ	transforming growth factor β
TIMP3	tissue inhibitor of metalloproteinase 3
TNF-α	tumour necrosis factor-α
TP53	tumor protein 53
TP53INP1	tumor protein p53 inducible nuclear protein 1
TSG101	tumor susceptibility gene 101
UBC	ubiquitin C
UC	ultracentrifugation
UTR	untranslated region
v/v	volume per volume
VCAM-1	vascular cell adhesion molecule-1
VE	vascular endothelial
VEGF-A	vascular endothelial cell growth factor A
VLDL	very low–density lipoprotein
wt	wild type
XBP1	x-box binding protein 1
ZNF271P	zinc finger protein 271
αSMA	alpha smooth muscle actin
µg/mL	micrograms per millilitre
µL	microlitre

Summary

Cardiovascular disease (CVD), a group of disorders affecting the heart and the vessels, is the leading cause of death worldwide. Atherosclerosis is the most common CVD and is involved in the majority of deaths. Current pharmacological interventions have succeeded to reduce morbidity from atherosclerosis, however cardiovascular events still occur. Low-density lipoprotein (LDL) retention in the arterial wall is considered the hallmark of fatty streak formation in early atherogenesis. Histological and *in vitro* studies have highlighted the important role of smooth muscle cells (SMCs) in initiation of atherosclerosis. Moreover, studies have highlighted the important role of endothelial cells (ECs) in atherogenesis with EC activation and dysfunction as a critical step during early atherogenesis. Extracellular vesicles (EVs) have gained a lot of attention in atherosclerosis progression and as therapeutic delivery vehicles in various pathologies. EV signaling and their miRNA cargo have been shown to participate in all stages of atherosclerosis progression. It was therefore hypothesised that SMC-EVs under atherogenic stimulus participate in atherosclerosis progression via a paracrine way of communication and transfer of their cargo.

Initial studies investigated the elution profile of EVs isolated via size exclusion chromatography (SEC) from conditioned media from cultured human coronary artery SMCs (HCASMCs). Characterisation of EV fractions isolated with SEC identified the purest EV containing fractions which were chosen for future experiments. EVs were isolated from the conditioned media of HCASMCs +/- oxLDL stimulation and successfully characterised in terms of size, protein concentration, EV marker detection, morphology and concentration of particles released from HCASMC though no significant differences were observed upon oxLDL stimulation. Next, the functional effects of SMC-EVs upon +/- oxLDL stimulation were determined. It was found that oxLDL-EV uptake was significantly lower compared to Control-EV uptake by human coronary artery EC (HCAEC). However, SMC-EVs after +/- oxLDL stimulation had no effect on HCASMC cell viability or serum induced viability and HCAEC cell viability.

Next, the small RNA cargo of SMC-EVs +/- oxLDL stimulation was profiled. Principal component analysis (PCA) showed transcriptional alterations between Control-EVs and oxLDL-EVs, however a mixed degree of separation was observed, possibly due to heterogeneity between individual donor cells. Small RNA sequencing showed

that oxLDL stimulation resulted in 4.5-fold downregulation of miR-125b-5p and 4.5-fold upregulation of 3 snRNAs, RNU2-7p, RNU2-29p, RNU2-57p in HCASMCs-EVs. Successful validation of the RNAseq results was performed by real-time quantitative polymerase chain reaction using samples from 4 patients to determine the expression levels of miR-125b-5p and U2 snRNAs. A different approach for RNA sequencing analysis identified miR-125b-5p and two other miRNAs, miR-199b-5p and miR-199a-5p, to be downregulated in SMC-EVs after oxLDL stimulation, while 3 different U2 snRNAs (RNU2-37p, RNU2-56p, RNU2-250p) and a snoRNA, SNORD36B, were found upregulated in EVs after oxLDL stimulation. MiR-199b-5p and miR-199a-5p were also successfully validated in SMC-EVs using real-time quantitative polymerase chain reaction. Interestingly, miR-125b-5p was identified to be differentially expressed in SMC-EVs by the two methods. Next, cellular expression of miR-125b-5p was assessed after oxLDL treatment and miR-125b-5p levels were found elevated in HCASMCs. However, miR-125b-5p expression was significantly reduced in oxLDL stimulated HCASMCs after 48 hours of EV secretion compared to control treated cells agreeing with miR-125b-5p reduced levels in SMC-EVs after oxLDL treatment. Bioinformatic analysis for miR-125b-5p identified 303 predicted and validated gene targets of miR-125b-5p. Pathway enrichment analysis identified biological pathways that regulate cell survival, cell growth and proliferation which are related to the disease. A pathway hypothesis was formed using gene ontology (GO) analysis which identified 6 genes, TP53, STAT3, SP1, ERBB2, ERBBE and PPP1CA. Pathway hypothesis suggested that miR-125b-5p would regulate cell survival and proliferation via transcriptional regulation of these genes.

Finally, the functional role of miR-125-5p loaded EVs in recipient cell proliferation, migration and transcriptional regulation of TP53, STAT3, SP1, ERBB2, ERBBE and PPP1CA was examined. MiR-125-5p loading into EVs was chosen as it was previously found that oxLDL treatment resulted in miR-125b-5p downregulation in SMC-EVs. First, successful loading into EVs and transfer of cel-miR-125b-5p to recipient HCASMCs via EVs was shown. MiR-125b-p was successfully loaded into SMC-EVs and EV characterisation showed no difference in terms of size or concentration after electroporation. MiR-125b-5p-EVs did not affect recipient HCASMC cell viability but they significantly suppressed HCASMC serum induced proliferation. Preliminary scratch assay results after miR-125b-5p-EV treatment indicated lower % of scratch closure (although statistacally non-significant) in

serum induced HCASMC migration compared to Naïve-EV treatment. No significant changes in mRNA expression of target genes was found after 6 hours and 12 hours of 5% FCS +/- EV treatment. It was also found that miR-125b-5p-EV treatment had no effect on recipient HCAEC cell viability.

These findings led to investigation of the profile of EVs isolated from wild type (wt) and apolipoprotein E (APOE) knockout (KO) mice under normal chow diet or high fat diet. Basic characterisation of wt and APOE KO mice showed that high fat diet did not alter the total body weight in both strains of mice. Imaging of paraffin embedded aortic tissue sections showed no histological alterations in aortic tissues from wt mice under both diets and APOE KO mice under standard chow diet. However, lesions were observed in aortic arch and thoracic aorta sections but not in abdominal aorta sections from APOE KO mice under high fat diet. Serum EVs from wt and APOE KO mice were successfully characterised in terms of size, particle concentration and detection of EV markers. Size analysis of serum EVs showed no alterations in size of EVs from wt and APOE KO mice under both diets. Serum EVs from APOE KO mice fed high fat diet had increased particle concentration compared to wt mice under both diets and APOE KO mice under standard chow diet. A pairwise comparison between wt and APOE KO mice on either normal chow or high fat diet showed that serum EVs from APOE KO mice fed chow diet had significantly higher concentration compared to serum EVs from wt mice fed chow diet indicating that the mouse strain may influence the concentration of circulating EVs. Secreted EVs from aortic tissues were successfully characterised in terms of size and particle concentration and no significant differences were observed between wt and APOE KO mice.

Next, miR-125b-5p levels were assessed in serum EVs from wt and APOE KO mice under both diets. Relative quantification revealed that high fat diet resulted in lower levels of EV-miR-125b-5p in wt and APOE KO mice, however not statistically significant. Another quantification method where miR-125b-5p levels were normalised to the particle concentration of each sample showed that EV-miR-125b-5p levels in wt mice fed high fat diet still were lower, again statistically non-significant, compared to wt mice under chow diet. However, this alternative quantification method revealed that high fat diet resulted in increased but not significant EV-miR-125b-5p levels in APOE KO compared to APOE KO mice fed standard chow diet. MiR-125b-5p levels were also successfully detected in

secreted EVs from aortic tissues indicating that EVs originating from the vasculature package miR-125b-5p, though no differences were detected regarding EV-miR-125b-5p expression between wt and APOE KO mice under both diets.

Altogether, these studies provide evidence that although HCASMC oxLDL stimulation did not alter SMC-EV release, it did alter the small RNA cargo of SMC-EVs resulting in miR-125b-5p downregulation. Significantly increased EV concentration was observed in mice with experimental atherosclerosis and analysis of these EVs showed lower miR-125b-5p-EV levels. Moreover, secreted EVs from mice aortic tissues were isolated in these studied using a novel protocol and miR-125b-5p was found to be packaged into EVs secreted from the vasculature. *In vitro* studies showed that miR-125b-5p loaded EVs reduced serum induced HCASMC cell proliferation but did not alter serum induced HCASMC migration. Finally, these studies add to the knowledge of EVs and their cargo in VSMCs and in atherosclerotic rodent models, but further work is required in the future to dissect the mechanisms of action of the miRNAs and how EVs signal between different cells in atherosclerosis.

Chapter 1 Introduction

1.1 Atherosclerosis

1.1.1 Cardiovascular disease

Cardiovascular disease (CVD) is a class of diseases affecting the heart and vessels and is the leading cause of death worldwide causing more than 4 million deaths in Europe each year (Mach et al., 2020). CVDs include coronary artery disease (CAD), stroke, peripheral arterial disease, congenital heart disease, and deep vein thrombosis and pulmonary embolism (WHO, 2019). Fundamental risk factors for CVD include hypertension, hyperlipidaemia, obesity, diabetes and smoking (Franco et al., 2011). Other characteristics including age, sex, and family history of CVD have been linked with increased risk of future CVD (Wood, 2001). Modification of risk factors is essential for CVD prevention and reduction of CVD morbidity and mortality. Traditional approaches for CVD prevention had focus on management of a single risk factor such as hypertension or hyperlipidaemia, however, CVD is driven by multiple factors, so current prevention approaches take into consideration multiple risk factors (Wood, 2001).

1.1.2 Atherosclerosis

Atherosclerosis is a chronic inflammatory disease where build-up of fatty deposits in the arteries (atheroma) can cause myocardial infarction (MI), stroke, unstable angina and sudden cardiac death (Falk et al., 1995)(Lusis, 2000)(Libby et al., 2011). Despite pharmacological advances in recent years, atherosclerosis is the underlying cause of 50% of all deaths (Pahwa and Jialal, 2021). Clinical manifestations of the disease include CAD, ischemic stroke, and peripheral arterial disease (PAD) (Herrington et al., 2016). In 1995, William and Tabas, formulated the Response-to-Retention Hypothesis of Early Atherogenesis, where they suggested that lipoprotein retention in the arterial wall was the driving force of atherosclerosis development in contrast with the earlier Response to Injury theory formulated by Ross et al, in 1973 (Ross and Glomset, 1973)(Ross et al., 1977)(Williams and Tabas, 1995). Current theory around atherosclerosis progression is based upon the Response-to-Retention Hypothesis with Low Density Lipoprotein (LDL) retention to the arterial wall to be considered the beginning of atherosclerosis (Mach et al., 2020)(Borén et al., 2020). However, experimental and clinical data indicate that inflammation drives atherogenesis along with lipid retention (Libby and Hansson, 2019).

1.1.3 Epidemiology and risk factors of the disease

Atherosclerosis is a chronic condition where symptom manifestation is quite late in life compared to disease initiation so to quantify the incidence of the disease is challenging (Pahwa and Jialal, 2021). Atherosclerosis is the most common cause of CVDs (Song et al., 2020). According to WHO, CVDs are the primary cause of death worldwide with an estimated 32% of all deaths (17.9 million deaths) (WHO, 2019). Most common events causing death are MIs and stroke caused by an occluded artery due to lipid deposition (Timmis et al., 2018)(WHO, 2019). In the UK, it is estimated that 7.6 million people are living with a heart or a circulatory disease while the annual number of deaths is estimated at around 168,000 (BHF, 2021). It is worth mentioning that since 1969, the death rate due to CVD has decreased, however Glasgow, Scotland has the highest rate of premature death due to CVD around the UK (BHF, 2021).

Hyperlipidemia, hypertension, diabetes mellitus, obesity and smoking are primary risk factors for atherosclerosis but each one of these conditions alone cannot drive atherosclerosis (Singh et al., 2002). Many epidemiological and Mendelian randomization studies have shown a strong relationship between LDL-Cholesterol (LDL-C) and progression of atherosclerosis (Baigent et al., 2010)(Collaboration*, 2012)(Willer et al., 2013)(Nikpay et al., 2015)(Ference et al., 2012)(Mach et al., 2020). Modification and reduction of risk factors is one approach to reduce the burden of atherosclerotic disease.

Epidemiologic studies of CVD usually assess CVD events such as MI or stroke to point out factors associated with the disease's progression. New study designs focus on unravelling subclinical features for earlier detection and prevention of the disease. A combination of non-traditional risk factors with family history of premature CAD and physical inactivity can better predict coronary artery calcification, a clinical feature of CAD (Desai et al., 2004)(Greenland et al., 2018). The Multi-Ethnic Study of Atherosclerosis (MESA) found that coronary artery calcification measurement could predict future CVD events like CAD, whereas carotid intima-media thickness was a better predictor of stroke (Folsom et al., 2008).

1.1.4 Pathophysiology of atherosclerosis

The consensus mechanism of coronary atherosclerosis in humans suggests that LDL-C subendothelial retention is the hallmark of the disease and also that the endothelium consists of one cell layer (Subbotin, 2016). However, that model disregards the fact that the endothelium consists of multiple cell layers and that lipid depositions happen in the deepest layers of the endothelium (Subbotin, 2016). Clinical evidence have shown that lipoprotein retention is not responsible for atherosclerosis initiation (Subbotin, 2016). In humans and large mammals, intimal thickness happens after birth, and excessive cell proliferation transforms intimal thickness to intimal hyperplasia inducing cell hypoxia and neovascularisation (Subbotin, 2016). Coronary atherosclerosis is a result of hyperplasia and subsequent effects facilitating LDL-C retention in coronary arteries (Figure 1-1) (Subbotin, 2016).

The mechanism of plaque formation (Figure 1-2) resembles atherosclerosis development in mice and not in humans as explained above. However, the majority of literature describes the disease model as depicted in Figure 1-2, so that model was described in detail below.

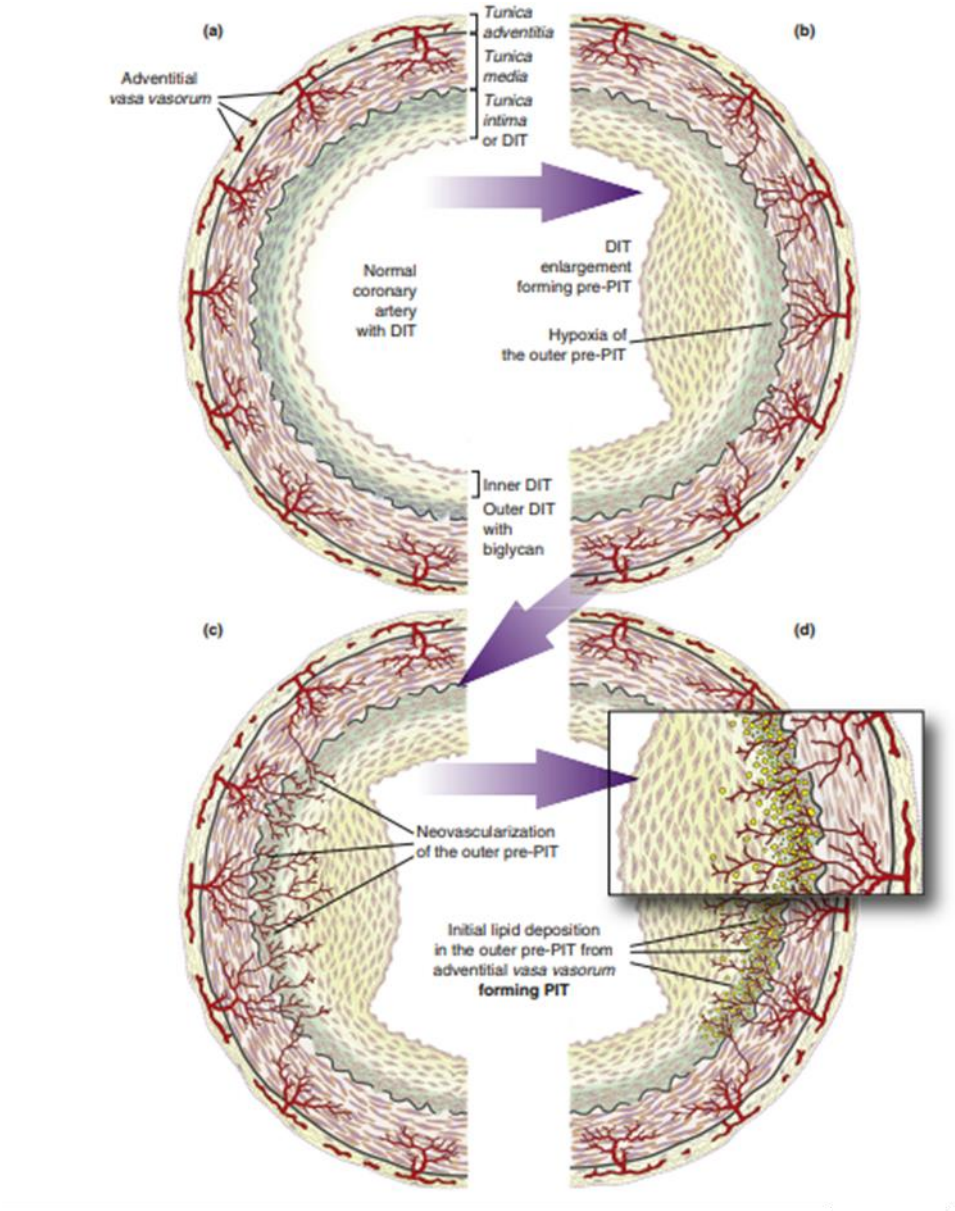

Figure 1-1 Schematic representation of coronary atherosclerosis mechanism in humans.

(A) Human normal coronary artery with intimal thickness. (B) Increased cell proliferation transforms intimal thickness into pre-pathologic intimal thickening with cell undergoing hypoxia. (C) Neovascularization occurs in the pre-pathologic intimal thickening with permeable vessels. (D) Cells in hyperplasia retain LDL-C in the outer area. Adapted from ((Subbotin, 2016) published under a Creative Commons CC-BY license).

1.1.4.1 Fatty streak and lesion progression

Fatty streak formation can begin in early childhood and remain asymptomatic for years (Song et al., 2020). High levels of LDL particles in plasma are linked with coronary events, as seen in lipid lowering studies which result in reduced CVD events (Shepherd et al., 2002)(Silverman et al., 2016). Numerous studies have shown lipoprotein retention at atherogenic arterial sites is the hallmark of fatty streak formation (Schwenke and Carew, 1989a)(Schwenke and Carew, 1989b)(Tabas et al., 2007)(Hermansson et al., 2010). Non-laminar and turbulent blood flow (atheroprone flow) can alter endothelial susceptibility for LDL retention and thus regional points in the artery with these hemodynamic disturbances (artery bifurcations) are considered atherogenic sites (Figure 1-2) (Zand et al., 1991)(VanderLaan et al., 2004). Endothelial cells (ECs) are sensitive to molecular, mechanical and hemodynamic changes (VanderLaan et al., 2004). Exposure to atheroprone flow results in nuclear factor kappa B (NF-κB) activation and inflammatory cytokine expression (Kraiss, 2005). LDL retention and inflammatory activation of ECs, results in vascular cell adhesion molecule-1 (VCAM-1) and intercellular adhesion molecule-1 (ICAM-1) expression allowing monocyte migration into the intact vessel wall (Cybulsky and Gimbrone, 1991)(Li et al., 1993)(Khan et al., 1995). LDL oxidation *in vivo* takes place in the subendothelial area of the artery (Matsuura et al., 2008). Oxidation to LDL lipid components (phospholipids, cholesteryl esters and cholesterol) or ApoB100 occurs enzymatically (e.g. peroxidases) or non-enzymatically (e.g. release of reactive oxygen species by activated endothelial cells) (Kattoor et al., 2017)(Borén et al., 2020). LDL oxidation *in vitro* has been shown to promote oxidised LDL (oxLDL) uptake by macrophages (Singh et al., 2002). Hypercholesterolemia results in upregulation of scavenger lipoprotein receptors such as Scavenger Receptor Class A type I and II (SRAI/II), Scavenger Receptor Class B, type I (SR-BI) and CD63 in monocytes which transform into macrophages, transmigrate into the sub-endothelial space and take up oxLDL (Han et al., 1997)(Singh et al., 2002)(Osterud and Bjorklid, 2003). OxLDL accumulation by macrophages results in the formation of lipid-laden foam cells and is considered the hallmark of fatty streak formation in the vessel wall (Singh et al., 2002)(Matsuura et al., 2008). B cells localized in atherosclerotic plaques secrete antibodies expressing epitopes for oxLDL and further enhance the inflammatory process (Borén et al., 2020).

1.1.4.2 Atheroma formation

Typical atheroma formation describes lipid core and fibrous cap formation (Owens et al., 2004). Figure 1-2 depicts several vascular modifications that follow LDL retention in the vessel wall. When smooth muscle cells (SMCs) are under stress, they can produce proteoglycans that facilitate LDL retention and oxidation and thus promote inflammatory responses during lesion formation (Lee et al., 2001). SMCs can express scavenger receptors, uptake LDL and contribute to foam cell formation (Allahverdian et al., 2014). Another study showed that both ECs and SMCs when treated with modified LDL *in vitro* produced the monocyte chemotactic protein-1 (MCP-1), also known as chemokine (C-C motif) ligand 2 (CCL2), aiding recruitment of inflammatory cells such as monocytes and SMCs exposure to modified lipids also promotes the secretion of chemoattractants like the CCL2 and the chemokine (C-C motif) ligand 5 (CCL5) which further promotes monocyte recruitment (Cushing et al., 1990)(Stocker and Keaney, 2004)(Soehnlein and Libby, 2021). SMC retain phenotypic plasticity, enabling them to undergo a switch from a contractile, quiescent phenotype to a synthetic, proliferative and migratory phenotype (Owens et al., 2004). Upon inflammatory stimuli, SMCs dedifferentiate to a proliferative and migratory phenotype which contributes to fibrous cap formation (Rzucidlo et al., 2007). Several studies have suggested multiple stimuli responsible for SMC phenotypic switching including activated macrophages (Rzucidlo et al., 2007), tumour necrosis factor-α (TNF-α), interleukin-1 beta (IL-1ß) and interferon gamma (IFN-γ) secreted from immune cells (Barillari et al., 2001), TNF-a and IL-1ß secreted from proinflammatory ECs (Sorokin et al., 2020), platelet derived growth factor (PDGF) via inhibition of contractile SMC proteins (Ha et al., 2015), oxLDL and oxidised phospholipids (Cherepanova et al., 2009)(Vengrenyuk et al., 2015). This phenotypic change is the critical step for intimal thickening and atherosclerosis progression (Rzucidlo et al., 2007). SMCs contribute to fibrous cap formation by migrating and populating the fibrous cap area and extracellular matrix production (Soehnlein and Libby, 2021). SMCs that lack normal SMC markers can express macrophage-like markers such as cluster of differentiation 68 (CD68) and galectin-3 (Gomez et al., 2013). In atherosclerotic mice lesions, it was observed that 30-70% of macrophage/foam cells were SMCs with similar findings in human lesions (Vengrenyuk et al., 2015)(Shankman et al., 2015)(Y. Wang et al., 2019)(Allahverdian et al., 2014). Cordes et al., showed with single-cell RNA

sequencing which allows the analysis of messenger RNA (mRNA) from a single cell and fate-mapping technologies, which involves the marking of a group of cells or a single cell during embryogenesis and tracing the descendants of these cells or one cell after the development has been completed, that SMCs in lesions can dedifferentiate into fibroblast- like cells (Cordes et al., 2009)(Tang et al., 2009)(VanHorn and Morris, 2021).

Macrophages located in lesion sites can take up lipids and promote foam cell formation. Interestingly, the number of macrophages has been found to significantly increase (20-fold) in mouse aorta during atherogenesis underling their contribution to foam cell formation and as a result lipid accumulation and inflammation (Galkina et al., 2006)(Barrett, 2020). Macrophages can also enhance inflammatory responses by releasing several cytokines (including IL-6, IL-12, IL-23, TNF-α and IL-1ß), chemokines (including CXCL-9, CXCL-10 and CXCL-11), reactive oxygen species and nitric oxide (Poznyak et al., 2021). They also interact with SMCs, enhancing the inflammatory response by secreting further proinflammatory cytokines and extracellular matrix components, which further promote lipoprotein retention and lipid core expansion (Barrett, 2020)(Poznyak et al., 2021). The inability of macrophages to migrate results in a failure to reduce inflammation, thus leading to atheroma progression towards an advanced/vulnerable plaque phenotype (Barrett, 2020). Moreover, their inability to migrate and resolve inflammation promotes macrophage apoptosis, accumulation of dead cells at the plaque site and necrotic core formation (Barrett, 2020)(Poznyak et al., 2021). Under physiological conditions, clearance of apoptotic macrophages and SMCs by phagocytes takes place, a process called efferocytosis (Tabas, 2007). However, efferocytosis is defective in advanced plaques promoting necrosis and thus the formation of a necrotic core (Tabas, 2007).

1.1.4.3 Calcification

Vascular calcification is prevalent in atherosclerosis and other pathologies and is defined as mineral accumulation into the intima or media of the artery wall (Kapustin et al., 2015). A meta-analysis study showed that vascular calcification in the artery wall is linked with 3-4 fold increased risk for CVD events and mortality (Rennenberg et al., 2009). Another study examined coronary artery calcium scores validated with electron-beam tomography in asymptomatic patients and showed

that coronary artery calcium could independently predict mortality (Budoff et al., 2007). A meta-analysis study confirmed the results mentioned above showing that the absence of coronary artery calcium was associated with low risk of cardiovascular events (Abuzaid et al., 2021). However, other studies suggest that plaque calcification is associated with plaque stability, stable fibrous cap formation and limited macrophage infiltration (Shaalan et al., 2004)(Wahlgren et al., 2009). Computerised tomography (CT) scans of calcified coronary aortas showed increased SMC markers and decreased macrophage markers and inflammation, characteristic of stable plaques (Karlöf et al., 2019). Carotid plaque calcification was proposed as a novel marker for ischemic event risk prediction (Shaalan et al., 2004). On the contrary, microcalcifications located in thin usually fibrous caps can advance plaque instability (Vengrenyuk et al., 2006). These findings highlight the dual role of vascular calcification in atherosclerosis. A possible explanation comes from high-resolution imaging and clinical data, showing that microcalcification is found in areas with low levels of collagen (collagen is responsible for formation of the thick fibrous cap (Nadkarni et al., 2009)), whereas heavily calcified regions are bordered with collagen fibers (Hutcheson et al., 2016). Studies showed loss of SMCs in calcified aortas and that SMC phenotypic transdifferentiation to chondrocytic, osteoblastic and osteogenic phenotypes drive the calcification process (Steitz et al., 2001)(Tyson et al., 2003)(Speer et al., 2009)(Briot et al., 2014).

1.1.4.4 Advanced/vulnerable plaques

Most complications associated with atherosclerosis are caused due to plaque rupture (Fishbein, 2010). A vulnerable plaque is characterised as a plaque prone to rupture usually due to a thin fibrous cap (Fishbein, 2010). Pathological evidence suggests that plaques with enlarged lipid cores, thin fibrous caps, prominent inflammation in the area and limited SMCs and collagen present in the region are prone to rupture; however, these data provide associations but do not provide mechanisms explaining plaque rupture (Fishbein, 2010). The necrotic core expansion due to macrophage and SMC cell death leads to increased inflammation in the plaque region possibly because of phagocyte's inability to further remove cell debris from the area, thus transforming a stable plaque to a vulnerable plaque (Bentzon et al., 2014). Increased proteolysis in atherosclerotic plaques has been shown to contribute to plaque rupture (Chen et al., 2002). Activated macrophages have been located in caps of ruptured plaques (Lendon et al., 1991). Macrophages

secrete proteolytic enzymes like matrix metalloproteases (MMPs) that are responsible for plaque destabilization and rupture through collagen degradation (Gough et al., 2006)(Fabrice et al., 2008)(Quillard et al., 2011)(Peeters et al., 2011). Detection of MMPs and other proteases has been proposed as a biomarker for early vulnerable plaque detection (Chen et al., 2002)(Peeters et al., 2011)(Scholtes et al., 2012). Two MMPs, MMP-8 and MMP-9, have been reported to contribute to plaque destabilization and rupture by degradation of the fibrous cap (Loftus et al., 2000)(Molloy et al., 2004).

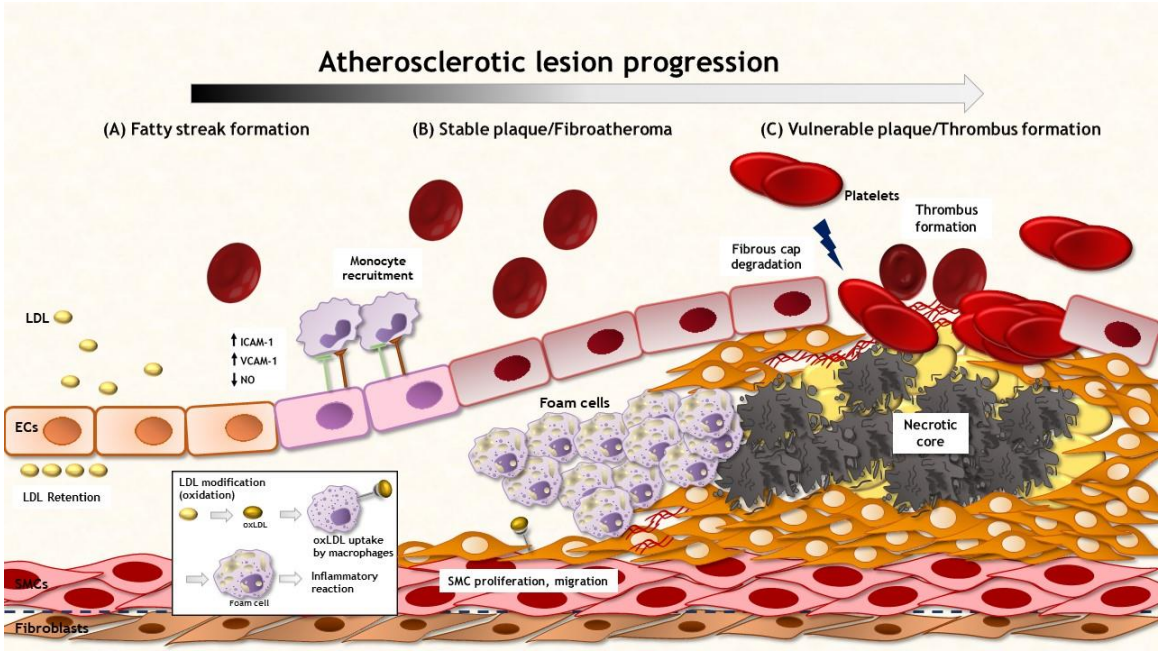

Figure 1-2 Atherosclerotic plaque formation

The diagram depicts both early and late stages of atherosclerotic development: (A) Low density lipoprotein (LDL) retention to the vascular wall along with disturbed flow induce the expression of adhesion molecules like vascular cell adhesion molecule-1 (VCAM-1) and intercellular adhesion molecule-1 (ICAM-1)) on ECs. Adhesion molecules are responsible for monocyte migration to the sub endothelial space where they differentiate to macrophages. By uptake of oxidised LDL (oxLDL), macrophages transform into foam cells. (B) Upon inflammatory activation, foam cells undergo apoptosis and necrosis forming the lipid core of a stable atherosclerotic plaque. SMCs contribute to the development of thick stable fibrous cap via macromolecule secretion including collagen, elastin, fibronectin and extracellular matrix. (C) A vulnerable plaque prone to rupture and subsequent thrombus formation is mainly caused by a thin fibrous cap. Plaque rupture has been associated with matrix metalloproteinase (MMPs) activity secreted from macrophages. Adapted from ((Charla et al., 2020), published under a Creative Commons CC-BY license).

1.1.5 Role of SMCs and ECs in atherosclerosis progression

Endothelial dysfunction is a driving force in atherosclerosis and studies have highlighted its prognostic value (Ludmer et al., 1986)(Bonetti et al., 2003). Evidence suggests that endothelial dysfunction occurs early in disease progression even when no structural alterations in the vessel wall are visible (Liao et al., 1991)(Reddy et al., 1994). Many factors can affect normal endothelial function including hyperlipidaemia, hypertension, diabetes, oxidative stress, disturbed blood flow or pro-inflammatory cytokines (Gimbrone and García-Cardeña, 2016). Endothelial dysfunction leads to reduced production of nitric oxide (NO) and impaired vasodilation while one of NO's main functions is the prevention of LDL oxidation (Hogg et al., 1993)(Davignon and Ganz, 2004). Moreover, ECs can differentiate into mesenchymal stem cells (MSCs) a process known as endothelial-to-mesenchymal transition (EndMT) (Souilhol et al., 2018). That transition comes with the loss of endothelial markers such as vascular endothelial (VE) cadherin, cluster of differentiation 31 (CD31) and von Willebrand factor and expression of mesenchymal markers such as smooth muscle protein 22α (SM22α), alpha smooth muscle actin (αSMA) and calponin (Frid et al., 2002)(Krenning et al., 2008). Mesenchymal cells have been associated with plaque development, stability and calcification (Boström et al., 2016)(Souilhol et al., 2018). Lineage tracking studies in apolipoprotein E (APOE) knockout (KO) mice have confirmed the presence of endothelial origin mesenchymal cells in atherosclerotic plaques (Chen et al., 2015)(Evrard et al., 2016). In both studies, approximately 30% of all plaque cells were mesenchymal cells expressing Notch3 or fibroblast activation protein and had originated from the endothelium (Chen et al., 2015)(Evrard et al., 2016).

SMCs regulate vascular tone. To do so, mature SMCs are terminally differentiated into a contractile phenotype expressing contractile proteins and ion channels (Rzucidlo et al., 2007). However, they retain remarkable phenotypic plasticity and can undergo phenotypic change towards a proliferative phenotype upon certain stimuli (Rzucidlo et al., 2007). After vascular injury e.g., after stent implantation or angioplasty, or exposure to pro-inflammatory or atherogenic molecules like oxLDL, SMCs demonstrate increased rates of proliferation and migration, increased synthesis of extracellular matrix proteins and decreased expression of contractile markers (Rzucidlo et al., 2007)(John Liu et al., 2014). These processes are considered key steps during disease progression (Rzucidlo et al., 2007). Studies have showed that enzymatically modified LDL induces SMC phenotypic switching

towards a migratory osteoblast phenotype (Chellan et al., 2018). Studies have also shown phenotypic switching of SMCs towards a macrophage phenotype (Vengrenyuk et al., 2015)(Chattopadhyay et al., 2021). A lineage tracking study showed that macrophages with phagocytic activity and MSCs identified in atherosclerotic plaques were of SMC origin (Shankman et al., 2015). Evidence suggests that the phenotypic switching to a macrophage-like foam cell may exacerbate the disease progression by reduced lipid clearance, expansion of necrotic core and plaque size and promotion of plaque instability via reduced SMC proliferation and strengthening of the fibrous cap (Vengrenyuk et al., 2015)(Bennett et al., 2016). The phenotypic transition of SMCs during atherosclerosis has a great impact on the disease development.

ECs and SMCs are key cell types populating the vessel wall and participating in vascular homeostasis. Studies have focused on the role of individual cell types in atherosclerosis progression, but little is known regarding EC-SMC communication during disease development. Reports suggest that communication could be facilitated by direct contact of these two cell types (Li et al., 2018). Other signals like endothelium-derived hyperpolarizing factor (EDHF) or NO transfer from ECs to SMCs via gap junctions is another way of interaction between these two cell types in the vessel wall (Griffith et al., 2004)(Griffith, 2004)(Li et al., 2018).

1.1.6 Treatment of atherosclerosis

No current treatment can reverse atherosclerosis; however, current treatments aim to slow down the disease's progression. Managing atherosclerosis risk factors could help slow down the disease and other heart or circulatory diseases (Bergheanu et al., 2017). Studies have shown that risk factor modification like adopting a healthy diet, active lifestyle and cessation of smoking have led to reduced mortality, stoke or MI incident (Libby and Theroux, 2005). Front-line drug treatment for atherosclerosis involves statin prescription which inhibits the 3-hydroxy 3-methyl glutaryl CoA (HMG-CoA) reductase, which catalyses the conversion of HMG-CoA to mevalonic acid, an important step during cholesterol biosynthesis, in order to reduce LDL-C in circulation for primary and secondary prevention of CVD (Welsh et al., 2017)(Bergheanu et al., 2017). Clinical studies have shown the positive effect of lipid lowering therapies with subsequent LDL reduction and reduced cardiovascular risk in these patients (Aronow et al., 2001)(Mihaylova et al., 2012)(Sabatine et al., 2015)(Mach et al., 2020). Other

studies debate that statins have pleiotropic effects and can ameliorate inflammation by reducing c-reactive protein (CRP) levels apart from reducing LDL-C levels (Kinlay et al., 2003)(Goicoechea et al., 2006)(Ridker et al., 2008)(Ridker et al., 2009)(Khurana et al., 2015).

Even though lipid lowering therapies have reduced cardiovascular risk, cardiovascular events can still occur (Libby, 2005)(Geovanini and Libby, 2018). Inflammation has been suggested to be responsible for the residual cardiovascular risk after lipid lowering therapy so targeting the inflammatory pathway of atherosclerosis could be an alternative approach to atherosclerosis treatment (Welsh et al., 2017)(Geovanini and Libby, 2018). Clinical data from the Canakinumab Anti-inflammatory Thrombosis Outcome Study (CANTOS) and the Colchicine Cardiovascular Outcomes Trial (COLCOT) support that hypothesis, showing that anti-inflammatory treatment resulted in the reduction of recurrent cardiovascular events (Ridker et al., 2017)(Tardif et al., 2019). Targeting inflammation as a secondary prevention measure seemed to be effective as seen in the non-blinded "LoDoCo" trial (Nidorf et al., 2013). Co-administration of colchicine with statins was able to prevent recurrent cardiovascular events (Nidorf et al., 2013). The Justification for the Use of Statins in Primary Prevention: an Intervention Trial Evaluating Rosuvastatin (JUPITER) clinical trial examined the effect of preventative administration of rosuvastatin in healthy participants with low LDL levels but elevated high-sensitivity C-reactive protein (hs-CRP) levels (Ridker et al., 2008). The rosuvastatin group demonstrated significantly reduced risk for future cardiovascular events (Ridker et al., 2008). Other potential anti-inflammatory agents for atherosclerosis treatment have been proposed. Briefly, some anti-inflammatory agents include: methotrexate, aspirin, inhibitors of phospholipase A2 (PLA2) and cyclooxygenase-2 (COX-2), inhibitors of leukotriene pathway, interleukin-6 (IL-6) inhibition, TNF-α inhibitors and IFN-γ inhibitors (summarized in (Charo and Taub, 2011)(Bäck and Hansson, 2015)(Chistiakov et al., 2018)).

Another druggable target for atherosclerosis treatment is inhibition of proprotein convertase subtilisin/kexin type-9 (PCSK-9). PCSK-9 is responsible for the degradation of LDL receptors in the liver and inhibition of the enzyme results in better liver absorption of LDL-C and lower LDL-C plasma concentration (Bergheanu et al., 2017). PCSK9 inhibitors, alirocumab and evolocumab, were shown to

effectively reduce LDL-C levels (Cannon et al., 2015)(Bohula et al., 2018). A metanalysis of Studies of PCSK9 Inhibition and the Reduction of Vascular Events (SPIRE)-1 and −2 clinical trials showed that both statin therapy and bococizumab did not reduce residual inflammatory risk (Pradhan et al., 2018). The authors suggest that around 47% of all participants received statin therapy and bococizumab demonstrated residual inflammatory risk assessed by hsCRP levels (Pradhan et al., 2018). Kühnast et al., showed that administration of alirocumab alone and in combination with atorvastatin in APOE KO mice under high fat diet resulted in reduced number of macrophages and reduced necrotic core in the plaque area (Kühnast et al., 2014). The authors suggested that alirocumab not only reduced plaque size but improved plaque composition by reducing monocyte and macrophage recruitment and increasing SMCs and collagen content (Kühnast et al., 2014).

RNA interference (RNAi) based therapies for atherosclerosis are also being developed (Kettunen et al., 2022). This includes the use of small interfering RNAs (siRNAs) and antisense oligonucleotides (ASOs) targeting mRNAs to reduce vascular inflammation or lipid levels (Kettunen et al., 2022). Inclisiran, which targets PCSK9, is a siRNA drug in phase III clinical trials for homozygous and heterozygous familial hypercholesterolemia which has been shown to cause a reduction in LDL levels (Ray et al., 2020)(M. M. Zhang et al., 2021). Two other clinical trials are ongoing to investigate the safety and efficacy of inclisiran and ORION-4 is estimated to finish in 2026 will provide evidence regarding inclisiran's effect on cardiovascular outcomes (Byrne et al., 2021). Despite greater understanding of the process of atherosclerosis and the development of new and innovative therapies there is still a large global disease burden highlighting that increased understanding of the disease and identification of new therapeutic targets is still required.

1.2 Extracellular vesicles

1.2.1 Biogenesis of extracellular vesicles

The term extracellular vesicle (EV) was first used in 1971 (Bonucci, 1970)(Aaronson et al., 1971). EVs are small membrane-bound vesicles secreted from all types under normal and pathological conditions. EVs have attracted increasing interest recently for the role they may play in intercellular signalling in the setting of health and disease and as biomarkers. EVs have been implicated in atherosclerosis development in early and late stages of the disease (see later). The Minimal Information for Studies of Extracellular Vesicles 2018 (MISEV2018) clearly state that since no consensus has been reached as what could be a specific EV marker for each category, categorising EVs based on a biogenesis pathway should be avoided, instead the generic term EVs should be used (Théry et al., 2018). In this study the biogenesis pathway of EVs with endosomal origin (traditionally called exosomes) and the biogenesis of shedding EVs from the plasma membrane (traditionally called microvesicles) will be described. These two vesicle types have been studied the most regarding their role in cardiovascular pathology, including atherosclerosis.

Classification of EVs is traditionally based on their size and biogenesis with 3 distinct categories: exosomes, microvesicles and apoptotic bodies (Boulanger et al., 2017). Smaller EVs are called exosomes with sizes ranging from 30 nm to 150 nm while larger EVs are called microvesicles with sizes ranging from 100 nm to 1 μm. That overlap in size makes distinction between the two populations difficult. Apoptotic bodies have larger sizes from 1 μm up to 5 μm and are released during cell apoptosis (Charla et al., 2020). Biogenesis of EVs of endosomal origin begins with the capture of active molecules from the extracellular space via invagination of the plasma membrane during endocytosis (Figure 1-3). The early-sorting endosome (ESE), an early station for eukaryotic cells to sort cargoes through the endocytic pathways, is formed which either can mature into late-sorting endosomes (LSEs), which is a later station of cargo sorting via the endocytic system, or molecules can be recycled back to plasma membrane (Kalluri and LeBleu, 2020). The LSEs are responsible for the biogenesis of intraluminal vesicles (ILVs) leading to generation of multivesicular bodies (MVBs) and sorting of proteins for lysosomal degradation (Hu et al., 2015). The formation of MVBs inside LSEs through inward budding of the endosomal membrane is mediated by proteins of

the endosomal sorting complex required for transport (ESCRT) (Mayers and Audhya, 2012). MVBs can follow one of two pathways through either degradation by fusion with lysosomes or they can fuse with the plasma membrane and release their cargo, endosomal EVs or exosomes, into the extracellular space (Kahlert and Kalluri, 2013). The ESCRT machinery is responsible for enrichment of ILVs with lipids like sphingomyelins, phospholipids and cholesterol (ALIX dependent process), thus enhancing the maturation process of EVs (Kobayashi et al., 1999)(Kobayashi et al., 2002)(Chevallier et al., 2008)(Trajkovic et al., 2008)(Bissig and Gruenberg, 2014). MVBs which did not follow lysosomal degradation are filled with ILVs, these are pre-cursor vesicles which lead to the formation of endosomal EVs. Endosomal EVs or exosome release is mediated via the fusion of MVBs with the plasma membrane and release of their cargo into the extracellular space (Kahlert and Kalluri, 2013).

A tetraspanin, CD63 which is also an EV-associated marker, has been found to be abundant in ILVs and endosomal membranes (Pols and Klumperman, 2009). Studies have found that CD63 regulates ILV formation in an ESCRT dependent and independent way and depletion of CD63 inhibited ILV production (van Niel et al., 2011)(Edgar et al., 2014). Other tetraspanins like CD9, CD81 and CD82, which are EV-associated markers as well, have been shown to regulate cargo sorting inside ILVs (Buschow et al., 2009)(Chairoungdua et al., 2010). The ESCRT pathway is comprised of four complexes: ESCRT-0 is responsible for cargo gathering, ESCRT-I and ESCRT-II are responsible for budding formation, while ESCRT-III drives the vesicle scission (Henne et al., 2011). ALIX is an accessory protein to ESCRT-III that helps recruitment of ESCRT-III and is also an EV-associated marker (Henne et al., 2011)(Théry et al., 2018). ALIX is a cytoplasmic protein that has been shown to regulate cell death via caspase dependent and independent mechanisms and can also regulate the lysosome machinery by mediating the sorting of G protein-coupled receptors for lysosomal degradation (Trioulier et al., 2004)(Dores et al., 2016). Studies showed that ALIX binds to Tumor Susceptibility Gene 101 (TSG101) which is an ESCRT-I component and EV marker (Février and Raposo, 2004)(Théry et al., 2018). During budding of vesicles in the MVB, the ESCRT pathway transfers proteins to ILVs like TSG101 (Buschow et al., 2005)(Clague et al., 2012)(Colombo et al., 2013). Endosomal EV biogenesis can occur in an ESCRT-independent way as shown by silencing of ESCRT subunits which did not inhibit the formation of MVBs (Stuffers et al., 2009).

Either way, biogenesis of exosomes or endosomal EVs results in elimination of some proteins from the plasma membrane as the presence of receptors, ligands etc from the membrane of the origin cells has been confirmed on the surface of exosomes (Hu et al., 2020). Evidence suggests that EV secretion is also a way of receptor downregulation and thus maintaining cellular homeostasis (Johnstone et al., 1991)(Katzmann et al., 2002).

Biogenesis of microvesicles is different from that of EVs as rather than being of endosomal origin, it involves shedding of microvesicles from the plasma membrane where they are released from the cell (Tricarico et al., 2017) (Figure 1-3). Microvesicles are secreted from cells under normal and pathological conditions (Ståhl et al., 2019). Like EVs with endosomal origin, they also carry membrane proteins (Ståhl et al., 2019). Many pathways have been proposed as to how microvesicles are shed from the plasma membrane. The outward budding process begins with clustering of lipids and proteins in the plasma membrane (Tricarico et al., 2017). For microvesicles to be released, cytoskeletal changes in the cell are required. Pasquet et al., showed that microvesicle release from platelets was calcium dependent and influx of calcium resulted in activation of calpain, a calcium-sensitive protease that phosphorylates target proteins of the cytoskeleton such as myosin heavy chain and talin (Pasquet et al., 1996). Microvesicle cargo is concentrated in the area close to where the budding of the membrane happens, so it can be incorporated inside the microvesicles (Tricarico et al., 2017). The unmasking of the cytoskeleton aids enrichment of the microvesicle cargo with proteins and genetic material (Tricarico et al., 2017).

One study suggested that microvesicle shedding from the plasma membrane is mediated through the ESCRT machinery which is also involved in EV generation via endosomal origin (Nabhan et al., 2012). This study suggested that TSG101, which is part of the ESCRT-I machinery, interacts with arrestin domain-containing protein 1 (ARRDC1) (Nabhan et al., 2012). That interaction caused TSG101 to relocate from the endosome to the plasma membrane and to facilitate the release of microvesicles enriched in TSG101 and ARRDC1 (Nabhan et al., 2012). Another study showed that ADP-ribosylation factor 6 (ARF6) is associated with microvesicle release from a tumour cell line (Muralidharan-Chari et al., 2009). Authors showed ARF6 GTP-binding protein induced phospholipase D activation and recruitment of the extracellular signal-regulated kinase (ERK) to the plasma membrane. ERK was

responsible for the phosphorylation and activation of myosin light-chain kinase (MLCK). The authors suggested that MLCK-ARF6 mediated activation was necessary for microvesicle release and that ARF6 inactivation resulted in disrupted microvesicle release from cells (Muralidharan-Chari et al., 2009). The mechanistic process of exosomes and microvesicles is different and thus explains their differences regarding surface markers and cargo.

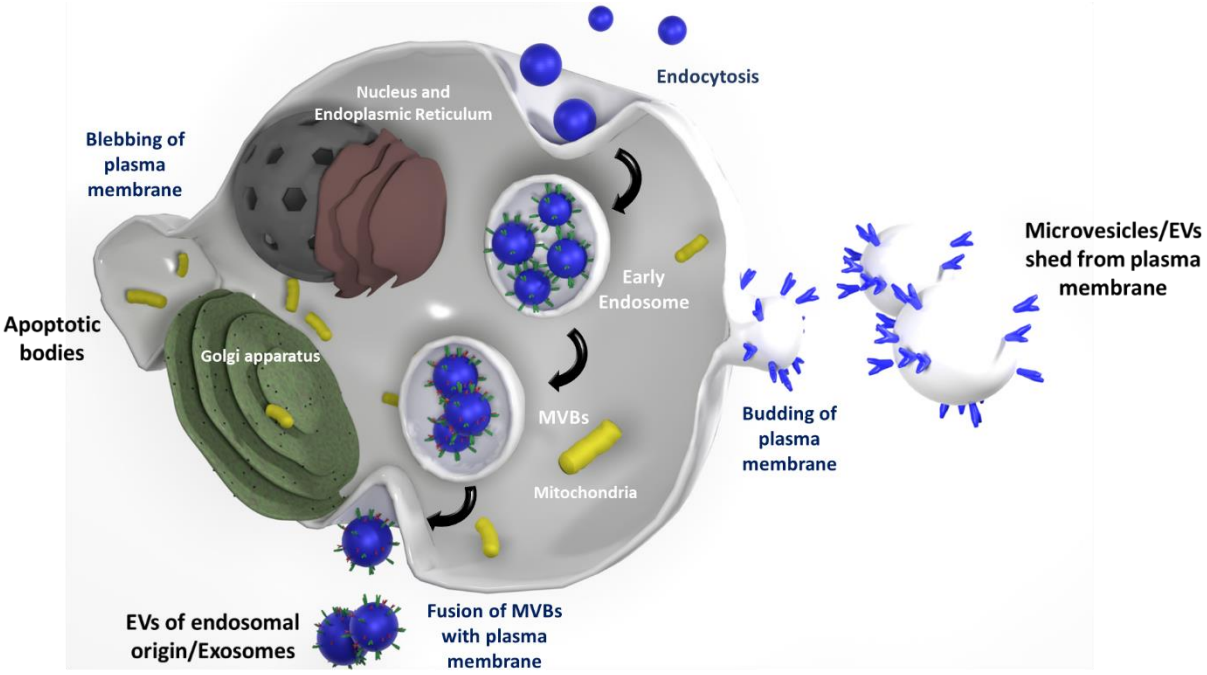

Figure 1-3 Biogenesis of EVs

EVs can be categorised based upon their size and biogenesis. Apoptotic bodies are large vesicles secreted from dying cells. They are formed after blebbing of the plasma membrane. Microvesicles or EVs shed from the plasma membrane are generated after the outward budding of the plasma membrane. Exosomes or EVs of endosomal origin are a product of inward budding of the MVBs with the plasma membrane. Figure elements were created using Blender 2.8 which is released for free use under a GNU General Public License (GPL). Adapted from ((Charla et al., 2020), published under published under a Creative Commons CC-BY license).

1.2.2 Heterogeneity of extracellular vesicles

EVs are a heterogenous population of vesicles with different subcellular origins, cellular origin, cargo and size. Classical EV characterisation suggests an overlap in size between exosomes and microvesicles, making their distinction impossible. EVs demonstrate diverse biological function with studies reporting contradicting results for the same EV populations. Current isolation protocols result in isolation of mixed sized EV populations including exosomes or microvesicles (van Niel et al., 2018). Willms et al., showed that cells released subpopulations of EVs and the authors classified these EV populations as exosomes, with distinct biological cargo and functions (Willms et al., 2016). All the above evidence render the study of individual classes of EVs and characterisation of EV populations extremely difficult (van Niel et al., 2018).

There are many steps during EV biogenesis that can affect the size of released vesicles. Studies have showed that MVBs can contain different sizes ILVs and this contributes to EV heterogeneity (Edgar et al., 2014)(Colombo et al., 2014). ILV size can be influenced by the cargo encapsulated in them (Edgar et al., 2014). However other mechanisms may regulate pinching off of ILVs and generation of heterogeneous size EVs (Edgar et al., 2014). The choice of isolation technique can also contribute to size heterogeneity of isolated EVs with studies showing that different isolation methods can isolate different EV subpopulations (Colombo et al., 2014).

Cargo sorting inside EVs has not been fully understood but mechanisms during EV generation like ESCRT machinery seem to have an important role (Colombo et al., 2014). The microenvironment of a cell or the cell type may dictate which microRNA (miRNA) for example will be enriched in EVs (van Balkom et al., 2015)(Bronisz et al., 2016). Studies have reported that EVs contain low copy numbers of miRNAs, as little as one copy per EV (Chevillet et al., 2014)(Lee et al., 2019). Lee et al., reported that only 6% of the total EV population was enriched in miRNAs (Lee et al., 2019). Thakur et al., made a similar observation regarding DNA cargo of EVs, reporting that only a subpopulation of EVs, around 10%, contained DNA (Thakur et al., 2014). Proteomic analysis of EVs revealed the existence of EV subpopulations with distinct protein markers (Kowal et al., 2016). The number of studies reporting functional miRNA-EV transfer has increased (Goetzl et al., 2017)(Chang et al., 2019).

All the above data indicate the existence of subpopulations of EVs with diverse composition and biological functions and can explain their varied and contrasting effects on recipient cells. Current limitations in isolation techniques limit the ability to study the role of EV subpopulations and their distinct biological functions. Single-vesicle methodologies could be used to study EV subpopulations and their diverse roles.

1.2.3 EV uptake by recipient cells

An overwhelming amount of studies suggest that EVs are being taken up by cells, however, the exact mechanism of uptake, needs to be elucidated as studies indicate various mechanisms of EV uptake by recipient cells (Mulcahy et al., 2014). Newer techniques allow visualisation of EV uptake by cells. Labelling of EVs with fluorescent lipid membrane dyes including PKH67, PKH26, rhodamine B, Dil, DiD or membrane dyes such as carboxyfluorescein succinimidyl ester and maleimide (fluorescently conjugated) allow visualisation of EVs by microscopy (Mulcahy et al., 2014). Different mechanisms of uptake have been reported including endocytosis, clathrin-mediated endocytosis, phagocytosis, micropinocytosis, plasma or endosomal membrane fusion, caveolin-mediated endocytosis and EV uptake via of lipid rafts and specific protein–protein interactions (Asuka et al., 2013)(Mulcahy et al., 2014). Studies have shown that different mechanisms of uptake can take place in different cells. Nanbo et al., showed that EV uptake by epithelial cells was mediated via caveola-dependent endocytosis while EV internalisation by dendritic cells was mediated via phagocytosis and endocytosis (Morelli et al., 2004)(Asuka et al., 2013). It has been suggested that the presence of certain ligands or receptors on the cell surface is required for EV uptake. Skokos et al., showed that blocking of CD91 on dendritic cells impaired EV uptake (Skokos et al., 2003).Cell-specificity of EV uptake is yet to be determined with reports suggesting that EVs are taken up by every cell type and other studies suggesting ligand dependent EV uptake by cells (Svensson et al., 2013)(Mulcahy et al., 2014). Either way, EV uptake by recipient cells mediates cell communication and can induce signalling pathways in recipient cells (Kwok et al., 2021). EV uptake by cells in atherosclerotic plaques could affect disease progression. Gao et al., showed that aorta of APOE KO mice internalised dendritic-EVs resulting in increased plaque size (Gao et al., 2016).

1.2.4 EV cargo and function

Initially, EVs were thought to function as a cell recycling system as was shown by early studies reporting the transfer of the transferrin receptor in vesicles formed during reticulocyte maturation (Harding et al., 1983)(Johnstone et al., 1987). It is now clear that EVs have numerous diverse biological functions like participating in the immune response, delivering proteins and nucleic acids to recipient cells and mediating cell-cell communication, as well as regulating biological process like apoptosis, proliferation and migration (Kalluri and LeBleu, 2020).

EV cargo includes proteins, lipids, and nucleic acids such as DNA and RNA (Jabalee et al., 2018). RNA cargo of EVs has attracted a lot of attention. Sequencing studies have found the presence of mRNA, ribosomal RNA, transfer RNA, miRNA and other small non coding RNAs (Jabalee et al., 2018). MiRNA abundance in EVs is different among cell types. It was found that miRNAs accounted for 5-30% of small RNA cargo in EVs secreted from colorectal cancer cell lines (DKO-1, Dks-8, and DLD-1 cells), breast cancer cell lines (MA-11, MDA-MB-231, Hs578T, AU565, HCC1428, MCF7, HCC1187, DU4475, HCC1569), pancreatic cancer cell line (HPAF-II) and prostate cancer cell line (LNCaP) (Cha et al., 2015)(Fiskaa et al., 2016). Another study showed that miRNA content in EVs isolated from HEK293T cells, which are human embryonic kidney 293 cells expressing a mutant version of SV40 large T antigen, accounted for less than 1% of small non-coding RNAs (Shurtleff et al., 2017). This variation could be explained by the different cell origin of EVs. Another study analysed the RNA profile of EVs isolated from two human breast cancer cell lines, a high metastatic cell line (MDA-MB-231) and a low metastatic cell line (MDA-MB-436) (Jenjaroenpun et al., 2013). Several RNAs were identified in the two EV populations and authors suggested that EV RNA content reflected their cell of origin RNA signature with unique small RNAs specific for low metastatic cell line (MDA-MB-436) and specific to the high metastatic cell line (MDA-MB-231) (Jenjaroenpun et al., 2013). Circulating EV miRNA profiles have also been studied in patients with other cancer types including gallbladder cancer and prostate cancer (Shin et al., 2021)(Ueta et al., 2021). This study, as many others, set the scene for the use of EV-miRNA as a biomarker in various diseases (Kinoshita et al., 2017)(Chong et al., 2019). MiRNA-EV transfer has been suggested as a way of cell-cell communication. Fernández-Messina et al., showed that EV-transfer of mmu-miR-20-a-5p, mmu-miR-24-3p and mmu-miR-155-3p from CD4+T-cell-derived EVs (isolated from wild type (wt) mice) to recipient B lymphocytes (B lymphocytes

were isolated from DICER-deficient mice thus unable to produce miRNAs and allowing the detection of transferred miRNAs) targeted key molecules regulating B lymphocyte function such as Bcl-2-like protein 11 (BCL2L11) and phosphatase and tensin homolog (PTEN) (Fernández-Messina et al., 2020). Another study identified 761 mature miRNAs (belonging to major miRNA families such as miR-21-5p, miR-100-5p and let-7) with miR-29a significantly enriched in human osteoblast-derived EVs (Simian virus 40-immortalized human osteoblast cells) (Morhayim et al., 2016). Expression of PTEN, B-cell lymphoma 2 (BCL2), HMG-Box Transcription Factor 1 (HBP1) and CDC42 Effector Protein 2 (CDC42EP2), which are targets of miR-29a, were found reduced in hematopoietic stem and progenitor cells (HSPCs) and osteoblast treatment of these cells promoted proliferation and cell cycle progression of HSPCs indicating that osteoblast-EVs and their miRNA cargo may regulate proliferation in HSPCs (Morhayim et al., 2016). The studies mentioned above show that miRNA-EV transfer may regulate cellular signalling related to cell proliferation, cell function and cell cycle progression.

Messenger RNA contributes little to EV cargo, unlike miRNAs. Next generation sequencing of human glioma stem cell derived EVs showed that mRNA content of EVs was below 10% of total RNA reads (Wei et al., 2017). Authors showed that the majority of reads corresponded to fragments of mRNA rather than full length mRNA (Wei et al., 2017). An interesting observation after correlation and clustering analysis of human glioma stem cell transcriptome was that larger EVs such as microvesicles demonstrated greater similarity with their cell transcriptome compared to smaller EVs (Wei et al., 2017). Another difference between larger and small EVs was that larger EVs were found to be more enriched in mRNAs whereas smaller EVs were found to be more enriched in miRNAs, which also could explain why larger EVs demonstrated high transcriptome similarity to human glioma stem cells (Wei et al., 2017). Transcriptomic analysis of EVs of mouse mast cells (MC/9) identified 1272 transcripts in MC/9-derived EVs (including cytochrome C oxidase subunit 5b (COX5B), specificity protein 1 (SP1) and heat shock protein 8 (HSPA8)) and authors showed successful radioactive labelled MC/9-EV mRNA transfer to recipient MC/9 cells (Valadi et al., 2007). Moreover, proteomic analysis identified 3 mouse proteins, cell division control protein 6 (CDC6), zinc finger protein 271 (ZNF271P) and cytochrome c oxidase subunit 7A (COX7A2) whose mRNA transcripts were identified in MC/9-EVs, to be present in human mast cells (HMC-1) after MC/9-derived EVs treatment suggesting that mRNA

delivery by EVs to recipient cells could be translated into proteins (Valadi et al., 2007). A study that profiled the mRNA of circulating tumour cells and EVs isolated from plasma in patients with metastatic breast cancer showed that cells and EVs shared only 5% common positive signals (Keup et al., 2018). Differences were observed in transcripts poly(ADP-Ribose) Polymerase 1 (PARP1), epidermal growth factor receptor (EGFR), anaplastic lymphoma kinase (ALK), aurora kinase A (AURKA), KIT proto-oncogene receptor tyrosine kinase (KIT), AKT serine/threonine kinase 2 (AKT2), erb-b2 receptor tyrosine kinase 2 (ERBB2), phosphatidylinositol-4,5-bisphosphate 3-kinase catalytic subunit alpha (PIK3CA) and mechanistic target of rapamycin kinase (MTOR) in the EVs vs circulating tumour cells in the same patient cohort; transcripts related to cell growth, proliferation and division of cancer cells (Keup et al., 2018). However, the authors underlined that since only 5% common signals were shared between EV mRNA profile and tumour cell mRNA profile, caution in choosing the biomarker source should be applied (Keup et al., 2018).

EVs also carry DNA which can be either genomic or mitochondrial (Lázaro-Ibáñez et al., 2014)(Sansone et al., 2017). Németh et al., also showed that ciprofloxacin exposure of Jurkat cells induced surface associated DNA on the surface of EVs which could be degraded with DNase treatment and interacted with fibronectin indicating a mechanism for how EVs interact with extracellular matrix molecules (Németh et al., 2017). An interesting observation was that the DNA identified on EVs aligned with both mitochondrial sequences (including mitochondrial (mt) control region and mitochondrially encoded 12S RNA (MT-RNR1)) and chromosomal sequences (including glyceraldehyde 3-phosphate dehydrogenase (GAPDH) and tumor protein 53 (TP53)) (Németh et al., 2017). Authors mentioned that ciprofloxacin treatment resulted in increased percentage of DNA binding proteins such as histone H4 and histone H2B, proteins related to oxidative stress such as heat-shock protein 90 alpha (HSP90a) and heat shock cognate 71 kDa protein (HSP7C), and proteins related to defence responses such as L-lactate dehydrogenase B chain (LDHB) on the surface of Jurkat-derived EVs (Németh et al., 2017). However, the answer to the question on how or why DNA was recruited on the surface of EVs remained unknown. Fischer et al., also detected surface associated DNA on human bone marrow derived mesenchymal stromal cells (BM-hMSC)-derived EVs and intravesicular DNA in BM-hMSC-EVs (Fischer et al., 2016). Thakur et al., showed that when EVs were treated with deoxyribonuclease

(DNase), an enzyme that degrades DNA via cleavage of phosphodiester bonds on the DNA backbone, DNA molecules with sizes larger than 2.5 kb were degraded but DNA molecules with sizes between 100 bp and 2.5 kb were intact (Thakur et al., 2014). The authors concluded that EVs packaged DNA molecules with sizes between 100 bp and 2.5 kb and the larger DNA molecules were not enriched in EVs (Thakur et al., 2014). Studies have showed that EV-DNA can be transferred from EVs to recipient cells and result in increased mRNA expression by transcription of EV-DNA into mRNA (Cai et al., 2013)(Lee et al., 2014). Sansone et al., showed horizontal transfer of mitochondrial EV-DNA from cancer-associated fibroblast EVs to recipient cancer stem-like cells (Sansone et al., 2017). The mitochondrial DNA was identified in recipient cells and authors suggested that the DNA participated in resistance of cancer cells induced from hormone therapy (Sansone et al., 2017). Another study identified cell-free tumour DNA packaged in EVs which previously was thought to derive from tumour cells (Fernando et al., 2017). These studies pave the way for discovery of DNA-EV and miRNA-EV biomarkers for disease prevention and diagnosis.

Protein cargo of EVs sometimes reflects their biogenesis process and their cell of origin as they carry protein markers from the cell membrane of their secreted cell. EVs are enriched in tetraspanins like CD63, CD9 and CD81, ESCRT pathway components like TSG101 and ALIX, integrins and glycoproteins (Heijnen et al., 1999)(Akers et al., 2013). Receptors and ligands have been identified on the surface of EVs which can regulate EV uptake by recipient cells or EV cellular signaling (Hu et al., 2020). Their lumen cargo include receptors, peptides, and enzymes (Al-Nedawi et al., 2008)(Y. T. Wang et al., 2020). EVs can transfer their protein cargo retaining functionality and exert a biological effect on recipient cells. Al-Nedawi et al., showed that EVs derived from glioblastoma cells packaged an oncogenic form of the epidermal growth factor receptor which was functionally transferred to recipient glioma cells (Al-Nedawi et al., 2008). EV transfer of the oncogenic receptor, induced activation of MAPK and Akt signaling pathways, altered VEGF, Bcl-x(L) and p27 gene expression and increased cell proliferation of tumour cells (Al-Nedawi et al., 2008). This study showed that EV protein exchange between cells is a way of EV mediated cell-cell communication. Proteomic analysis of EVs has been used to find protein-EV biomarkers in disease. Proteomic analysis of urinary EVs identified eleven proteins to be upregulated in samples from prostate cancer patients compared to healthy participants with FABP5 showing

highest levels (Fujita et al., 2017). FABP5 is a fatty acid protein which has been implicated in prostate cancer metastasis (Carbonetti et al., 2019). Another study examined the proteomic profile of urinary EVs from Parkinson's disease patients and neurologically healthy donors (Wang et al., 2019). They found disease related proteins to be enriched in EVs from patients with Parkinson's disease (SNAP23, Rab7a, calbindin, and FRK) (Wang et al., 2019). The above studies demonstrate the clinical significance of protein EV cargo for the use of disease prognosis.

The EV lipidome profile is not as well characterised as that of RNA and protein cargo of EVs. The EV lipidome involves a variety of lipids identified in EVs such as glycerophospholipids (phosphatidylcholine, phosphatidylethanolamine, phosphatidylglycerol, phosphatidylserine, phosphatidic acid, phosphatidylinositol), sphingolipids (sphingomyelin, ceramide), free cholesterol and cholesteryl esters (Baig et al., 2013). Evidence suggests that presence of lipids on EV membranes enhances EV stability and allows interaction with recipient cells (Subra et al., 2007). Lipids on EVs participate in EV biogenesis and may participate in EV uptake or cellular signalling. A study showed that phosphatidylserine on the surface of EVs secreted from ovarian carcinoma cells was necessary for EV uptake by immune cells (Keller et al., 2009). EVs derived from astrocytes which were enriched in ceramides, have been shown to induce astrocyte apoptosis with implications in Alzheimer disease progression (Wang et al., 2012). Another study showed that ceramide, that is a product of sphingomyelin breakdown, is responsible for miRNA sorting inside ILVs and that pharmacological inhibition of ceramide generation by GW4869 (or N,N′-Bis[4-(4,5-dihydro-1H-imidazol-2-yl)phenyl]-3,3′-p-phenylene-bis-acrylamide dihydrochloride blocks the ceramide-mediated inward budding of MVBs and the release of mature EVs from MVBs) reduced small RNA content of EVs and EV release (Trajkovic et al., 2008)(Kubota et al., 2015). Studies have focused on the clinical use of lipids from EVs as biomarkers. Differences in lipid abundance were observed in EVs from non-tumorigenic, tumorigenic and metastatic prostate cell lines (Brzozowski et al., 2018). Analysis of lipid content from EVs from prostate cancer patients and healthy donors revealed distinct differences among the two groups with phosphatidylserine, lactosylceramide and hexosylceramide to be found elevated in EVs from prostate cancer patients (Skotland et al., 2017).

Taken together these studies demonstrate that EV cargo is diverse, from nucleic acids to lipids, can be transferred to target cells and exert biological effects on

these cells. Numerous clinical studies have studied the use of EV cargo as a potential diagnostic tool.

1.2.5 EVs and atherosclerosis

EVs are released from all cell types and especially from cells that participate in atherosclerosis development and progression (Charla et al., 2020). The presence of EVs has been identified in fatty streak formation where authors observed increased number of EVs originating from SMCs in atheroprone areas compared to atherosclerosis-resistant areas (Bobryshev et al., 2013). Imaging analysis of atherosclerotic plaque samples identified the presence of EVs in advanced atherosclerotic plaques (Perrotta and Saveria, 2016). Analysis of cellular origin of EVs in atherosclerotic plaques showed that the majority of EVs originated from leukocytes (52%), including macrophages (29%), erythrocytes (27%), lymphocytes (15%), SMCs (13%) and ECs (8%) with plasma EV profile demonstrating a majority of platelet derived EVs and no EVs originating from SMCs (Leroyer et al., 2007). The role of EV signalling and their miRNA (see later) in atherosclerosis progression is summarised in Figure 1-6.

1.2.5.1 Fatty streak and atheroma progression

EC derived EVs have been studied extensively with studies showing elevated levels of these EVs in patients with underlying cardiovascular risk factors (Preston et al., 2003)(Arteaga et al., 2006)(Amabile et al., 2014). EC-derived EVs have been proposed as a marker for monitoring endothelial health as indicated by their increased secretion in endothelial dysfunction (Dignat-George and Boulanger, 2011). Studies have shown that EC-EVs can aggravate endothelial function *in vivo* and *in vitro* via reduced NO production (Brodsky et al., 2004)(Densmore et al., 2006). Atherogenic stimulus can alter their cargo and induce upregulation of molecules such as ICAM-1 and VCAM-1 (Huber et al., 2002)(Jansen et al., 2013).

Immune cells including monocytes and macrophages are important cell types participating in lesion progression. Wang et al., found that EVs secreted from lipopolysaccharide (LPS)–treated THP-1 monocytic cells induced ERK1/2 phosphorylation and upregulation of ICAM-1, VCAM-1 and E-selectin in recipient ECs thus activating ECs (Wang et al., 2011). Another study showed that macrophage foam cell EVs could promote SMC migration via activation of the ERK pathway and lesion progression (Niu et al., 2016). Keyel et al., showed that

macrophage derived EVs induced foam cell formation by promoting cholesterol uptake by recipient macrophages (Keyel et al., 2012).

1.2.5.2 Vascular calcification

EVs have been identified in calcified plaques with studies providing evidence for their involvement during plaque calcification (Kapustin et al., 2011)(Kapustin et al., 2015)(Buendía et al., 2015). EV monitoring has been proposed as a biomarker for coronary calcification (Jayachandran et al., 2008)(Del Turco et al., 2014). Interestingly, EVs isolated from calcified human atherosclerotic plaques demonstrated differences from EVs isolated from calcified SMCs *in vitro* as EVs in atherosclerotic plaque originate from various cell types (Krohn et al., 2016). Furthermore, Kapustin et al., showed that SMC-secreted calcified EVs had endosomal origin in contrast to what was believed before, in that they were budded from the plasma membrane (Kapustin et al., 2015). Authors also showed that certain atherogenic stimulus such as TNF-α and PDGF increased EV secretion and consequently SMC calcification in calcifying conditions (Kapustin et al., 2015). Another study showed that calcified SMC secreted EVs can promote calcification to neighbouring cells aggravating the existing calcification in the vessel wall (Chen et al., 2018).

1.2.5.3 Advanced/Vulnerable plaques

EV signalling has been implicated in plaque destabilisation and subsequent thrombus formation. Levels of circulating leukocyte EVs were examined in patients undergoing thromboendarterectomy and it was found that leukocyte-EVs were elevated in patients with unstable plaques indicating that they could be used as a biomarker to detect unstable plaques (Sarlon-Bartoli et al., 2013). Another study analysed the connection between ceramides and phosphatidylcholines in plasma EVs and cardiovascular outcome after carotid endarterectomy and authors showed that lipids on plasma EVs were independently associated with increased risk of a cardiovascular outcome (Timmerman et al., 2022).

Weakening of the fibrous cap is the main cause of plaque rupture with studies suggesting that EVs are responsible for plaque destabilisation (Boulanger et al., 2017). SMCs are crucial for plaque stability as they are responsible for cap formation and their secreted molecules (collagen, elastin, fibronectin and extracellular matrix) produce a thick fibrous cap (Owens et al., 2004). Plaque destabilisation has been mainly attributed to proteolytic properties of MMPs either

carried by EVs or MMPs on the plasma membrane or in case of MMP14, secreted from cells (Nawaz et al., 2018). Tobacco exposure, a risk factor for atherosclerosis, induces enrichment of active mature MMP-14 as confirmed by gelatin zymography in macrophage-EVs (Li et al., 2013). Other studies showed that EC-EVs encapsulated MMP-2 (active and pro-enzyme forms and activity confirmed by gelatin zymography), MMP-10 (enzyme activity was not examined) MMP-9 (active and pro-enzyme forms and activity confirmed by gelatine zymography)and MMP-14 (active and pro-enzyme form and activity was confirmed with MMP activity assay with the use of fluorogenic MMR substrate) (some studies provide *in vitro* and *in vivo* evidence) (Taraboletti et al., 2002)(Lozito and Tuan, 2012)(Martínez de Lizarrondo et al., 2012). EVs isolated from atherosclerotic lesions encapsulated the metalloprotease TNF-α converting enzyme (TACE) which has been detected on atherosclerotic lesions (Canault et al., 2007). TACE cleaves the precursor of TNF-α into a soluble active cytokine maintaining a balance between anti- and pro-inflammatory molecules (Canault et al., 2007). Authors suggested that the potential cell origin of these EVs could be leukocytes or erythrocytes (Canault et al., 2007).

Once the plaque is ruptured, the plaque's thrombogenic material is exposed to circulating platelets activating them and leading to thrombus formation (Badimon et al., 2012). It was found that circulating monocyte and platelet- EVs can enhance thrombus formation (Falati et al., 2003)(Suades et al., 2012). EVs expressed on their surface phospholipids and tissue factor and their presence on the surface may promote coagulation and thrombosis (Nielsen et al., 2018). Interestingly, a proteomic analysis of EVs revealed that EVs isolated from people who smoked demonstrated elevated levels of tissue factor compared to control-EVs, a fact which could be correlated with thrombosis (Benedikter et al., 2019).

1.3 MicroRNAs

1.3.1 Biogenesis

MiRNAs are a class of small non-coding single strand RNA molecules with average size of 22 nucleotides (20-30 nucleotides) (Ha and Kim, 2014). The first miRNA, lin-4, was discovered in 1993 (Lee et al., 1993)(Wightman et al., 1993). What the authors thought was a protein coding gene that regulated larval development in Caenorhabditis elegans, was a gene transcribing a pair of small RNAs (Lee et al., 1993)(Wightman et al., 1993). MiRNAs are encoded by introns or exons of both protein coding genes or non-coding genes (Rodriguez et al., 2004)(O'Brien et al., 2018). Several miRNAs can be transcribed as one long transcript called a cluster (O'Brien et al., 2018). These genes are located in close proximity and transcription of these genes may be regulated by the same mechanisms (Lee et al., 2002). If miRNAs in a cluster have similar seeding regions they may comprise a family of miRNAs (O'Brien et al., 2018). MiRNA biogenesis can be categorised into two pathways, canonical and non-canonical.

The canonical pathway is the prevailing way of miRNA production (Figure 1-4). A miRNA gene is transcribed into a primary miRNA (pri-miRNA) by RNA polymerase II (Lee et al., 2004)(O'Brien et al., 2018). The pri-miRNA can be over 1 kb long and contains a stem loop of 33-35 bp (Lee et al., 2004). The pri-miRNA is processed by the microprocessor complex into precursor miRNA (pre-miRNA) in the nucleus (O'Brien et al., 2018). The microprocessor complex is composed of a RNA binding protein DiGeorge Syndrome Critical Region 8 (DGCR8) and a ribonuclease III enzyme, Drosha (O'Brien et al., 2018). During the maturation process, DGCR8 recognises certain motifs on the pri-miRNA while Drosha cleaves the stem-loop releasing a hairpin-shaped ~65 nucleotide long pre-miRNA (Han et al., 2004). Drosha cleaves the pri-miRNA in a way that results in the generation of nucleotide overhang on the pre-miRNA (Han et al., 2004). Following that, the pre-miRNA is transferred to the cytoplasm by an exportin 5 (EXP5)/RanGTP complex (O'Brien et al., 2018). The pre-miRNA is then processed by the RNase III endonuclease Dicer which cleaves the hairpin loop from the pre-miRNA resulting in the formation of a duplex of mature miRNAs with size around 22 nucleotides, one mature miRNA and a passenger strand (O'Brien et al., 2018). It was shown that Dicer has one catalytic centre with two RNA cleavage sites which may favour the pre-miRNA end with the overhang (Han et al., 2004).

The direction of each miRNA strand dictates their name as the -5p strand comes from the 5' end of the pre-miRNA and respectively the -3p strand comes from the 3' end of the pre-miRNA (O'Brien et al., 2018). Next, the mature miRNA duplex is loaded into the Argonaute (AGO) family of proteins (AGO1-4 in humans) forming the RNA-induced silencing complex (RISC) in an ATP dependent way (Yoda et al., 2010). All 4 AGO proteins can bind the miRNA duplex as it was shown by Yoda et al. (Yoda et al., 2010). Maturation of the RISC complex involves the degradation of passenger miRNA while the other strand, the mature miRNA, is still bound to the AGO protein (Wahid et al., 2010). The thermodynamic stability of each strand regulates which strand will be degraded or not (Wahid et al., 2010). Factors like cell type or cellular environment may also affect which mature strand of miRNA (-3p or -5p) will stay bound to the RISC complex (Meijer et al., 2014). A study suggests that there is a preference for the miRNA strand with low thermodynamic 5' end stability (Khvorova et al., 2003). The strand that does not stay bound to the RISC complex is called the passenger strand and is cleaved by AGO2 and then degraded (O'Brien et al., 2018).

The non-canonical pathway of miRNA biogenesis involves various mechanisms which result in miRNA generation in a Drosha or Dicer independent way (O'Brien et al., 2018). However, only 1% of miRNAs have been found to originate via a non-canonical miRNA biogenesis pathway (Ha and Kim, 2014). Biogenesis of miR-451 is an example of Dicer independent biogenesis pathway (Ha and Kim, 2014). The pri-miRNA is cleaved by Drosha and produces a short hairpin stem loop of 18 bp which is too short a molecule to be cleaved by Dicer (Yang et al., 2010). AGO2 is responsible for the maturation of this miRNA. When the pre-miR-451 is loaded into AGO2 and AGO2 cuts the -3p strand of the pre-miRNA (Yang et al., 2010). MiRNA biogenesis via non-canonical mechanisms is still poorly understood.

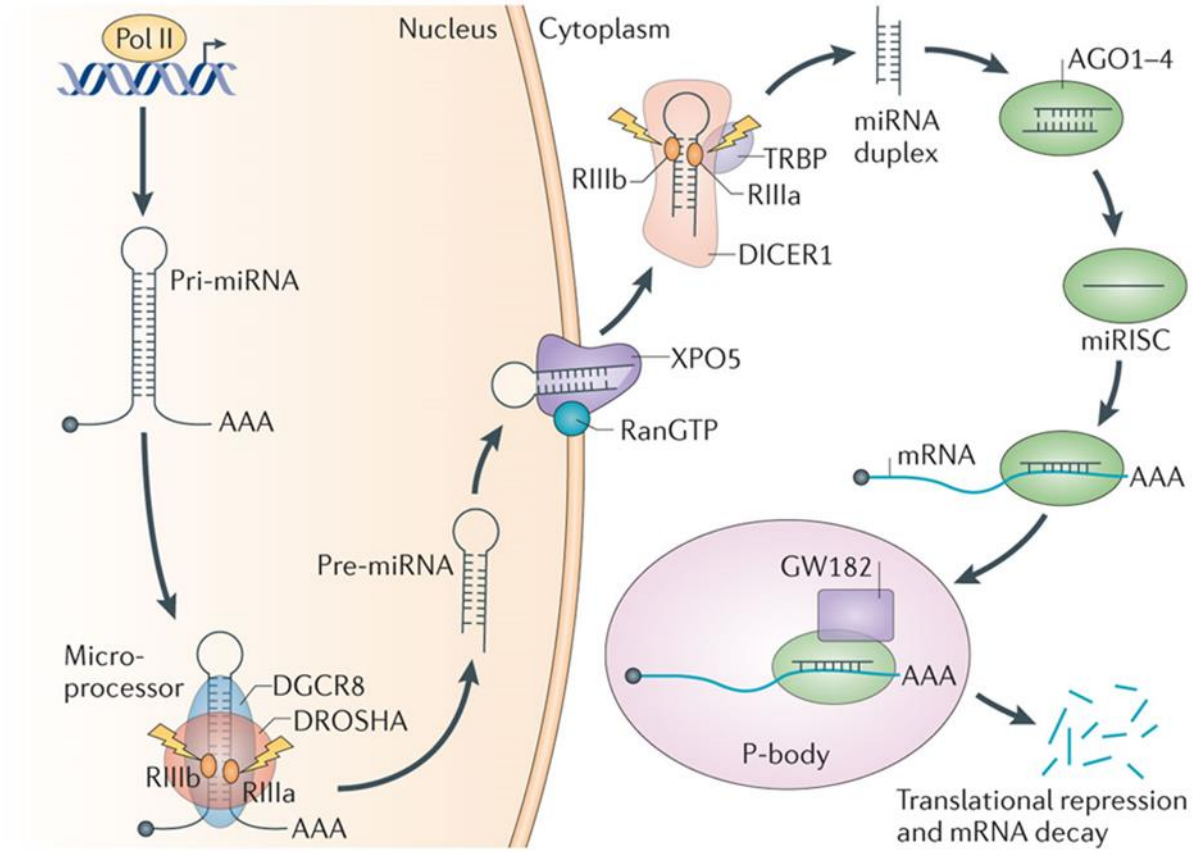

Figure 1-4 MiRNA biogenesis

MiRNA genes are initially transcribed as primary miRNA or pri-miRNAs in the nucleus by RNA polymerase II. Pri-miRNAs are cleaved into smaller precursor miRNAs or pre-mRNAs by microprocessor complex comprised of an RNA binding protein DiGeorge Syndrome Critical Region 8 (DGCR8) and the Drosha ribonuclease III enzyme. Next, the pre-miRNAs are exported from the nucleus to the cytoplasm by an exportin 5 (EXP5)/RanGTP complex and are further processed by RNase III endonuclease Dicer where cleavage of the hairpin loop results in the formation of a duplex of mature miRNA duplex. The mature miRNA strand is loaded into the RNA-induced silencing complex (RISC) where is guided by RISC and Argonaute (AGO) proteins to find its mRNA target. Adapted by ((Lin and Gregory, 2015), Licensed Content Publisher Springer Nature, License Number 5453120387891).

1.3.2 miRNA Function

MiRNAs are phylogenetically conserved, and they participate in development amongst various other physiological processes (Zhao and Srivastava, 2007). Their main function is post-transcriptional regulation of gene expression (Figure 1-5). The miRNA is guided by the RISC complex and AGO2 to find its target mRNA (O'Brien et al., 2018). MiRNA recognises its target mRNA by base pairing at the 3' untranslated region (UTR) of the mRNA. Studies have found that miRNAs can bind to the 5' UTR region or coding domain sequence (CDS) (Lee et al., 2009)(Brümmer and Hausser, 2014). It was shown that miRNAs can bind to promoter regions and induce gene transcription as opposing to binding to 5'UTR that has a silencing effect (Dharap et al., 2013). Nucleotides 2-7 at the 5' end of the miRNA constitute the seed sequence of the miRNA and complementarity of the seed sequence and the mRNA determine whether a mRNA will be recognised as a target of a miRNA molecule (Zhao and Srivastava, 2007). However, miRNA-mRNA complementarity is not the only factor determining if a miRNA will bind a mRNA molecule (Zhao and Srivastava, 2007). In many cases miRNA-mRNA interaction is not fully complementary and base pairing at the 3' end of the miRNA solidifies the interaction (O'Brien et al., 2018).

MiRNA binding to their target mRNA usually negatively regulates gene expression (Macfarlane and Murphy, 2010). However, studies have shown that miRNA could upregulate gene expression (Truesdell et al., 2012)(Bukhari et al., 2016). A single miRNA molecule can bind to several mRNA target molecules and many miRNA molecules can regulate a single mRNA target (Macfarlane and Murphy, 2010). Generally, miRNA-mRNA interaction promotes the mRNA cleavage by AGO2 (Macfarlane and Murphy, 2010). Ribonucleoproteins, complexes of proteins and miRNAs, deploy enzymes resulting in mRNA degradation (Valinezhad Orang et al., 2014). Another way of miRNA silencing gene expression is via translation inhibition. Studies have shown that miRNAs can inhibit initial and later steps of the translation process (Pillai et al., 2004)(Petersen et al., 2006). Guo et al., performed a large *in vitro* ribosome profiling study showing that silencing of gene expression occurred mostly via mRNA destabilization and as frequently via translation inhibition (Guo et al., 2010).

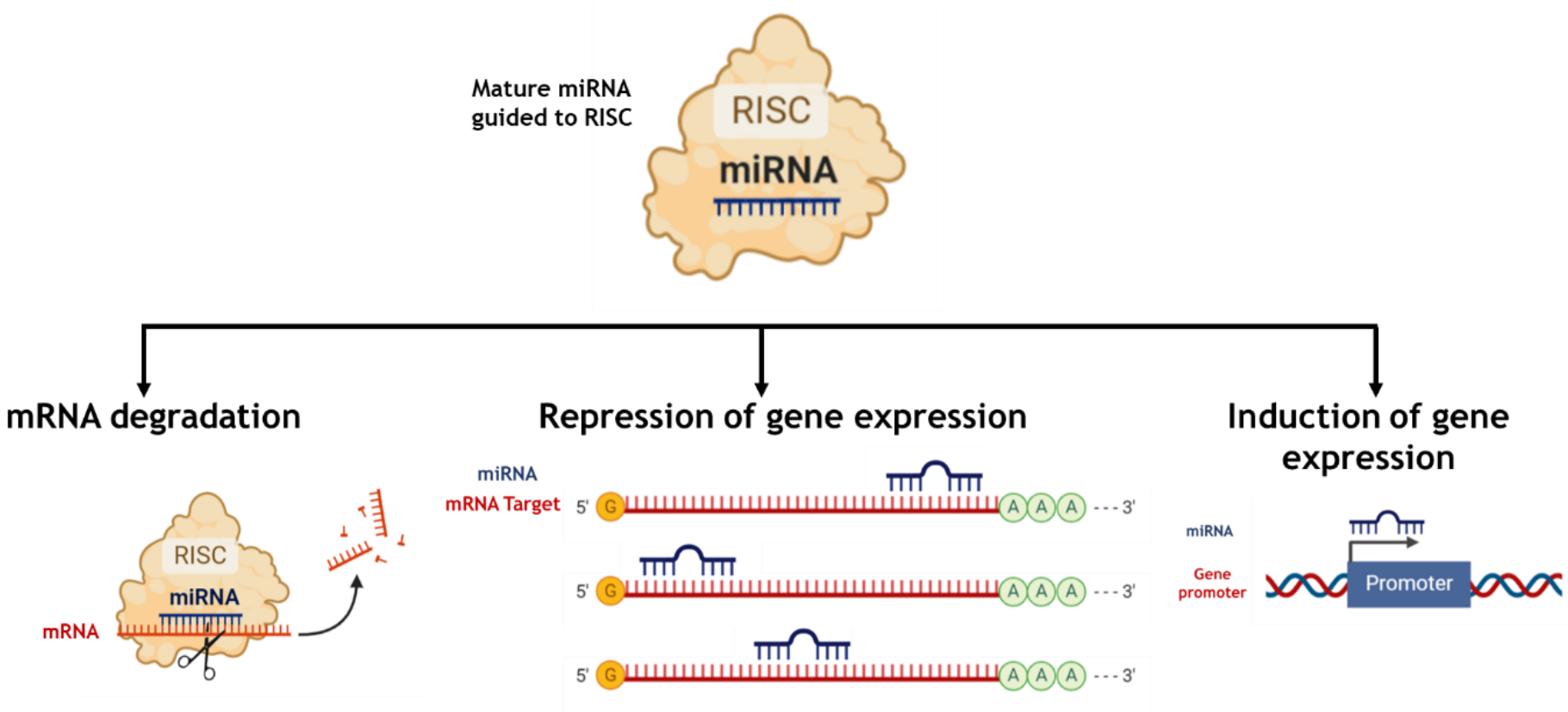

Figure 1-5 MiRNA functions and gene transcription regulation

The mature miRNA strand is guided by RISC and AGO to find its complementary mRNA target. MiRNAs usually negatively regulate gene expression either by inducing mRNA degradation due to mRNA cleavage from AGO2 or via inhibition of RNA translation. MiRNA usually binds to the 3'UTR of mRNA, however in some case miRNA can bind to the 5'UTR or CDS of a gene. In some cases, miRNAs can bind to gene promoter regions and positively regulate gene transcription. The figure was created by using pictures from BioRender.com.

1.3.3 miRNA as biomarkers in disease

Previously, the role of miRNAs in atherosclerosis progression was summarised. The fact that abrogated miRNA expression has been observed in many pathologies and circulating miRNAs are stable have paved the way for the use of miRNAs as biomarkers in disease detection. A miRNA profiling study examined the circulating miRNAs of patients with CAD vs healthy donors identifying miR-126, miR-17, miR-92a, miR-145, and miR-155 to be significantly downregulated in CAD patients (Fichtlscherer et al., 2010). However, another clinical study examined the tissue expression profile of miRNAs from human advanced coronary atherosclerotic plaque versus non-atherosclerotic internal human arteries (Parahuleva et al., 2018). They found miR-21, miR-92a and miR-99a to be significantly upregulated in advanced atherosclerotic plaques compared to non-atherosclerotic arteries (Parahuleva et al., 2018). A large clinical study of CAD patients found that elevated circulating levels of miRNA-197 and miRNA-223 were predictors of cardiovascular death amongst these patients (Schulte et al., 2016). A clinical cohort profiled miRNA expression from patients with symptomatic and asymptomatic atherosclerotic plaques and identified some miRNAs (miR-100, miR-127, miR-145, miR-133a, and miRNA-133b) to be differentially expressed between the two groups (Cipollone et al., 2011). Interestingly, the altered miRNA expression correlated with unstable plaques providing potential prognostic markers for vulnerable plaque identification (Cipollone et al., 2011). Pereira-da-Silva et al., conducted a systematic review of eighteen studies which analysed miRNA biomarkers for atherosclerosis (ten studies focused on carotid atherosclerosis, six on lower limb atherosclerosis and two on renal artery atherosclerosis) and identified four miRNAs, miR-21, miR-30, miR-126, and miR-221-3p to be commonly downregulated in all studies (Pereira-da-Silva et al., 2018). Taken together these studies, they highlight the clinical and prognostic values of miRNAs as biomarkers in atherosclerosis, although further larger scale clinical studies are needed to draw definite conclusions.

1.4 MiRNA and EV-miRNA signaling in atherosclerosis

MiRNAs have been recognised as regulators of many physiological and pathological conditions. Their important role in CVD has been supported by various studies (Romaine et al., 2015). Abnormal expression of miRNAs has also been linked with many pathologies (O'Brien et al., 2018)(Paul et al., 2018). MiRNAs modulate early and late stages of atherosclerosis development via modulation of pathways implicated in the disease development. MiRNAs are the main cargo of EVs and miRNAs encapsulated in EVs have been implicated in atherosclerosis progression (Xu et al., 2021). Several studies have examined the effect of miRNAs in lesion progression while others have examined the EV-miRNAs in disease progression while often different studies have examined the same miRNAs/EV-miRNAs.

1.4.1 Fatty streak and lesion progression

Firstly, miRNAs can regulate cholesterol metabolism. MiR-122 is highly expressed in the liver and studies have showed that it is responsible for regulating cholesterol synthesis and its inhibition resulted in reduced plasma cholesterol levels (Esau et al., 2006)(Elmén et al., 2008). MiR-122 inhibition with an antisense oligonucleotide in normal C57BL/6 male wt mice resulted in reduced plasma cholesterol levels and decreased cholesterol synthesis rate (Esau et al., 2006). The authors identified several genes related to fatty acid metabolism such as acetyl-CoA carboxylase 2 (ACACB), sterol regulatory element-binding protein 1 (SREBP-1) and sterol regulatory element-binding protein 2 (SREBP-2), and a gene related to cholesterol metabolism, phosphomevalonate kinase (PMVK), which were significantly downregulated after miR-122 inhibition in mice (Esau et al., 2006). MiR-223 has been implicated in cholesterol homeostasis by inhibiting its synthesis via targeting of HMG-CoA, targeting SR-BI and regulating HDL-C uptake (Vickers et al., 2014). Authors found that APOE KO mice under high fat diet had elevated levels of miR-223 and miR-223 KO mice demonstrated significantly increased plasma cholesterol levels compared to wt mice (Vickers et al., 2014). MiR-148a has been found to negatively regulate LDL receptor (LDLR) expression as mice treated with antisense oligonucleotides targeting miR-148a had elevated expression of LDLR in the liver and decreased LDL-C levels in plasma (Goedeke et al., 2015). Genome-wide association studies (GWAS) have identified miRNAs, miR-128-1, miR-148a, miR-130b, and miR-301b, to be involved in lipoprotein homeostasis (Wagschal et al., 2015). Authors showed *in vitro* that these four

miRNAs targeted the LDLR at the 3' UTR resulting in low internalisation of labelled LDL-C by HepG2 cells (Wagschal et al., 2015).

LDL accumulation into subendothelial space and EC activation are first steps of fatty streak formation. A study found that miR-92a is enriched in ECs under atherogenic conditions and EV-miR-92 transfer to recipient macrophages induced LDL uptake and inflammatory activation (Chang et al., 2019). Inhibition of EV-miR-92 transfer reversed these effects highlighting the role of EV-miRNA cargo in atherosclerosis progression (Chang et al., 2019). He et al., showed that oxLDL induced the miR-155 enrichment in EC-EVs and EV-miR-155 transfer to recipient monocytes promoted their phenotypic change to macrophages (He et al., 2018). Moreover, tail vein injection of miR-155 enriched EVs in APOE KO mice fed a high fat diet resulting in increased lesion area (He et al., 2018). A great number of miRNAs has been identified to be responsible for foam cell formation by unbalancing cholesterol efflux from macrophages such as miR-26, miR-33, miR-106,30 miR-144, miR-128-1, miR-130b, miR-148a, miR-301b, miR-302a, and miR-758 (Feinberg and Moore, 2016). These miRNAs have been shown to target genes related to lipid and energy metabolism such as LDLR, ATP binding cassette subfamily A member 1 (ABCA1), carnitine palmitoyltransferase 1A (CPT1A), salt inducible kinase 1 (SIK1), insulin receptor substrate 1 (IRS1) and silent information regulator 1 (SIRT1) (Feinberg and Moore, 2016).

EC-EVs can exert an atheroprotective role in the development of the disease. Jansen et al., showed that EC-EVs enriched in miR-126 promoted EC migration and proliferation after vascular injury *in vivo* (Jansen et al., 2013). Another study showed that EC secreted EV-miR-222 transfer to recipient ECs resulted in reduced ICAM1 but not VCAM1 expression and reduced monocyte adhesion *in vitro* (Jansen et al., 2015). To correlate their findings with clinical practice, both studies examined the levels of miR-126 and miR-222 in patients with CAD and found reduced levels for both miRNAs in CAD patients compared to donors without CAD (Jansen et al., 2013)(Jansen et al., 2015). Kruppel-like factor 2 (KLF2) transcription factor regulates EC behaviour via inhibition of VCAM-1 and E-selectin expression on ECs and thus inhibiting proinflammatory activation of ECs (Atkins and Jain, 2007). He et al., showed that KLF2 transduced ECs secreted EVs with atheroprotective properties via reduced monocyte activation and reduced inflammatory activation and EV treatment in APOE KO mice resulted in reduced

plaque size (He et al., 2018). The authors showed that oxLDL stimulation enhanced miR-155 expression in EC-EVs whereas KLF2 had the opposite effect (He et al., 2018). Another study demonstrated that KLF2 transduced ECs secreted EVs enriched in miR-143/145 and that EV-miRNA transfer to co-cultured SMCs reduced the expression of dedifferentiation related genes indicating an atheroprotective role of EC secreted EVs (Hergenreider et al., 2012). Tail vein injection of these EVs to APOE KO mice resulted in reduced lesion area (Hergenreider et al., 2012). Stamatikos et al., showed that EC-EVs enriched with anti-miR-33a-5p (ECs were transduced with an adenoviral vector expressing an antagomiR for miR-33a-5p) increased cholesterol efflux of recipient SMCs and macrophages (Stamatikos et al., 2019). This study shows that targeting of EV cargo could be a potential target for atherosclerosis treatment. Taken together, these studies demonstrate that different stimulus can alter the properties of EC secreted EVs and their cargo reflecting the importance of the microenvironment and the EV biological properties and why there is not a clear conclusion regarding their contribution to the disease development.

Monocyte-EV interaction with ECs resulted in adhesion molecule upregulation (ICAM-1, VCAM-1, E-selectin), vascular cell death and inflammation either via miRNA transfer (miR-155, miR-223) or cytokine enrichment (IL-1β) (Aharon et al., 2008)(J.-G. Wang et al., 2011)(Tang et al., 2016). Endothelial migration can be induced by monocytic EV-miR-150 transfer (Zhang et al., 2010). Macrophage stimulation with an atherogenic stimulus such as oxLDL induced miRNA enrichment, including miR-146a, miR-128, miR-185, miR-365, and miR-503 in macrophage EVs and authors showed that EV-miR-146a transfer to recipient macrophages reduced macrophage motility resulting in macrophage entrapment in the vessel wall and acceleration of disease progression (Nguyen et al., 2018).

MiRNAs can also modulate vascular inflammation and EC permeability. MiR-10a was found to inhibit expression of VCAM-1, E-selectin, and NF-κB in ECs (Fang et al., 2010). By regulating the expression of adhesion molecules like ICAM-1, VCAM-1 and E-selectin, miR-126, miR-31 and miR-17-3p are also important regulators of EC inflammation (Suárez et al., 2010)(Ásgeirsdóttir et al., 2012). EC senescence has been associated with atherosclerosis with evidence suggests that cell senescence aggravates the disease's progression (Wang and Bennett, 2012). MiRNAs like miR-34a, miR-217, and miR-146a have been associated with EC

senescence (Lu et al., 2018). Mouse lineage-negative bone marrow cells (lin− BMCs), which are enriched in endothelial progenitor cells, were transfected with pre-miR-146a mimic resulting in polo like kinase 2 (PLK2) reduced expression, a cell cycle regulator in response to DNA damage, and increased expression of p16Ink4a and p19Arf, the most well studied cell cycle inhibitors, cyclin dependent kinase inhibitor 2A (CDKN2A) with evidence suggesting that they regulate stem cell senescence (Nishino et al., 2008)(Deng et al., 2017). Menghini et al., showed that miR-217 can induce a senescence-like phenotype in ECs via targeting of SIRT1 while miR-217 inhibition (cells treated with miR-217 inhibitor) in ECs reduced senescence via increased SIRT1 expression (Menghini et al., 2009). MiR-34a was also found to regulate EC senescence via targeting of SIRT1 (Zhao et al., 2010). Endothelial progenitor cells (EPCs) were transfected with miR-34a mimic inducing EC senescence and reduced SIRT1 expression (Zhao et al., 2010). MiR-146a has been proposed as marker for early detection of senescence and vascular remodeling by Olivieri et al. (Olivieri et al., 2013). MiR-146a levels were found elevated in senescent human umbilical vein ECs (HUVECs) and levels of its target gene, interleukin-1 receptor-associated kinase 1 (IRAK-1) were found reduced (Olivieri et al., 2013). Analysis of circulating angiogenic cells showed that miR-146a expression was significantly elevated and IRAK-1 expression downregulated in patients with chronic heart failure, compared to healthy control subjects (Olivieri et al., 2013).

The role of platelet-EVs in lesion progression has been studied extensively. Studies showed that platelet-EVs can induce a SMC phenotypic change towards a synthetic phenotype and thus promoting vascular remodeling (Weber et al., 2000)(Vajen et al., 2017). A transcriptomic sequence study identified several miRNAs (miR-144-3p, miR-486-5p, miR-142-5p, miR-451a, miR-25-3p, miR-145-5p, and let-7f-5p) in platelet EVs during senescence and target analysis of these miRNA species identified genes involved in lipid metabolism, inflammation and coagulation (Pienimaeki-Roemer et al., 2017). Mause et al., showed that platelet-EVs were responsible for monocyte recruitment to atheroprone areas inducing inflammation and lesion progression (Mause et al., 2005). Platelet-EVs have been shown to modulate macrophage phenotype by promoting their polarisation towards a M2 anti-inflammatory phenotype (Sadallah et al., 2011)(Vasina et al., 2011). Laffont et al., showed that platelet EV-miR-126–3p transfer to macrophages altered the macrophage gene expression profile (ATF3 (activating transcription factor 3),

ATP1B1 (ATPase Na^+/K^+ Transporting Subunit Beta 1), ATP9A (ATPase Phospholipid Transporting 9A) and RAI14 (Retinoic Acid Induced 14) expression), downregulated the production of inflammatory cytokines including CCL4, CSF1 and TNF-α, and resulted in increased phagocytic capacity of macrophages (Laffont et al., 2016). In conclusion, platelet-EVs demonstrate both atherogenic and atheroprotective roles regarding disease development. The studies discussed previously used the same EV isolation method, ultracentrifugation, so a possible explanation for their ambiguous roles is either the different cell types that were treated with theses EVs or the different cargo being transferred from platelet-EVs.

SMC phenotype during atherosclerosis development is also regulated by miRNAs. MiR-143 and miR-145 are known to regulate SMC differentiation via negative regulation of kruppel-like factor 4 (KLF4) and positive regulation of myocardin (MYOCD), thus promoting the SMC differentiated phenotype and also decreased expression of these miRNAs was found in injured carotid arteries (Cordes et al., 2009). MiR-143/145, miR-1 and miR-10a can be considered atheroprotective as they can suppress expression of KLF2, KLF4, kruppel-like factor 5 (KLF5), histone deacetylase 4 (HDAC4) and ETS transcription factor (ELK1) in SMCs that will stop them differentiating into a proliferative phenotype (Hergenreider et al., 2012)(Lu et al., 2018). Evidence suggests that miR-143/145 overexpression resulted in reduced plaque size and necrotic core and increased fibrous cap area thus promoting plaque stability in APOE KO mice (Lovren et al., 2012). Cellular plaque composition analysis showed increased levels of SMC contractile proteins, calponin and α-smooth muscle cell actin, and decreased expression of KLF4 and increased expression of MYOCD differentiation markers (Lovren et al., 2012). MiR-221 and miR-222 were found elevated in rat injured arteries and in vitro findings suggested that they promoted SMC proliferation and migration via targeting cyclin-dependent kinase inhibitor 1C (CDKN1C) and cyclin-dependent kinase inhibitor 1B (CDKN1B), inhibitors of cell cycle progression (Liu et al., 2009)(Liu et al., 2012). Additionally, miR-21 has been shown to induce vascular SMC proliferation and migration by targeting tropomyosin 1 (M. Wang et al., 2011). MiR-155's role in atherosclerosis has not been elucidated as studies report contradicting results with atheroprotective and atherogenic properties (Feinberg and Moore, 2016). Bone marrow deficiency of miR-155 in LDLR KO mice under high fat diet aggravated atherosclerosis and plaque instability with an increased number of circulating inflammatory cells (granulocytes and monocytes) and increased IL-6

production by macrophages (Donners et al., 2012). On the contrary, Du et al., showed that miR-155 deletion in APOE KO mice fed a high fat diet resulted in reduced plaque size compared to APOE KO mice with decreased numbers of T cells (CD3+/CD4+, and CD3+/CD8+) Th17 cells (CD4+/IL17+) found in the spleen and also decreased circulating levels of TNF-α and IL-6 compared to APOE KO mice (Du et al., 2014).

Communication in and between vascular cells is crucial for atherosclerosis development. Zhao et al., showed that the X-box binding protein 1 (XBP1) regulated miR-150 expression in SMCs and its subsequent enrichment in SMC-EVs (Zhao et al., 2016). EV-miR-150 transfer to recipient ECs induced EC migration via the vascular endothelial cell growth factor A (VEGF-A) VEGF-A/VEGFR/PI3K/Akt pathway activation and thus affecting vessel wall homeostasis (Zhao et al., 2016). Inhibition of EV-miR-150 transfer abolished EC migratory effects indicating that EV-miRNA transfer could be a new target for atherosclerosis treatment (Zhao et al., 2016). Another study showed that KLF5 transduced SMCs secreted EVs enriched in miR-155 and EV-miR transfer to recipient ECs resulted in the destruction of EC tight junctions, increased endothelial permeability and atherosclerosis progression (Zheng et al., 2017). Impaired endothelial autophagy has been associated with the progression of atherosclerosis (Grootaert et al., 2018). Li et al. showed that co-culture of SMCs and ECs reduced endothelial autophagy (Li et al., 2016). Intracellular communication was mediated via SMC secreted EVs enriched in miR- 221/222 and EV-miR-221/222 transfer inhibited autophagy via regulation of the PTEN/Akt signaling pathway (Li et al., 2016).

MiRNA involvement in atherosclerosis has also been extensively discussed. Studies have showed miRNA transfer between ECs/SMCs participates in the disease pathology. Zhou et al., showed that miR-126 transfer from ECs to SMCs controls SMC phenotypic switching towards a proliferative and migratory phenotype by regulating SMC gene expression (Zhou et al., 2013). Another study showed that SMC secreted miR-143/145 was transferred to ECs via tunnelling nanotubes, plasma membrane structures important in cell-cell communication (Climent et al., 2015). This study shows that EC-SMC communication is not a one-way street. The miRNA cargo of EVs and specifically EV-miRNA transfer has proven to be a potentially effective target in atherosclerosis.

1.4.2 Fibrous stable plaque

The need to find biomarkers that would enable the detection of a coronary events such as MI is of great importance as early diagnosis would allow early interventions to reduce ischemic damage to the myocardium. Endothelial dysfunction has been associated with cardiovascular complications and platelets can regulate angiogenesis and thrombus formation so they can provide information regarding status of plaques (Nozaki et al., 2009)(Nording et al., 2015). EC and platelet-EVs are the prime type of vesicles circulating in blood and studies have shown that they can be used as independent biomarkers for CAD status (Bernal-Mizrachi et al., 2003)(Nozaki et al., 2009)(Werner et al., 2006)(Sinning et al., 2011). EVs isolated from endarterectomy specimens were found to transfer ICAM-1 molecules from the membrane of ECs and promote monocyte recruitment indicating that plaque EVs themselves promote plaque progression (Rautou et al., 2011).

Evidence suggests that macrophage apoptosis and necrotic core expansion is also mediated via EV or miRNA signalling. It was shown that EVs secreted from Jurkat T cells were cleared by macrophages through phagocytosis and as a result T-cell EVs promoted macrophage apoptosis (Distler et al., 2005). Additionally, T-cell EVs induced EV secretion by macrophages, possibly promoting secretion of EVs containing new apoptotic messages that would result in enhanced cell death (Distler et al., 2005). Another study showed that T-cell EVs induced macrophage apoptosis via impaired lipid homeostasis (Huber et al., 2007). Authors showed that T-cell EVs activated the phospholipid-ceramide pathway, induced the production of arachidonic acid and increased levels of proapoptotic ceramides in macrophages (Huber et al., 2007). However, other cell derived-EVs have been found to promote macrophage and SMC apoptosis and plaque stability. MiR-155 has been shown to promote macrophage cell death and thus expansion of the necrotic core (Sampat et al., 2012). MiR-29b, via suppression of IFN-γ, promotes collagen secretion from SMCs resulting in a thick fibrous cap and stable plaque (Andreou et al., 2015). Caspase-3, cell death related caspase, has been found in EC-EVs and platelets-EVs with studies showing that these EVs promoted macrophage apoptosis but it was not clear if apoptosis was mediated by EV-caspase transfer to recipient cells (Abid Hussein et al., 2005)(Böing et al., 2008). Monocyte-EVs encapsulating caspase-1 have been found to promote SMC apoptosis (Sarkar et al., 2009). Cell apoptosis is considered the turning point of a stable plaque to an unstable plaque. Studies have shown that apoptosis takes places in

advanced stable and ruptured plaques (Lutgens et al., 1999). Bennett et al, discussed SMC apoptosis in atherosclerosis progression and stated that cell origin was detrimental to the effect that apoptosis will have on the disease progression, reducing or promoting inflammation (Bennett et al., 2016).

1.4.3 Vascular calcification

EVs and their cargo have been implicated in vascular calcification (Zhang et al., 2018). A number of miRNAs have also been associated with vascular calcification (Goettsch et al., 2013). MiR-204 has been found to negatively regulate mouse SMC calcification *in vitro* via targeting Runx2 and thus inhibiting osteocalcin secretion (Cui et al., 2012). Another study showed that inhibition of endogenous miR-125b in calcified human coronary artery SMCs (HCASMCs) aggravated vascular calcification by increasing matrix mineralisation and alkaline phosphatase activity *in vitro* (Goettsch et al., 2011). EC-EVs were found enriched in bone morphogenetic protein 2 (BMP-2) and calcium after TNF-α stimulation and promoted calcification and induction of an osteogenic phenotype in SMCs (Buendía et al., 2015). Another study showed that EC-EVs isolated after high inorganic phosphate stimulation induced vascular calcification in recipient SMCs via STAT3/BMP-2 signalling pathways (Xiang et al., 2022). Macrophage-derived EVs can aggravate calcification processes in chronic kidney disease as they encapsulate molecules like S100A9 that forms complex with Annexin V and allows hydroxyapatite nucleation (New et al., 2013).

In physiological conditions, SMC-EVs are enriched with calcification inhibitors (endogenously expressed matrix Gla protein, circulating fetuin-A) but mineral imbalance, stress and/or inflammation results in enrichment of EVs with phosphatidylserine and annexin A6, molecules that alter the SMC-EVs into calcifying EVs (Reynolds et al., 2005). Kapustin et al., showed that certain atherogenic stimulus such as TNF-α and PDGF increased EV secretion and consequently SMC calcification in calcifying conditions (Kapustin et al., 2015). Xu et al., found that melatonin induced miR-204/miR-211 in SMC secreted EVs and EV-miRNA transfer attenuated osteogenic differentiation of SMCs via BMP-2 targeting indicating a protective role of SMC secreted EVs (Xu et al., 2020). Another study found that EC secreted EVs containing miR-26a could control SMC contractile phenotype via miRNA transfer to target ARF6 and NCX1 (Lin et al., 2016). Hutcheson and colleagues, showed in a 3-D *in vitro* model collagen hydrogel

resembling the atherosclerotic fibrous cap structure that SMC secreted EVs that aggregated led to the formation of small microcalcifications that could evolve into large, calcified areas (Hutcheson et al., 2016).

1.4.4 Advanced/Vulnerable plaques

MiRNAs and EVs have been studied extensively regarding their role in atherosclerosis and plaque stability. A study found that EV-miRNA levels of miR-199b-3p, miR-27b-3p, miR-130a-3p, miR-221-3p, and miR-24-3p were significantly elevated in patients with asymptomatic carotid stenosis (Dolz et al., 2017). Bi et al., found increased EV- miR-208a levels in patients with acute coronary syndrome (ACS) indicating its contribution to thrombus formation (Bi et al., 2015). Another study examined the effect of EVs isolated from explant-derived cardiac stromal cells from patients with normal angiography results vs EVs from patients with heart failure in a mouse model of MI (Qiao et al., 2019). Authors found that intramyocardial injection of EVs from heart failure patients increased infarct size aggravating cardiac function and vascular remodeling while injection with EVs from non-heart failure patients reduced infarct size (Qiao et al., 2019). Profiling of these EVs revealed that miR-21-5p expression was reduced in EVs from patients with heart failure (Qiao et al., 2019). *In vitro* studies in HUVECs showed that miR-21-5p silencing in EVs resulted in increased cell apoptosis while transfection of HUVECs with miR-21-5p to increase miR-21-5p levels in EVs resulted in reduced cell apoptosis (Qiao et al., 2019). Finally, several studies have reported evidence on how miRNAs are implicated in fibrous cap thinning and plaque destabilisation, plaque erosion and calcification (summarised in (Andreou et al., 2015)). MiR-29b levels were found elevated in biopsies of human thoracic aneurysms and its expression was induced in models of genetically induced aneurysms in Fibulin-4$^{R/R}$ KO mice which demonstrate extracellular matrix components defects suggesting their implication in fibrous cup thickening (Boon et al., 2011). MiR-24 via targeting of MMP-14 has been suggested to promote plaque stability with stable plaques containing higher levels of miR-24 and unstable plaques containing lower levels of miR-24 (Di Gregoli et al., 2014).

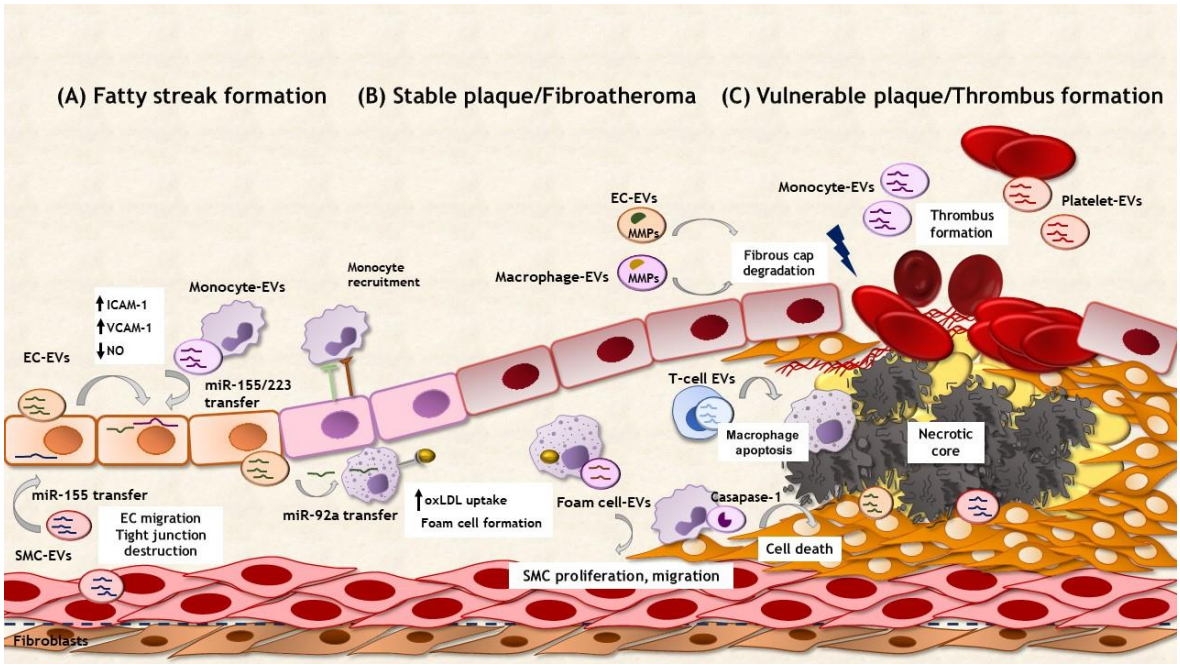

Figure 1-6 EVs and their miRNA cargo signalling in vascular inflammation and atherosclerosis.

Schematic representation of EVs and their cargo participating in early and late steps of atherosclerotic lesion progression. (A) In early stages of atheroma formation, EC-EVs via transfer of their cargo induce endothelial ICAM-1, VCAM-1 expression, reduction of NO production. Endothelial EV-miR-92a promotes oxLDL uptake by macrophages. Monocyte-EVs and miR-155/223 aggravate vascular inflammation and ICAM-1 and VCAM-1 expression by ECs. Macrophage turned into foam cell-EVs and induce SMC proliferation and migration, aggravating the progression of the disease. Crosstalk between cells is fundamental; SMC-EVs can promote EC migration and via EV-miR-155 transfer promote tight junction destruction. (B) Dead cells accumulate in the plaque's necrotic core. Casapse-1 transfer form monocyte-EVs to SMCs promoted vascular death and participate in formation of the atherosclerotic plaque. (C) Weakening of the fibrous cap is the main cause of plaque rupture. EVs from various sources (macrophage, endothelial) encapsulate MMPs and may degrade extracellular matrix and destabilize the plaque. Platelet and monocyte derived EVs can also enhance thrombus formation. Adapted from ((Charla et al., 2020), published under published under a Creative Commons CC-BY license).

1.5 Aims and Hypothesis

Atherosclerosis is still the main cause of death worldwide due to its subsequent complications and EVs have been recognised for their contribution to lesion development. The hypothesis of this study is that intracellular communication of vascular cells, including SMCs and ECs, is mediated by EVs via transfer of their cargo, thereby acting as second messengers and participating in atherosclerosis progression. Atherogenic stimuli like oxLDL will alter EV properties along with their cargo and, as a result, the biological properties of EVs.

- To characterise the effect of oxLDL stimulation on EV release from SMCs and analyse their biological effects including cellular uptake and cell death on recipient cells.

- To profile the small RNA cargo of SMC-EVs after oxLDL stimulation, identify gene targets for specific miRNAs and formulate a pathway hypothesis on how identified miRNAs regulated disease related biological functions via target gene regulation.

- To characterise EVs from mice with and without atherosclerosis and the EV-miRNA expression from serum EVs of mice with and without atherosclerosis.

- To modulate the miRNA expression of SMC-EVs and study the biological outcome and regulation of gene targets by specific miRNAs.

Chapter 2 Materials and Methods

2.1 Solutions

Table 2-1 Solutions

Solutions	
RIPA buffer (5 mL)	5 mL of RIPA Lysis and Extraction Buffer (Thermo Scientific™, Renfrewshire Scotland, UK) were supplemented with ½ tablet cOMPLETE protease inhibitor (Roche, Switzerland) and 50 µL phosphatase inhibitor (Sigma Aldrich, Irvine, UK)
1X TBS (1 L)	100 mL 10X TBS (Thermo Scientific™ TRIS-buffered saline (TBS, 10X) pH 7.4, for Western blot) diluted in 900 mL H_20
1X TBST (1 L) (TBS-0.05% Tween)	500 µL Tween 20 (Sigma Aldrich, Irvine, UK) in 1L 1XTBS
1X Tris-EDTA (TE) (100 mL)	0.121 g Tris, 0.037 g EDTA diluted in 100 mL H_2O, pH 8. Solution was autoclaved
0.1X TE (50 mL)	5 mL 1X TE diluted in 45 mL RNAse free H_2O
4% PFA	4 g of paraformaldehyde (PFA) were dissolved in 100 mL of DPBS. The solution was heated to 60ºC to ensure complete dissolution of PFA. pH was measured. Aliquots of 5 mL were stored at -20ºC
50 mM trehalose	0.0378 g of trehalose were dissolved in 2 mL of sterile DPBS. Solution was filtered prior to use
1% BSA	0.3 g of BSA were dissolved in 30 mL of sterile DPBS. Solution was filtered prior to use. Solution was filtered prior to use

2.2 Cell culture

2.2.1 Cell maintenance

Primary human coronary artery SMC (HCASMC; PromoCell, Heidelberg, Germany and Thermo Scientific™, Renfrewshire Scotland, UK) were cultured in Smooth Muscle Cell Growth Medium 2: Basal Medium and Supplement Pack (C-22162 PromoCell, Heidelberg, Germany), supplemented with 100 international units (I.U)/mL penicillin, 100 µg/mL streptomycin. The supplement pack contained: Fetal Calf Serum (0.05 mL/mL), Epidermal Growth Factor (recombinant human) (0.5 ng/mL), Basic Fibroblast Growth Factor (recombinant human) (2 ng/mL) and Insulin (recombinant human) (5 µg/mL). Cells were grown in a T75 cm^2 tissue culture flask and incubated at 37°C with 5% carbon dioxide (CO_2).

Primary human coronary artery EC (HCAEC; Sigma Aldrich, Irvine, UK) were cultured in Endothelial Cell Growth Medium MV: includes Basal Medium and Supplement Pack (C-22120 PromoCell, Heidelberg, Germany), supplemented with 100 international units (I.U)/mL penicillin, 100 µg/mL streptomycin. The supplement pack contained: Fetal Calf Serum (0.05 mL/mL), Endothelial Cell Growth Supplement (0.004 mL/mL), Epidermal Growth Factor (recombinant human) (10 ng/mL), Heparin (90 µg/mL), Hydrocortisone (1 µg/mL). Cells were grown a T75 cm^2 tissue culture flask and incubated at 37°C with 5% carbon dioxide (CO_2).

For both cell types: every 2 days cell culture media was changed until cells reached 80% confluence. Culture media was removed, and cells were washed twice with 5 mL of sterile Dulbecco's phosphate-buffered saline (DPBS 1X W-OUT CALCIUM, Invitrogen™, Renfrewshire Scotland, UK) and incubated with 5 mL of 1x Trypsin-ethylenediamine tetra-acetic acid (EDTA) (10x 0.5% trypsin-EDTA, Gibco, Renfrewshire Scotland, UK) at 37°C for approximately 5 minutes or until the majority of cells detached from the surface of the flask. Next, 13 mL of Trypsin Neutralizing media (10% (v/v) FBS (FBS HEAT INACTIVE S American, Invitrogen™, Renfrewshire Scotland, UK) in Dulbecco's Modified Eagle Medium (DMEM), Invitrogen™, Renfrewshire Scotland, UK) was added to neutralize the enzyme. Cell supernatant was subjected to centrifugation at 220g for 5 minutes, the supernatant was removed, and the pellet of cells was resuspended in 1 mL of Smooth Muscle Cell Growth Medium 2 or Endothelial Cell Growth Medium MV. Cells were transferred to a T75 cm^2 flask containing 14 mL of Smooth Muscle Cell Growth Medium 2 or Endothelial Cell Growth Medium MV. Cells were grown to 70-80%

confluence before subculturing and all experiments were conducted on HCASMC between passages 5-7.

Table 2-2 HCASMC Donor details

HCASMC Donor details				
Donor ID	Sex	Age	Comments	Provider
1689414	Female	32		Thermo Scientific™
2206118	Female	32		Thermo Scientific™
416Z048.4	Female	63	Asian	Promocell
C0175	Unknown	Unknown	Donor cells provide by Dr Bradshaw without further information	Thermo Scientific™

2.2.2 Cell counting and plating

After trypsinization and centrifugation, cells were resuspended in 5 mL of cell culture media. Next, 10 µL of cell suspension was placed on a hematocytometer across the chamber. The hematocytometer was placed on a light microscope and the number of cells in each square was counted. The sum of 4 squares was divided by 4 to generate the average cell count. The following equation was used to calculate the concentration of cells per mL:

$$\frac{Cells}{mL} = \frac{average\ cell\ count\ x\ 10^4}{5\ mL}$$

The equation could be modified if the volume which the cells were resuspended changed.

Plate	Cell density (cells/mL)	Media added (mL)
6-well plate	$1x10^5$	2
12-well plate	$1.5x10^5$	1
24-well plate	$1x10^5$	0.5
96-well plate	$4x10^4$	0.2

Based on cell density needed for each plate, the appropriate volume of cell suspension was added to each well. When passaging HCASMC, 7,500 - 10,000 cells

per cm^2 were added to each T75 cm^2 flask as per Promocell recommendation. When passaging HCAEC, 5,000–10,000 cells per cm^2 were added to each T75 cm^2 flask as per Promocell recommendation.

2.2.3 Cryo-preservation and recovery of cells

To prepare cells for cryo-preservation, confluent cells were subjected to trypsinization and centrifugation as described in section 2.2.1. The cell pellet was then resuspended in 1 mL complete media supplemented with 10% (v/v) dimethyl sulphoxide (DMSO; Thermo Scientific™, Renfrewshire Scotland, UK) and 10% (v/v) FBS. The cell suspension was transferred into a cryo-preservation vial and cooled at a constant -1ºC/minute to -80ºC using a Mr Frosty™ Freezing Container (Thermo Scientific™, Renfrewshire Scotland, UK) containing isopropanol. Next day, frozen cells were transferred to liquid nitrogen storage where they were stored indefinitely.

Prior to the recovery of the cells, 14 mL of Smooth Muscle Cell Growth Medium 2 or Endothelial Cell Growth Medium MV was added into a T75 cm^2 flask and the flask was placed into the incubator. Frozen cells were recovered from liquid nitrogen and thawed as per manufacturer's instruction. The cryo-vial was partially submerged inside the water bath for 2 minutes until cells were thawed. Next, cryo-vial was sprayed with 70% ethanol, placed inside the hood and cells were transferred into the flask using a Gibson pipette. The next day, media was replaced.

2.3 Functional *in vitro* assays

2.3.1 DiI-oxLDL uptake by HCASMCs

HCASMCs at a density of $5x10^4$ cells/mL were plated in a 96-well plate (96 well plate, SCREENSTAR, black, sterile, Stonehouse, UK). No cell starvation was performed. Cells were washed with DPBS prior to treatment. Cells were treated with DiI-oxLDL (DiI-Lipoprotein, low density, oxidized, human plasma, Alpha Aesar, Ward Hill, Massachusetts, US) with a range of concentrations from 5 µg/mL to 200 µg/mL and control cells were left untreated with for 5 hours. Next, cells were washed 2 times with DPBS and then fixed with 4% PFA in DPBS for 10 minutes. PFA was removed from the cells and washed 2 times with DPBS to ensure removal of PFA. Nuclei were stained with 4′,6-Diamidine-2′-phenylindole dihydrochloride

(DAPI) (Sigma Aldrich, Irvine, UK) (1:1000 in DPBS) for 10 minutes in the dark. DAPI stain was removed from cells and washed with DPBS to remove unbound stain from cells. Cells were kept in DPBS in the fridge in the dark until they were imaged.

Cells were imaged with the Leica DMi8 Inverted Microscope (Leica Microsystems, Wetzlar, Germany) and images were acquired using the LAS X software (Leica Microsystems, Wetzlar, Germany) at 40x magnification. Lasers were always tested, and settings were applied based on fluorescence detected in the negative control sample and then the rest of the samples were imaged. A scale bar of 100 μm was selected and was added to each captured image. For quantitative analysis, 3 images per well were taken and all of them were included in the analysis. Dil-oxLDL fluorescence was analysed using ImageJ software. The merged tiff or jpg image was opened in ImageJ. On the menu bar, image option was selected, the colour option and then split channels where each channel/fluorescent dye was imaged separately. The image for one channel was selected, the option adjust was selected and then threshold. The greyscale threshold was adjusted until the white specks (DAPI stain or Dil-oxLDL stain) were separated from background. By clicking apply, a black and white image was generated. To measure the white area which represented fluorescence stain, the option analyse was chosen and set measurements option was chosen. Then by clicking analysis and measure, a window was created where the % Area represented the black area/ background. Therefore, to estimated % fluorescence (white area): % fluorescence intensity (white area) = 100% - % Area (black area/background). The same process was followed for each fluorescent dye within each image captured. The % fluorescence for DAPI and Dil-oxLDL were calculated. The final % fluorescence was calculated by dividing the % fluorescence of Dil-oxLDL with % fluorescence of DAPI and that ratio was multiplied by 100.

$$\%\ fluorescence\ in\ DAPI = \left(\frac{\%\ fluorescence\ Dil - oxLDL}{\%\ fluorescene\ DAPI}\right) * 100$$

2.3.2 MTT Assay

Estimation of cell metabolic activity after EV treatment was performed using the CyQUANT™ MTT Cell Viability Assay (Thermo Scientific™, Renfrewshire Scotland, UK). The MTT assay exploits the ability of certain enzymes to reduce the soluble MTT dye into insoluble purple formazan crystals. Metabolically active cells or viable cells can reduce the MTT dye into the insoluble purple formazan crystal.

The formazan crystal become soluble SDS-HCL addition resulting in a colorimetric change in the cell culture media. The assay was performed as per manufacturer's instructions. Cells were seeded into a 96-well plate at a density of $4x10^4$ cells/mL. After EV treatment, media was removed and replaced with 100 µL of fresh media. 10 µL of 12 mM MTT stock was added to each well and mixing by pipetting up and down. The 12 mM MTT stock was prepared by adding 1 mL of sterile DPBS to one 5 mg vial of MTT. MTT stock was vortexed thoroughly until crystal was dissolved. Cells were incubated with MTT dye in the dark for 4 hours in the incubator. After the 4-hour incubation, 100 µL of SDS-HCL solution was added to each well and mixing was achieved using a pipette. To prepare the SDS-HCL solution, 10 mL of filtered 0.01 M HCL was added to one tube containing 1 g of SDS. The solution was mixed gently until the SDS was completely dissolved. The plate was incubated for 4 hours in the dark at 37°C. Each sample well was mixed again, and plate absorbance was measured at 570 nm using a PerkinElmer 2030 plate reader. Blank measurements, empty wells with fresh media, 12 mM MTT and SDS-HCL, were subtracted from all absorbance values before analysing the data.

2.3.3 BrdU cell proliferation assay

Estimation of cell proliferation was performed using the Cell Proliferation ELISA, BrdU (colorimetric) (Sigma Aldrich, Irvine, UK). Bromodeoxyuridine (BrdU) is a thymidine analog that incorporates into the DNA of dividing cells during the S-phase of the cell cycle. Monoclonal antibodies/labelled probes against BrdU have been developed and allow the detection of proliferating cells (Crane and Bhattacharya, 2013). The assay was performed as per manufacturer's instructions. Cells were seeded into a 96-well plate at a density of $4x10^4$ cells/mL. Cells were quiesced for 48 hours before treatment. Before adding the treatment, BrdU labelling reagent was diluted 1:1000 in media used for the treatment. The media containing BrdU labelling reagent was used to prepare appropriate treatments apart from one blank/background control sample in which wells contained cells with media without BrdU labelling reagent. Two blank/background controls were prepared for this type of assay, one where wells contained cells without BrdU labelling reagent so the background absorbance of cells could be estimated and, the second where there were no cells + media + BrdU labelling reagent so background binding of BrdU labelling reagent to the plastic could be estimated. After 24 hours treatment, labelling media was removed by suction. Cells were dried by incubating the plate at 60°C for 1 hour. Next, 200 µL of FixDenat solution

was added to cells for 30 minutes at room temperature. The FixDenat solution was removed by flicking off and tapping the plate. The Anti-BrdU-POD was diluted 1:100 with antibody dilution solution and 100 µL of anti-BrdU-POD working solution was added to each well. Next, the plate was incubated for 90 minutes at room temperature. The antibody conjugate was removed by flicking off and tapping the plate. Wells were washed 3 times with 200-300 µL per well with Washing solution. To prepare the Washing solution, the Washing buffer was diluted 1:10 with ddH_2O. The Washing solution was removed by tapping the plate. After, 100 µL of Substrate solution was added to each well for 30 minutes to allow sufficient colour development for photometric detection. To stop the reaction, 25 µL of H_2SO_4 were added to each well and the absorbance of the samples was measured in a PerkinElmer 2030 plate reader at 450 nm. The higher mean background value was subtracted from other absorbance values.

2.3.4 Scratch assay

Estimation of cell migration was performed using an *in vitro* scratch assay. When cells were confluent, a "wound" was created with a 1000 µL tip. In this assay cells at the edge of the wound polarize and start to migrate from the edge of the wound (starting position), perpendicular to the wound edge towards the scratched wound so to ensure complete closure (Cory, 2011). Prior to cell seeding into a 12 well plate, a marker pen was used to draw 3 lines, equally distanced to each other, on the back of the plate for all the wells. Primary HCASMCs, $1{,}5x10^5$ cells/mL, were seeded into a 12 well plate and were grown until 80-90% confluence was achieved. Cells were quiesced for 48 hours. A scratch was performed in the middle of each well using a sterile 1000 µL pipette tip. Cells were washed once with DPBS and media was replaced with migration stimulation media. In each well, the scratch was imaged at 3 locations using the EVOS XL Core microscope (Thermo Scientific™, Renfrewshire Scotland, UK) at 10x magnification. On each well, scratch was imaged at 3 same locations for each timepoint (0 hours, →timepoint). Images were analysed using ImageJ software. Each image bmp file was opened with ImageJ. On the menu bar, the option analyse was selected, then tools and then grid was selected. The area per point was set to 10,000 $pixels^2$. Then, 15 lines were formed within the image. The distance between the edges for only the top 10 lines were measured for each image. Values were expressed as % wound closure compared to 0 hour wound distance.

2.3.5 oxLDL Elisa assay

Levels of oxLDL in EV samples were measured with Human Oxidized Low-Density Lipoprotein (OxLDL) ELISA Kit (Human Oxidized Low-Density Lipoprotein (OxLDL) ELISA Kit, Upper Heyford, UK). Before EV isolation, treatment ± (v/v) 500 µg/mL Proteinase K (Proteinase K, recombinant, PCR Grade, Sigma Aldrich, Irvine, UK) was performed. Proteinase K (PK) treatment is usually used to remove contaminants from EV samples (Foers et al., 2018)(Rekker et al., 2014). Conditioned culture media (CCM) (150 µL) prior to EV isolation was divided into 3 samples of 50 µL (native condition, -PK, +PK). In the native sample no PK was added with no further manipulation and EVs were isolated as described in 2.4.1. In the -PK sample, 50 µL of DPBS was added and in the +PK sample, 50 µL of 500 µg/mL PK in DPBS was added. Both -PK and +PK samples were incubated at 37°C for 1 hour and at 60°C for 10 minutes to deactivate the enzyme, prior to EV isolation. EVs isolated as described and concentrated to 100 µL. To lyse EV sample, 25 µL of RIPA lysis buffer was added (1:4 RIPA/EV). Lysed samples were diluted to 200 µL via the addition of 85 µL Diluent Buffer. All kit components were brought to room temperature prior to usage. Standards were reconstituted with 2 mL of Diluent Buffer and mixed gently. A series of dilutions using Diluent Buffer was performed to prepare the rest of the standards and blank as per manufacturer's instructions. Next, 100 µL of standards, samples and blank were added to the assigned wells. Plates were covered with plate sealer and incubated for 2 hours at 37°C. Liquid from each well was removed, 100 µL of Detection Reagent A working solution was added to each well and the plate was incubated for 1 hour at 37°C. The solution was aspirated from each well and 350 µL of 1x Wash Solution was added to each well. The Wash solution was left for 1-2 minutes, and then removed from the wells, and the same process was repeated twice. Next, 100 µL of Detection Reagent B working solution was added to each well and the plate was incubated for 1 hour at 37°C. The aspiration/wash process was repeated 5 times as described previously. After, 90 µL of Substrate Solution was added to each well, the plate was covered with a new plate sealer and incubated for 15-25 minutes at 37°C. Finally, 50 µL of Stop Solution was added to each well and absorbance was measured at 450 nm using a PerkinElmer 2030 plate reader. The oxLDL concentration was determined by interpolation of x-values from the standard curve.

2.3.6 PKH-67 labelled-EV uptake by HCAEC

HCAECs at a density of $5x10^4$ cells/mL were plated in a 96-well plate (96 well plate, SCREENSTAR, black, sterile, Stonehouse, UK). No cell starvation was performed. Cells were washed with DPBS prior to EV treatment. Cells were incubated with $2x10^{10}$ particles per well of labelled Control-EVs, oxLDL-EVs and negative control sample for different timepoints. After incubation, treatment was removed, and cells were washed with DPBS. Cells were fixed by adding 100 µL of 4% PFA in DPBS in each well for 10 minutes. PFA was removed and cells were washed with DPBS. DAPI nuclei staining followed for 10 minutes in the dark. DAPI was diluted to 1:1000 in DPBS before staining and 100 µL of DAPI was added to each well. Next, DAPI was removed, and cells were washed again with DPBS to remove unbound dye. Cells were kept in DPBS in the fridge in the dark until they were imaged with Leica DMi8 Inverted Microscope (Leica Microsystems, Wetzlar, Germany). Images were acquired using the LAS X software at 40x magnification (Leica Microsystems, Wetzlar, Germany).

2.4 General molecular biology techniques

2.4.1 RNA extraction

For the purpose of this study, RNA was extracted from EVs and cells. For RNA extraction, the miRNeasy mini kit (Qiagen, Manchester, UK) was used as per manufacturer's instructions.

EVs were isolated from cell conditioned media and concentrated after isolation to a final volume of 100 µL as described in Section 2.5.1. EVs were spiked with a known amount of synthetic miRNA as described in Section 2.4.3.1. After this, 500 µL QIAzol Lysis Reagent was added to each EV sample. When isolating RNA from serum EV samples, 500 µL of QIAzol was added to total 50 µL of serum EV sample. Regarding RNA isolation from cells (1xT75, 12-well plate etc), 700-1000 µL of QIAzol was added, cells were scraped using a Corning® cell scraper (Sigma Aldrich, Irvine, UK) and homogenate was transferred to a 1.5 mL eppendorf. As seen in Table 2-2, when adding variable volume of QIAzol the volume of chloroform and ethanol was adjusted accordingly.

After QIAzol lysis reagent addition, homogenate was vortexed for 1 minute to achieve homogenization and left at room temperature for 5 minutes. Chloroform

was added to each homogenate and was shaken for 15 seconds. The homogenate was left at room temperature for 3 minutes and underwent centrifugation for 15 minutes at 12,000g at 4ºC. The upper aqueous phase containing RNA was transferred to a new collection tube, an appropriate volume of 100% ethanol was added and was mixed thoroughly by pipetting. The sample was transferred into a RNeasy Mini spin column and subjected to centrifugation at 8,000g for 15 seconds at room temperature for the RNA to bind in the column. Column was washed with 700 µL of Buffer RWT at 8,000g for 15 seconds and the flow through was discarded. Next, 500 µL of Buffer RPE was added and centrifugation was performed at 8,000g for 15 seconds at room temperature. Another 500 µL of Buffer RPE was added and the column was subjected to centrifugation at 8,000g for 2 minutes at room temperature. The column was transferred to a new 2 mL collection tube and underwent centrifugation at maximum speed for 1 minute. The RNeasy Mini spin column was transferred to a new 1.5 mL eppendorf, 20 µL of RNase-free water were pipetted into the centre of the column. Centrifugation of the column was performed at 8,000g for 1 minute at room temperature to elute RNA. RNA samples were stored at -80ºC until use.

Table 2-3 QIAzol Lysis Reagent volumes for various sample volumes

QIAzol (µL)	Chloroform (µL)	Ethanol (µL)
500	100	450
700	140	525
1000	200	900

2.4.2 Determination of nucleic acid concentration

To determine the concentration of samples, 1-2 µL of RNA was measured using a Nanodrop™ ND-1000 spectrophotometer (Thermo Scientific™, Renfrewshire Scotland, UK) at 260 nm wavelength. Nanodrop V.5 software was used to calculate the concentration of the sample. Two measurements per sample were performed and the average of the two values was used to estimate the concentration. The measurement at 280nm was used to determine the purity of the nucleic acid as the ratio 260 nm/280 nm is the ratio of DNA or RNA to protein. In high purity solutions this ratio is from 1.7 to 1.9.

2.4.3 Reverse Transcription Polymerase Chain Reaction (RT-PCR)

2.4.3.1 RT-PCR to investigate miRNA expression

When investigating miRNA expression in EV samples (cell secreted EVs, serum or aortic tissue EVs), samples were spiked with an already known amount, 2 x10-3 picomoles or 27 pg, of Caenorhabditis elegans miR-39 (Syn-cel-miR-39-3p miScript miRNA Mimic, MSY0000010) or Arabidopsis thaliana ath-miR159a (Syn-ath-miR159a miScript miRNA Mimic, MSY0000177) (Qiagen, Manchester, UK). A synthetic miRNA was added to EV samples to be used as a control for miRNA normalization as there is no consensus to an appropriate EV-miRNA housekeeping gene (Mitchell et al., 2008)(Zampetaki and Mayr, 2012). When investigating the miRNA expression in cells RNU48 was used as housekeeping miRNA gene for normalization (Schwarzenbach et al., 2015).

cDNA synthesis for detection and quantification of miRNA was performed using TaqMan™ MicroRNA Reverse Transcription Kit (Thermo Scientific™, Renfrewshire Scotland, UK). The reaction contained 1X Reverse Transcription buffer, 1 mM of each dNTP, 0.25 U/μL RNase inhibitor, 3.33 U/μL MultiScribe™ Reverse Transcriptase enzyme and 1X TaqMan® microRNA Reverse Transcription primer. Additionally, 2.5 μL of RNA were added to the reaction and nuclease-free water was added to make up the final volume to 7.5 μL. When transcribing RNA from EVs, 2.5 μL of RNA were added to the reaction. When investigating miRNA in cells, 2.5 μL of 2 ng/μL RNA were added to the reaction (El-Khoury et al., 2016). Several studies suggest that in certain cases where RNA quantification is performed with a NanoDrop spectrophotometer it can prove to be challenging, such as EV RNA quantification, and therefore a fixed RNA volume rather than fixed RNA quantity is preferable (Tiberio et al., 2015)(Zampetaki and Mayr, 2012)(El-Khoury et al., 2016).

Next, 7.5 μL reactions were prepared in 96-well PCR plates (Starlab, Milton Keynes, UK) on ice and were covered with adhesive PCR plate seals (Thermo Scientific™, Renfrewshire Scotland, UK). A non-template control was prepared for each miRNA primer where instead of RNA, nuclease free water was added to detect contamination. Reverse transcription was performed in a Tetrad PTC-225 Thermal Cycler (MJ research, Ramsey, USA) under the following conditions: 16ºC for 30 minutes (binding of the miRNA stem-loop primer), 42ºC for 30 minutes

(reverse transcription) and 85ºC for 5 minutes (inactivation of the reverse transcription enzyme). cDNA samples were stored at -20ºC until used.

2.4.3.2 RT-PCR to investigate gene expression

cDNA synthesis for gene expression investigation, was performed using Superscript II reverse transcriptase according to the manufacturer's instructions (Thermo Scientific™, Renfrewshire Scotland, UK). As a housekeeping gene, ubiquitin C (UBC) gene was used. Each reaction mix contained: First-strand buffer (250mM Tris-HCl (pH 8.3), 375mM KCl, 15mM $MgCl_2$), DTT, dNTP mix, Random Hexamer primer, RNasin® Ribonuclease Inhibitor and SuperScript II Reverse Transcriptase. Briefly, 200 ng of total RNA was diluted in 10 µL nuclease-free water in a 96-well PCR plates (Starlab, Milton Keynes, UK) on ice and were covered with adhesive PCR plate seals (Thermo Scientific™, Renfrewshire Scotland, UK). A non-template control was prepared where instead of RNA, nuclease free water was added to detect contamination. Reverse transcription was performed in a Tetrad PTC-225 Thermal Cycler (MJ research, Ramsey, USA). The plate was incubated for 10 minutes at 70ºC to denature the RNA followed by a 10 minute incubation step at 4ºC. Next, 10 µL of reaction mix (prepared as described above) was added to each well. The plate was incubated for 10 minutes at 25ºC, 60 minutes at 42ºC, 15 minutes at 72ºC (inactivate enzyme) and incubated at 4ºC. cDNA samples were stored at -20ºC until used.

2.4.4 RT-qPCR

TaqMan™ Universal Master Mix II, no UNG (Thermo Scientific™, Renfrewshire Scotland, UK) was used for mRNA/miRNA expression analysis in EVs, cells etc. Each TaqMan® Gene/miRNA Expression Assay includes a pair of unlabelled primers and a TaqMan probe with a VIC/FAM™ dye label on the 5' end and nonfluorescent quencher on the 3' end. Denaturation of double-stranded cDNA is achieved with increases in temperature. Next, temperature reduction allows the primers and probe to bind to the sequence of interest. Taq DNA polymerase which is present in TaqMan™ Universal Master Mix synthesizes new strands and cleaves the quencher molecule from the probe, thus releasing the fluorescent dye. The fluorescence produced in each cycle is proportional to the amount of mRNA/miRNA amplified in each cycle.

2.4.4.1 RT-qPCR for miRNA expression

Amplification of cDNA template was performed with TaqMan™ Universal Master Mix II, No UNG (Thermo Scientific™, Renfrewshire Scotland, UK). A list of all miRNA assays used in this study can be found in Table 2-4. Next, 10 μL triplicate reactions were prepared in MicroAmp™ Optical 384-well reaction plates (Thermo Scientific™, Renfrewshire Scotland, UK) on ice and plates were covered with MicroAmp™ Optical Adhesive Film (Thermo Scientific™, Renfrewshire Scotland, UK). Control from RT-PCR plate and a non-template control were used where instead of cDNA, nuclease free water was added. Amplification was performed with QuantStudio 12K Flex Real-Time PCR System using standard TaqMan qPCR thermal cycling conditions: 95ºC for 10 minutes (Taq activation), 95ºC for 15 seconds (denaturation), 60ºC for 60 seconds (annealing, extension) (40 cycles). The reactions were prepared as follows:

Master mix reagents	Volume (μL)	miR-39/miR-159
2X TaqMan Universal Master Mix	5	5
20X TaqMan microRNA probe	0.5	0.5
Nuclease-free water	2.5	3.8
cDNA product	2	0.7

Table 2-4 List of Thermo Fisher Scientific TaqMan miRNA assays

miRbase ID	Assay ID
hsa-miR-125b-5p	000449
hsa-miR-125b-2-3p	002158
cel-miR-39-5p	000200
ath-miR159a	000338
hsa-RNU2	CTFVKZ3
hsa-miR-199a-5p	000498
hsa-miR-199b-5p	000500
RNU48	001006

2.4.4.2 RT-qPCR for Gene expression

Amplification of cDNA template was performed with TaqMan™ Universal Master Mix II, No UNG (Thermo Scientific™, Renfrewshire Scotland, UK). A list of all TaqMan™ gene expression assays used in this study can be found in Table 2-5. Next, 10 µL triplicate reactions were prepared in MicroAmp™ Optical 384-well reaction plates (Thermo Scientific™, Renfrewshire Scotland, UK) on ice and plates were covered with MicroAmp™ Optical Adhesive Film (Thermo Scientific™, Renfrewshire Scotland, UK). Control from RT-PCR plate and a non-template control were used where instead of cDNA, nuclease free water was added. Amplification was performed with QuantStudio 12K Flex Real-Time PCR System using standard TaqMan qPCR thermal cycling conditions: 50ºC for 2 minutes, 95ºC for 10 minutes (Taq activation), 95ºC for 15 seconds (denaturation), 60ºC for 60 seconds (annealing, extension) (40 cycles). The reactions were prepared as follows:

Master mix reagents	Volume (µL)
2X TaqMan Universal Master Mix	5
20X TaqMan Gene Expression Assay	0.5
Nuclease-free water	2.5
cDNA product	2

Table 2-5 List of Thermo Fisher Scientific TaqMan™ gene expression assays

Gene abbreviation	Gene name	Assay ID
STAT3	Signal transducer and activator of transcription 3	Hs00374280_m1
TP53	Tumor protein p53	Hs01034249_m1
SP1	Specificity Protein 1	Hs00916521_m1
ERBB2	Erb-b2 receptor tyrosine kinase 2	Hs01001580_m1
ERBB3	Erb-B2 Receptor Tyrosine Kinase 3	Hs00176538_m1
PPP1CA	Protein Phosphatase 1 Catalytic Subunit Alpha	Hs00267568_m1
UBC	Ubiquitin C	Hs00824723_m1

2.4.5 Relative Quantification

Data analysis and relative gene/miRNA expression was performed using the 2^{-ddCt} method (Livak and Schmittgen, 2001). The cycle threshold (Ct) from the exponential phase of the reactions was used for analysis. Ct represents the number of cycles required for fluorescent signal to cross the detection threshold. The Ct value is inversely proportional to the amplified target sequence. Data normalization is required by the calculation of dCt: Ct value of sample - Ct value of a housekeeping gene or miRNA. When experiments were performed in triplicate, the average dCt for each condition was calculated. For statistical analysis, the dCt values were used. The ddCt was calculated as described below:

$$ddCt = dCt_{(\text{treated sample})} - dCt_{(\text{untreated sample/control})}$$

Relative quantification (RQ), is the fold-change of the treated sample versus control/untreated samples was calculated as described below:

$$RQ = 2^{-ddCt}$$

2.5 EV experimentation

2.5.1 EV generation and isolation by Size Exclusion Chromatography (SEC)

2.5.1.1 EV generation and isolation from CCM from 3xT75 cm^2 flasks

For experiments using quiesced HCASMC to isolate EVs, cells were cultured in serum starvation medium/serum free medium (SF) (0% FBS, 100 I.U/mL penicillin, 100 µg/mL streptomycin and 2mM L-glutamine) for 48 hours prior to EV collection. HCSMCs in 3xT75 cm^2 flasks were starved for 24 hours prior to stimulation. For most stimulation experiments, quiescent HCASMCs were treated with SF media or oxLDL (10 µg/mL) in SF media (Low Density Lipoprotein from Human Plasma, oxidized (OxLDL); Thermo Scientific™, Renfrewshire Scotland, UK) for 24 hours. Cells were washed twice with sterile DPBS and then were cultured in SF media for 48 hours. After that, CCM was collected for EV isolation. The EV isolation protocol was kindly provided by Professor Sean Davidson (University College London, London). CCM underwent centrifugation at 300g at 4°C for 10 minutes to removed dead cells and debris from the collected media. The supernatant was collected and was subjected to centrifugation at 10,000g at 4°C for 40 minutes to remove microvesicles from the collected media. The supernatant was concentrated to final volume of 200 µL with Vivaspin 20 centrifugal concentrator-MWCO 30 kDa (Sigma Aldrich, Irvine, UK) by centrifugation at 2,000g at 4°C. CCM was concentrated up to 200 µL as that was the lowest concentration volume of the Vivaspin 20 centrifugal concentrator. For EV isolation, the qEVsingle/35nm column (qEVsingle/35nm, Cat.no: SP6, IZON, UK) and the Automatic Fraction Collector (AFC) by IZON were used. Next, 100 µL of the concentrated media was added to the qEV single column, the column was flushed with filtered DPBS and the void volume and 3 fractions were collected (described in Section 2.5.1.2). The remaining 100 µL of concentrated media was isolated the same way. Then, the void volume and 3 fractions of two isolations were pooled together and concentrated with centrifugation at 2,000g at 4°C using the Amicon® Ultra-4 Centrifugal Filter Unit (Sigma Aldrich, Irvine, UK) to approximately 100 µL. The reason for pooling together the fractions from two isolations was with the aim to isolate EVs from the whole of CCM and maximize the isolated EV yield. EVs were stored at 4°C short term and -80°C long term.

2.5.1.2 Optimisation of EV elution profile by Size Exclusion Chromatography (SEC)

Cells were grown, trypsinized and counted as described in Sections 2.2.1 and 2.2.2, respectively. HCASMCs in 3xT75 cm^2 flasks were starved for 24 hours prior to stimulation experiments. For most stimulation experiments, quiescent HCASMCs were treated with SF media or oxLDL (10 μg/mL) in SF media (Low Density Lipoprotein from Human Plasma, oxidized (OxLDL); Thermo Scientific™, Renfrewshire Scotland, UK) for 24 hours. Cells were washed twice with sterile DPBS and then were treated with SF media for 48 hours. After that, media was collected for EV isolation. Media was processed as described in Section 2.5.1.1. For EV isolation the qEVsingle/35nm column (qEVsingle/35nm, Cat.no: SP6, IZON, UK) and the AFC by IZON were used. The column was flushed with 5 mL of filtered DPBS, then 100 μL of the concentrated media was added to the column, the column was flushed with DPBS and the Void volume and 13 fractions of 200 μL were collected. Nanoparticle Tracking Analysis (NTA) analysis was performed to void volume and all 13 fractions as described in 2.5.3.1. The protein content of the void volume and 13 fractions was measured as described in 2.5.3.2.1. When performing protein quantification for elution fractions, some replicates among samples regarding the void volume and fractions 1-4, demonstrated negative absorbance values lower than the blank sample while in others the absorbance values detected were higher than the blank sample. The samples with absorbance values lower than the blank demonstrated negative protein concentration. To generate the EV purity ratio, particles/μg protein, the protein concentration of samples with low absorbance values was replaced with 0.5 similar to the protein concentration of samples with higher than the blank absorbance.

2.5.2 EV isolation from serum

EVs were isolated from 50 μL of mice serum samples using the Invitrogen Total Exosome Isolation Kit (Thermo Scientific™, Renfrewshire Scotland, UK). Briefly, serum samples first were subjected to centrifugation at 2,000g for 30 minutes at room temperature to remove cells and debris. Supernatant was collected and centrifugation was performed at 10,000g for 40 minutes at room temperature to remove microvesicles. Next, approximately 50 μL of serum supernatant was transferred to a new collection tube and mixed with 0.2 volumes of Total Exosome Isolation reagent (Thermo Scientific™, Renfrewshire Scotland, UK) by vortexing

and incubated at 4°C for 30 minutes. Samples then underwent centrifugation at 10,000g for 10 minutes at room temperature to pellet EVs. Supernatant was discarded and the EV pellet was resuspended in 50 µL DPBS. EVs were stored at 4°C short term and -80°C long term.

2.5.3 EV characterisation

2.5.3.1 Nanoparticle Tracking Analysis (NTA)

To determine EV sample size and concentration, EVs were imaged on NanoSight LM14 (Malvern Instruments Ltd, Worcestershire, UK) using Nanoparticle Tracking Analysis 3.4 (NTA). Samples for NTA were diluted in DPBS (1 mL of sample). The correct dilution was assessed based on the number of particles/frame which should be between 20-60 particles (Gardiner et al., 2013). NanoSight was cleaned with dH_2O before loading each sample. The capture settings used were: Screen gain: 1, Camera level: variable. Samples was injected into the LM14 Viewing Unit using a syringe. Particles are illuminated using a laser beam and the camera images light scatter by each particle and makes each particle visible. NTA follows the movement of each particle under Brownian motion and calculates the average distance it moves per frame and converts the distance each particle moved in the liquid into particle size. Five videos of 1 minute each were recorded and analysed to obtain particle size and concentration for each sample.

2.5.3.2 Western blot analysis

2.5.3.2.1 Quantification of Protein Concentration

Total protein concentration of EV samples used in western immunoblotting was measured using the Micro BCA™ Protein Assay Kit (Thermo Scientific™, Renfrewshire Scotland, UK). Proteins in alkaline solution will cause reduction of Cu^{2+} to Cu^{1+}, bicinchoninic acid (BCA) in the solution is responsible for the sensitive and selective colorimetric detection of the Cu^{1+}. The protein assay was performed according to the manufacturer's protocol (Thermo Scientific™, Renfrewshire Scotland, UK). Briefly, a dilution series with range of 0 µg/mL to 200 µg/mL of bovine serum albumin (BSA) (Thermo Scientific™, Renfrewshire Scotland, UK) was prepared by dilution in 0.2M NaOH. Next, 5 µL of non-lysed sample was transferred to an eppendorf with 95 µL of 0.2M NaOH. Sample was sonicated 3x 10 seconds (Pulse: 30 seconds, 10 seconds, Amplitude 50%). Next, 100µL of the standard solutions or sample (diluted with NaOH) were pipetted into a 96 well-plate and 100 µL of working reagent was added to each standard and sample.

The plate was incubated for 2 hours at 37ºC. The absorbance of standards and samples was measured at 562 nm using a PerkinElmer 2030 plate reader. Total protein concentration of cell samples was determined by interpolation of x-values from the standard curve.

2.5.3.2.2 Western Blot with Licor system

For protein detection in EV samples, EVs were lysed using RIPA Buffer (Table 2-1) with 1:4 (RIPA/EV ratio e.g., 20 µL RIPA Lysis Buffer were added to 80 µL of EV sample for proper lysing). After the correct amount of RIPA Lysing Buffer was added to EV sample, sample was vortexed and incubated on ice for 30 minutes. Samples were sonicated 3x 10 seconds (Pulse:30 seconds, 10 seconds, Amplitude 50%).

After protein quantification 5-10 µg of protein were prepared for gel electrophoresis. Samples were diluted if need with DPBS up to 37 µL, 9 µL of NuPAGE™ LDS Sample Buffer (4X) (Thermo Scientific™, Renfrewshire Scotland, UK) was added and denaturation was performed by heating the samples on a thermal cycler to 95ºC for 5 minutes. As a positive control, 10 µg of protein lysate from HCASMC was used. Denaturation of the positive control was performed as described previously.

Protein lysates were loaded onto NuPAGE Bis-Tris protein gels, 10% polyacrylamide concentration (NuPAGE™ 10%, Bis-Tris, 1.0 mm, Mini Protein Gel, Thermo Scientific™, Renfrewshire Scotland, UK) along with 2.5 µL of protein ladder as a reference for protein detection (Chameleon® Duo Pre-stained Protein Ladder, Fisher Scientific, Loughborough, UK). Protein separation was resolved at a running system of 1x MES SDS Running Buffer (NuPAGE™ MES SDS Running Buffer (20X), Thermo Scientific™, Renfrewshire Scotland, UK) at 120 V until the dye migrated to the end of the gel.

Semi-dry protein transfer was performed using Power Blotter System (Power Blotter System, Invitrogen™, Renfrewshire Scotland, UK). Nitrocellulose membrane and the gel were incubated in Power Blotter Transfer Buffer for 5 min prior to transfer and transfer was performed at 25 V and 2.5 A for 8.5 minutes (Power Blotter 1-Step™ Transfer Buffer (5X), Invitrogen™, Renfrewshire Scotland, UK) (Power Blotter Pre-cut Membranes and Filters, nitrocellulose, mini, Invitrogen™, Renfrewshire Scotland, UK). Upon transfer completion, the membrane was blocked for 1 hour at room temperature under constant shaking

using blocking buffer (Intercept Blocking Buffer (Intercept® (PBS) Protein-Free Blocking Buffer, LI-COR Biosciences, Cambridge, UK).

After blocking, the membrane was incubated at 4ºC overnight under constant shaking with primary antibody which was diluted to the correct concentration in blocking buffer as described previously. The membrane was washed 3 times with 1xTBST for 5 minutes. Membrane was incubated with secondary antibody at the correct dilution in blocking buffer for 1 hour at room temperature under shaking in the dark. Membrane was washed 3 times with 1xTBST for 5 minutes and scanned using the Odyssey® CLx imaging system (LI-COR Biosciences, Cambridge, UK). Images were exported and analysed using Image Studio Light (LI-COR Biosciences, Cambridge, UK).

Antibody	Dilution	Host	Blocking Solution
Annexin-2 (ab189473)	1:5000	Rabbit	Intercept Blocking Buffer
Annexin 11 (D-12) (sc-46686)	1:200	Mouse	Intercept Blocking Buffer
CD81 (B-11) (sc-166029)	1:500	Mouse	Intercept Blocking Buffer
CD63 [TS63] (ab59479)	1:2000	Mouse	Intercept Blocking Buffer
TSG101 [EPR7130(B)] (ab125011)	1:5000	Rabbit	Intercept Blocking Buffer
Anti-Mouse IgG (H+L) Highly Cross-Adsorbed Secondary Antibody, Alexa Fluor 790 (A11357)	1:15000	Goat	Intercept Blocking Buffer
Anti-Rabbit IgG (H+L) Cross-Adsorbed Secondary Antibody, Alexa Fluor 790 (A11367)	1:15000	Goat	Intercept Blocking Buffer

2.5.3.3 Transmission electron microscopy (TEM)

EVs were resuspended in 4% PFA (1:1) and were processed as described (Théry et al., 2006). Samples were processed and imaged by Mrs. Margaret Mullin based on the School of Life Sciences, University of Glasgow, UK. Briefly, 5 µL of fixed EVs were placed onto glow discharged (Quorum Q150T ES) carbon coated filmed 400 mesh copper grids and left to attach for 20 minutes. Grids were placed so the sample faced side down on to 6 droplets of PBS for 2 minutes followed by 1% glutaraldehyde/PBS fixative for 5 minutes. Samples were then transferred through 8x dH_2O washes for 2 minutes each. EV samples were contrast stained with uranyl-

oxalate solution, pH 7 for 10 minutes followed by 2% methyl-cellulose-UA incubation for 10 minutes on ice. Grids were picked up on platinum loops, excess stain gently removed with filter paper and left to dry. Then, grids were carefully detached from the loops with forceps before digital imaging samples on a JEOL 12OO EX TEM (JEOL, Japan) running at 80kV. Images (tif) were captured at x6,000 and x10,000 magnifications on a CANTEGA 2K x 2K camera using Olympus ITEM software.

2.5.4 PKH67 labelling of EVs

EVs were labelled using the PKH67 Green Fluorescent Cell Linker Mini Kit for General Cell Membrane Labeling (Sigma Aldrich, Irvine, UK) as described by Takov et al., (Takov et al., 2017). PKH67 is a green, fluorescent lipophilic dye that can be incorporated into lipid membranes. Briefly, 100 µL of Control-EVs and oxLDL-EVs were stained with 4µM PKH67 in Diluent C in final volume of 500 µL for 10 min at RT: 400 µL of 4µM PKH67 to the 100 µL EV prep. A negative control, containing particle free DPBS in which EVs were eluted, was stained following the same process. Samples were transferred to Amicon Ultra-0.5 Centrifugal Filter Unit (Merck, Glasgow, UK) and were subjected to centrifugation at 14,000g for 5 minutes. The flow through was discarded and the filter unit was topped up with DPBS. In total, another two centrifugation steps were performed to ensure the removal of unbound dye. After the third centrifugation, the labelled EVs were collected and NTA analysis was performed to determine the sample concentration after PKH67 labelling. Labelled EVs were stored in the dark at 4^{o}C short term and -80^{o}C long term.

For imaging labelled EV uptake by HCAEC the same process as described in Section 2.3.1 was followed. Cells were imaged with Leica DMi8 Inverted Microscope (Leica Microsystems, Wetzlar, Germany) and images were acquired using the LAS X software (Leica Microsystems, Wetzlar, Germany) at 40x magnification. Quantitative analysis of PKH67 fluorescence was analysed using ImageJ software as described in 2.3.1. The final % fluorescence was calculated by dividing the % fluorescence of PKH67 with % fluorescence of DAPI and that ratio was multiplied by 100.

$$\%\ fluorescence\ in\ DAPI = \left(\frac{\%\ fluorescence\ PKH67}{\%\ fluorescene\ DAPI}\right) * 100$$

2.5.5 miRNA loading in EVs

The EV-miRNA loading protocol was provide by Dr Lorraine Work's group (University of Glasgow) and miRNA loading concentration was optimised by Antoniya Pashova (University of Glasgow) based on the study of Pomatto et al., (Pomatto et al., 2019). The synthetic mimic hsa-miR-125b-5p was which was used is the following: mirVana® miRNA mimic (hsa-miR-125b-5p, Assay ID MC10148) (Thermo Scientific™, Renfrewshire Scotland, UK). The synthetic mimic cel-miR-39-3p which was used to optimise electroporation is the following: mirVana® miRNA mimic (cel-miR-39-3p, Assay ID MC10956) (Thermo Scientific™, Renfrewshire Scotland, UK). The EV sample concentration was estimated by NTA analysis. The sample was divided into two separate eppendorfs. One sample consisted of the Naïve-EVs, meaning EVs which were electroporated without the addition of mimic. The other sample consisted of the miR-125b-5p-EVs/cel-miR-39-3p-EVs meanings EVs which were electroporated with the addition of synthetic mimic. For $1x10^9$ particles, 66 picomole of mimic were added in order to result in 40 picomole of mimic electroporated into the appropriate number of particles needed to treat one well of cells. The required amount of mimic was diluted in 50 mM Trehalose (Sigma Aldrich, Irvine, UK) to make up an equal volume as to the EV prep. For naïve-EVs the equal volume of trehalose was added to the EV prep. MiR-125b-5p-EVs/cel-miR-39-3p-EVs were mixed with mimic + trehalose and Naïve-EVs were mixed with trehalose and incubated on ice for 45 minutes. Trehalose was used to prevent EV aggregation (Johnsen et al., 2016).

Next, 125 µL of EV/mimic or EV/trehalose mixture was added to a Geneflow Electroporation Cuvette (Sterile, 1mm electrode, Red Cap; Geneflow) (Geneflow, Staffordshire, UK). The sample was pulsed at 400 mV using a Bio-Rad MicroPulser™ Electroporator. Immediately after the pulse, 875 µL of ice cold 1% (w/v) BSA (Sigma-Aldrich, Irvine, UK) was added to the cuvette and mixed by pipetting. The sample was then transferred to a falcon tube and incubated at 4ºC overnight before re-purification of EVs. The next day, the sample was concentrated by centrifugation at 2,000g at 4ºC using the Amicon® Ultra-4 Centrifugal Filter Unit (Sigma Aldrich, Irvine, UK). EV isolation was performed using qEV single columns as described in Section 2.5.1.1.

2.6 Next Generation Sequencing

2.6.1 EV small RNA component sequencing

EVs were generated and isolated as described in Section 2.4.2. RNA was extracted as described in 2.3.1. RNA samples were sent to Glasgow Polyomics for sequencing. Sequencing of the samples was performed by Julie Galbraith (Glasgow Polyomics). Samples were subjected to quality control before the cDNA libraries were constructed. Quality control was performed by Julie Galbraith (Glasgow Polyomics). Briefly, microRNA Sequencing libraries were prepared from total RNA using the Qiagen QiaSeq miRNA Library Kit (Qiagen, Manchester, UK). Libraries were sequenced in 75 base, single end mode on the Illumina NextSeq 500 platform.

2.6.2 RNAseq data analysis by Deseq2

Initial bioinformatic data analysis was performed by Graham Hamilton (Glasgow Polyomics). Raw sequence reads were trimmed to remove the Qiagen microRNA adapters and poor quality bases using the program Cutadapt (Martin, 2011). Bases with an average Phred score lower than 15 were trimmed for, the 3' end of the sequence reads. Only reads with the adapters present were retained for analysis, those without the adapters were discarded. Post-filtration read properties were assessed with Fastqc program (http://www.bioinformatics.babraham.ac.uk/projects/fastqc/) before and after trimming. The quality trimmed reads were aligned to the reference genome (GRCH38) using the program Bowtie version 1.0.0 (Langmead et al., 2009). The number of reads aligning to known small non coding RNAs, defined by the biotypes miRNA, small nuclear RNAs (snRNA), small nucleolar RNAs (snoRNA), small Cajal body-specific RNAs (scaRNAs) or small RNA (sRNA) in gtf file for human (GRCH38), was obtained using bedtools (Quinlan and Hall, 2010). The resulting raw read counts per miRNA species tables were used to create a combined counts per sample counts table for input into DESeq2 for differential expression analysis (Love et al., 2014).

2.6.3 Validation of RNAseq results

RNA was extracted as described in 2.4.1. RT-PCR to investigate miRNA expression was performed as described in 2.4.3 and 2.4.4.

2.6.3.1 miRNA probe identification

The name of miRNA genes including the stem-loop pre-miRNA was given. Integrative Genomics Viewer (IGV) software was used to identify the seeding sequence for each miRNA. Sample BAM alignments and corresponding BAM index files were loaded to the program. The ENSG row number for a gene was inserted to search the BAM file for a specific ENSG ID. As a reference genome, the hg38 genome was used. The sequence that matches the RNA seq read was extracted and was compared with the sequence of the stem-loop pre-miRNA, -5p and -3p strand sequence to identify at what position of the miRNA gene the hit of the RNAseq was positive.

2.6.4 miRNA target prediction from differentially expressed miRNA

After the small RNAs identified by RNAseq were validated in EVs, potential miRNA-gene interactions were generated in silico using computational methods. For this purpose, 12 different miRNA prediction methods and software were used: miRWalk 3.0, MicroT4, miRanda, miRbridge, miRMap, miRNAMap, Pictar2, PITA, RNA22, RNAhybrid, MiRDB and Targetscan. miRNA-gene interactions generated by each prediction tool was gathered and inserted into an Excel file. Only the gene targets which were predicted by 7 or more out of 12 prediction tools were considered as predicted gene targets. To find the gene targets overlapping among the 12 prediction tools, an online tool was used (Bioinformatics & Evolutionary Genomics). The predicted gene targets that passed the threshold were cross referenced with experimentally validated gene targets found on an online curated list of validated gene targets for many miRNAs, termed Tarbase (Karagkouni et al., 2018).

2.6.5 Gene set enrichment analysis

Once, a list with predicted and validated genes was created, the next step was to perform enrichment analysis. Next, the predicted and validated selected gene targets were inserted into Database for Annotation, Visualization and Integrated Discovery (DAVID) (Huang et al., 2009)(Sherman et al., 2022). By doing that, a list of 303 genes was sorted by DAVID into smaller clusters of genes associated with Gene Ontology (GO) terms and by using statistical analysis (Fishers exact test), DAVID highlighted genes which were over-represented in certain pathways or linked with certain GO terms (Huang et al., 2007). DAVID generated a list of

enriched pathways KEGG and Biocarta databases. KEGG and Biocarta are collection of databases including manually curated biological pathways. A list with GO terms regarding biological process, cellular compartment and molecular function was also generated.

2.6.6 Pathways hypothesis

To form a pathway hypothesis, GO terms for Biological Process, Molecular Function and Cellular Compartment were examined. For each GO term list, the gene frequency was calculated, and each gene and respective gene frequency were plotted in a pie chart in Excel. Gene frequency represents how many times each gene was identified in separated GO term. For each GO term group, a list including genes hierarchically based on the gene frequency was created. The top two or three genes with the highest gene frequency from the three lists were selected.

2.7 Animal experimentation

2.7.1 Design of the study

For this study, two groups of animals were used: C57BL/6J wt female mice (Charles River, Maidstone, UK) and APOE KO female mice (Charles River, Maidstone, UK). APOE KO mice were gifted from Professor Pasquale Maffia (University of Glasgow, UK). Animals were housed in a room with a controlled light-dark cycle (12 hrs light-12 hrs dark) and ad libitum access to food and water. At 12 weeks age, mice were put under western high fat diet (+HFD) or standard chow diet (-HFD) for 12 weeks. All animal work was conducted under Home Office licence (Project License number PE1AF6E8B) and in accordance with the Animals Scientific Procedures Act (1986).

2.7.2 EV isolation from serum

Described in section 2.5.2.

2.7.3 EV isolation from aortic tissues

Whole aorta was dissected, and three parts of the aorta were separated: aortic arch, thoracic aorta and abdominal aorta. The perivascular adipose tissue (PVAT) was not separated from the aorta during dissection. Each tissue was incubated in 2 mL of MiR05-Kit (Mitochondrial Respiration Medium, Oroboros Instruments GmbH, Innsbruck, Austria) for 24 hours at 37^{o}C. After, the media was collected

and EVs were isolated as described in section 2.5.1.1. EVs were stored at 4°C short term and -80°C long term.

2.7.4 Schedule 1 procedure (termination)

Mice were terminated using the Schedule 1 method of termination in accordance with the Animals Scientific Procedures Act (1986), where mice were exposed to increasing concentrations of CO_2. Mice one by one were placed into the CO_2 chamber under gas exposure (approximately 2 minutes). When the mouse was unconscious, increase in CO_2 flow was performed for 2 minutes. The CO_2 flow was then turned off, the mouse was taken out of the chamber and the reflexes of the mouse were checked to confirm the absence of signs of life. Confirmation of death was performed by cervical dislocation.

2.7.5 Organ/Blood harvest

For blood collection, cardiac puncture was performed as described: mice were placed in the supine position where an incision was made to expose the sternum. The rib cage was cut open to allow exposure of the heart. A 19-gauge needle attached to a 1 mL syringe was then inserted into the right ventricle and blood was removed slowly to prevent the heart collapsing. Blood was transferred to 1.5 mL eppendorf and kept at room temperature to allow formation of the clot. Blood was centrifuged at 2,000g for 10 minutes at 4°C. Serum was collected as supernatant and stored at -80°C.

Next, a 19-gauge needle attached to a 10 mL syringe with DPBS was inserted to the heart at the puncture site and mice were perfused with 20 mL of DPBS prior to dissection. Aorta and hearts were dissected and cleaned. Aorta was separated into 3 distinct anatomical parts: aortic arch, thoracic aorta and abdominal aorta. The lower part of the heart was separated with a longitudinal cut and the rest of the heart where the aortic arch originates was embedded in optimum cutting temperature (OCT) compound.

2.7.6 Histology

2.7.6.1 Preparation of paraffin-embedded tissues

Tissues were fixed in 4% PFA in DPBS, pH 7.2 overnight. Tissues were washed for 5 minutes with DPBS and then placed in 70% ethanol. Tissues were dehydrated, placed into Shandon Biopsy Cassettes (Shandon, Thermo Scientific™, Renfrewshire Scotland, UK) and were processed using an automated tissue processor and

embeddor (Shandon, Thermo Scientific™, Renfrewshire Scotland, UK) as described: 70% alcohol for 30 minutes, 95% alcohol for 30 minutes, 2x 100% alcohol for 30 minutes, 2x 100% alcohol for 45 minutes, 100% alcohol for 60 minutes, 100% alcohol/xylene for 30 minutes, 2x xylene for 30 minutes, 3x xylene for 30 minutes, 2x paraffin was for 30 minutes and 2x paraffin wax for 45 minutes.

2.7.6.2 Tissue sectioning

Paraffin embedded tissue blocks were cooled to 4°C and cut into 5 µm thick sections using a bench top Leica microtome (Leica, Milton Keynes, UK). Tissue sections were transferred to a Leica water bath (Leica, Milton Keynes, UK) at 40°C prior to mounting on silane treated glass slides (Dixon, Kent, UK). Slides were left on the bench to dry and were baked overnight at 60°C.

2.7.6.3 Haematoxylin/Eosin (H/E) staining

Paraffin sections (5 µm) were stained with haematoxylin-eosin. Sections were deparaffinized, and then rehydrated through an ethanol gradient. Slides were incubated for 2 min in Harris' modified Haematoxylin (CellPath, Newtown, UK) and 2 min in Eosin Y solution (CellPath, Newtown, UK). Slides were mounted with DPX mounting medium (CellPath, Newtown, UK). Images were acquired using EVOS® FL Auto Imaging System (Thermo Scientific™, Renfrewshire Scotland, UK) at 20x and 40x magnification.

The protocol followed is described below:

Histoclear	7 minutes
Histoclear	7 minutes
100% ethanol	7 minutes
95% ethanol	7 minutes
70% ethanol	7 minutes
dH_2O	7 minutes
Harris modified Haematoxylin	2 minutes
Running tap H_2O	5 minutes
70% ethanol	30 seconds
Eosin Y solution	2 minutes
95% ethanol	30 seconds
95% ethanol	30 seconds
100% ethanol	1 minute

100% ethanol	7 minutes
100% ethanol	5 minutes
Histoclear	5 minutes
Histoclear	5 minutes

2.8 Statistical analysis

GraphPad prism 7 software was used to generate graphs presented in this thesis and to perform data statistical analysis. Data were plotted as mean ± standard error of the mean (SEM). When comparing EVs, cell's miRNA levels etc from control or oxLDL treated conditions, a two-tailed paired Student's t-test was used. For each experiment, cells which were isolated from the same patient were cultured and expanded until the correct number of T75 cm^2 flasks was acquired. Then, half of the flasks were stimulated with SF media (control cells) and the rest of the flask were stimulated with oxLDL (oxLDL cells). Since the cells originated from the same patient and 3xT75 cm^2 flasks were combined for each condition (all T75 cm^2 flasks used for each experiment were cultured in parallel), it was determined that a paired t-test should be used as advised by statistician Dr John McClure (School of Cardiovascular and Metabolic Heath, University of Glasgow). When comparing more than 2 groups, Repeated measures (RM) One-way ANOVA and Tukey's post hoc test was used. Since the comparisons for two groups were performed using a two-tailed paired Student's t-test, comparisons for more than two groups were performed using RM one-way-ANOVA. For example, experimental values obtained from one donor may be elevated in all measurements and other donor may demonstrate lower values at all measurements. RM One-way ANOVA like a paired Student's t-test will focus on how much different these values on the Y axis are so it can account for variability between groups. Statistical analysis of TaqMan data was performed on dCt values. Comparisons between groups regarding the animal studies were made using an unpaired Student's t-test or a 2 x 2 mouse phenotype by diet analysis or Two-way ANOVA and Tukey's post hoc correction. A p-value of $p<0.05$ was considered statistically significant in all experiments.

Chapter 3 Isolation and characterization of EVs from SMC-EVs +/- oxLDL treatment

3.1 Introduction

EVs are present in many biological fluids including serum, plasma, saliva, urine, amniotic fluid, breast milk, cerebrospinal fluid, nasal secretions, cell culture media after incubation with cells as well as cells in tissues (Crossland et al., 2016a)(Lobb et al., 2015)(Gai et al., 2018)(Liang et al., 2017)(Asea et al., 2008)(Lässer et al., 2011a)(Street et al., 2012)(Lässer et al., 2011b)(Hurwitz et al., 2019)(Charla et al., 2020). Various methods for EV isolation have been developed for EV research and many comparative studies among isolation methods discuss their efficacy and EV yield purity (Tauro et al., 2012)(Takov et al., 2019). A major limitation in many isolation methods regarding blood samples is the co-isolation of lipoproteins like LDL particles. For this study, size exclusion chromatography (SEC) was chosen. Ultracentrifugation (UC) is one of the most popular techniques used for EV isolation, however SEC is gaining more attention as a finer EV isolation method for better preserving EV structure and particle functionality (Takov et al., 2019)(Monguió-Tortajada et al., 2019). Several studies demonstrated the use of SEC for successful EV isolation from various sources (Nordin et al., 2015)(Benedikter et al., 2017)(Roura et al., 2018). The argument for using SEC instead of UC is the better separation of protein aggregates from EVs, as proteins have smaller sizes than EVs they will be trapped in the resin pores and thus elute later than EVs (Böing et al., 2014)(Roura et al., 2018)(Monguió-Tortajada et al., 2019).

Evidence suggests that oxLDL promotes SMC migration and proliferation in atherosclerotic plaques and SMCs also express scavenger receptors that facilitate SMC transformation into foam cells when exposed to lipoproteins (Gleissner et al., 2007)(Allahverdian et al., 2014). Other forms of LDL like acetylated LDL can induce SMC transformation into foam cells (Shen et al., 2001). SMCs co-cultured with ECs exposed to minimally modified LDL upregulated MCP-1 expression and increased monocyte transmigration into the subendothelial space of co-cultures (Cushing et al., 1990)(Navab et al., 1991). OxLDL is a potent atherogenic stimuli and according to literature, high oxLDL concentrations (>60 µg/mL) could be toxic for vascular SMCs (Kataoka et al., 2001). Hsieh et al, showed that 3 hour oxLDL treatment induced dose-dependent (100-400 µg/mL) apoptosis in recipient SMCs via the production of reactive oxygen species (Hsieh et al., 2001). The authors highlighted that naïve LDL did not affect the viability of SMCs compared to oxLDL (Hsieh et al., 2001). Another study showed that 10 µg/mL enzymatically modified

LDL significantly promoted HCASMC foam cell formation when compared to 200 µg/mL of oxLDL or 200 µg/mL native LDL (Chellan et al., 2018). Claims that oxLDL is a potent stimulator of HCASMC, it is of interest to determine a working concentration that would not be toxic for SMCs.

Studies suggest that immune, vascular or platelet derived-EVs drive atherogenesis by aggravating inflammation or thrombosis at the atheroma site (Afonyushkin and Binder, 2018)(Charla et al., 2020). Nguyen et al., showed that oxLDL treatment (50 µg/mL) altered the prolife of macrophage secreted EVs and reduced recipient macrophage migration to the vessel wall (Nguyen et al., 2018). Endothelial, immune and platelet derived EVs have been studied extensively for their participation in atherogenesis. However, few studies have characterised SMC-derived EVs after oxLDL treatment and their contribution to disease development leading to the hypothesis of this chapter, that oxLDL could alter SMC-secreted EVs in terms of size or concentration (Zheng et al., 2017). OxLDL stimulation was chosen as LDL retention to the vessel wall and its subsequent oxidation to oxLDL is considered the first step of the disease (Di Pietro et al., 2016)(Mach et al., 2020).

3.1.1 Aims

- Optimise SEC for isolation of EVs from conditioned media of cultured cells.
- Determine an oxLDL dose for HCASMC treatment that does not induce toxicity.
- Characterise EVs derived from HCASMCs after oxLDL treatment and determine the effect of oxLDL stimulation on EV release from HCASMCs.
- Study SMC-EV uptake by HCAECs.
- Examine the role of Control and oxLDL-EVs on recipient HCASMC and HCAEC cell viability.

3.2 Results

3.2.1 Optimisation of EV elution profile by Size Exclusion Chromatography (SEC)

Size exclusion chromatography was developed for EV isolation from plasma samples and therefore the first step was the optimisation of the method for EV isolation from conditioned media of cultured cells. EV elution profile when isolating EVs by SEC was assessed in this section. EV generation from HCASMCs and CCM clearance was performed as described in 2.5.1 and seen in Figure 3-1. The qEVsingle column 35nm (IZON, UK) was chosen for EV isolation from CCM as the optimum recovery range of particles, is particles with sizes <110 nm. The elution fractions 1 to 3 were suggested by the manufacturer; however, the EV elution profile was only stated for EV isolation from plasma samples. Therefore, for accurate isolation, it was essential that first the elution profile from CCM from HCASMC was determined. Briefly, the Void volume, which is the volume of liquid phase held inside the qEV single column, was collected along with 13 fractions of 200 µL each. NTA analysis of particle size showed that all fractions isolated had a particle mean size of 120-150 nm (Figure 3-2 A). NTA analysis of mode size showed that the majority of particles within each sample had size of 80-110 nm (Figure 3-2 B). Mean particle size represents the average of all particle's sizes being recorded during NTA analysis, while mode size represents the majority of particle sizes within the sample during NTA analysis. Mode size is mentioned for qualitative purposes and mean particle size was considered for EV size quantification for all experiments. NTA analysis of particle concentration showed increased particle concentration up to fraction 4, with the highest particle containing fraction being fraction 1 ($3.2x10^{11}$±$8.6x10^{10}$ particles/mL), and after fraction 5, a continuous reduction in particle concentration was observed (Figure 3-2 C).

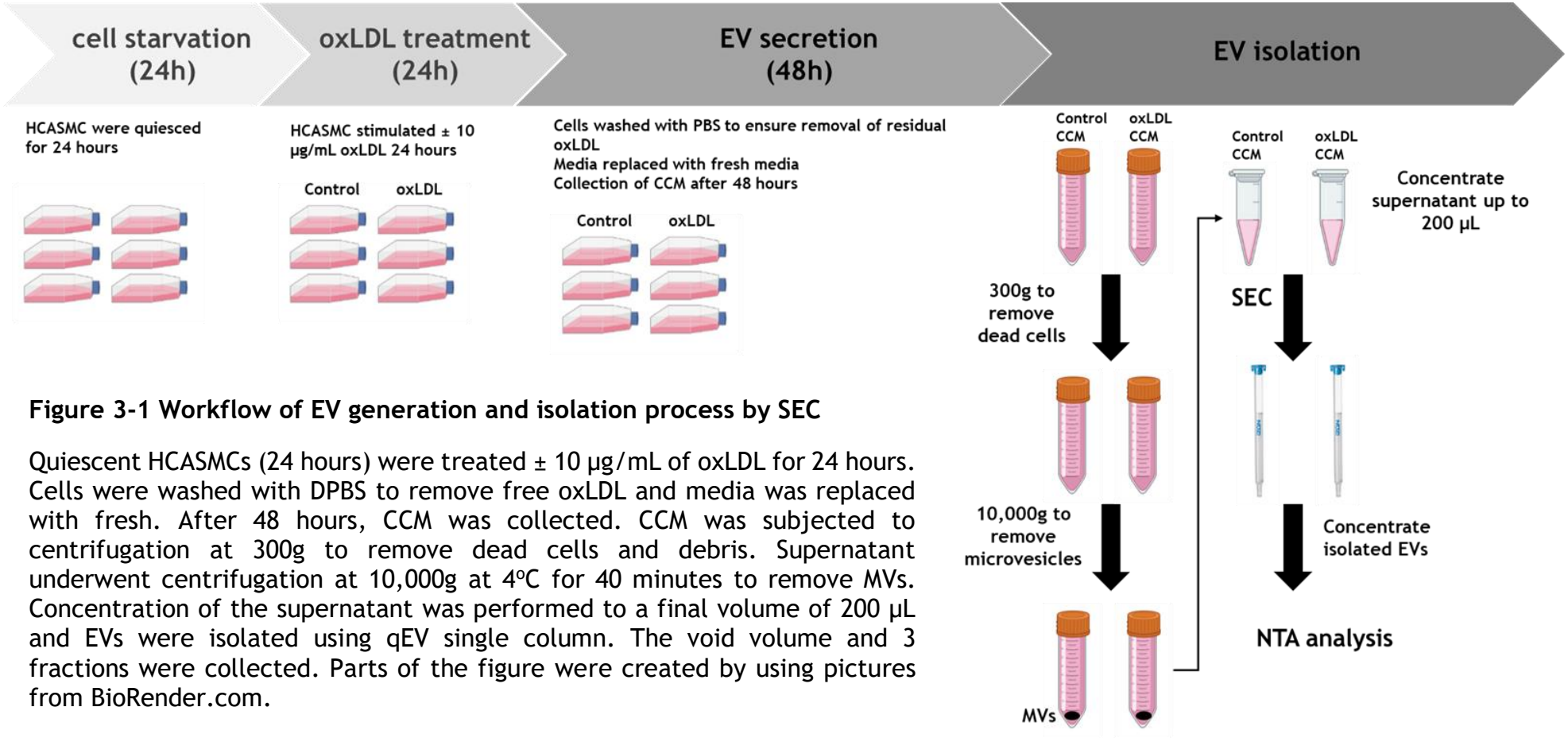

Figure 3-1 Workflow of EV generation and isolation process by SEC

Quiescent HCASMCs (24 hours) were treated ± 10 µg/mL of oxLDL for 24 hours. Cells were washed with DPBS to remove free oxLDL and media was replaced with fresh. After 48 hours, CCM was collected. CCM was subjected to centrifugation at 300g to remove dead cells and debris. Supernatant underwent centrifugation at 10,000g at 4°C for 40 minutes to remove MVs. Concentration of the supernatant was performed to a final volume of 200 µL and EVs were isolated using qEV single column. The void volume and 3 fractions were collected. Parts of the figure were created by using pictures from BioRender.com.

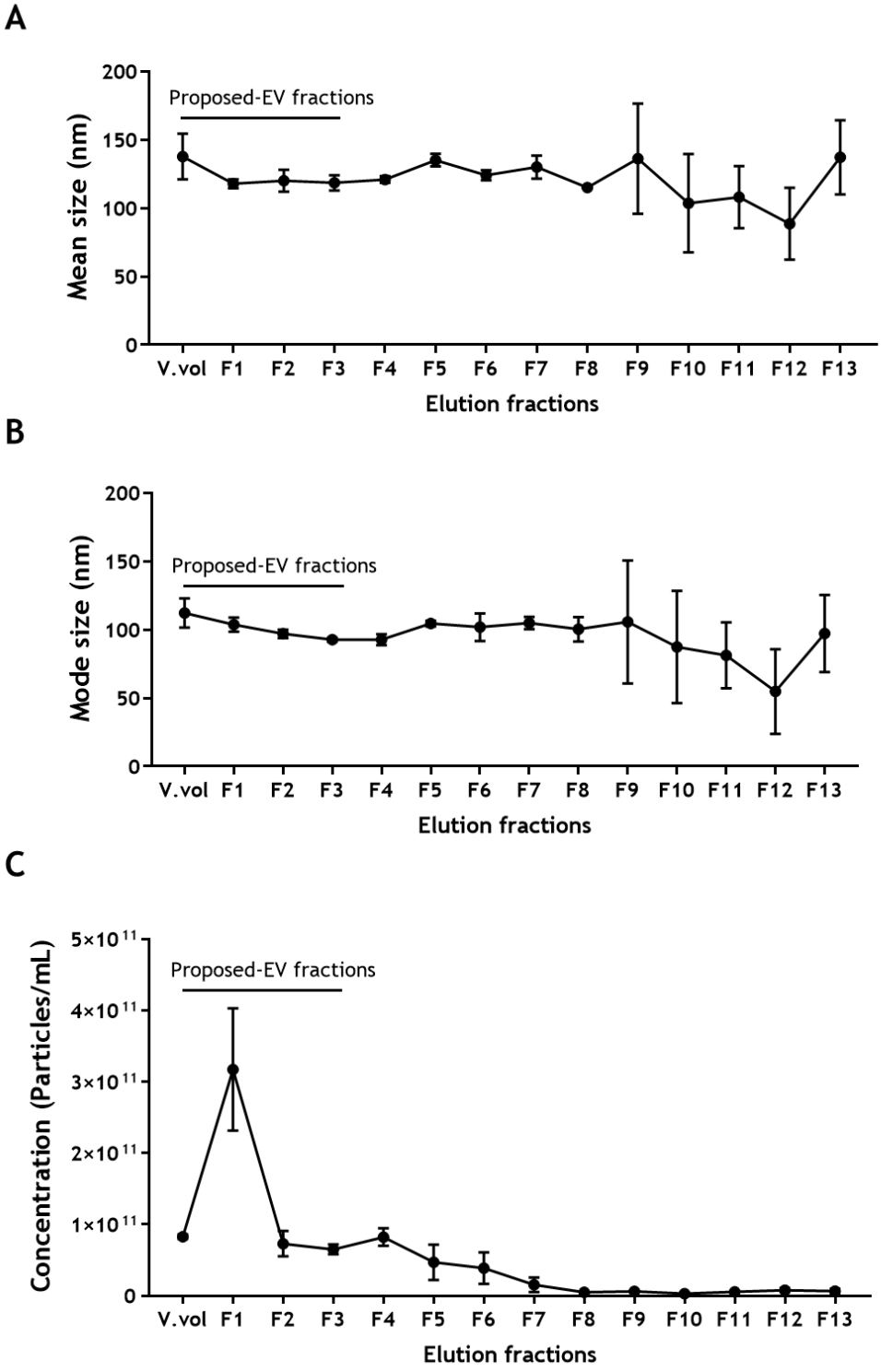

Figure 3-2 Characterisation of elution fraction by SEC

Collected elution fractions by SEC were analysed using a NanoSight LM14. (A) NTA analysis of mean particle size of SEC fractions (n=3 technical replicates, 1 patient). (B) NTA analysis of mode size of SEC fractions (n=3 technical replicates, 1 patient). (C) NTA analysis of particle concentration of SEC fractions (n=3 technical replicates, 1 patient). V.vol stands for void volume and F stands for fraction. Data are expressed as the mean ±SEM.

Next, the protein concentration of all fractions and void volume was quantified using the Micro BCA™ Protein Assay Kit. Most replicates of Void volume and fractions 1-4 when analysed with the Micro BCA™ Protein Assay Kit, had a negative absorbance value. The reason for this observation was not clear. Due to lack of additional material, the Micro BCA could not be repeated. For that purpose, the negative absorbance values were arbitrarily replaced with a value of 0.5 OD to facilitate comparison. As seen in Figure 3-3 A, fraction 10 has high protein concentration (1681.0±88.54 µg/mL) while fraction 11 was the fraction with the highest protein concentration (1975.0±272.2 µg/mL). Fractions 12 and 13 had lower protein concentration (Fraction 12 922.1± 366.5 µg/mL, Fraction 13 295.6±120.6 µg/mL). The ratio of number of particles to µg of protein in each fraction was determined (Figure 3-3 B). Literature suggests that a pure EV sample has a ratio of $>3\times10^{10}$ particles/µg protein, while samples with a ratio $<1.5\times10^{9}$ particles/µg protein is indicative of an impure sample (Webber and Clayton, 2013). Based on these values, void volume and fraction 1-4 contained the purest EV samples (Figure 3-3 B). The manufacturer's guidance for the purification of plasma-derived EVs suggests to collect only fractions 1-3, so the proposed EV-fractions were void volume, fraction 1, fraction 2 and fraction 3. Fraction 4 was not collected as it was not recommended by the qEV single column manufacturer. For all future experiments, only these proposed EV-containing fractions (void volume, fraction 1-3) were collected. These data from cell culture media derived EVs together, correlate with column manufacturer's data for plasma-derived EVs indicating that purest EV containing fractions are void volume, fraction 1-3 and that proteins are eluted in later fractions and not in EV containing fractions. Hence the SEC method was appropriate to be used to isolate EVs from conditioned cell culture media. This can be clearly seen in Figure 3-4 where both data sets were superimposed to show that the EV concentration peak is observed at fraction 1 and protein elution peak is seen at fraction 11. However, the manufacturer's protocol proposed that only the first 3 fractions should be collected and observed the protein peak in fraction 9 whereas in these studies it was observed that the peak of protein concentration was in fraction 11.

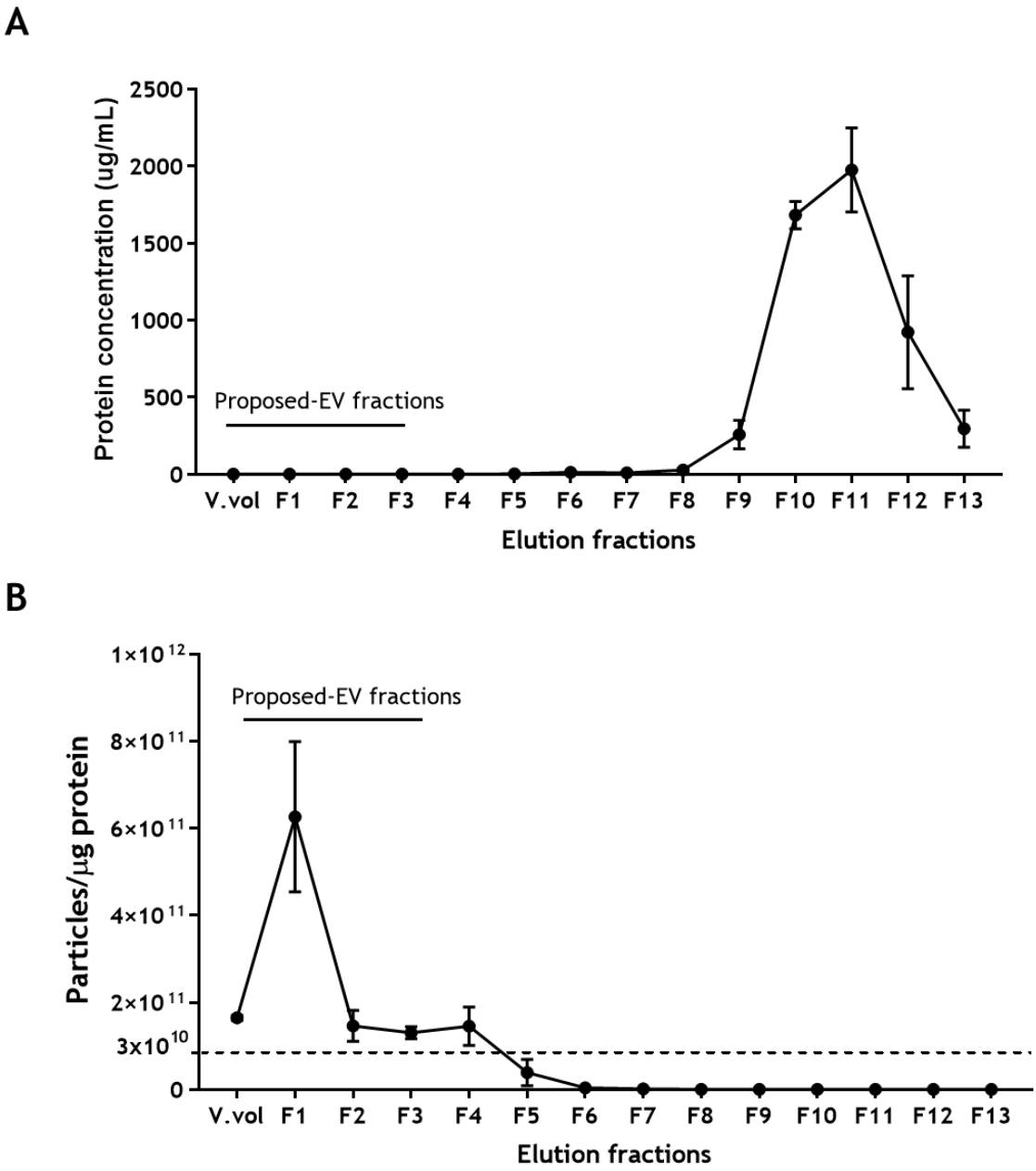

Figure 3-3 Characterisation of protein elution by SEC

Protein concentration of collected elution fractions by SEC was measured analysed using the Micro BCA™ Protein Assay Kit. (A) Protein elution profile of void volume and 13 collected fractions. (B) EV purity ratio of number of particles per µg protein for all isolated fractions (n=3). V.vol stands for void volume and F stands for fraction. Data are expressed as the mean ±SEM.

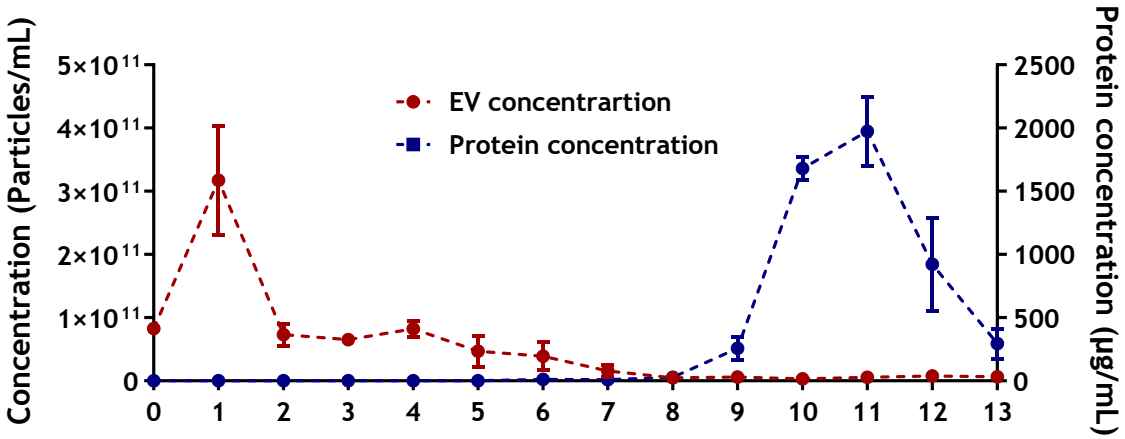

Figure 3-4 Comparison of total protein levels and EV concentration of elution fractions

The graph represents superimposed data from Figure 3-2 C andFigure 3-3 B. Red line dots represent that NTA analysis of particle concentration of void volume (0) and all fraction 1-13 isolated by SEC (n=3 technical replicates, 1 patient). The blue line dots represents the protein concentration of void volume (0) and fractions 1-13 isolated by SEC (n=3 technical replicates, 1 patient). Comparison of these data indicates that EVs are eluted first with EV concentration peak at fraction 1 and protein elution follows EV elution with protein concentration peak at fraction 11. Data are expressed as the mean ±SEM.

3.2.2 Optimisation of oxLDL stimulation of recipient HCASMCs

HCASMCs were treated with or without fluorescently labelled oxLDL for 5 hours and a range of oxLDL concentrations were used. After 5 hours, cells were fixed with PFA and images were acquired as described in 2.3.1. Quantification of oxLDL uptake reveals that oxLDL was taken up in a dose-dependent way by HCASMCs. The lower concentration of oxLDL (5 µg/mL) showed negligible uptake compared to control cells (% uptake of oxLDL 8.8±1.6) (Figure 3-5 A). Treatment with 10 µg/mL of oxLDL showed increased uptake by HCAMSCs compared to control cells (% uptake of oxLDL 38.0±7.3) (Figure 3-5 A). The other oxLDL concentrations showed increased uptake, with the peak at 150 µg/mL of oxLDL (% uptake of oxLDL 189.3±19.9), compared to control cells (Figure 3-5 A). As seen in Figure 3-5 B, oxLDL uptake by HCASMCs is visible when HCASMCs were treated with 10 µg/mL of oxLDL for 5 hours. It was assumed that at 24-hour oxLDL (10 µg/mL) treatment would be sufficient for oxLDL to be taken up by the cells and mediate a role in cellular signaling. A lower dose for oxLDL treatment was preferred as higher concentrations could alter the SMC phenotype and not only cause changes in cellular signaling but also lead to toxicity (Guyton et al., 1995)(Chellan et al., 2018).

Next, HCASMCs were treated with 10 µg/mL, 40 µg/mL and 60 µg/mL of oxLDL to determine the cell viability after oxLDL treatment for 24 hours. HCASMCs were serum starved for 48 hours and then treated with 10 µg/mL, 40 µg/mL and 60 µg/mL of oxLDL for 24 hours (Figure 3-5 C). Treatment with 10 µg/mL of oxLDL did not affect the viability of recipient HCASMCs (% viable cells 100.3±3.5), whereas 40 µg/mL of oxLDL showed lower cell viability compared to control cells (% viable cells 77.7±6.6) (Figure 3-5 C). The 60 µg/mL of oxLDL concentration had little effect on recipient cell viability (% viable cells 92.8±6.5), however, since 40 µg/mL of oxLDL reduced cell viability, it was decided that this concentration could not be used. These preliminary data suggest that 10 µg/mL of oxLDL is a sufficient concentration that is taken up by HCASMCs but does not affect the cell viability of recipient HCASMCs. Since no change was observed in cell viability, it was decided not to examine other SMC phenotypic markers.

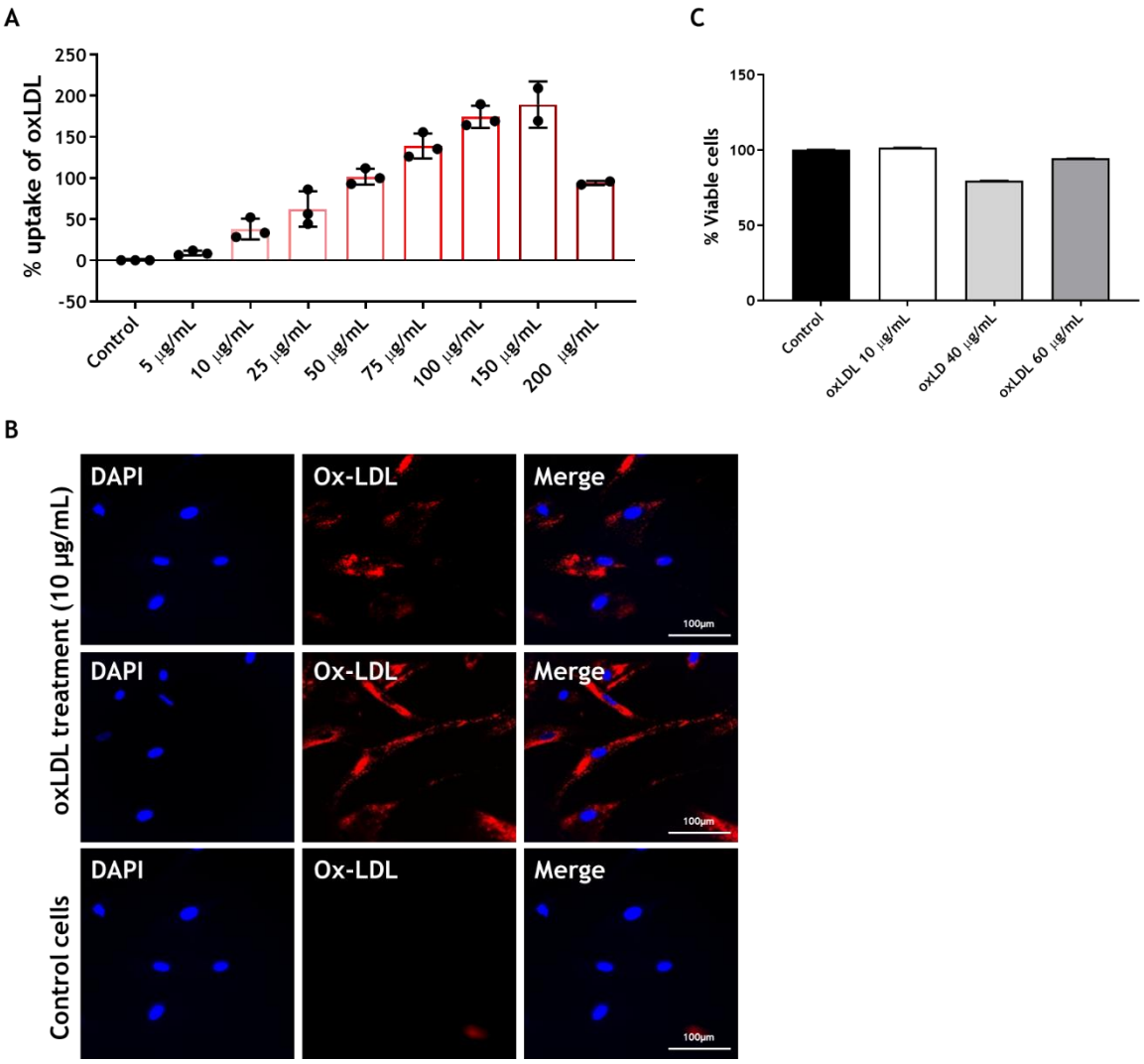

Figure 3-5 Concentration-dependant oxLDL uptake by HCASMCs

(A) HCASMCs were treated with or without a range of fluorescently labelled oxLDL concentrations for 5 hours (n=3 technical replicates, 1 patient). (B) Representative images of the 10 µg/mL concentration of oxLDL treatment at 40x magnification (n=3 technical replicates, 1 patient). (C) MTT cell viability assay on HCASMCs after 12-hour treatment of 10 µg/mL, 40 µg/mL and 60 µg/mL oxLDL (n=3 technical replicates, 2 patients). Data are expressed as the mean ±SEM. Scale bar: 100 µm.

3.2.3 oxLDL treatment does not alter the EV profile isolated with SEC

Human coronary artery SMCs were either untreated (Control cells) or treated with 10 µg/mL oxLDL in SF media for 24 hours. EVs isolated from control cells were named Control-EVs and EVs isolated from cells after oxLDL treatment were referred as oxLDL-EVs. Media was replaced and 48 hours later, EVs were isolated from CCM. EV isolation was performed via SEC and EV populations were characterised in terms of size and concentration using NTA. TEM was used to observe the cup shaped structure of EVs. Micro BCA™ Protein Assay was used for protein quantification and EV markers were detected in EV populations by western immunoblotting.

EVs were visualised and quantified using a Nanosight LM14 (Figure 3-6). An example Nanosight trace for Control-EVs showed the majority of quantified EVs had sizes ranged from 30 to 120 nm (Figure 3-6 A). An example Nanosight trace for oxLDL-EVs showed that the majority of quantified EVs had a size range of 30-150 nm (Figure 3-6 A). The size distribution of Control and oxLDL-EVs was found to be different, possibly indicating different EV populations among the samples and EV populations with different biological functions (Kowal et al., 2016). However, further studies are required so that further conclusions can be drawn. NTA analysis of mean particle size revealed that oxLDL treatment did not affect the size of released EVs, as Control-EVs were found to have a size of 116.9±5.8 nm and oxLDL-EVs was found to have size of 130.9±5.3 nm with no statistical significance detected (n=4) (Figure 3-6 B). NTA analysis of mode size showed that the majority of Control-EVs had smaller size (89.5±10.2) compared to oxLDL-EVs (114.6±10.1), but this did not reach significance (Figure 3-6 C). NTA analysis revealed no difference in concentration of released EVs after oxLDL treatment, as the concentration of Control-EVs was found to be $1.0x10^{12}$±$3.5x10^{11}$ particles/mL and the concentration of oxLDL-EVs was found to be $8.9x10^{11}$±$2.1x10^{11}$ particles/mL (Figure 3-6 D). The number of particles released per cell was calculated to further estimate release of EVs after oxLDL treatment and to ensure that the concentration profile observed was not because of cell death (Figure 3-6 E). The total number of cells in 3xT75 cm^2 flasks was measured, total particle number after isolation was measured and particle number was divided by total cell number (Figure 3-6 E). No statistical difference was found in EV release after

oxLDL treatment (Control cells: 27,547±16,404 particles/cell vs oxLDL cells:16,847±4,882 particles/cell).

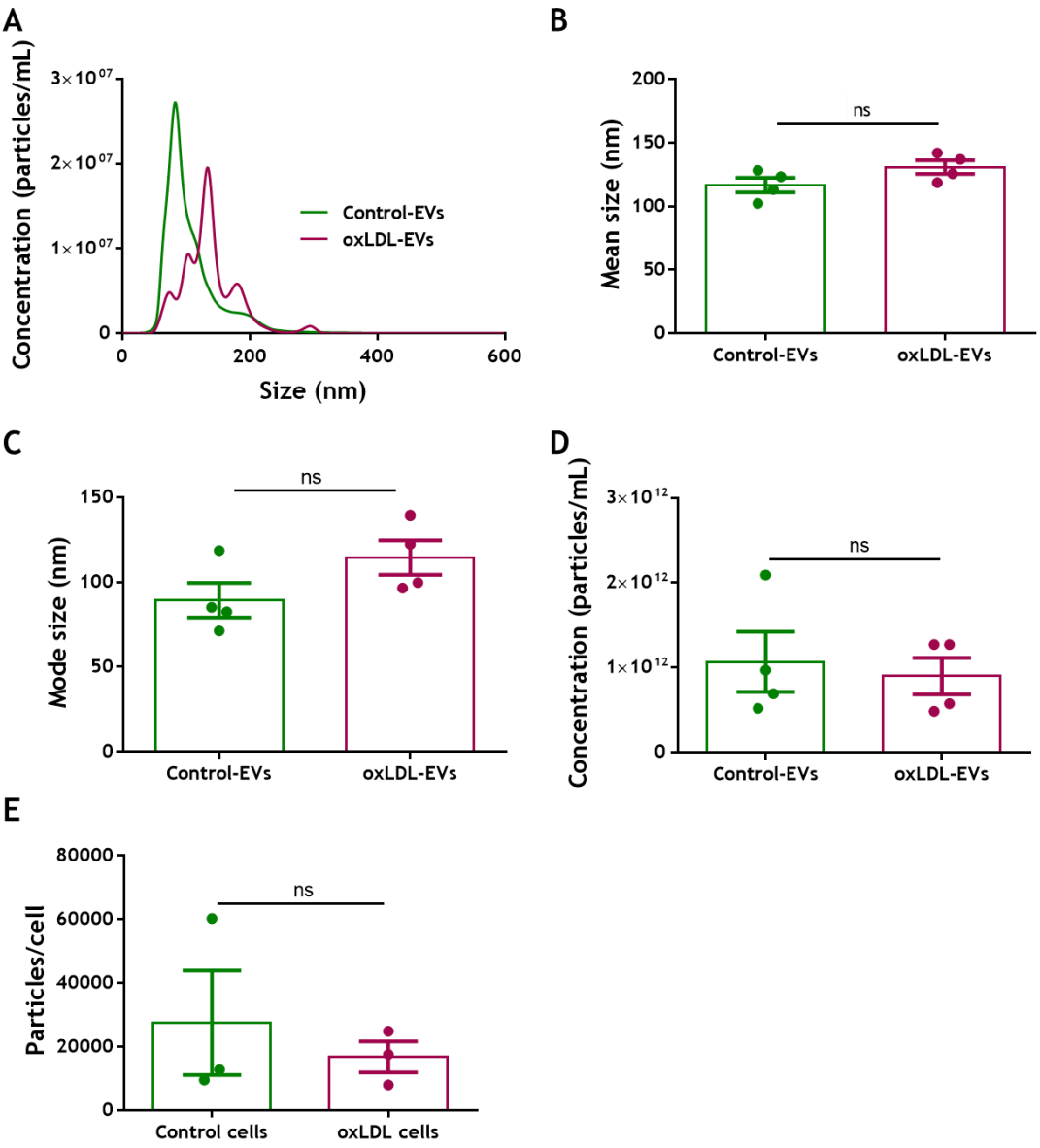

Figure 3-6 NTA Characterization of EV populations derived from HCASMC after oxLDL treatment

(A) Representative trace for Control and oxLDL-EVs produced by NanoSight showing particle size vs particle concentration. The black line corresponds to representative trace of Control-EVs, and grey line corresponds to a representative trace of oxLDL-EVs. (B) NTA analysis of particle size of EV samples (n=4 patients). (C) NTA analysis of mode size of EV samples (n=4 patients). (D) NTA analysis of particle concentration (n=4 patients). (E) Secreted particles per cell (n=3 patients). Statistical probability of differences was calculated using paired Student's t-test (ns= nonsignificant). Data are expressed as the mean ±SEM.

Electron microscopy of both EV populations derived from HCASMCs was performed, and representative images are seen in Figure 3-7 A. TEM images revealed cup-shaped vesicles indicative of EV-structure for Control and oxLDL-EVs (Figure 3-7 A). Quantification of images from TEM analysis was performed by measuring the diameters of representative images for Control and oxLDL-EVs. Quantification analysis showed that visualised Control-EVs had average diameter of 85.3±7.2 nm and oxLDL-EVs had smaller average diameter of 65.5±6.1 nm (Figure 3-7 B). However, it is worth mentioning that TEM image analysis is not a recommended method of EV size determination by the International Society of Extracellular Vesicles (ISEV) (Théry et al., 2018). It was performed in these studies only for completeness of the study. For this purpose, these values were not considered in the characterisation of EV size.

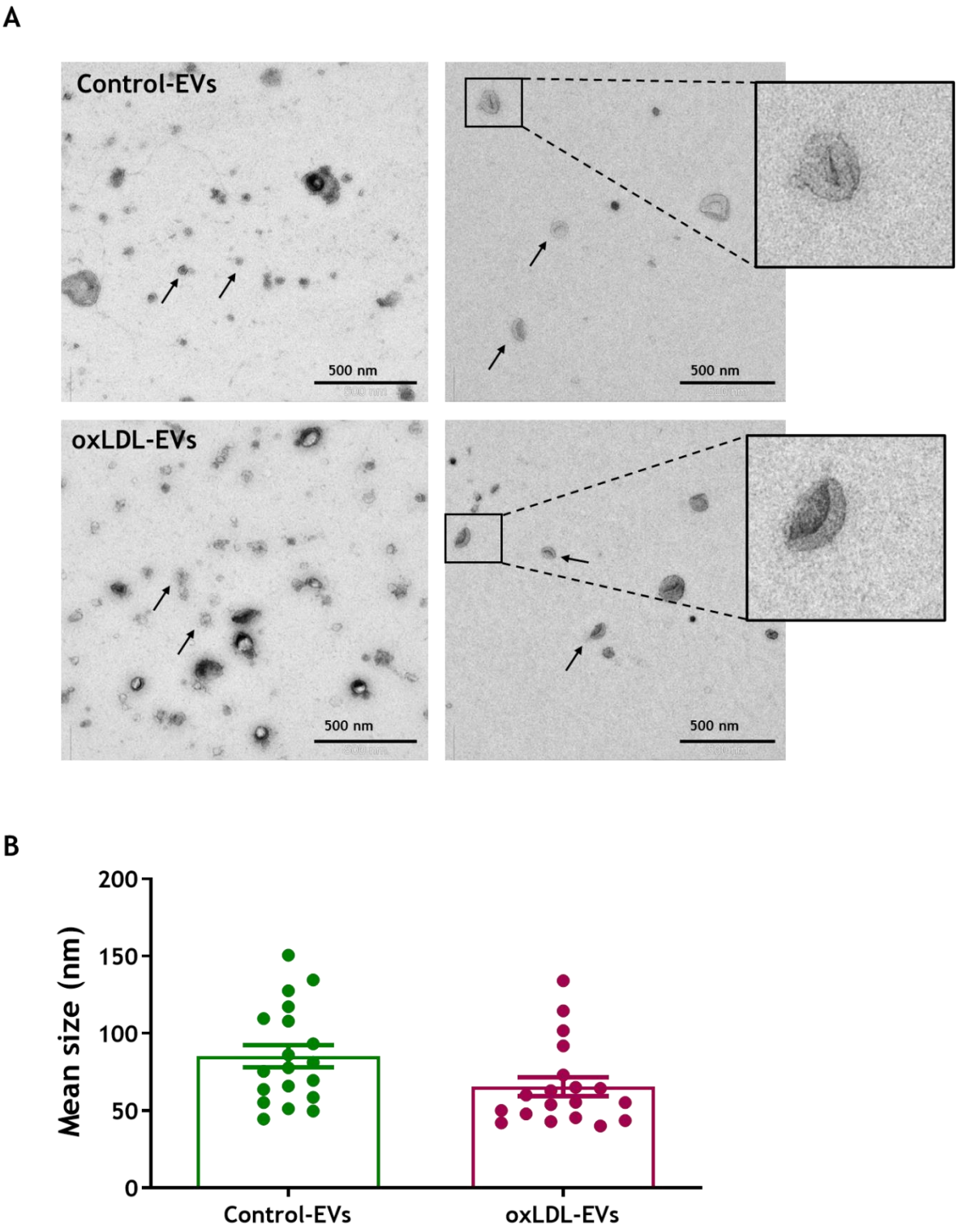

Figure 3-7 Characterisation of EV populations derived from HCASMC after oxLDL treatment

(A) Representative TEM images from Control and oxLDL-EVs indicating cup-shaped vesicles from EV populations. Arrows are pointing out EV structures. The inserts on the right side correspond to one magnified EV from each condition. Images were captured at x6,000 magnification using the Olympus ITEM software (n=2 patients). (B) Size comparison of EV diameter from Control and oxLDL-EVs after TEM image quantification (n=19 replicate, one replicate corresponds to one image acquired, n=2 patients). Data are expressed as the mean ±SEM. Scale bar: 500 nm.

Micro BCA assay was used to determine protein concentration of Control-EVs and oxLDL-EVs. No statistically significant differences were observed in protein concentration for the two EV populations (Figure 3-8 A). Control-EVs were found to have an average protein concentration of 318.2±20.7 µg/mL whereas oxLDL-EVs were found to an have average protein concentration of 389.5±78.1 µg/mL (n=4). EV marker detection was performed using western immunoblotting. HCASMC lysate was used as a positive control since the EVs were secreted from HCASMCs. CD81 was found to be enriched in both Control and oxLDL-EVs (Figure 3-8 B). The expected molecular weight of CD81 per manufacturer's guidance is 22-26 kDa whereas in these studies it was detected at an apparent molecular weight of 20 kDa. In both EV populations, detection of Annexin A2 and CD63 was also successful (Figure 3-8 B). The manufacturer of Annexin A2 antibody suggested the detection of a band of approximately 36, 34 kDa. It these studies, Annexin A2 was detected at an apparent molecular weight of 35 kDa. CD63 was detected in Control and oxLDL-EVs from HCASMCs at 30-60 kDa agreeing with its predicted detected size per the manufacturer's suggestion which ranges from 30-60 kDa.

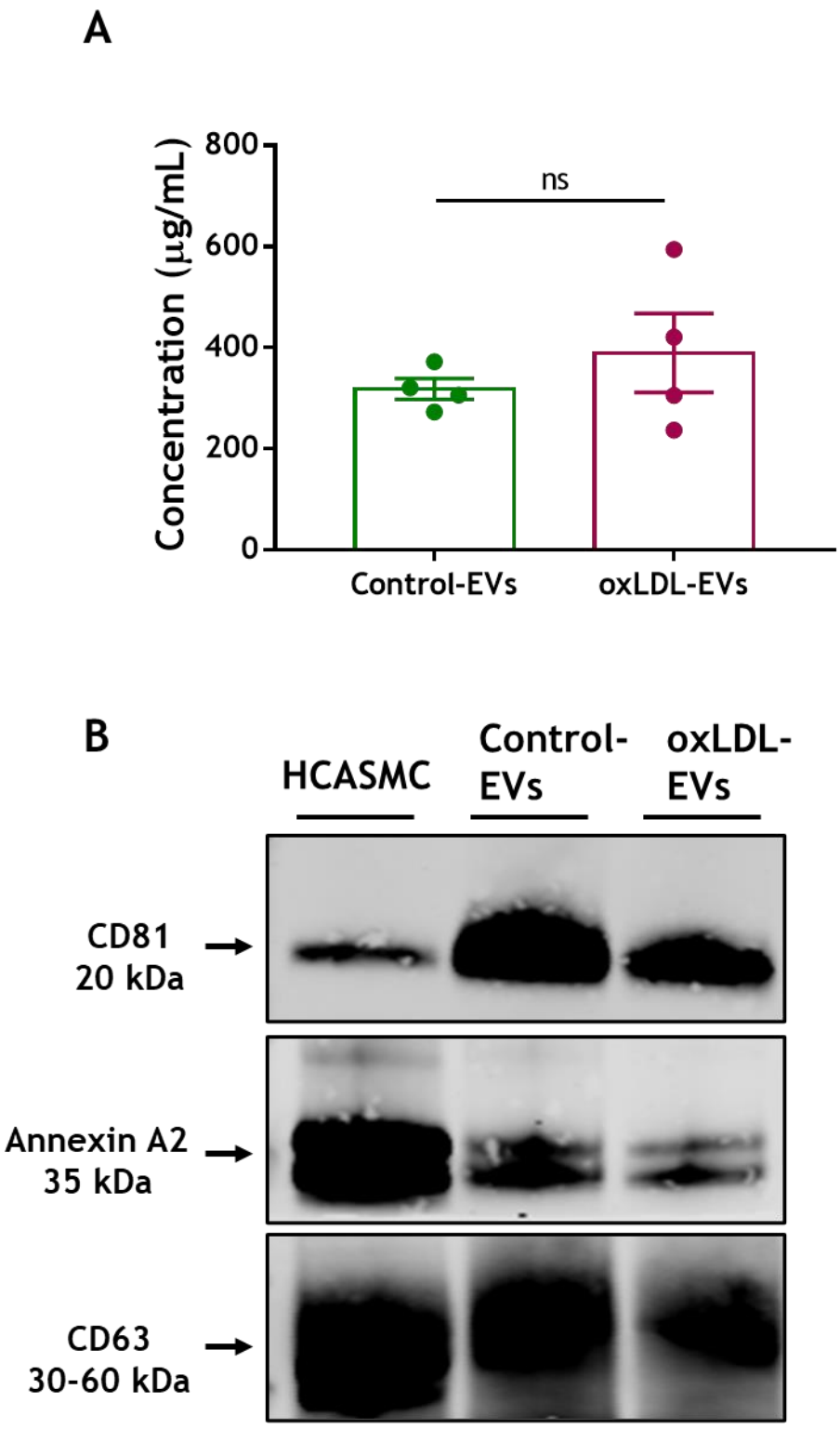

Figure 3-8 Analysis of HCASMC-derived EV protein content by BCA assay and western immunoblotting

(A) Comparison of protein concentration of EVs after oxLDL treatment (n=4 patients). (B) Detection of EV-markers CD81, Annexin A2 and CD63 on EV populations derived from HCASMC (n=2 patients for all EV markers, WB images from one patient but are representative of experiments performed in two individual patients). HCASMC cell lysate was used as a positive control. Statistical probability of differences was calculated using paired Student's t-test (ns= nonsignificant). Data are expressed as the mean ±SEM.

OxLDL levels were assessed in SMC-EVs after control treatment and oxLDL treatment by ELISA (Figure 3-9). CCM was collected from control or oxLDL treated SMCs. During the isolation process, MVs were collected for both conditions after the 10,000g centrifugation step. OxLDL levels in MVs were assessed to examine whether oxLDL was co-isolated with MVs. After incubation, EVs were isolated as seen in Figure 3-1. PK treatment is usually used to remove contaminants from EV samples (Foers et al., 2018). EVs were incubated with or without PK to determine whether oxLDL was carried with EVs or co-isolated by SEC or was enclosed in EVs. For example, if oxLDL was enclosed in EVs, PK treatment would not digest oxLDL. Absorbance levels of Control native EVs, Control -PK EVs or Control +PK EVs indicate that oxLDL is not enclosed or carried co-purified by SEC with Control-EVs in the presence or absence of PK treatment (Figure 3-9). Absorbance levels of oxLDL native EVs, oxLDL -PK EVs or oxLDL +PK EVs are similar indicating that oxLDL in not carried or co-purified by SEC or enclosed in oxLDL-EVs in the presence or absence of PK treatment (Figure 3-9). No significant increase was observed in absorbance values of MVs from control or oxLDL treated cells (Figure 3-9).

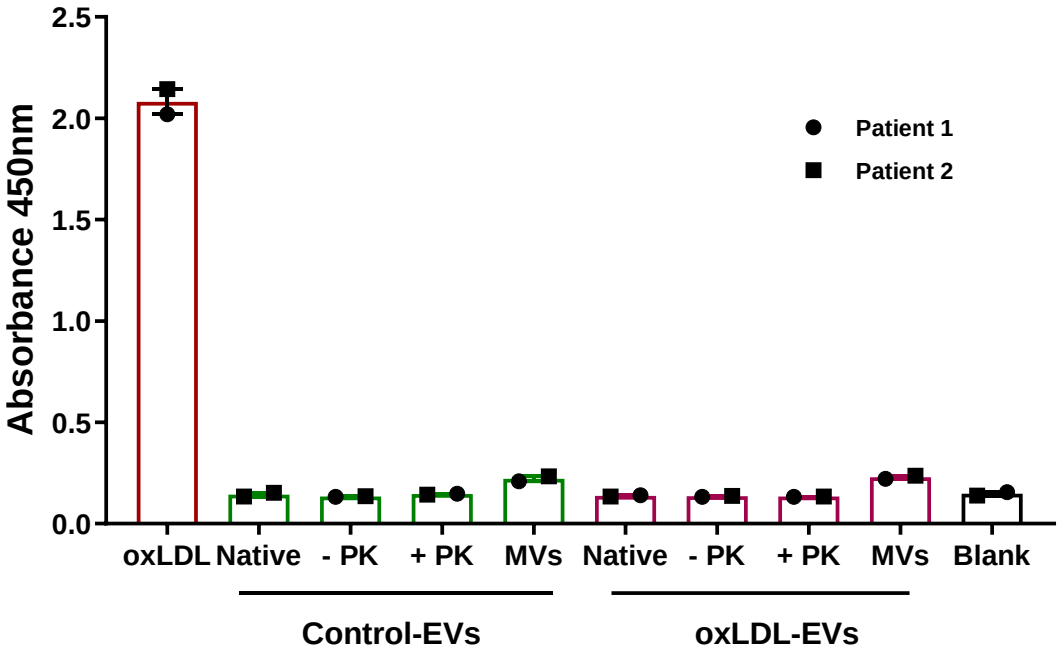

Figure 3-9 Detection of oxLDL in HCASMC-derived EVs after control or oxLDL treatment by ELISA

Control and oxLDL-EVs were treated with ± (v/v) 500 µg/mL PK for 1 hour at 37 ^{o}C. Prior EV isolation, CCM was divided into 3 parts of 50 µL (native condition, -PK, +PK). The native sample was not treated with PK and EVs were isolated as described in 2.5.1.1. Both -PK (added DPBS prior incubation) and +PK (added PK prior incubation) samples were incubated at 37^{o}C for 1 hour and 60^{o}C for 10 minutes. EVs and MVs were isolated as described previously and the oxLDL Elisa protocol as per manufacturer's guidance was followed to measure oxLDL levels in Control and oxLDL-EVs (n=2 patients). Data are expressed as the mean ±SEM.

3.2.4 SMC-EV uptake by HCAEC

After characterisation of SMC-EVs, EV uptake by recipient HCAECs was examined. Control and oxLDL-EVs were labelled with the fluorescent dye, PKH67 (green) and HCAECs were treated. Optimisation of the treatment timepoint for EV uptake by HCAECs was performed. HCAECs were incubated with PKH67 labelled Control and oxLDL-EVs ($2x10^{10}$ particles per well) for 2 hours, 6 hours and 24 hours. Then cells were fixed, nuclei counterstained with DAPI to observe EV uptake by recipient HCAECs (Figure 3-10). Imaging analysis revealed that EVs were being taken up by HCAECs at 2 hours but achieved high accumulation at 24 hours, based on mean fluorescent intensity observed (Figure 3-11). Both Control-EVs and oxLDL-EVs at the three timepoints studied were localised around the nuclei and cytoplasm. The 24-hour EV treatment was chosen to compare the Control and oxLDL-EV uptake by recipient HCAECs.

HCAECs were treated with PKH67 labelled Control and oxLDL-EVs for 24 hours, cells were fixed and stained with DAPI. Both Control and oxLDL-EVs were observed to be internalised by HCAECs (Figure 3-12 A). Quantification of mean fluorescence intensity showed that oxLDL-EV uptake was significantly lower (RQ=0.5±0.3, * $p<0.05$) compared to Control-EV uptake (RQ=1.0±0.1) (Figure 3-12 B).

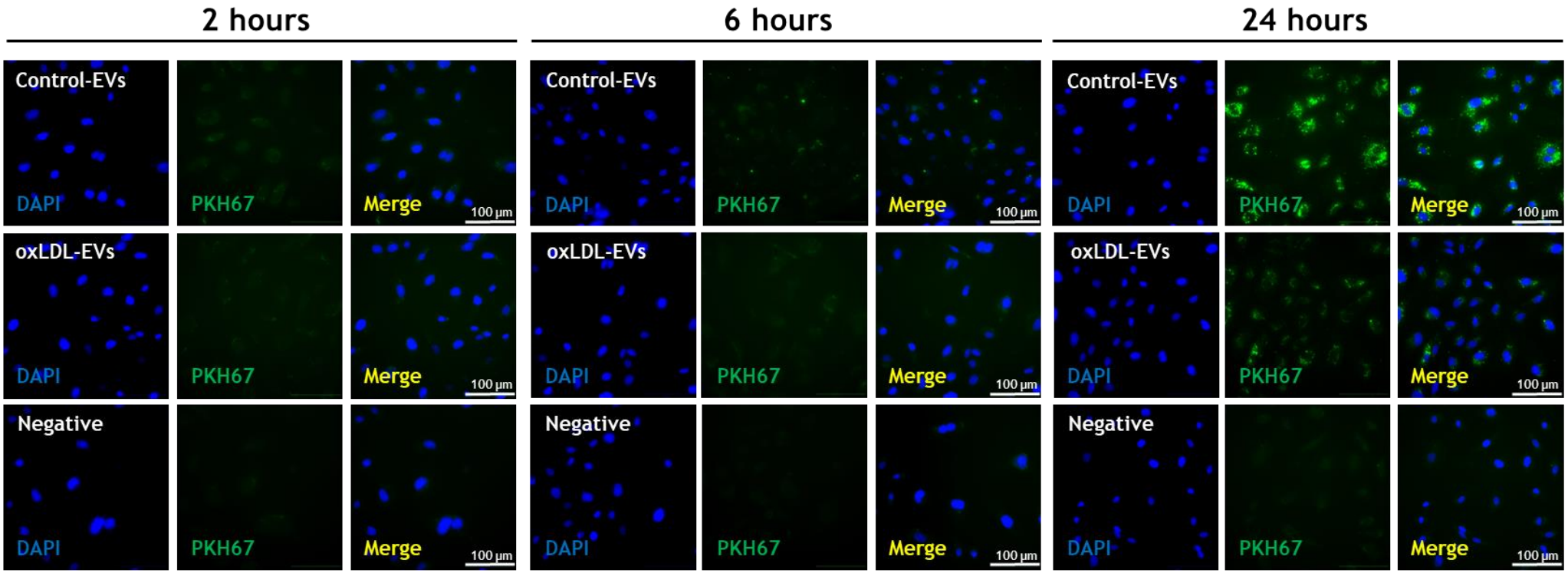

Figure 3-10 Optimisation of SMC-EV uptake by HCAEC

Human coronary artery endothelial cells (HCAEC) were incubated with 4µM PKH67 fluorescently labelled SMC-EVs for 2 hours, 6 hours and 24 hours. HCAEC were stained for DAPI (blue). Representative images at 2 hours, 6 hours and 24 hours indicate that SMC-EVs are being taken up by HCAEC. Images were taken on a confocal microscope at 40x magnification. Scale bar: 100 µm.

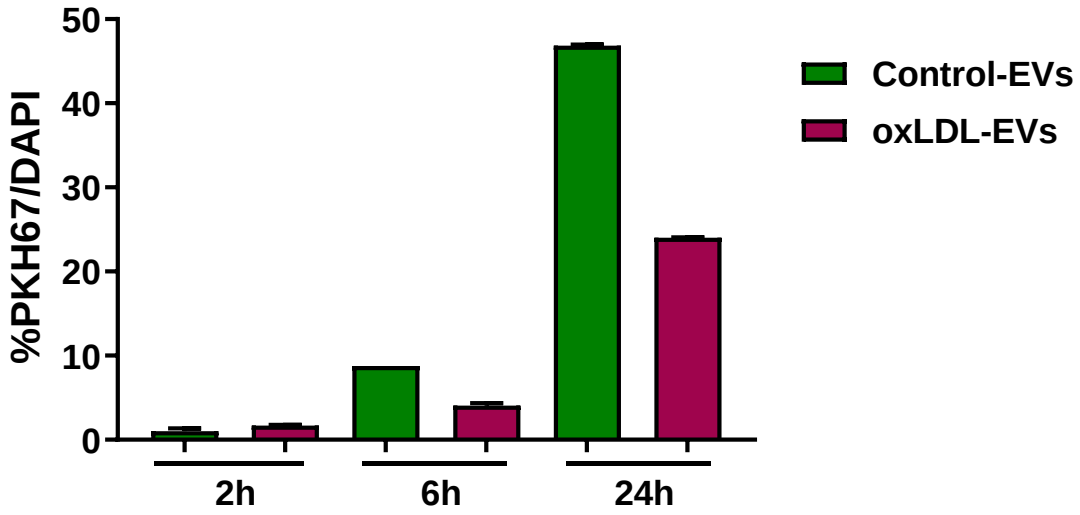

Figure 3-11 Optimisation of SMC-EV uptake by HCAEC

Internalized EVs were quantified by means of fluorescence intensity. Background signal was subtracted for every single image before obtaining the relative fluorescence per field (n=2 technical replicates, 1 patient). Data are expressed as the mean ±SEM.

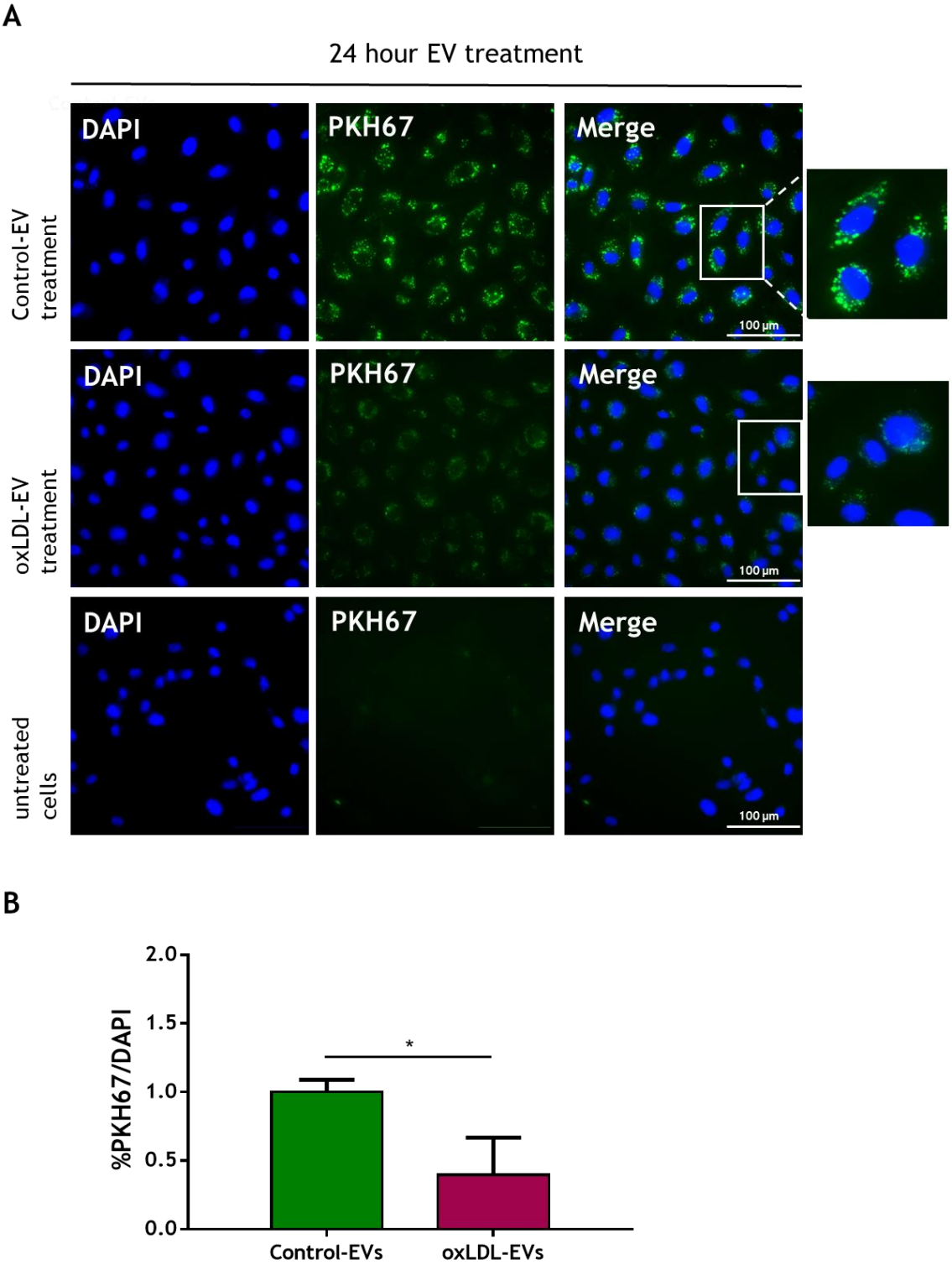

Figure 3-12 SMC-EV uptake by HCAEC

(A) HCAECs were incubated with 4µM PKH67 fluorescently labelled SMC-EVs for 24 hours. HCAECs were stained for DAPI (blue). Representative images from n=3 at 24 hours indicate that SMC-EVs are being uptaken by HCAEC. Images were taken on a confocal microscope at 40x magnification. (B) Internalized EVs were quantified by means of fluorescence intensity. Background signal was subtracted for every single image before obtaining the relative fluorescence per field. Statistical significance was determined with paired Student's t-test (n=3 patients, *p<0.05). Data are expressed as the mean ±SEM. Scale bar: 100 µm.

3.2.5 Effect of Control and oxLDL-EVs isolated from SMCs on recipient SMC and EC cell viability

The biological effect of Control-EVs and oxLDL-EVs on recipient HCASMC cell viability was investigated. HCASMCs were seeded into a 96 well plate ($4x10^4$ cells/mL) and quiesced for 48 hours in SF media. Cells were treated either with 10% FCS or Control-EVs or oxLDL-EVs for 24 hours in SF media or Complete media which contained 5% FCS. Cells were treated with 3 different EV doses: $3x10^9$ particles per well, $8x10^9$ particles per well, $1x10^{10}$ particles per well. After, the cell viability of HCASMCs was measured using the CyQUANT™ MTT Cell Viability Assay. A positive control, 10% FCS, was used to ensure the assay was working. Significantly increased cell viability was observed after the 10% FCS treatment (% viable cells 165.4±0.0) compared to control cells (% viable cells 100.0±0.1) (Figure 3-13 A). Lower viability, however statistically non-significant, was observed in cells treated with $3x10^9$ particles/well of Control-EVs (% viable cells 97.9±0.1) compared to control cells but significant reduction in cell viability was observed when compared with 10% FCS treated cells (**** $p<0.0001$). Higher viability (non-significant) was observed in cells treated with $8x10^9$ particles/well Control-EVs (% viable cells 113.2±0.1) compared to control cells but significant reduction in cell viability was observed when compared with 10% FCS treated cells (****$p<0.0001$). Again, higher viability was observed in cells treated with $1.0x10^{10}$ particles/well Control-EVs (% viable cells 119.5±0.1) compared to control cells with no statistical significance detected, but significant reduction in cell viability was observed when compared with 10% FCS treated cells (***$p<0.001$). No difference in cell viability was observed in cell treated with $3x10^9$ particles/well oxLDL-EVs (% viable cells 101.4±0.01) compared to control cells but cell viability was significant reduced compared to 10% FCS treated cells (****$p<0.0001$) (Figure 3-13 A). Higher viability was observed in $3x10^9$ particles/well oxLDL-EVs (% viable cells 101.4±0.01) compared to same dose Control-EV treated cells (% viable cells 97.9±0.1). Higher viability was observed in cells treated with $8x10^9$ particles/well oxLDL-EVs (% viable cells 106.0±0.01) compared to control cells with no statistical significance detected. Cell viability of these cells was significantly reduced when compared with 10% FCS treated cells (****$p<0.0001$). Cells treated with $8x10^9$ particles/well oxLDL-EVs (% viable cells 106.0±0.01) demonstrated lower viability compared to same dose Control-EV treatment (% viable cells 113.2±0.1) (Figure 3-13 A). Higher viability was observed in cell treated with $1x10^{10}$ particles/well oxLDL-EVs (%

viable cell 114.6±0.1) compared to control cells (% viable cells 100.0±0.1), but significant reduction in cell viability was observed when compared with 10% FCS treated cells (****p<0.0001)(Figure 3-13 A). Lower viability, albeit non-significant, was observed in cells treated with $1x10^{10}$ particles/well oxLDL-EVs (% viable cell 114.6±0.1) compared to same dose of Control-EVs (% viable cells 119.5±0.1).

Next, the biological effect of Control and oxLDL-EVs was examined in serum induced cell viability, meaning the EV treatment was performed in Complete media containing 5% FCS (Figure 3-13 B). Higher viability was observed in cells treated with 10% FCS (% viable cells 103.6±0.1) compared to control cells (% viable cells 100.0±0.1) but no statistical significance was detected (Figure 3-13 B). No difference in cell viability was observed in cells treated with $3x10^9$ particles/well Control-EVs (% viable cells 100.5±0.1) compared to control cells (% viable cells 100.0±0.1). Increased cell viability was observed in cell treated with $8x10^9$ particles/well Control-EVs (% viable cells 118.6±0.1) compared to control cells but no statistical significance was detected. Again, higher viability was observed in cells treated with $1x10^{10}$ particles/well Control-EVs (% viable cell 123.0±0.1) compared to control cells but no statistical significance was detected (Figure 3-13 B). Cells treated with $1x10^{10}$ particles/well Control-EVs showed significantly increased cell viability compared to control cell (*p<0.05). Cells treated with $3x10^9$ particles/well oxLDL-EVs demonstrated increased cell viability with no statistical significance (% viable cells 114.4±0.1) compared to control cells and same dose Control-EV treated cells (% viable cells 100.5±0.1). Higher cell viability was observed in cells treated with $8x10^9$ particles/well oxLDL-EVs (% viable cells 118.0±0.1) compared to control cells and a similar effect on cell viability was observed when compared with the same dose Control-EVs (% viable cells 118.6±0.1) with no statistical signifigance beign detected (Figure 3-13 B). Again, higher viability was observed in cells treated with $1x10^{10}$ particles/well oxLDL-EVs (% viable cells 128.4±0.1) compared to control cells and the same dose of Control-EVs (% viable cell 123.0±0.1), however significantly increased cell viability as observed compared to 10% FCS treated cells (#p<0.05) (Figure 3-13 B).

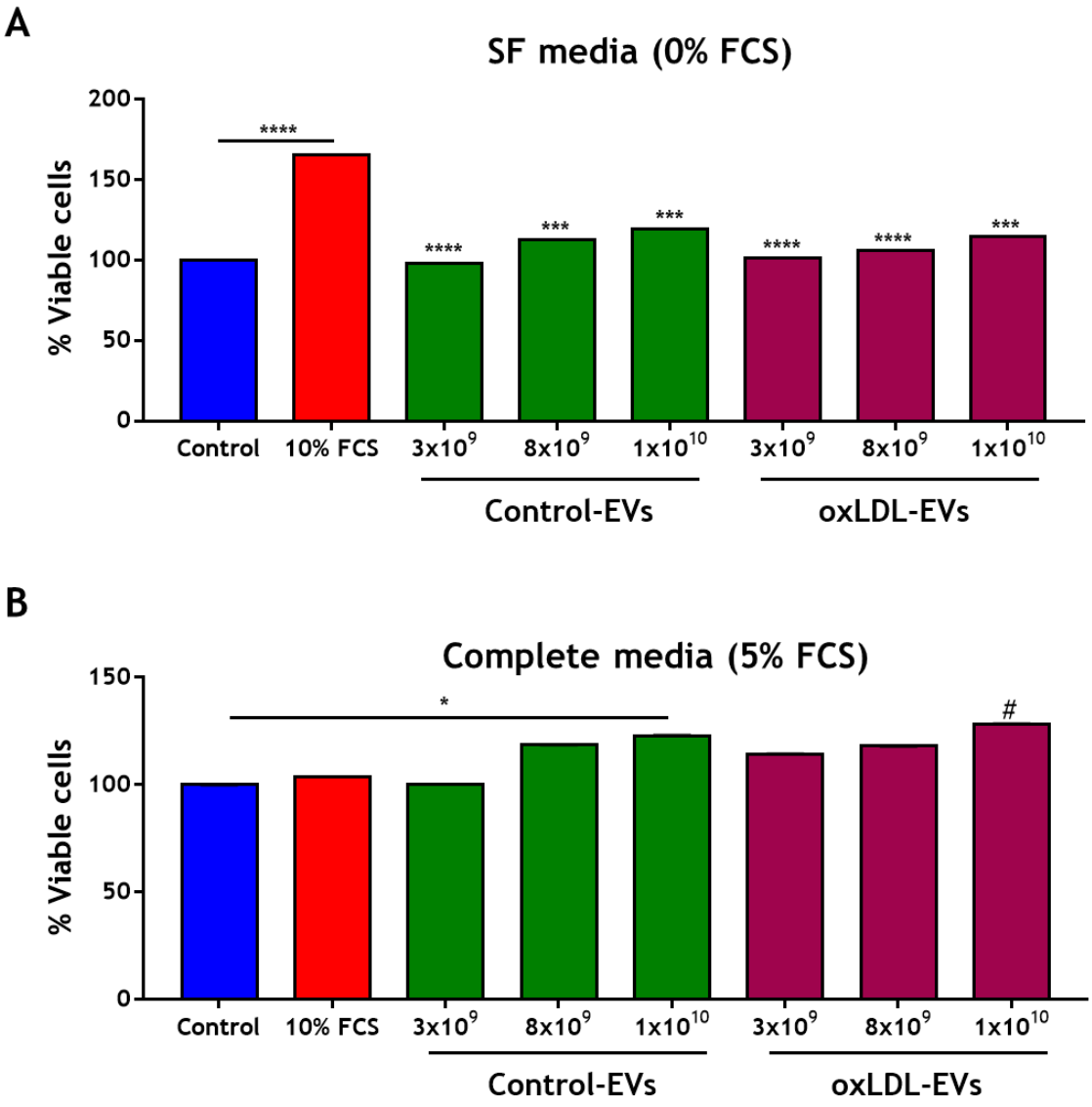

Figure 3-13 Effect of Control and oxLDL-EVs on HCASMC cell viability

HCASMCs were quiesced for 24 hours and then treated with 10% FCS or Control-EVs or oxLDL-EVs in SF or Complete media for 24 hours. Cell viability was measured using the CyQUANT™ MTT Cell Viability Assay. (A) Cell viability of recipient HCASMCs treated with EVs in SF media (n=3 patients, ***$p<0.001$ vs 10% FCS, ****$p<0.0001$ vs 10% FCS). (B) Cell viability of recipient HCASMCs treated with EVs in Complete media (5% FCS) (n=3 patients, *$p<0.05$ Control vs $1x10^{10}$ particles/well Control-EVs, #$p<0.05$ 10% FCS vs $1x10^{10}$ particles/well oxLDL-EVs). Statistical probability of differences was calculated using RM One-way ANOVA with post-hoc Tukey's test. Data are expressed as the mean of % viable cells ±SEM.

Next, the Control and oxLDL-EV effect on recipient HCAEC cell viability was investigated. HCAECs were seeded into a 96 well plate ($4x10^4$ cells/mL). Cells were not quiesced as pilot studies to optimise the assay revealed that when HCAECs were quiesced in low serum media this caused significant cell death and it was not possible to complete the assay (data are not shown). Therefore, the experimental design had to be adjusted. For this purpose, the effect of Control and oxLDL-EVs in cells in the presence of 5% EV-depleted serum media was estimated. Since cells were not starved like the HCASMCs, it was decided to perform EV treatment in EV-depleted serum to avoid any confounding effects of EVs that might be present in the serum. Cells were treated with 3 different EV doses: $3x10^9$ particles per well, $8x10^9$ particles per well, $1x10^{10}$ particles per well. Next, the cell viability of HCASMCs was measured using the CyQUANT™ MTT Cell Viability Assay. A positive control,10% FCS, was used to ensure the assay was working.

Increasing cell viability, but non-significant, was observed after 10% FCS treatment (% viable cells 122.8±0.1) compared to control cells (% viable cells 100±0.1)(Figure 3-14). Lower viability, however statistically non-significant, was observed in cells treated with $3x10^9$ particles/well of Control-EVs (% viable cells 95.8±0.1) compared to control cells. Lower viability, however statistically non-significant, was observed in cells treated with $8x10^9$ particles/well of Control-EVs (% viable cells 98.5±0.1) compared to control cells. Again, decreased viability, but not significant, was observed in cells treated with $1x10^{10}$ particles/well of Control-EVs (% viable cells 92.3±0.1) compared to control cells and a significant reduction in cell viability was observed compared to 10% FCS treated cells (*$p<0.05$). Cells treated with $3x10^9$ particles/well oxLDL-EVs did not show difference in cell viability (% viable cells 102.9±0.1) compared to control cells and the same dose of Control-EV treated cells (% viable cells 95.8±0.1). Cells treated with $8x10^9$ particles/well oxLDL-EVs demonstrated lower cell viability (% viable cells 95.4±0.1) compared to control cells and same dose Control-EV treated cells (% viable cells 98.5±0.1) with no statistical signifigance detected. Cells treated with $1x10^{10}$ particles/well oxLDL-EVs demonstrated lower cell viability with no statistical signifigance being detected (% viable cells 90.3±0.1) compared to control cells and same dose Control-EV treated cells (% viable cells 92.3±0.1). However, a significant reduction in cell viability was observed compared to 10% FCS treated cells (*$p<0.05$).

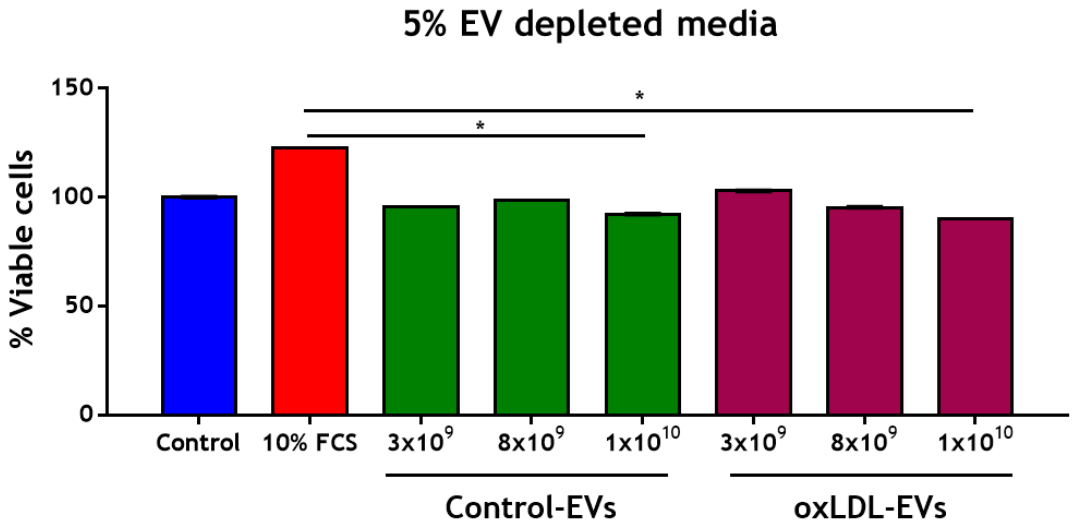

Figure 3-14 Effect of Control and oxLDL-EVs on HCAEC cell viability

HCAECs were seeded into a 96 well ($4x10^4$ cells/mL). Cells were not quiesced. Cells were treated for 24 hours with three EV doses. Cell viability was measured using the CyQUANT™ MTT Cell Viability Assay. HCAEC cell viability of cells treated with 10% FCS, Control-EVs and oxLDL-EVs in 5% EV depleted media. Statistical probability of differences was calculated using RM One-way ANOVA with post-hoc Tukey's test (n=3 patients, *$p<0.05$ 10% FCS vs $1x10^{10}$ particles/well Control-EVs, $1x10^{10}$ particles/well oxLDL-EVs). Data are expressed as the mean of % viable cells ±SEM.

3.3 Discussion

In this study, the use of SEC for purifying EVs from conditioned media from cultured cells was optimised through characterisation of the EV elution profile from CCM from HCASMCs and the purest EV containing fractions were chosen for future experiments. EVs were isolated from CCM from HCASMC and a selection of methods that have been proposed by the ISEV and MISEV2018 were chosen for SMC-EV characterisation (Théry et al., 2018). An oxLDL concentration for future HCASMC stimulation and EV release was chosen. EVs were characterised by NTA analysis, TEM and WB analysis. It was found that oxLDL had no effect on SMC-EV size or EV release from HCASMCs. Also, it was found that oxLDL is not co-isolated with EVs or it was not encapsulated by EVs after treatment. Moreover, it was found that oxLDL-EV uptake was significantly lower compared to Control-EV uptake by HCAEC. Finally, Control and oxLDL-EVs had no effect on HCASMC cell viability or serum induced viability and HCAEC cell viability.

SEC has been widely recognised as a superior method of EV isolation compared to UC (Takov et al., 2019)(Monguió-Tortajada et al., 2019). However, both methods suffer as they do not allow complete separation of EV and APOB lipoproteins as confirmed by studies showing LDL co-isolation with EVs and thus EVs samples may contain VLDL/IDL contaminants (Sódar et al., 2016)(Takov et al., 2019). Good practice dictates that when isolating EVs from a different source than defined by the qEV single column manufacturer, the need to assess the EV elution profile from that specific biological sample is important (Takov et al., 2017)(Gaspar et al., 2020). The qEV single columns used in this study were optimised by the manufacturer for EV isolation from plasma. In this study, it was found that the void volume and the first 3 fractions contained pure EVs based on EV purity ratio. If the elution profile from CCM was not examined and downstream analysis was based on the manufacturer's suggestion the void volume would not have been collected and that would have resulted in lower EV yield for the studies performed in this thesis.

Many factors such as the EV isolation protocol can affect the EV yield and downstream analysis (Gudbergsson et al., 2016). The lack of standardisation among isolation methods means direct comparison of the same isolation method is inefficient (Gudbergsson et al., 2016). A distinct example is the variability within the UC isolation protocol where different g forces, centrifugation times,

rotor properties or sample viscosity (increased viscosity results in reduced sedimentation efficiency) have been applied thus generating heterogenous EV populations (Momen-Heravi et al., 2012)(Livshits et al., 2015)(Monguió-Tortajada et al., 2019). In this study, NTA and EV protein content analysis showed that void volume and the first three collected fractions are the purest EV fractions when isolating SMC-EVs from CCM using the isolation method discussed previously by SEC.

Protein quantification of elution fractions showed that fraction 11 had the highest protein concentration. An increased protein concentration was observed after fraction 8, with a peak at fraction 11 and a reduction in fractions 12 and 13. These data correspond with the manufacturer's data indicating protein separation from EV containing fractions. Böing et al., showed successful vesicle separation from soluble proteins when isolating EVs from platelet-free supernatant, derived from platelet concentrates using single-step SEC (Böing et al., 2014). Authors also suggested HDL separation by vesicles when using SEC as an isolation method which was not accomplished with UC (Böing et al., 2014). Another study compared isolation efficiency of EVs from plasma of SEC and the exoEasy kit (membrane affinity spin column) and found that the SEC isolation method was superior as it showed higher particle/protein ratio and reduced co-isolation of plasma proteins (Stranska et al., 2018). Since EV marker detection due to low yield was not performed in all fractions, definitive conclusions cannot be drawn.

Traditionally, EVs can be categorised based on their biogenesis as exosomes, microvesicles or apoptotic bodies (Théry et al., 2018). The MISEV2018 clearly state that since no consensus has been reached as what could be a specific EV marker for each category, categorising EVs based on their biogenesis pathway should be avoided (Théry et al., 2018). These terms should be used only when clear evidence of the particle cellular compartment origin exists eg live imaging techniques (Théry et al., 2018). In the following study, live single-cell imaging was employed to observe MVB-plasma membrane fusion following exosome release from mammalian cells (Verweij et al., 2018). To avoid misleading labelling of EV populations, MISEV 2018 define as correct nomenclature of terms of EV subtypes: 1) terms regarding physical characteristics of EVs, such as size ("small EVs" (sEVs) and "medium/large EVs" (m/lEVs), or density, 2) terms regarding biochemical composition of EVs (CD63+EVs, CD81+EVs), 3) terms regarding cell origin of EVs

(SMC-EVs). As techniques for real time tracking of the origin of vesicles are difficult to perform daily, the simplified nomenclature proposed by MISEV 2018 was adopted in these studies and vesicles isolated from HCASMCs using the described isolation protocol were always referred to as SMC-EVs. Characterisation of SMC-EVs in this study followed the proposed techniques for EV characterisation by MISEV 2018 using NTA analysis, TEM and WB analysis (Théry et al., 2018).

OxLDL is a potent atherogenic stimuli and many studies showed that high oxLDL concentration (>60 µg/mL) resulted in increased cell death in recipient SMCs (Kataoka et al., 2001). In this study, a concentration range assay was performed to determine the lower oxLDL concentration which would allow sufficient cell uptake but would not cause detrimental effects to the cells e.g., phenotypic changes or cell death and also potentially result in reduced EV yield. According to the literature, many oxLDL uptake studies starve cells for 1 hour or not at all as long starvation periods are not required to study oxLDL uptake by recipient cells (Collins et al., 2009)(Luo et al., 2017). A lower oxLDL working concentration was chosen (10 µg/mL) as uptake could be easily visualised in stimulated cells using Dil-labelled oxLDL and MTT viability assay results suggested that this concentration did not reduce cell viability. A higher oxLDL concentration decreased cell viability as has been shown in these studies and by other studies (Liu et al., 2014). Lie et al., showed that SMC treatment with 50 µg/mL of oxLDL treatment after 24 hours significantly increased migration and proliferation of SMCs compared to 10 µg/mL of oxLDL treatment (Liu et al., 2014). Moreover, 50 µg/mL of oxLDL treatment resulted in increased expression of osteopontin whereas 10 µg/mL of oxLDL did not alter osteopontin's expression levels (Liu et al., 2014).

EV release under pathogenic stimulus has been studied extensively across many research fields as EVs have been proposed to participate in cell-cell communication. Nguyen et al., showed that mouse macrophages treated with 50 µg/mL of oxLDL for 24 hours released significantly larger EVs (mean size 125 nm) compared to control EVs (mean size 111 nm) (Nguyen et al., 2018). In our study, oxLDL treatment resulted in secretion of slightly larger EVs (130.9±5.3 nm) compared to control-EVs (116.9±5.8 nm) but that difference was not significant. However, analysis of TEM images from 2 patients showed significant differences in average EV size of Control and oxLDL-EVs (Control EVs 85.3±7.2 nm, oxLDL-EVs

65.5±6.1 nm). Quantification of TEM images indicating smaller average EV size for both EV populations compared to average EV size being detected by NTA. Moreover, image analysis showed that oxLDL-EVs were found to have smaller size compared to Control-EVs. TEM image analysis is not recommended by the ISEV for size quantification of EVs and these results were not included in the size characterisation of SMC-EVs. One explanation for the size difference is that with TEM, the way the EVs will be positioned on the grid to be imaged is random and sometimes a mixture of smaller EV population may be visualised. NTA analysis records the movement of all the particles visible in the capture frame. Another limitation of electron microscopy for EV size quantification is that a limited number of EVs can be found in a grid limiting the possibilities to analyse heterogenous EV populations (Hartjes et al., 2019).

No difference in the concentration of secreted EVs after oxLDL treatment was observed. Nguyen et al., did not report if oxLDL treatment altered the concentration of macrophage derived EVs after oxLDL treatment. Differences in EV profile release from HCASMCs observed in this study could be attributed to the different oxLDL concentration used and that EV release was being characterised from a different cell model. It was previously shown that apoptotic stimuli can increase EV release from Jurkat cells and that they exerted a dose-dependent apoptotic effect on recipient macrophages (Distler et al., 2005). Oxidative stress is another pathogenic stimulus inducing EV release. For example, it has been found that a retinal pigment epithelium cell line under oxidative stress conditions released significantly more EVs compared to cells under no oxidative stress conditions (Atienzar-Aroca et al., 2016). Another study showed that melanoma cell EV release was increased under stress conditions involving cytostatic and oxidative stress (Harmati et al., 2019). TNF-α stimulated HUVECs were found to secrete more EVs compared to unstimulated cells (Hosseinkhani et al., 2017). However, another study showed that different stimuli such as the atherogenic molecule LPS altered the EV-miRNA cargo but not the EV size or monocyte EV release (Tang et al., 2016). Bell et al, showed that AC16 human cardiomyocytes treated with a range of LPS doses released less and smaller EVs compared to untreated cells (Bell et al., 2019). These two studies clearly demonstrate that the same stimulus can exert two different effects on EV release in different cell types. Different pathological stimuli have been shown to induce or inhibit EV release,

however, not many studies have explored the role of oxLDL treatment on HCASMC EV release.

Understanding the EV internalisation by neighbouring cells in the vascular wall would be beneficial in understanding cell communication in atherosclerosis. In this study, it was shown that oxLDL-EV uptake by recipient HCAEC was lower compared to Control-EV uptake. It is worth mentioning that SMC-EV uptake by HCASMCs was not successful in recipient HCASMCs. The protocol was optimised as described previously but for unknown reasons, imaging of EVs in recipient HCASMCs was unsuccessful. Therefore, EV uptake was only observed by recipient HCAEC. Many studies have shown that EVs from various cell sources are taken up by endothelial cells (Durak-Kozica et al., 2018)(Khalaj et al., 2019). Although, the use of PKH67 to stain EVs for cell imaging is well established, many studies have highlighted limitations associated with this fluorescent stain (Takov et al., 2017)(Pužar Dominkuš et al., 2018). Pužar Dominkuš et al., showed that PHK26 non-EV particles are difficult to separate from stained EVs when using a PKH26 ultracentrifugation staining protocol. A negative control of particle free DPBS was used and stained with PKH26-labelled and non-EV stained PKH26 particles were detected (Pužar Dominkuš et al., 2018). In the studies presented here, confocal microscopy images for the negative control did not detect fluorescent particles in that sample. That difference may arise from the different PKH staining methods; PKH ultracentrifugation may cause particle aggregation where PKH filtration staining which was used for this study may not. Another difference is the PKH concentration used in the two studies, Pužar Dominkuš et al., report that 8 μM PKH26 in Diluent C was used to stain EV populations whereas in this study 4 μM PKH67 in Diluent C was used. Takov et al., highlighted the limitations of lipophilic EV staining as PKH67 staining showing that lipoprotein contaminants in EV preparations may be mistaken as EV uptake by recipient cells (Takov et al., 2017). The use of particle DPBS showed that unbound dye was removed during the filtration steps, however, standard BSA alone in the preparation was not removed by using filtration steps (100kDa filters, BSA MW 66 kDa) (Takov et al., 2017). PKH67 as for other lipophilic dyes could bind lipoprotein particles, protein contaminants or EVs. However, it was previously shown that the SEC allowed the protein separation from the collected EV fractions as protein elution was observed in later fractions and not in the EV containing fractions, and oxLDL was not detected in EV preparations. Another limitation of this protocol was the inability

to measure the staining efficiency of Control and oxLDL-EVs. One possible method to measure staining efficiency would be by measuring PKH67 fluorescent intensity of the same number of particles for Control and oxLDL-EVs using a plate reader for example, but with the low EV yield generated that was not possible. To conclude, PKH67 staining is useful to enable imaging of EV uptake into cells but may not be the best optimised tool to study EV uptake and enable definitive conclusions to be drawn.

The effect of Control and oxLDL-EVs on recipient HCASMC cell viability was detected by the CyQUANT™ MTT Cell Viability Assay. In SF conditions, neither EV population altered the recipient HCASMC cell viability. In serum induced HCASMC cell viability, it was found that both EV populations did not affect recipient SMC cell viability. Studies have showed that EVs derived from a plethora of cells could modulate SMC cell viability. Sarkar et al., showed that monocyte-derived EVs promoted SMC apoptosis and thus accelerated the progression of atherosclerosis (Sarkar et al., 2009). The authors identified caspase-1 to be enriched in monocyte-EVs and that is was responsible for the recipient SMC cell death (Sarkar et al., 2009). SMC cell death was detected using Annexin V and crystal violet assays whereas in this study the CyQUANT™ MTT Cell Viability Assay was used. But the main difference between the two studies is the cell source that EVs were isolated from. Platelet-derived EVs from septic patients transferred pro-apoptotic messages in SMCs inducing cell death (Janiszewski et al., 2004). In all the above studies, authors examined the effect of EVs produced by other cell types on SMC cell viability while in this study the autologous effect of SMC-EVs on SMC was examined.

The effect of Control and oxLDL-EVs on recipient HCAEC cell viability was detected by the CyQUANT™ MTT Cell Viability Assay. HCAECs were not quiesced as low serum media caused significant cell death (data not shown). The effect of EV treatment was examined in the presence of 5% EV depleted serum and it was found that a dose response treatment of Control and oxLDL-EVs from HCASMCs had no significant effect on recipient HCAEC cell viability. EVs from other cell sources have been shown to affect EC cell viability. Kong et al., showed that EVs isolated from platelets exposed to $PM_{2.5}$ (particulate matter, 2.5 refers to the size of the pollutant in microns) caused significant cell death to recipient human umbilical vein endothelial cells (HUVECs) (Kong et al., 2020). Some key differences between

the two studies are that in this study recipient HCAEC were used and in the publication the authors used HUVECs. Furthermore, cell viability in these studies was estimated using CyQUANT™ MTT Cell Viability Assay whereas in the publication the Cell Counting Kit-8 was used and the major difference was the source of EVs. Since cells were not quiesced due to the challenges with regard to cell toxicity and no synchronisation of the cell cycle was established, it is difficult to draw conclusions regarding the effect of SMC-EVs on recipient HCAEC cell viability. In conclusion, the reason for not detecting any biological effect after EV treatment could be that either Control or oxLDL-EVs do not affect HCASMC or HCAEC cell viability or a different experimental design is required, or finally the cargo of these EVs should be explored to determine whether molecules relevant to disease could be detected.

3.4 Summary

Optimisation of EV elution fraction by SEC was presented in this chapter. The analysis showed that void volume and the first three fractions were the purest EV containing fractions and the ones proposed to be collected for all future experiments. If the SMC-EV elution profile was not assessed and only the fractions proposed by the manufacturer were kept, the void volume which our analysis showed contained EVs would be discarded. EVs were released in abundance from HCASMCs after two types of treatment. OxLDL treatment did not alter either the EV release from HCASMCs nor the size of EVs as Control-EVs had similar mean particle size with oxLDL-EVs. The presence of oxLDL was quantified in EVs which indicated that the isolation protocol removes any remaining oxLDL that might have been in the culture media and furthermore that oxLDL is not secreted and co-isolated with EVs, or that oxLDL is not packaged with EVs in cells. These observations suggest that oxLDL does not affect the EV release from HCASMCs. SMC-EV uptake by HCAECs was observed using PHK67 labelled Control and oxLDL-EVs. Quantification of PKH67 mean fluorescent intensity revealed higher PKH67 signal in endothelial cells treated with Control-EVs compared to cells treated with oxLDL-EVs. Finally, SMC-EV effect on recipient HCASMC and HCAEC viability was observed. Control and oxLDL-EVs did not affect recipient HCASMC cell viability or serum induced cell viability. Control and oxLDL-EVs did not affect recipient HCAEC cell viability.

Chapter 4 Profiling the small RNA cargo of EVs from oxLDL-stimulated vascular smooth muscle cells

4.1 Introduction

MicroRNAs (miRNAs) and their function have been reported to participate in all stages of atherosclerosis development (Laffont and Rayner, 2017). MiRNA expression profiling studies showed a variety of miRNA being up or downregulated in patients with coronary artery disease (Zhong et al., 2018). Another study identified 3 miRNAs (miR-21,miR-92a, miR-99a) to be upregulated in coronary atherosclerotic plaques (Parahuleva et al., 2018). EVs are involved in intracellular communication via transfer of their EV cargo (lipids, proteins, and nucleic acids such as miRNA, lncRNA, snRNA, snoRNA, mRNA and DNA) (Hildebrandt et al., 2021). EV-RNA sequencing has been widely used to identify potential EV-miRNA biomarkers or targets for disease prevention (Bao et al., 2018)(Chettimada et al., 2020).

Small RNA sequencing is a rapid growing technology for transcriptomic identification and quantification (’t Hoen et al., 2013). Previous approaches to sequencing like Sanger sequencing were laborious and time consuming (McCormick et al., 2011). Next generation sequencing (NGS) is considered superior to microarray sequencing as it overcomes certain limitations associated with microarray experiments (McCormick et al., 2011) (Figure 4-1). Briefly, NGS does not require knowledge of the studied genome, sequencing is not dependent on hybridization as in microarray experiments (cross-hybridization, meaning signal will come from various sources apart from target, which can still occur during microarray experiments) and NGS offers single-nucleotide resolution, which increases specificity (Hurd and Nelson, 2009)(McCormick et al., 2011). Moreover, NGS can detect any sequence present in a sample varying from a novel transcript or transcript originating from alternative splicing (McCormick et al., 2011). Finally, only a few ng of material is sufficient for sequencing and NGS produces data in digital format by counting the number of copies of a sequence (Hurd and Nelson, 2009).

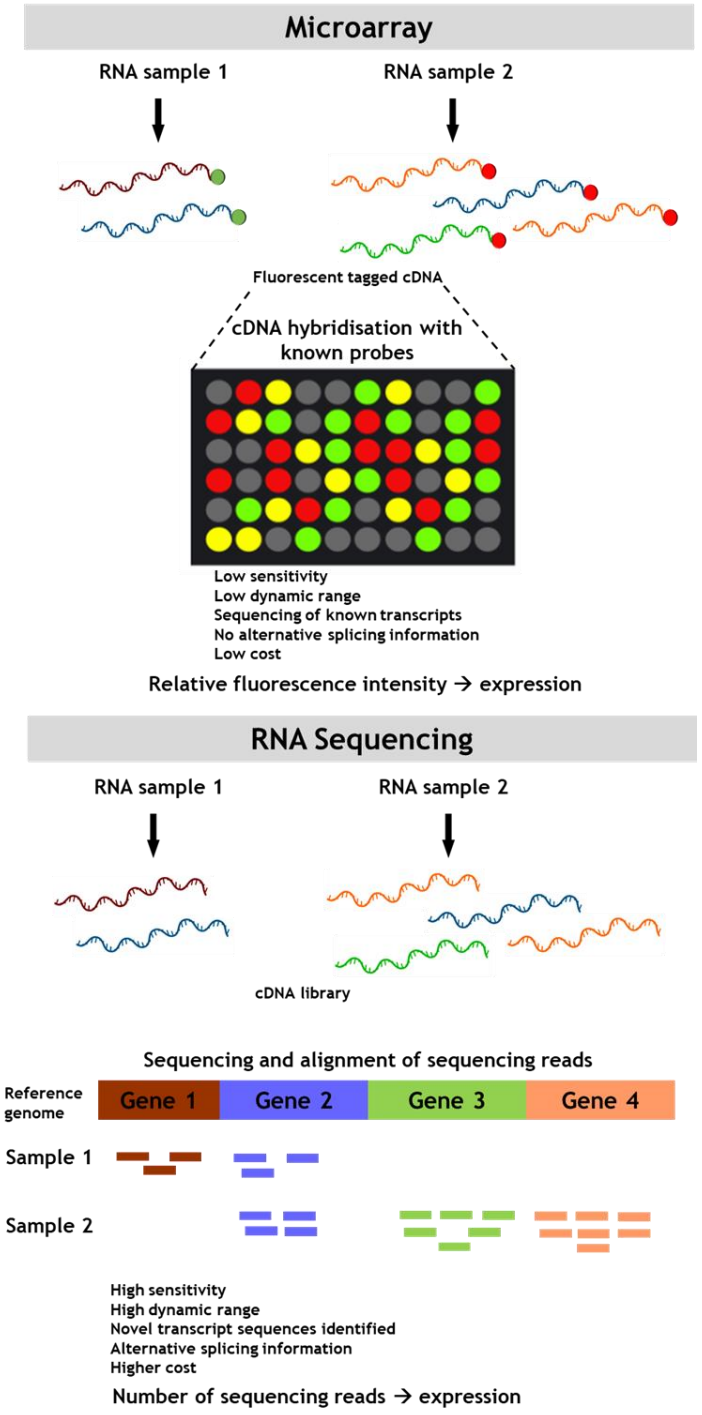

Figure 4-1 RNA transcript characterisation by Microarray and RNA Sequencing

Schematic representation of microarray sequencing vs RNA sequencing highlighting the key differences of the two methods. For microarray sequencing, RNA is extracted, reverse transcribed and labelled with fluorescent probes (green for control sample, red for treatment). Next, cDNA samples are hybridised to known complementary sequences on the microarray chip. Relative gene expression is quantified as relative fluorescence intensity of green vs red. Similarly, for RNA sequencing, RNA needs to be extracted, fragmented, reverse transcribed to cDNA and tagged with adaptors at the end of each fragment for better sequencing. While sequencing, fragmented sequence are aligned against a reference genome to quantify the expression levels of each gene in the sample. Parts of the figure were created by using pictures from BioRender.com. Image was adapted from Otogenetics corporation (Otogenetics, 2023).

MiRNAs are considered key regulators of gene expression as one miRNA can target more than one gene transcript generating numerous potential targeting sites for each miRNA (Peterson et al., 2014). Identifying these target sites via laboratory experimentation would be time consuming and costly (Peterson et al., 2014). For this purpose, a variety of computational prediction tools for miRNA-mRNA interactions have been developed allowing in silico prediction of numerous miRNA-mRNA interactions. Choosing the right prediction tool can be challenging. Most computation algorithms make the assumption that miRNA targets primarily the 3'UTR region of mRNA transcripts whereas studies have shown that miRNA can target other regions such as the 5'UTR region or CDS, thus regulating gene expression (Marín et al., 2013)(Gu et al., 2014). Taking into account the fact that each prediction tool is based on different features, different prediction tools will identify different interactions (Quillet et al., 2020). Some studies suggest that combining results from several computational prediction tools rather than separating them will generate optimal results (Quillet et al., 2020).

MiRNAs are the main cargo of EVs and miRNAs encapsulated in EVs have been implicated in atherosclerosis progression (Lu et al., 2018)(Xu et al., 2021). Several studies have examined the effect of miRNAs in lesion progression while others have examined the EV-miRNAs in disease progression while often different studies have examined the same miRNAs/EV-miRNAs. The hypothesis of this chapter was that oxLDL treatment would alter miRNA cargo of SMC-EVs.

4.1.1 Aims

- Examine if oxLDL treatment alters the small RNA cargo of SMC-derived EVs by small RNA sequencing.

- To validate candidate small RNA species (as identified by small RNA sequencing) by RT-qPCR.

- To apply bioinformatic prediction tools and predict gene targets for the RNA sequencing identified small RNA species.

4.2 Results

4.2.1 Differential expression analysis of small RNA species in EVs after oxLDL treatment

In Chapter 3, the effect of oxLDL treatment on EV release from HCASMCs was discussed. Control and oxLDL-EVs derived from HCASMC were isolated as described in 2.5.1. RNA was extracted as described in 2.4.1. Small RNA sequencing was performed by Glasgow Polyomics on samples extracted from three individuals under control (untreated) and oxLDL treatment. Principal component analysis (PCA) plot analysis revealed that there were transcriptional alterations in Control-EVs vs oxLDL-EVs (Figure 4-2). However, a mixed degree of separation between Control-EVs and oxLDL-EVs was observed, possibly reflecting heterogeneity between individual donor cells (Figure 4-2). Heterogeneity among donors to some degree is to be expected, however 3 out 4 donors were of the same sex. No further details on donors were available so further conclusions regarding donor heterogeneity can not be drawn. RNA sequencing identified 475 small non-coding RNAs. Of these, 112 or 23.6% of total small RNA species were identified as miRNAs, 206 or 43.4% were identified as snRNAs, 145 or 30.5% were identified as snoRNAs and 12 or 2.5% were identified as small Cajal-body specific RNAs. RNA species whose expression was differentially expressed between the two EV groups are depicted in a volcano plot and heatmap (Figure 4-3). Differential expression analysis showed that oxLDL treatment resulted in 4.5-fold downregulation of miR-125b-2 and 4.5-fold upregulation of 3 snRNAs, RNU2-7p, RNU2-29p, RNU2-57p in HCASMCs-EVs (Figure 4-3). The Volcano plot in Figure 4-3 was created using padplot and small RNA species with p.Adj<0.05 were considered to be differentially expressed. The heatmap in Figure 4-4 was created using padplot, columns represent each sample which was sent to be sequenced and rows represent small non-coding RNAs which were differentially expressed.

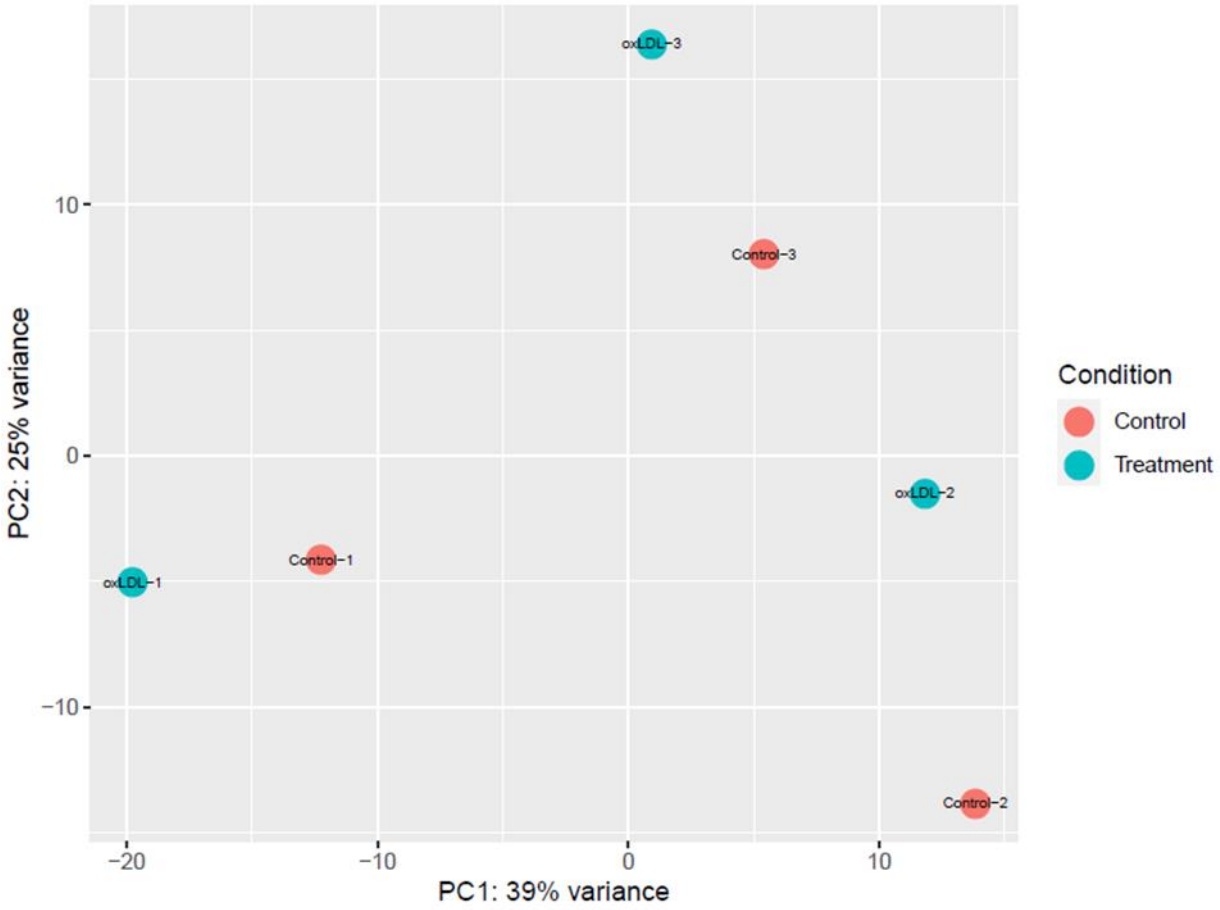

Figure 4-2 Principal component analysis (PCA) plot

PCA plot of RNAseq data was performed to identify variation between control and oxLDL-EVs. Samples are colour coded based on the treatment they received. Orange colour dots represent control-EVs and blue colour dots represent oxLDL-EVs. Each dot represents an analysed sample.

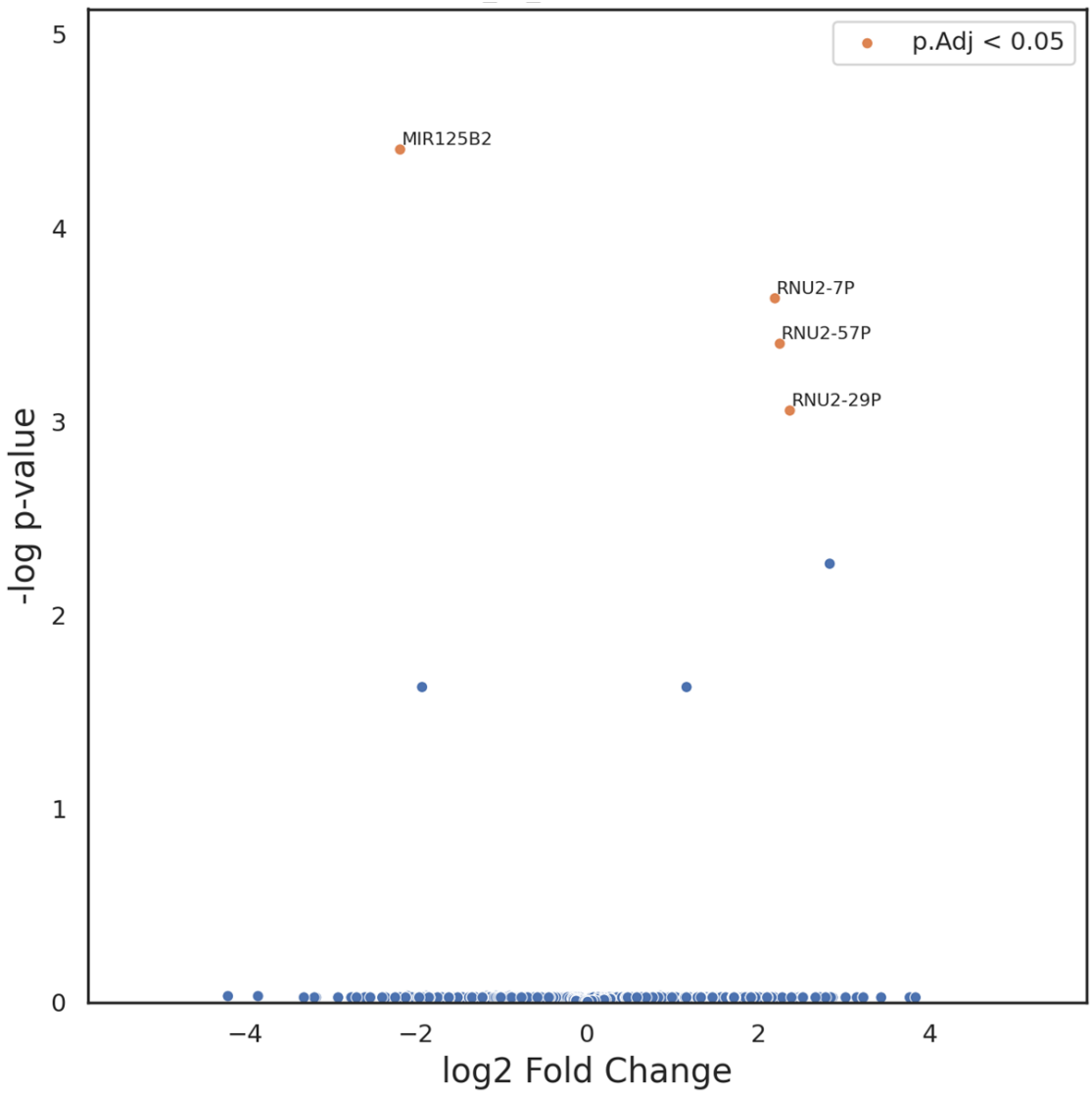

Figure 4-3 Differential expression analysis between Control-EVs and oxLDL-EVs

Volcano plot of statistical significance (p.Adg <0.05) against Log2 fold change between Control-EVs and oxLDL-EVs, demonstrating the most significantly differentially expressed small non-coding RNAs miR-125b-5p, RNU2-7p, RNU2-57p and RNU2-29p (orange dots). Volcano plot was created using padplot.

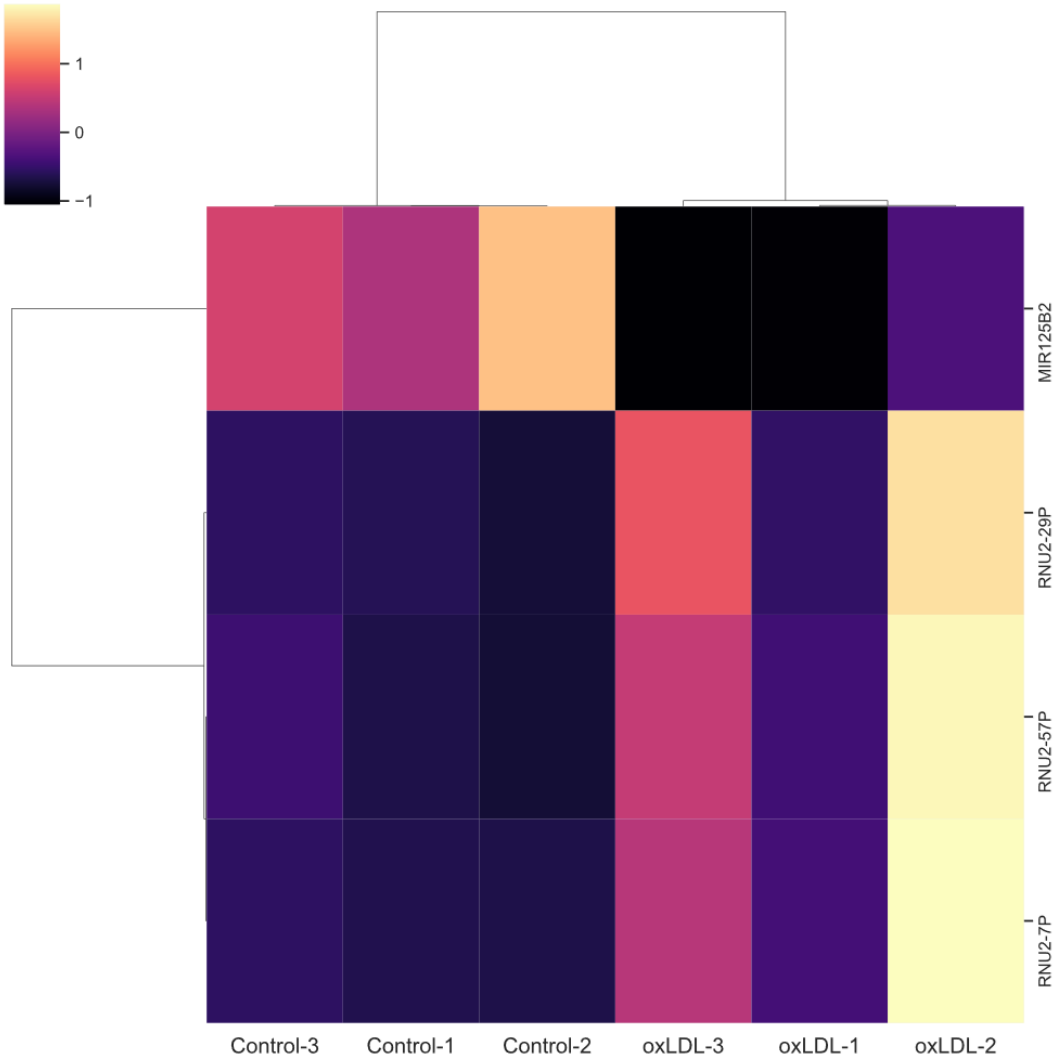

Figure 4-4 Differential expression analysis between Control-EVs and oxLDL-EVs

Heatmap was created using padplot. Rows refer to each small RNA component which was differentially expressed, and columns refer to each sample which was sequenced. Relative abundance for each small RNA is represented by colour (black, lower abundance; yellow, higher abundance), as indicated in the legend.

4.2.3 Validation of small RNA species in EVs

RNA sequencing analysis identified one miRNA, miR-125b-2, to be significantly reduced in oxLDL-EVs derived from HCASMCs (Figure 4-3). MiR-125b-2 is the pre-miRNA that gives rise to mature forms miR-125b-5p and miR125b-2-3p (Chao et al., 2019)(Wang et al., 2020). To determine if the gene name corresponds to the pre-miRNA or one of the mature strands, the process described in 2.6.3.1 was followed. Figure 4-5 depicts the process followed to identify the miRNA strand and read sequence for the 3 snRNAs identified by the RNA sequencing experiment.

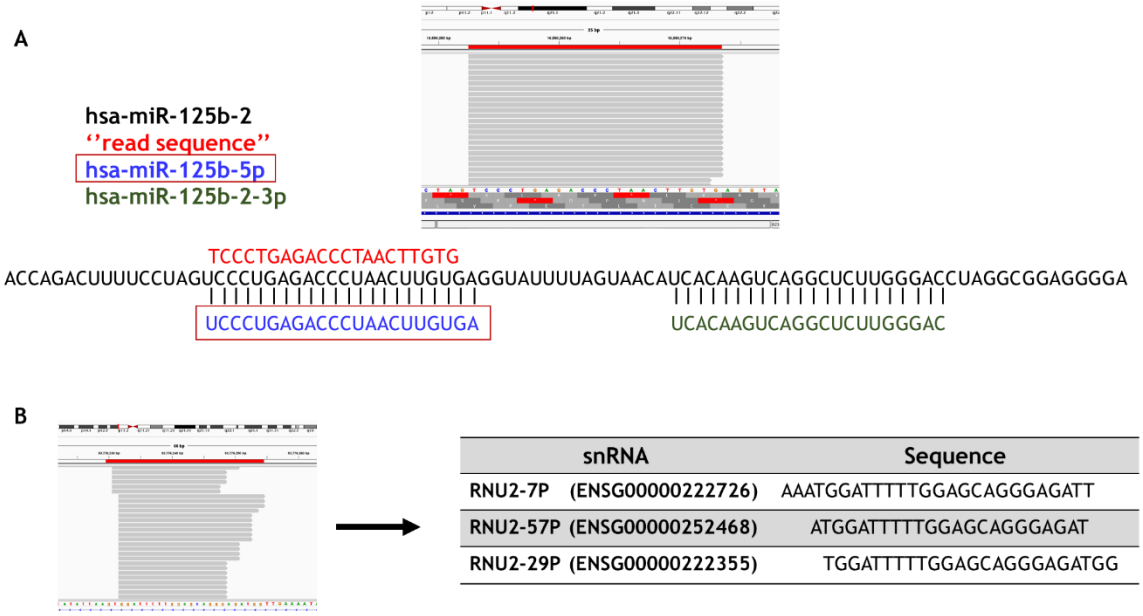

snRNA	Sequence
RNU2-7P (ENSG00000222726)	AAATGGATTTTTGGAGCAGGGAGATT
RNU2-57P (ENSG00000252468)	ATGGATTTTTGGAGCAGGGAGAT
RNU2-29P (ENSG00000222355)	TGGATTTTTGGAGCAGGGAGATGG

Figure 4-5 Workflow process for probe identification to validate small RNAs identified by RNA sequencing experiment

(A) Mapping of read corresponding to miR-125b-2 gene which was identified to be differentially expressed in EVs after oxLDL treatment according to RNA sequencing experiment. (B) Mapping of reads corresponding to RNU2-7P, RNU2-57P and RNU2-29P genes which were found to be differentially expressed in EVs after oxLDL treatment according to the RNA sequencing.

The mapping analysis of miR-125b-2 read from RNA sequencing showed that the differential change in expression identified in the RNASeq analysis corresponded specifically to the miR-125b-5p mature stand (Figure 4-5). However, for completeness, the pre-miR and both mature strands were quantified in the validation experiments (Figure 4-8).

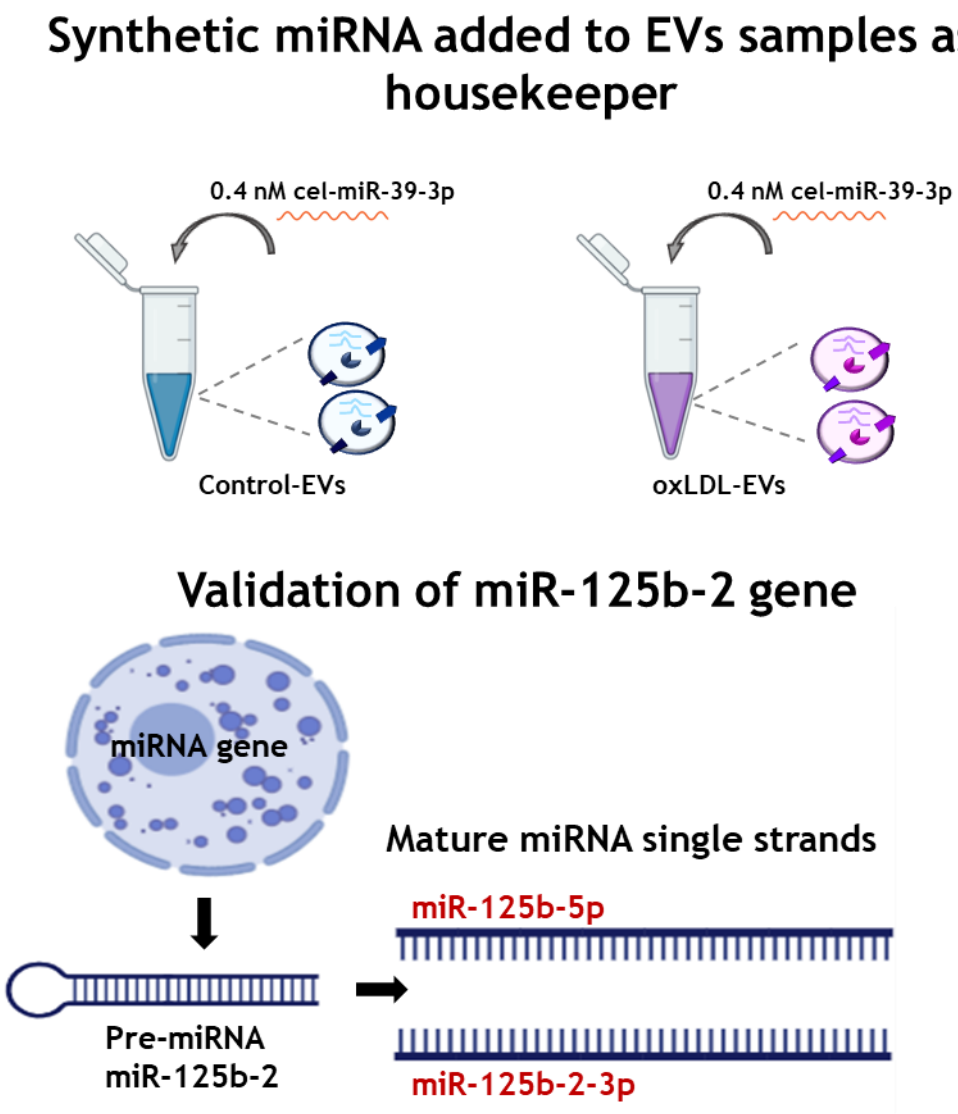

Figure 4-6 Schematic representation of spike-in protocol and validation process in isolated SMC-EVs.

SMC-EVs were spiked with 27 pg of synthetic cel-miR-39-3p before RNA isolation. The synthetic cel-miR-39-3p was added to EV samples to be used as a housekeeper miRNA for sample normalisation. The bottom part of the figure represents the pre-miRNA-miR-125b-2 and its two mature miRNAs strands. Validation of miR-125b-5p levels in SMC-EVs involved detecting the levels of pre-miRNA-miR-125b-2 and levels of two mature miRNAs which forms, miR-125b-5p which was identified by RNAseq and miR-125b-3p were measured in isolated SMC-EVs. Parts of the figure were created by using pictures from BioRender.com.

The mapping analysis of reads corresponding to RNU2-7P, RNU2-57P and RNU2-29P from the RNA sequencing experiment showed that all 3 reads had similar sequences with only 2 or 3 base differences (Figure 4-5 B). The design of 3 probes to separately detect the levels of 3 snRNAs was therefore not feasible, so a TaqMan probe was designed to detect the levels of snRNA RNU2 (**Error! Reference source not found.**).

To validate the small RNA sequencing results in-house, RT-qPCR was identified as the most suitable method. A defined amount (27 pg) of synthetic cel-miR-39-3p was added to EVs (spike-in) before RNA was extracted from SMC-EVs (Figure 4-6). The exogenous miRNA was used as a housekeeper miRNA for sample normalisation. Cel-miR-39-3p levels were detected after spike-in in EVs and miRNA levels were stable and unchanged in Control-EVs (Ct value 20.27±0.26) and oxLDL-EVs (Ct value 20.56±0.10) (Figure 4-7).

Relative quantification revealed that miR-125b-5p levels were significantly reduced in oxLDL-EVs (RQ=0.84±0.35) compared to Control-EVs (RQ=1.0±0.40) (Figure 4-8 A). MiR-125b-2-3p was detected in Control and oxLDL-EVs (Figure 4-8 B). No statistical difference was observed in miR-125b-2-3p in EVs isolated from HCASMCs (Control-EVs RQ=1.0±0.24, oxLDL-EVs RQ=1.21±0.98) (Figure 4-8 B). Relative quantification of miR-125b-2 (pre-miRNA) expression demonstrated the pre-miRNA was not packaged in EVs as CT values detected in Control and oxLDL-EVs were undetermined (Figure 4-8 C). Regarding the validation of RNU2 snRNA, RT-qPCR showed significant increased levels of RNU2 snRNA in oxLDL-EVs (Control-EVs RQ=1.0±0.4, oxLDL-EVs RQ=1.7±0.4,Figure 4-9). Overall, the RT-qPCR data for each miRNA and small RNA agreed with the analysis reported from the RNASeq data.

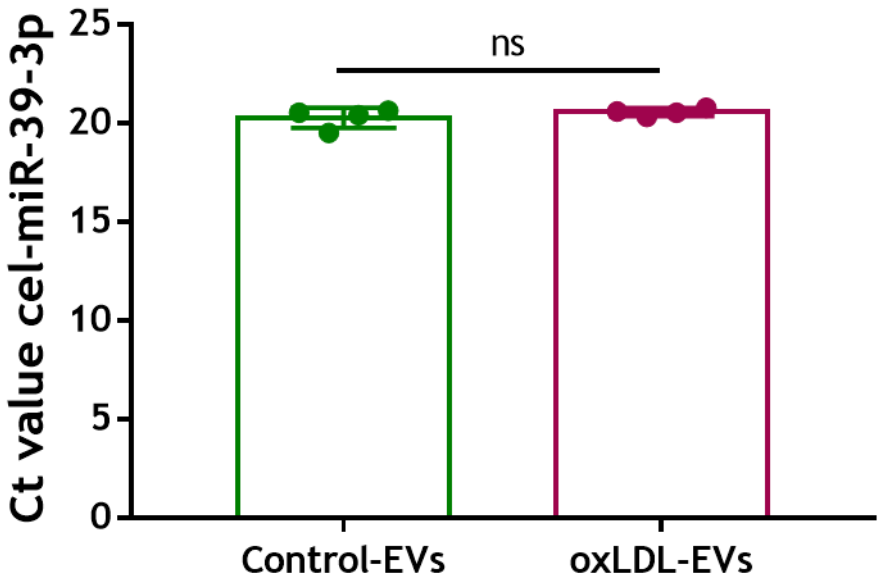

Figure 4-7 Cel-miR-39-3p detection in SMC-EVs after spike-in

qPCR confirmed that cel-miR-39-3p was detected in Control and oxLDL-EVs after spike-in. Statistical probability of differences in expression observed were calculated using paired Student's t-test, vs Control-EVs (ns= nonsignificant). Data are shown as Ct values ±SEM (n=4 patients).

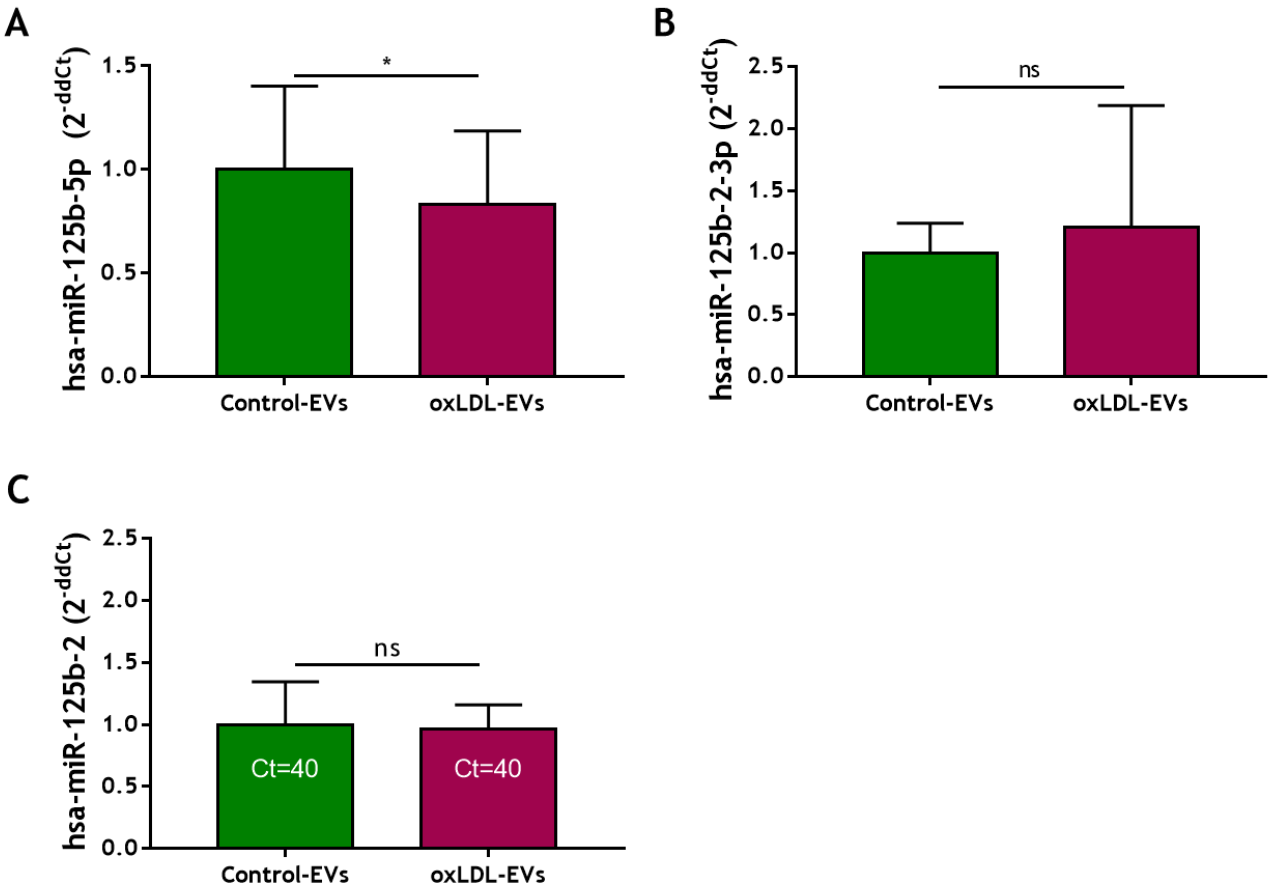

Figure 4-8 Validation of miR-125b-5p in isolated SMC-EVs

(A) qPCR analysis confirmed that miR-125b-5p was downregulated in oxLDL-EVs as suggested by RNAseq experiment. (B) qPCR analysis revealed no difference in levels of miR-125b-2-3p between Control and oxLDL-EVs. (C) Pre-miRNA miR-125b-2 was undetected in Control and oxLDL-EVs as indicated by qPCR analysis. Ct values were normalised to a spike housekeeper miRNA, cel-miR-39. Statistical probability of differences in expression observed were calculated using paired Student's t-test, vs Control-EVs (*$p<0.05$, **$p<0.01$). Data are shown as RQ values ±SEM (n=3 or 4 patients).

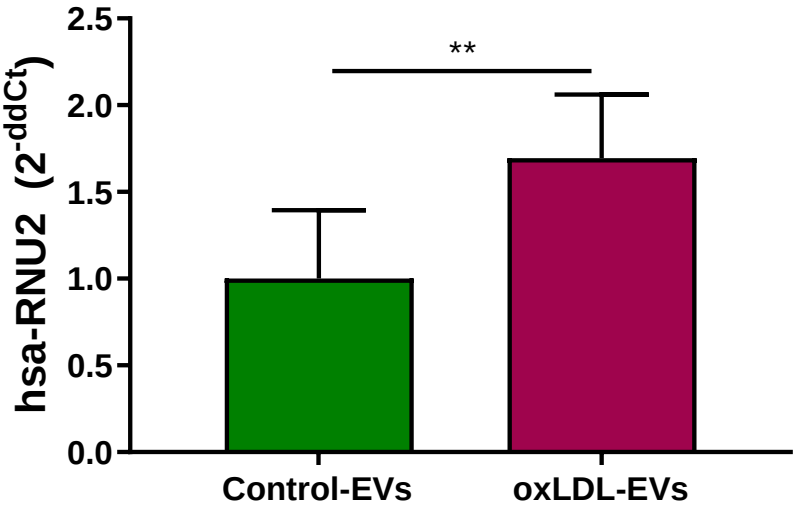

Figure 4-9 Validation of U2 snRNA in isolated SMC-EVs

qPCR analysis confirms that U2 snRNA is upregulated in oxLDL-EVs in agreement with the RNAseq data. Ct values were normalised to a spike housekeeper miRNA, cel-miR-39. Statistical probability of differences in expression observed were calculated using paired Student's t-test, vs Control-EVs (**$p<0.01$). Data are shown as RQ values ±SEM (n=4 patients).

A different approach to analyse data from the RNAseq experiment was performed with Dr Simon Fisher (University of Glasgow) (Figure 4-10). The raw counts obtained by Polyomics were subjected to a normalisation strategy of log2CPM+1. The counts were normalised to the total genetic material within that sample, then those normalised counts were logged. Adding 1 to these values helped to prevent the error when attempting to log0 (all the zeros in the dataset become 1). From these normalised counts, a Welch's test was applied. Welch's t-test is a parametric test comparing two independent groups with unequal variance. This is a simplified test versus differential expression analysis negative binomial regression Wald test. Differential expression analysis relies on an abundance of counts across many genes, so may not be ideal for very small quantities of RNA detected in EVs. This strategy was presented to statistician Dr John McClure and bioinformatician Dr Graham Hamilton (University of Glasgow). Both approaches have their limitations, thus the two different approaches were investigated.

RNA species whose expression was differentially expressed between the two EV groups are depicted in a volcano plot (Figure 4-10). This different approach for analysis of RNAseq data showed that oxLDL treatment resulted in downregulation of miR-125b-5p, thus validating the differential expression analysis, plus also identified downregulation of miR-199b-5p, miR-119a-5p and upregulation of RNU2-37p, RNU2-56p, RNU2-250p, SMORD36B as other potential candidates. The volcano plot in Figure 4-10 was created using padplot and small RNA species with p.Adj<0.05 were considered to be differentially expressed. Differential expression analysis identified miR-125b-5p to be downregulated in oxLDL-EVs and variants of U2 snRNA (RNU2-7p, RNU2-29p, RNU2-57p) to be upregulated in oxLDL-EVs. Using the different analysis, two new miRNAs, miR-199b-5p and miR-199a-5p, were found downregulated in oxLDL-EVs, while 3 different U2 snRNAs (RNU2-37p, RNU2-56p, RNU2-250p) and a snoRNA, SMORD36B, were found upregulated in oxLDL-EVs. However, miR-125b-5p was identified by the two different methods of analysis to be downregulated in oxLDL-EVs highlighting that the two methods, both identified miR-125b-5p to be differentially expressed.

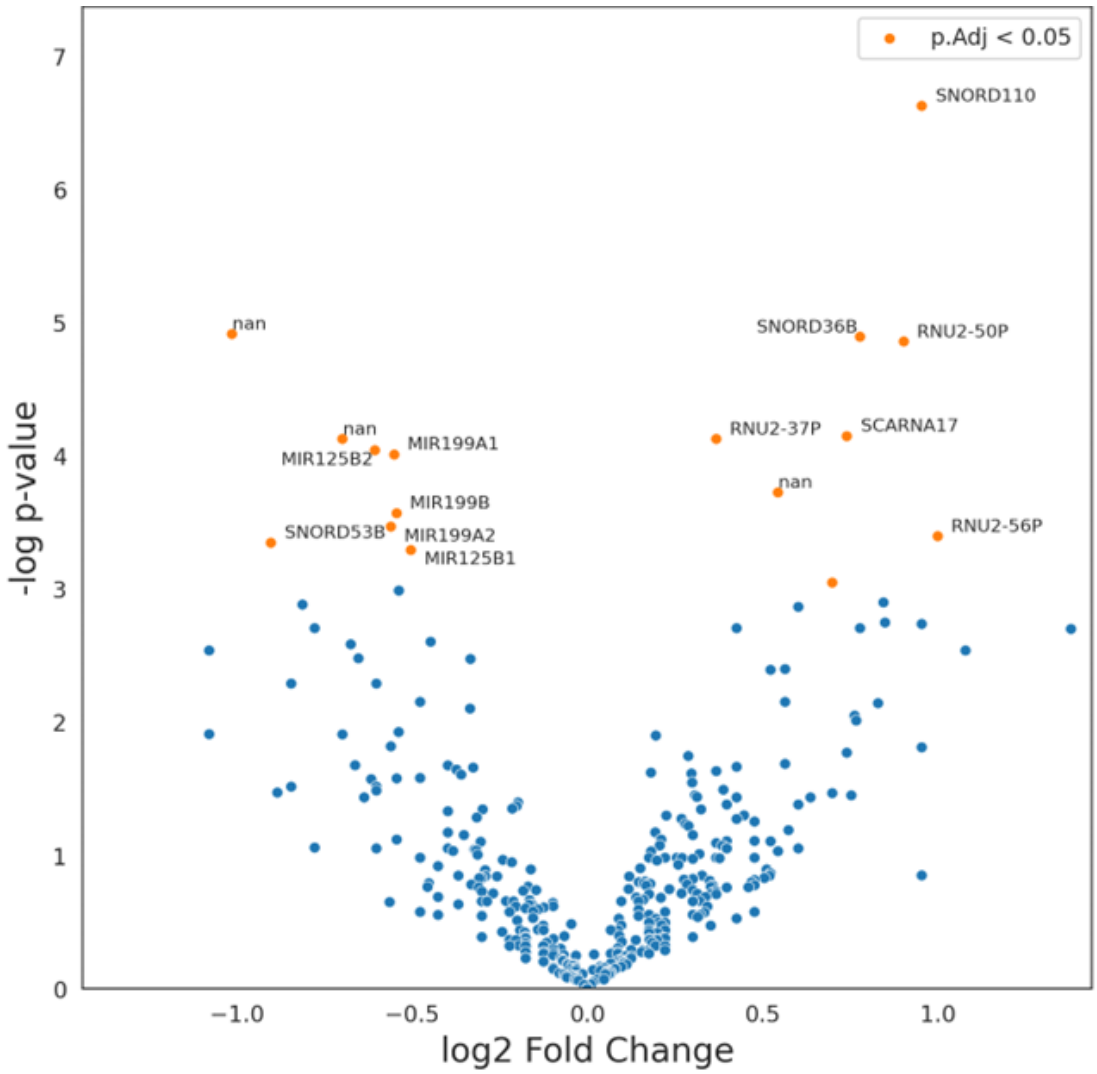

Figure 4-10 Differential expression analysis between Control-EVs and oxLDL-EVs

(A) Volcano plot of statistical significance (p.Adg <0.05) against Log2 fold change between Control-EVs and oxLDL-EVs, demonstrating the most significantly differentially expressed small non-coding RNAs miR-125b-5p, miR-199b-5p, miR-199a-5p, RNU2-37p, RNU2-56p, RNU2-250p, SNORD36B. The volcano plot was created using padplot by Simon Fisher.

The mapping analysis of miR-199b reads and miR-199a-2 reads from the RNA sequencing was performed as explained (Figure 4-5) and showed that both reads correspond to the -5p mature miRNA strand: miR-199b-5p and miR-199a-5p (data are not shown). Validation of the two new miRNAs identified by this approach was performed using RT-qPCR (Figure 4-11). EVs were spiked with a known amount of a synthetic miRNA, cel-miR-39-3p (Figure 4-6). Relative quantification revealed that miR-199b-5p levels were significantly reduced, 0.68-fold reduction, in oxLDL-EVs (RQ=0.32±0.77) compared to Control-EVs (RQ=1.0±0.52) in agreement with analysis of the small RNA sequencing experiment (Figure 4-11 A). Relative quantification of miR-199a-5p showed significant reduction for this miRNA in oxLDL-EVs (RQ=0.53±1.64) compared to Control-EVs (RQ=1.0±1.62) in agreement with analysis of the small RNA sequencing experiment (Figure 4-11 B). However, a large degree of variability across individual patients was observed regarding the validation of miR-199b-5p and miR-199a-p in Control and oxLDL-EVs.

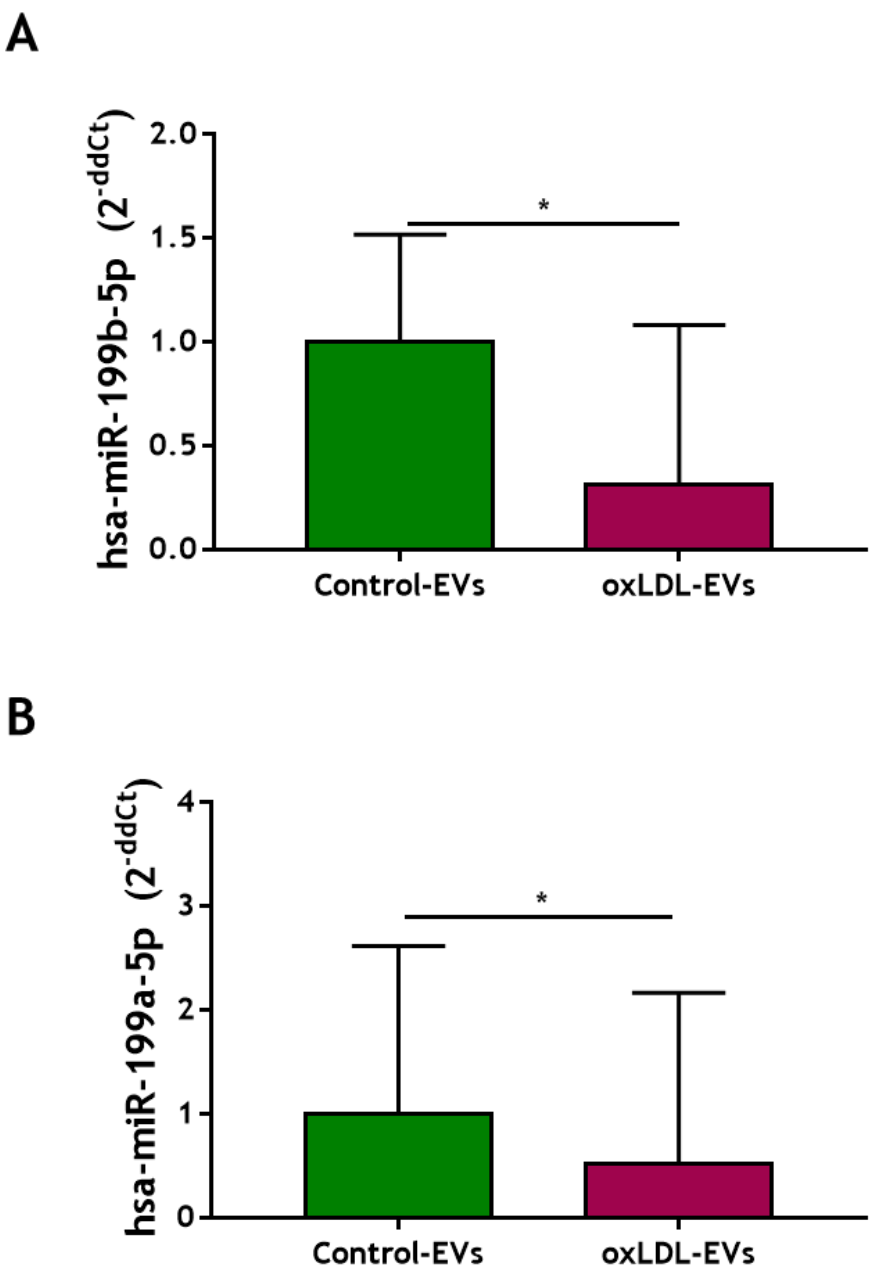

Figure 4-11 Validation of miR-199b-5p and miR-199a-5p in SMC-EVs

(A) qPCR analysis confirms that miR-199b-5p is downregulated in oxLDL-EVs as suggested by alternative analysis of the RNAseq data. (B) qPCR analysis shows that miR-199a-5p is downregulated in oxLDL-EVs. Ct values were normalised to a spike housekeeper miRNA, cel-miR-39-3p. Statistical probability of differences in expression observed were calculated using paired Student's t-test, vs Control-EVs (*$p<0.05$). Data are shown as RQ values ±SEM (n=4 patients).

Table 4-1 Summary of small RNA species validation

A table summarising Ct values and RNAseq reads for all RNA species identified from the two methods of RNA sequencing analysis.

		Av Ct value	Av RNAseq reads
miR-125b-5p	Control-EVs	24.31	103.61
	oxLDL-EVs	24.44	25.69
RNU2	Control-EVs	24.77	27.88
	oxLDL-EVs	24.16	133.51
miR-199b-5p	Control-EVs	34.70	27.99
	oxLDL-EVs	36.01	8.22
miR-199a-5p	Control-EVs	35.25	26.34
	oxLDL-EVs	35.88	7.57

All of the miRNAs, miR-125b-5p, miR-199b-5p and miR-199a-5p, were successfully validated by RT-qPCR. However, the average number of RNA sequencing reads was low for both miR-199b-5p and miR-199a-5p indicating that future work might be better focused on miR-125b-5p (Table 4-1)

4.2.4 MiR-125b-5p expression after oxLDL treatment

After candidate small RNAs were successfully validated in SMC-EVs, miR-125b-5p was chosen for further analysis and, miR-125b-5p levels in HCASMCs in response to oxLDL stimulation was assessed. MiR-125b-5p levels were examined at 2 timepoints (Figure 4-12 A). Briefly, HCASMCs were quiesced for 24 hours and then treated with or without oxLDL (10 μg/mL) for 24 hours (0 h timepoint). After the oxLDL treatment (0 h timepoint), stimulation media was removed and replaced with new media without oxLDL. After 48 hours, media was collected for EV isolation and QIAzol was added to the cells to examine miR-125b-5p expression in cells after EV collection (48 h timepoint).

MiR-125b-5p expression after 24 hour oxLDL stimulation (0 h timepoint) was found significantly upregulated in HCASMCs treated with oxLDL (RQ=1.30±0.15) compared to control HCASMCs (RQ=1.0±0.09) (Figure 4-12 B). Next, miR-125b-5p levels were quantified in HCASMCs after EV collection at the 48 h timepoint (Figure 4-12 C). MiR-125b-5p expression was found significantly downregulated in HCASMCs after oxLDL stimulation and 48 hour EV production (RQ=0.72±0.56) compared to control HCASMCs after 48 hour EV production (RQ=1.0±0.49) (Figure 4-12 C). In EVs isolated from the media that was collected at 48 hours, miR-125b-5p levels were found significantly reduced in oxLDL-EVs compared to control-EVs, in agreement with the previous validation data (Figure 4-8 A). These new data demonstrate there may be temporal regulation of miR125b-5p levels in the HCASMCs at different timepoints and that this may influence the levels in secreted EVs.

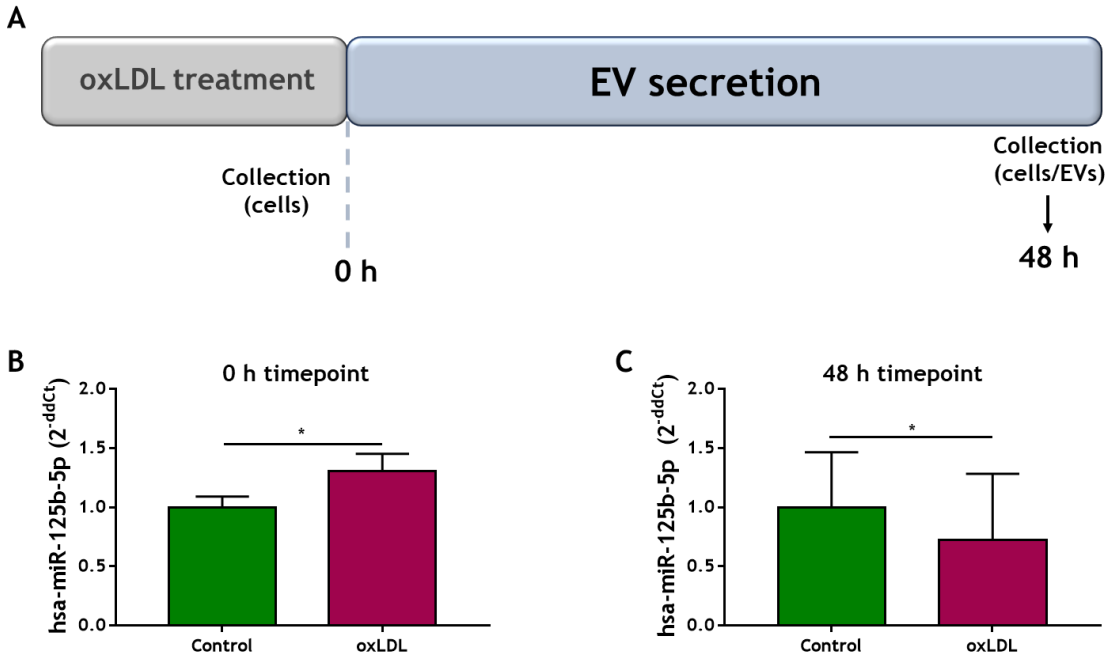

Figure 4-12 MiR-125b-5p expression in HCASMCs in response to oxLDL treatment

(A) Schematic representation of oxLDL stimulation in HCASMCs and sample collection timepoints. HCASMCs were quiesced for 24 hours and then treated with or without oxLDL (10 µg/mL) for 24 hours. After the oxLDL treatment (0 h timepoint), stimulation media was removed and replaced with new media. After 48 hours, media was collected for EV isolation and QIAzol was added to the cells to examine miR-125b-5p expression in cells after EV collection (48 h timepoint). (B) Relative quantification shows that miR-125b-5p is upregulated in response to 24 hour oxLDL treatment. (C) Relative quantification shows that miR-125b-5p levels are downregulated in HCASMCs after 24 hour oxLDL treatment and 48 hour EV production compared to control treated cells after 48 hour EV production. Ct values were normalised to RNU48. Statistical probability of differences in expression observed were calculated using paired Student's t-test, vs Control (*$p<0.05$). Data are shown as RQ values ±SEM (n=3 patients).

4.2.5 miRNA target prediction and Gene-set Enrichment analysis

Twelve different miRNA prediction methods and software were used to predict gene targets: miRWalk 3.0 (Sticht et al., 2018), MicroT4 (Vlachos et al., 2015), miRanda, miRbridge, miRMap, miRNAMap, Pictar2, PITA, RNA22, RNAhybrid, MiRDB (Chen and Wang, 2020) and Targetscan (Friedman et al., 2009). The overall predicted targets by combining the 12 predictions tools were 59,775 (Table 4-2). There were 1373 predicted gene targets which were predicted by 7 or more out of 12 prediction tools. That cut-off was used to maximize the chances of keeping "true" targets of miR-125b-5p and to try to eliminate false positive targets of miR-125b-5p that may have been generated by these algorithms. It has been reported that some prediction algorithms that depend on conservation of the seed match of the miRNA (seed match is a conserved sequence which is mostly situated at positions 2-7 from the miRNA 5´end and is the sequence of miRNA that binds to mRNA) can lead to many false positive hits (Pinzón et al., 2017). By using only this parameter, these algorithms do not consider other factors like thermodynamic stability of the miRNA-mRNA complex. The 1373 predicted gene targets were cross referenced with Tarbase, an online curated database of experimentally validated miRNA gene targets (Karagkouni et al., 2018). Only 303 gene targets were reported to be validated based on results generated from Tarbase (Table 4-2) (Karagkouni et al., 2018).

DAVID was used for pathway enrichment analysis (Huang et al., 2009)(Sherman et al., 2022). Predicted and validated gene targets generated previously (303 gene targets) were inserted into DAVID which generated a list with biological pathways that were enriched with the genes inserted. DAVID used KEGG and Biocarta Pathways for pathway analysis which are collections of manually curated common metabolic pathways. Pathway analysis showed that miR-125b-5p may regulate genes related to cell growth, proliferation and apoptosis (Figure 4-13).

Table 4-2 Summary of miRNA target prediction

List of 12 prediction tools and predicted gene targets for each prediction tool, number of predicted gene targets that passed the cut-off, number of validated target genes and number of predicted and validated gene targets.

Prediction tool	Predicted Gene Targets	Targets predicted by 7 or more out of 12 Prediction tools	Validated Gene Targets	Predicted and Validated Gene Targets
miRWalk 3.0	11,205	1,373	1,109	**303**
MicroT4	4,531			
miRanda	6,028			
miRbridge	55			
miRMap	5,406			
miRNAMap	1,189			
Pictar2	673			
PITA	4,088			
RNA22	6,586			
RNAhybrid	18,158			
MiRDB	925			
Targetscan	931			
Total predicted Gene Targets	59,775			

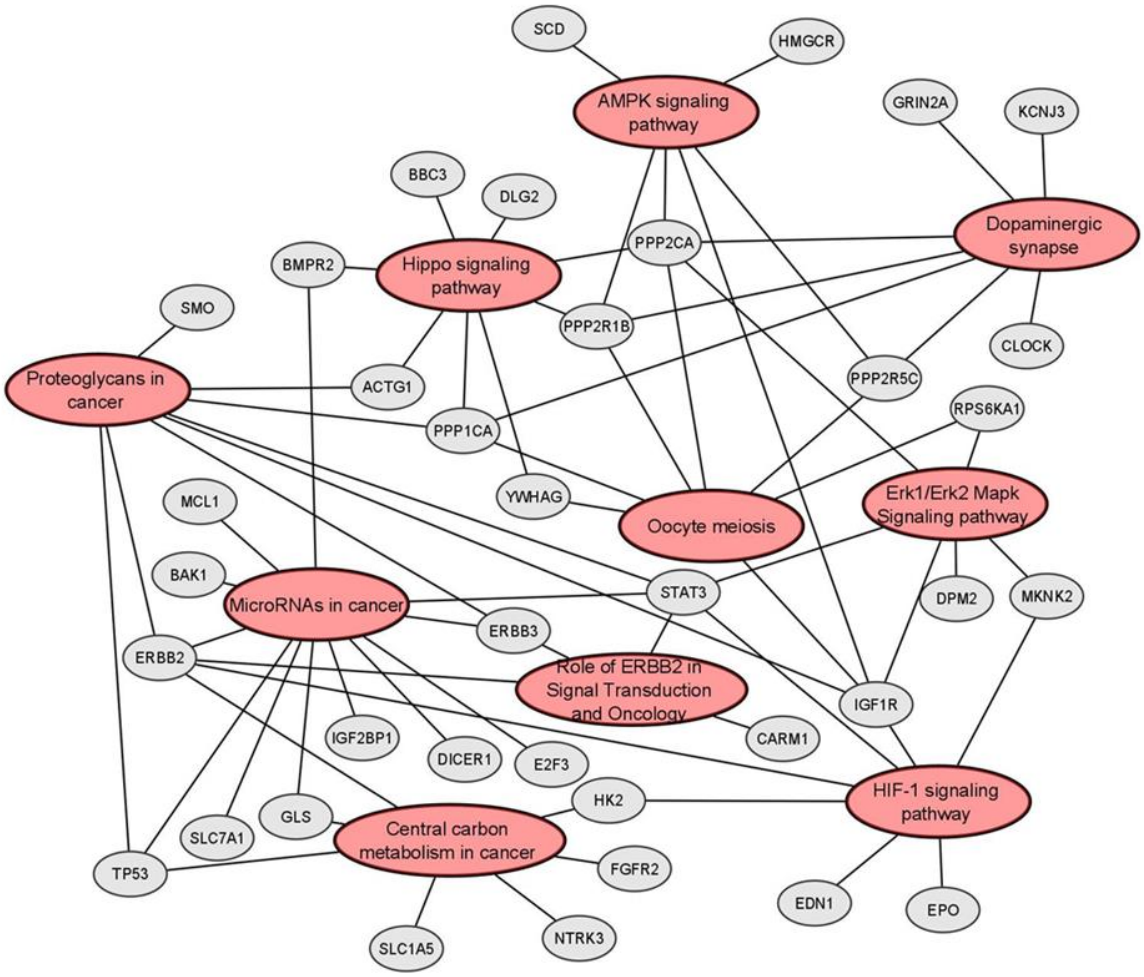

Figure 4-13 Pathway Enrichment analysis for miR-125b-5p predicted gene target

The string network depicts enriched pathways generated by DAVID and the target genes found enriched in these pathways. The dark red nodes or circles represent the pathway found enriched and the smaller grey nodes represent the target genes enriched in every pathway which are connected with a grey edge to the pathway they belong. The string network was generated by Cytoscape.

4.2.6 Pathway hypothesis

To form a pathway hypothesis, the GO terms related to Biological Process, Molecular Function and Cellular Compartment, generated from DAVID were examined. As seen in Figure 4-13, DAVID generated a list with 10 pathways that miR-125b-5p may regulate through genes related to cell growth, proliferation and apoptosis. DAVID enrichment software mapped genes to their associated pathways or GO terms. Most of the time there was not perfect enrichment, meaning that only a few genes, e.g. two or three, map to a certain pathway while a certain pathway may be regulated by far more genes. To avoid bias by choosing only one pathway over the other and make analysis less complicated, the GO term approach was chosen for further analysis (Young et al., 2010). During GO term analysis, a gene is associated with a GO term based on common characteristics or functions that it shares with the specific term. A list with GO terms regarding biological process, cellular compartment and molecular function was generated by DAVID enrichment software. The gene frequency, (how many times a gene was found in a separate GO term), was calculated (Figure 4-14). Six genes, TP53, STAT3, SP1, PPP1CA, ERBB2 and ERRB3, were identified from the three GO term lists with the higher gene frequency (Figure 4-14). To summarize, the pathway hypothesis which was formed following the bioinformatic analysis was that ERBB2/ERBB3 dimer activation leads to MAPK/ERK signalling pathway activation (Olayioye, 2001). The MAPK/ERK pathway was identified by DAVID enrichment software too. That results in p53, STAT3 and SP1 activation and cell proliferation via regulation of gene transcription. MAPK/ERK activation also results in PP1 activation and cell survival regulation (Figure 4-15).

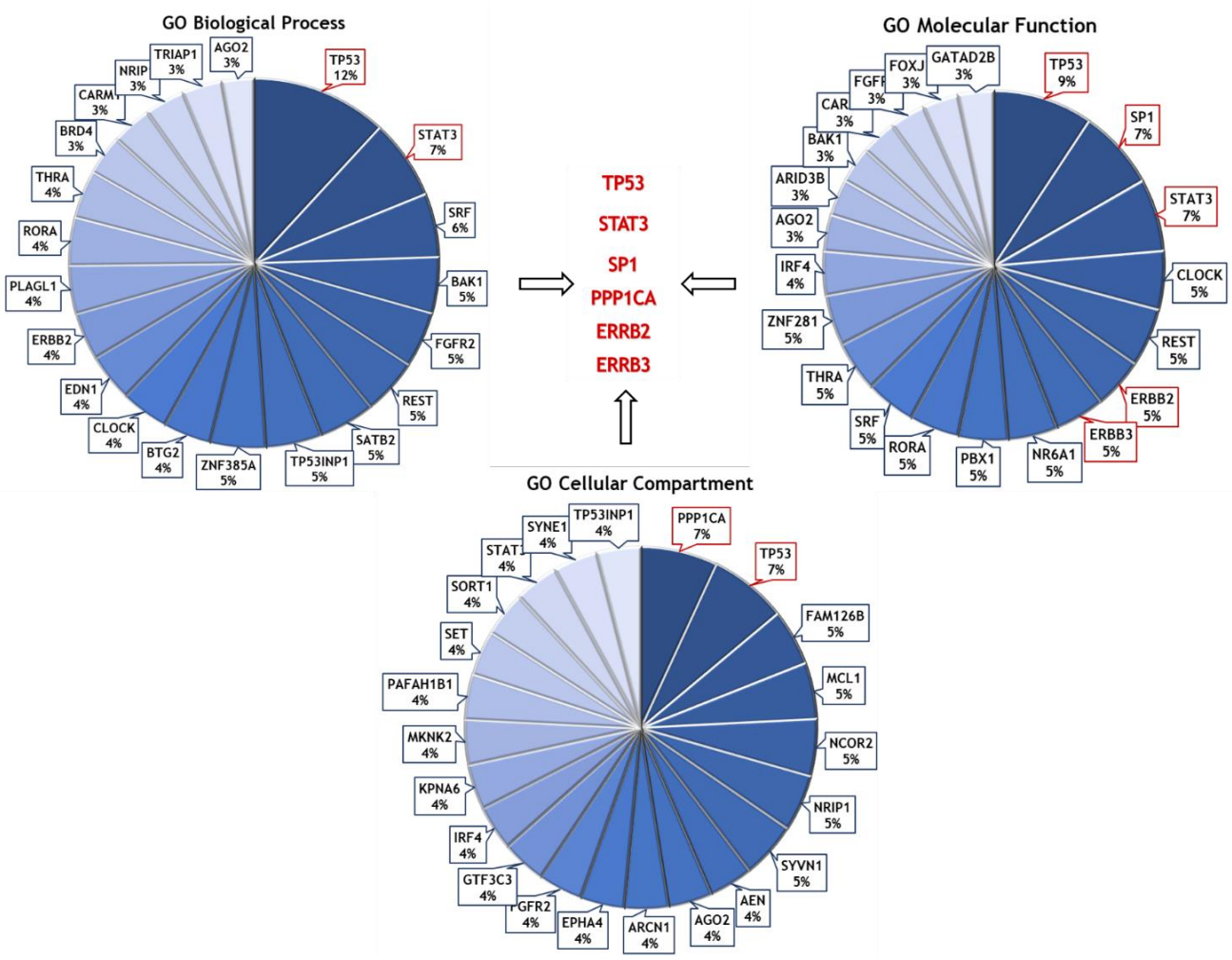

Figure 4-14 GO term analysis of predicted gene targets for miR-125b-5p

Each chart pie depicts gene frequency of genes in GO terms list for Biological Process, Molecular Function and Cellular Compartment generated by DAVID. Red boxes highlight genes with higher frequency.

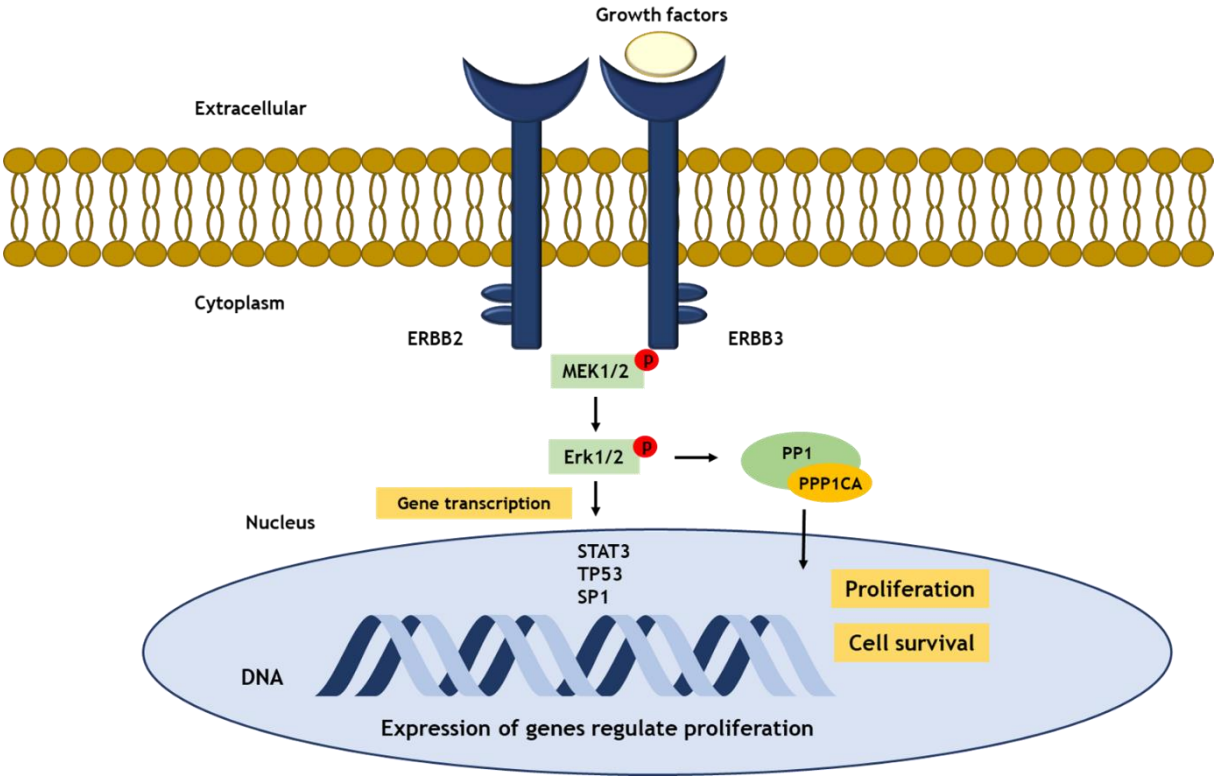

Figure 4-15 Schematic representation of pathway hypothesis formed upon bioinformatic analysis

Six genes were identified from GO term analysis and a pathway hypothesis was formed. Three genes, STAT3, TP53 and SP1, are transcription factors that regulate cell survival and proliferation.

4.3 Discussion

In this chapter, the small RNA cargo of SMC-EVs after control or oxLDL treatment was sequenced. Differential expression analysis identified one miRNA, miR-125b-5p, to be downregulated in oxLDL-EVs compared to Control-EVs and 3 snRNAs, RNU2-7p, RNU2-29p, RNU2-57p, which were found to be upregulated in oxLDL-EVs compared to Control-EVs. Validation of small RNAs in house was successful using RT-qPCR. A different approach for RNA sequencing analysis also identified miR-125b-5p as well as two other miRNAs, miR-199b-5p and miR-199a-5p, to be downregulated in oxLDL-EVs, while 3 different U2 snRNAs (RNU2-37p, RNU2-56p, RNU2-250p) and a snoRNA, SNORD36B, were found upregulated in oxLDL-EVs. MiR-199b-5p and miR-199a-5p were also successfully validated in SMC-EVs using RT-qPCR, although there was more donor-to-donor variation. Interestingly, miR-125b-5p was identified to be differentially expressed by the two methods. MiR-125b-5p expression was found elevated in HCASMCs after oxLDL treatment and significantly reduced in HCASMCs in oxLDL stimulated cells after 48 hours EV secretion compared to control cells. Bioinformatic analysis focused on finding gene targets for miR-125b-5p. In total, 59,775 gene targets were predicted from 12 algorithm prediction tools and 1373 gene targets were present in 7 or more of these databases. Finally, only 303 predicted gene targets were also validated gene targets of miR-125b-5p. Using pathway enrichment analysis software, all 303 gene targets were categorised into biological pathways, all related to regulating cell survival, cell growth and proliferation. Using the GO term list generated by DAVID, the most frequent genes for each category were chosen and a pathway hypothesis was formed as to how miR-125b-5p may regulate cell survival and proliferation via regulation of these genes.

Transcriptomic analysis of EV cargo is becoming popular since it was clear that EVs contain a variety of RNA types, including tRNA, miRNA, Y-RNA, mRNA, rRNA, lncRNA, piRNA, snRNA, snoRNA, and scaRNA (Gézsi et al., 2019). Transcriptomic studies focused on analysing EV-RNA cargo in pathologies where there was a need to identify biomarkers or miRNAs that may participate in the pathology. Analysis of RNA cargo of EVs deriving from cells participating in atherosclerosis progression has provided a lot of insight into the role of EV-miRNA in disease pathology. Not many studies have focused on the active cargo of SMC-EVs during atherosclerosis in contrast with other cell type's EVs like ECs and platelets. Transcriptomic analysis of miRNA profile of platelet-EVs undergoing *in vitro* senescence identified

a plethora of miRNAs, miR-144-3p, miR-486-5p, miR-142-5p, miR-451a, miR-25-3p, miR-145-5p, and let-7f-5p, being upregulated (Pienimaeki-Roemer et al., 2017). Some of these miRNAs such as miR-451a, miR-25-3p, miR-145-5p, have been implicated in CAD (Pienimaeki-Roemer et al., 2017). The miR 143/145 axis is important for SMC homeostasis and differentiation. In animal models of atherosclerosis, miR-143/145 levels were found reduced and their overexpression suppressed lesion progression (Lovren et al., 2012). Moreover, circulating levels of miR-145 were found reduced in patients with stable CAD (Fichtlscherer et al., 2010). Another study profiled the small RNA cargo of EC-EVs after oxLDL treatment and identified miR-155 to be upregulated in EC-EVs after oxLDL treatment (He et al., 2018). Elevated levels of miR-155 were distinct of inflammatory macrophages and lesion progression (Wei et al., 2013). However, circulating levels of miR-155 in patients with CAD have been found reduced compared to healthy donors and have been proposed as a biomarker for disease diagnosis (Faccini et al., 2017).

In this study, small RNA sequencing was chosen to profile the RNA cargo of SMC-EVs after oxLDL treatment, an atherogenic molecule. Differential expression analysis identified miR-125b-5p to be downregulated in oxLDL-EVs. Jia et al., studied circulating miRNAs as biomarkers for acute myocardial infarction (AMI) in patients with ACS and identified miR-125b-5p to be upregulated in patients with AMI (n=3 AMI patients and n=3 healthy controls) (Jia et al., 2016). Further analysis of circulating levels of miR-125b-5p in 230 patient with ACS and 79 healthy controls found higher miR-125b-5p levels in patients with ACS compared to healthy patients, suggesting that levels of miR-125b-5p could be used for early diagnosis of AMI (Jia et al., 2016). The role of miR-125b in atherosclerosis progression has been discussed previously (Chao et al., 2019)(Wang et al., 2021). Another study showed that miR-125b-5p was upregulated in lesions from CAD patients and by using *in situ* hybridisation found that macrophages and SMCs in lesions highly expressed miR-125b-5p (Hueso et al., 2022).

MiR-125b-5p is highly expressed in vascular cells such as murine ECs and SMCs (Li et al., 2010)(Hueso et al., 2022). Li et al., showed that oxLDL treatment resulted in reduced miR-125b-5p expression in recipient ECs showing that oxLDL regulates miR-125b-5p expression in ECs (Li et al., 2010). Another study showed that when human aortic vascular smooth muscle cells (HAVSMCs) were treated with oxLDL (75 μg/mL) for 24 hours significant downregulation of miR-125b-5p was observed

(Li et al., 2015). In our study, upregulation of miR-125b-5p in HCASMCs was observed after 24 hour oxLDL treatment. That difference could be attributed either to the different VSMC type or the concentration of oxLDL used for the treatment (10 μg/mL vs 75 μg/mL). MiR-125b-5p levels were found reduced in cells after 24 hour oxLDL stimulation and 48 hour EV secretion compared to control cells at the same timepoint, in contrast with miR-125b-5p upregulation after 24 hour oxLDL simulation. Moreover, miR-125b-5p in HCASMCs after 48 hours EV secretion reflected the miR-125b-5p levels of Control and oxLDL-EVs isolated from these cells.

Small RNA sequencing identified 3 snRNAs which belong to the U2 snRNA family which are known to be regulators of mRNA splicing as components of the spliceosome (Guo et al., 2018)(van der Feltz and Hoskins, 2019). Alternative splicing participates in physiological and pathological responses including in cardiovascular diseases (Rizzacasa et al., 2017)(Hasimbegovic et al., 2021). This is better highlighted in the study of Jia et al., where they showed that mutations in the RNU2-8 gene in mice resulted in neurodegeneration through disruption of alternative splicing (Jia et al., 2012). Upregulation of snRNA variants could be associated with pathological conditions as suggested by Kuhlmann et al., where they showed that circulating levels of U2-1 snRNA fragment were significantly increased in ovarian cancer patients proposing that a circulating snRNA could be used to monitor the disease progression (Kuhlmann et al., 2014). This could be an explanation for the upregulation of RNU2-7p, RNU2-29p, RNU2-57p in oxLDL-EVs. However, Ding et al., observed downregulation of RNU5E-1 in tissues from hepatocellular carcinoma patients and suggested that levels of RNU5E-1 could be utilised as a diagnostic and prognostic biomarker (Ding et al., 2020). The direct effect of oxLDL treatment in the expression of these snRNAs in HCASMCs could have been tested, however downstream analysis was focused on the role of miR-125b-5p.

Bioinformatic analysis identified 303 predicted and validated gene targets for miR-125b-5p and 6 genes, TP53, STAT3, SP1, PPP1CA, ERBB2 and ERRB3, were identified from the three GO term lists with the higher gene frequency. Three out of 6 genes, TP53, STAT3 and SP1, are transcription factors. The role of transcription factors in pathway activation and atherosclerosis progression has been highlighted in many studies (Adhikari et al., 2006)(Niu et al., 2019). Studies

report that oxLDL can induce SMC proliferation via activation of ERK pathway, EGFR/PI-3K/Akt pathway and transcription factor activation (NF-κB) and apoptosis via p53 activation (Napoli et al., 2000)(Auge et al., 2002)(Chistiakov et al., 2015). Pro-inflammatory molecule expression like IL-1β and TNF-a by SMCs after oxLDL internalisation via LOX-1 receptor is mediated by NF-κB upregulation (Chistiakov et al., 2015). All these changes induced by oxLDL at molecular level promote SMC phenotypic switching towards a proliferative and migratory phenotype (Chistiakov et al., 2015). Changes induced by oxLDL in SMCs should be reflected in the cargo of the SMC-EVs according to the hypothesis of this study.

The role of p53 in atherosclerosis development has been discussed thoroughly suggesting that p53-deficiency can drive disease progression (Guevara et al., 1999)(Mercer and Bennett, 2006)(Cao et al., 2017). Analysis of clinical specimens confirmed the localisation of p53 in atherosclerotic plaques (Ihling et al., 1998). Elevated concentrations of oxLDL are toxic for many cell types such as SMCs. OxLDL macrophage apoptosis is part of atherosclerosis progression and Kinscherf et al., showed that oxLDL induced apoptosis in macrophages was associated with p53 induction and p53 inhibition resulted in reduced oxLDL induced apoptosis (Kinscherf et al., 1998). Stress-induced SMC apoptosis may be mediated by the MAPK/ERK pathway (Mayr and Xu, 2001). As a result, MAPK activation can lead to p53 activation or mechanical stress can lead to direct p53 activation as was shown in cardiac myocytes (Mayr and Xu, 2001).

STAT3 has also been implicated in atherosclerosis development and STAT3 inhibition has been proposed as a druggable target for disease treatment (Chen et al., 2019). Phosphorylated levels of STAT3 were found increased in atherosclerotic lesions from APOE KO mice (Zhou et al., 2008). Pravastatin treatment in APOE KO mice resulted in significant reductions in lesion area along with reduced STAT3 phosphorylation highlighting the importance of STAT3 in atherosclerosis progression (Zhou et al., 2008). Activation of STAT3 by oxLDL in ECs has also been shown (Mazière et al., 1999). Another study showed that oxLDL was crucial for miRNA cargo sorting in EC-derived EVs via phosphorylation of STAT3 (Liu et al., 2019).

Many studies have discussed the role of SP1 in vascular SMC normal function during atherosclerosis (Andrés et al., 2001)(Kavurma and Khachigian, 2003)(Osaki et al., 2004). Li et al., showed that endothelial progenitor cell-EVs were enriched in miR-

199a-3p and miR-EV transfer *in vivo* resulted in SP1 inhibition resulting in reduced EC cell death and delayed atherosclerosis progression (Li et al., 2021). SMC apoptosis is important for plaque stability, and it was shown that increased SP1 phosphorylation is a pro-apoptotic event in SMCs (Kavurma et al., 2001). In hepatic cells, it was found that increased oxLDL levels resulted in SR-BI expression via SP1 phosphorylation by the ERK pathway (Yang et al., 2016). SP1 is implicated in atherosclerosis progression via another mechanism. SP1 can regulate the expression of LDLR as it demonstrates SP1 binding sites and SP1 binding to LDLR is mediated by the ERK pathway (Ochiai et al., 2016). It is worth mentioning that direct activation of the ERK pathway by oxLDL has been showed in vascular SMCs (Yang et al., 2001).

The PPP1CA gene encodes one of the catalytic subunits of PP1 protein phosphatase (Rebelo et al., 2015). Research suggests that PP1 phosphatase may regulate cell division via transcriptional regulation (Rebelo et al., 2015) (Flores-Delgado et al., 2007). Phosphatase and actin regulating protein 1 (PHACTR1) is an PP1 binding protein and it has been shown that PHACTR1 deficiency promotes necrotic core formation in atherosclerotic plaques (Kasikara et al., 2021). The authors showed that PHACTR1 mediated macrophage efferocytosis via a PP1 dependent mechanism (Kasikara et al., 2021). Moreover, the PHACTR1 loci was identified by GWAS as a genetic risk factor for atherosclerosis (Holdt and Teupser, 2013). The final two genes identified by bioinformatic analysis were ERBB2 and ERBB3. Interestingly, all members of the epidermal growth factor receptor family have been found to be expressed in SMCs (Forrester et al., 2016). HER2 or ERBB2 receptor has been associated with atherosclerosis development and induction of proliferation via ERK pathway activation (Spencer et al., 2000)(Jian et al., 2020). Rat SMCs under intermittent hypoxia (an alternation between hypoxic conditions and normoxic conditions) demonstrated increased cell proliferation which contributes to atherosclerosis development, along with increased ERBB2 levels (Kyotani et al., 2013). Wang et al., showed that ERBB1 phosphorylation was found elevated in aortas of APOE KO mice under high fat diet and inhibition of ERBB1 reduced lesion size in mice (Wang et al., 2017). Although ERBB3 has no kinase activity, heterodimerization of ERBB2/ERBB3 can induce signal transduction (Dreux et al., 2006)(Wieduwilt and Moasser, 2008). All the above studies underlie the relevance of the genes identified by bioinformatic analysis in atherosclerosis development.

4.4 Summary

Small RNA sequencing identified miR-125b-5p to be downregulated in oxLDL-EVs and 3 snRNAs, RNU2-7p, RNU2-29p, RNU2-57p, to be upregulated in oxLDL-EVs indicating that oxLDL altered the small RNA cargo of SMC-EVs. Bioinformatic analysis focused on miR-125-5p and revealed 303 predicted and validated gene targets for this miRNA. Pathway enrichment analysis identified pathways regulating cell survival, proliferation, and apoptosis. The most frequent genes in each GO term category were identified and a pathway hypothesis on how miR-125b-5p may regulate cell growth and proliferation via regulation of gene expression.

Chapter 5 Investigating the characteristics of EVs isolated from wild type and APOE knockout mice on normal or high fat diets

5.1 Introduction

EVs can be found in many biological fluids from saliva and blood to breast milk in health and disease (Chiabotto et al., 2019)(Tripisciano et al., 2020)(Hildebrandt et al., 2021). Therefore, EVs have attracted a lot of attention as biomarkers. Many studies have suggested that EV profile alter under pathological conditions and profiling circulating EVs from plasma or serum to discover novel biomarkers or assess their functions in disease development may contribute to increased knowledge of pathological process. Increased levels of circulating EVs had been shown to correlate with cardiovascular outcome in patients with stable CAD (Bernal-Mizrachi et al., 2003)(Werner et al., 2006)(Nozaki et al., 2009)(Sinning et al., 2011). In all these studies, authors highlighted the importance of endothelial-derived EVs and that increased circulating levels of these EVs could indicate endothelial dysfunction and act as an independent risk factor for cardiovascular outcomes in patients with CAD. Numerous studies examined the circulating levels of EVs in patients with ACS (Boulanger et al., 2017). Circulating EVs of patients with acute myocardial infarction were found elevated compared to patients with stable coronary disease (Stępień et al., 2012)(Biasucci et al., 2012).

The mouse became a predominant model to study experimental atherosclerosis due to high reproduction rates, easy genetic manipulation and induction of atherosclerotic lesions in a reasonable amount of time (Gisterå et al., 2022). The WT mouse is resistant to lesion development due to increased levels of anti-atherogenic HDL and decreased levels of atherogenic LDL (Wouters et al., 2005). The majority of mouse models of experimental atherosclerosis are based on genetic manipulation of genes involved in lipid metabolism such as APOE or LDLR, or other mechanical interventions such as injury models e.g. carotid artery ligation in combination with high fat diet (Ilyas et al., 2022). The APOE knockout mouse model is most frequently used followed by the LDLR knockout mouse model based on an analysis of the number of publications from PubMed (Ilyas et al., 2022). Generation of the APOE knockout mice is achieved via gene knockout or inactivation of the APOE gene and thus lack of APOE glycoprotein (Meir and Leitersdorf, 2004). APOE is mainly synthesised in the brain and liver and acts as a ligand for receptors that clear chylomicrons and very low–density lipoprotein (VLDL) from the blood. Deletion of APOE gene resulted in increased cholesterol levels which were reported to be at least quadrupled when mice were fed high fat diet and about 10-fold normal human levels (Meir and Leitersdorf, 2004). Lesion

development can be achieved in APOE KO mice with normal chow diet at 10 weeks, but APOE KO mice can develop lesions in less than 8 weeks after being fed a high fat diet (Nakashima et al., 1994)(Getz and Reardon, 2012)(Gisterå et al., 2022). The model develops lesions similar to ones developed in humans with an extensive necrotic core and stable fibrous cap (Getz and Reardon, 2012)(Emini Veseli et al., 2017). However, the model exhibits some limitations in terms of patient translation. The APOE KO mouse model for atherosclerosis can only be used to study the mechanism of lesion progression in aortic sinus and aortic arch but not to study coronary lesion progression, nor plaque instability or thrombus formation (Ilyas et al., 2022). However, the APOE KO mouse model has been used to study the mechanism of plaque rupture either with the use of a stimulus e.g. continuous infusion of angiotensin II or prolonged feeding of high fat feeding of APOE KO or APOE and LDLR double KO or crossbreeding of APOE KO mice with mice presenting a mutant fibrillin-1 allele results in impaired elastin structure of the vessel wall and vulnerable atherosclerotic plaques in mice (Matoba et al., 2013)(Van der Donckt et al., 2015)(Karel et al., 2020).

The LDLR KO mouse model is the second most popular mouse model to study experimental atherosclerosis. The LDLR is expressed in the liver and is responsible for the clearance of LDL-C and its expression is regulated by PCSK9 (Ilyas et al., 2022). Although APOE gene mutations are rare in patients with hypercholesterolemia, pathogenic mutations in the LDLR gene have been linked with human familial hypercholesterolemia (Brautbar et al., 2015). Knockout of the LDLR gene results in inhibition of LDL-C clearance through the liver and thus ~ 2 fold increased LDL-C levels in plasma (Ilyas et al., 2022). One advantage of this model is that it exhibits a lipid profile similar to humans while the APOE KO mouse does not (Ilyas et al., 2022). However, LDLR KO mice require a high fat diet in order to develop atherosclerotic lesions (Ilyas et al., 2022). Moreover, the model cannot be used to study coronary lesion progression or plaque instability or thrombus formation (Ilyas et al., 2022). Both models have their strengths and limitations, however the APOE KO mouse model is perhaps more widely utilised as a model of atherosclerosis than the LDLR KO mouse model due to the fact that it can develop complex vascular lesions under chow diet when plasma cholesterol levels are not elevated and lesion progression is accelerated under high fat diet (Getz and Reardon, 2012).

Both APOE and LDLR KO mice have been widely used to study the effect of lipid lowering therapies on lesion progression (Ilyas et al., 2022). Furthermore, another popular surgical mouse model has emerged through demonstration that carotid ligation surgery on APOE or LDLR KO mice fed a high fat diet accelerates atherosclerosis from 3–4 months to 2–4 weeks (Nam et al., 2009)(Mitra et al., 2018). Additionally, the adeno associated virus (AVV)-mediated PCSK9-overexpression mouse model has emerged as a new tool to study atherosclerosis (Gisterå et al., 2022). PCSK9 is responsible for endosomal and lysosomal degradation of the LDLR (Ilyas et al., 2022). Overexpression of PCSK9 with to a gain-of-function mutation through adeno-associated viral vector-mediated gene transfer leads to accelerated LDLR degradation and impaired clearance of LDL-C resulting in hyperlipidaemia (Ilyas et al., 2022). PCSK9-AAV mice develop atherosclerotic lesions and high fat diet aggravates lesion progression (Roche-Molina et al., 2015).

Many studies have suggested that EV profile alters under pathological conditions and profiling circulating EVs from plasma or serum is utilised to discover novel biomarkers or assess their functions in disease development. During atherogenesis, EVs secreted from aortic tissue may influence the disease progression. Ultrastructural analysis of human healthy aorta and atheromatous lesions showed EV localisation in ECs and SMCs, but also EVs present in the lesion area were secreted either from ECs or lesion SMCs (Perrotta and Saveria, 2016). Moreover, after quantification, they observed significantly higher number of EVs in atherosclerotic aortas compared to healthy ones (Perrotta and Saveria, 2016). A study analysed tissue EVs from human calcified aortic plaques collected after endarterectomy and aortic valves collected after aortic valve replacement after aortic valve stenosis (Blaser et al., 2020). They observed that EVs from carotid arteries had increased average size and distinct proteomic profile compared to EVs from aortic valves (Blaser et al., 2020). These studies offer observations regarding the potential role for tissue-derived EVs in atherosclerosis progression. For this reason, it was worthwhile to isolate secreted EVs from aortic tissues of wt and APOE mice to study the EV profile of secreted aortic tissue EVs.

MiRNAs as the active cargo of EVs have attracted a lot of research interest as biomarkers. Numerous studies suggest that EV-miRNA levels could be used as diagnostic markers for CAD prediction. Jansen et al., showed that EV-miRNA levels

of miR-126 and miR199a but not circulating soluble miRNAs were inversely correlated with cardiovascular events in patients with stable CAD (Jansen et al., 2014). Numerous other EV-derived miRNAs, such as miR-133a, miR-143/145, miR-150, miR-155, miR-214, miR-223, and miR-320b have also been reported as biomarkers for atherosclerosis risk prediction, summarised in (Lu et al., 2019). EV cargo could be a potential biomarker of atherosclerosis progression. Since miR-125b-5p was detected by RNA sequencing in cultured human coronary artery SMC-derived EVs after oxLDL treatment, it was of interest to determine whether miR-125b-5p was also present in EVs isolated from a relevant model of atherosclerosis.

5.1.1 Aims

- Characterise circulating EVs derived from female wt and female APOE knockout mice ±HFD.

- Characterise aortic tissue secreted EVs from wt and Apoe knockout mice ±HFD.

- Detect miR-125b-5p in serum EVs and aortic tissue secreted EVs from wt and Apoe knockout mice ±HFD.

5.2 Results

5.2.1 Serum EV profile from wt and APOE KO mice

In the previous chapter, the effects of oxLDL, a pro-atherogenic stimulus, on EV release from cultured human coronary artery SMCs was examined. In these studies, the circulating EV profile of an animal model of atherosclerosis compared to control animals was examined. Females were used instead of males as group-housed male mice in cages tend to be more aggressive, territorial and display dominance behaviours (Lidster et al., 2019). Moreover, studies have shown that the use of female mice does not induce variability within the study (Beery, 2018). EVs were isolated from 50 μL of serum obtain from blood of APOE knockout or wt mice. EVs were characterised by NTA analysis for average size and concentration and by western immunoblotting for EV protein marker detection. The design of the study is summarised in Figure 5-1.

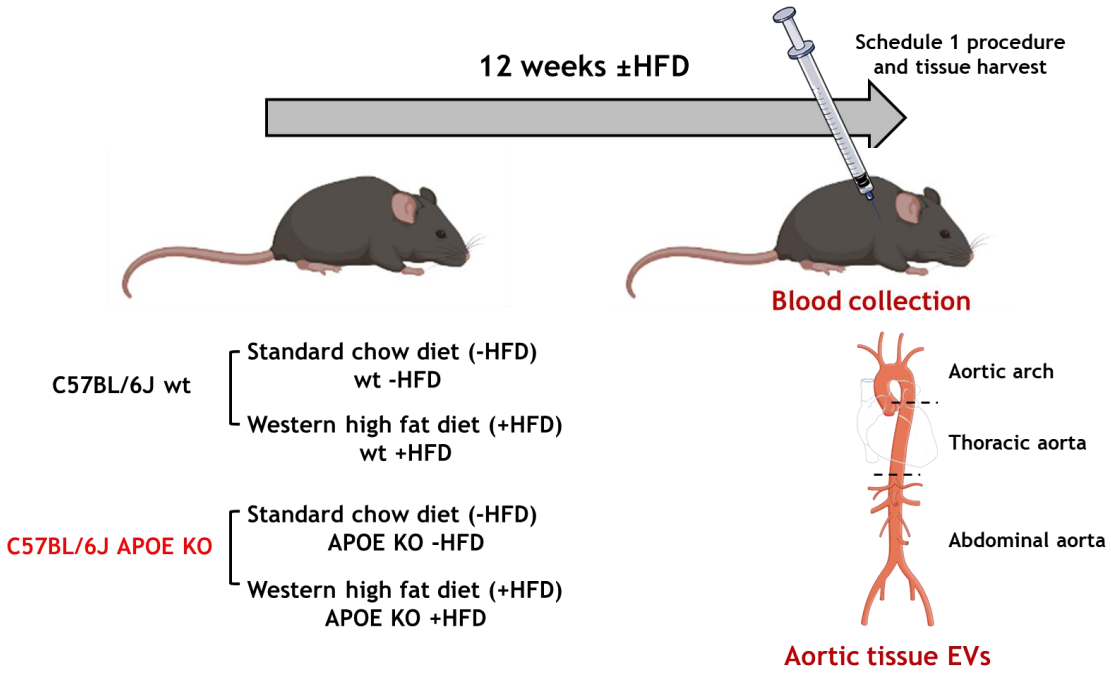

Figure 5-1 Design of the study

Following the 12 week diet, mice were terminated. Blood was collected by cardiac puncture and serum was isolated. The whole aorta was dissected along with the PVAT. Then it was separated into 3 distinct anatomical parts: aortic arch, thoracic aorta and abdominal aorta. Parts of the figure were created by using pictures from Servier Medical Art and BioRender.com. Servier Medical Art by Servier is licensed under a Creative Commons Attribution 3.0 Unported License.

A characterisation of female wt and APOE KO mouse models under both diets was performed. The total body weight of mice after Schedule 1 termination was measured (Figure 5-2). Body weight measurements showed that high fat diet did not alter the total body weight of wt mice (wt -HFD Body weight=24.7±0.6, wt +HFD Body weight=24.8±0.5) (Figure 5-2**Error! Reference source not found.**). I ncreased total body weight of APOE KO -HFD mice (Body weight=26.7±2.4) and APOE KO +HFD mice (Body weight=27.9±1.9) was observed, but no statistical significance was detected (Figure 5-2). Body weight measurements showed that high fat diet did not alter the total body weight of APOE KO mice.

Furthermore, observation of the morphology of aortic tissues of wt and APOE KO mice was performed. Aortic tissues were incubated in MiR05-Kit to allow EV secretion and media was collected for EV isolation. Next, tissues were embedded in paraffin and stained with H/E to observe histological changes or lesions as described in 2.7.6. Imaging analysis was used only for qualitative purposes and to quantify percentage of lesion areas. No plaque formation was observed in H/E stained aortic tissues from wt mice (Figure 5-3). Imaging of H/E stained aortic tissues from APOE KO mice fed chow diet did not detect any lesion formation in these mice (Figure 5-3). However, lesions were observed in H/E stained aortic arch and thoracic aorta sections from APOE KO mice fed a high fat diet (Figure 5-3**Error! Reference source not found.**). No lesions were observed in section from abdominal aorta from APOE KO mice fed a high fat diet (Figure 5-3).

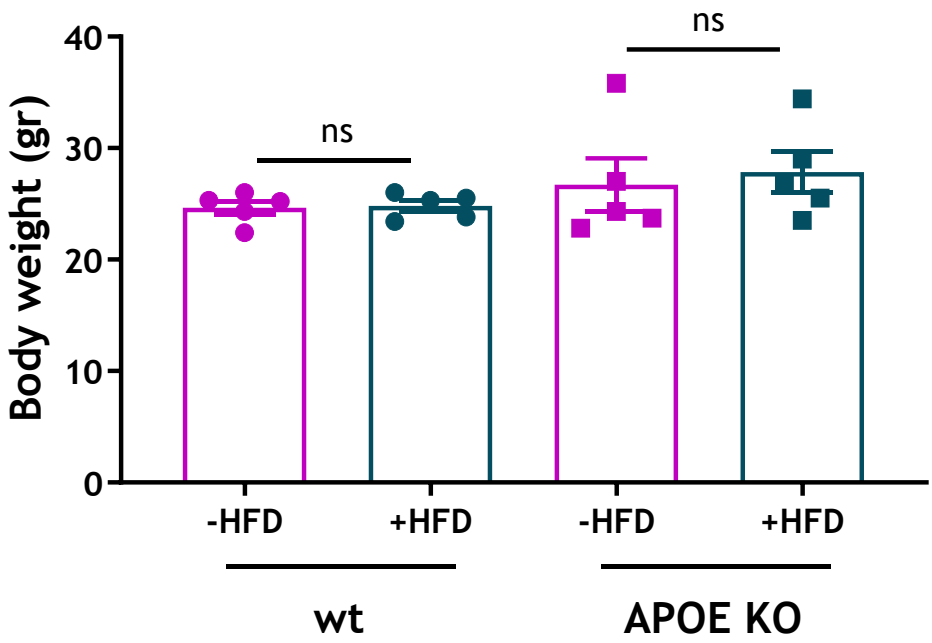

Figure 5-2 Characterisation of total body weight of wt and APOE KO mouse models

Measurements in grams (gr) of total bod wight of 6 months old female wt (-HFD =5, +HFD=5) and APOE KO mice (-HFD=5, +HFD=5) under normal chow diet or high fat diet. Body weight was measured after the mice were terminated using the Schedule 1 method of termination. No difference was observed in weight of 4 groups of mice. Statistical probability of differences was calculated using One-way ANOVA with post-hoc Tukey's test (ns= nonsignificant). Data are expressed as the mean ±SEM.

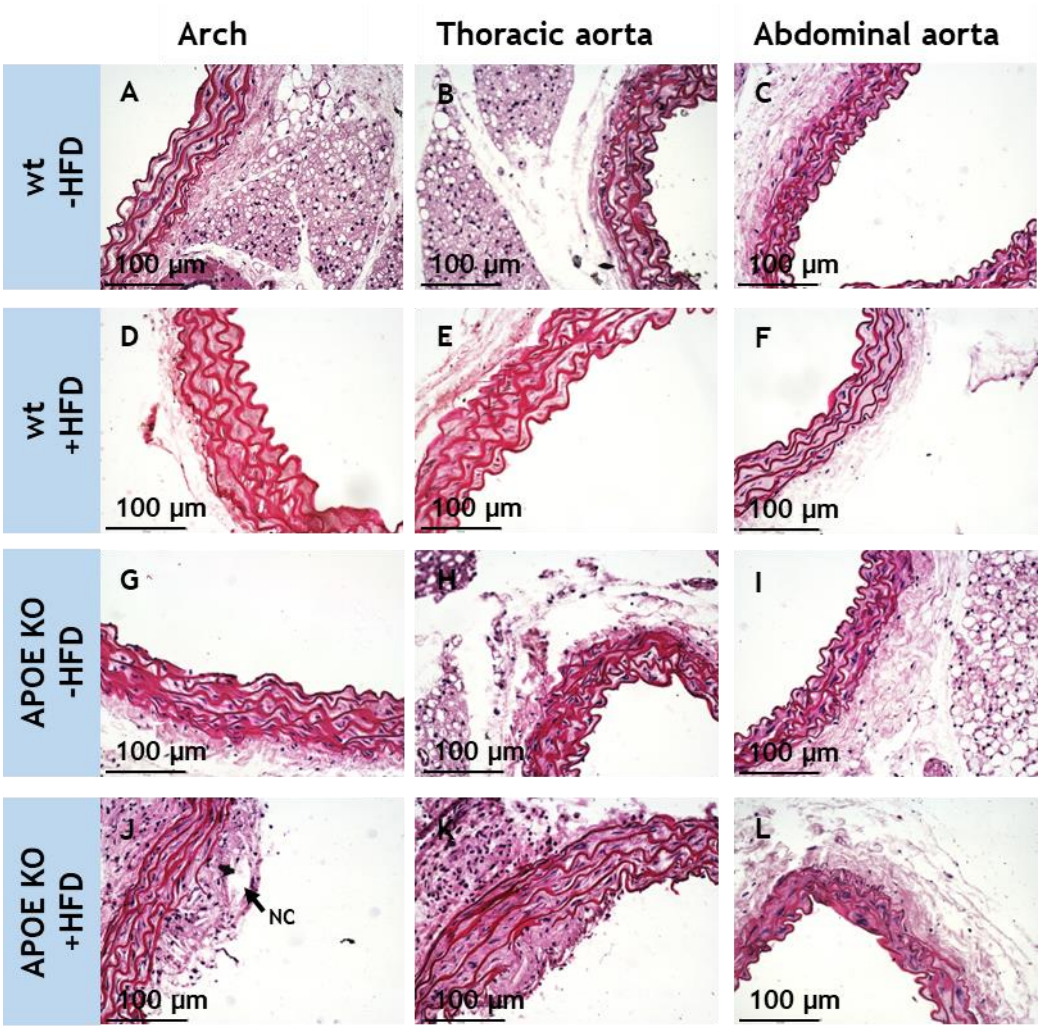

Figure 5-3 Histology of aortic tissues: arch, thoracic aorta and abdominal aorta from wt and APOE KO mice

After aortic tissues were incubated in MiR05-Kit and media was collected for EV isolation, tissues were embedded in paraffin and stained with H/E as described in 2.7.6. Images were acquired at 40x magnification using the EVOS® FL Auto Imaging System. H/E staining was performed to determine histological changes or plaque development. (A, B, C) No plaque formation was observed in aortic tissues from wt -HFD mice. (D, E, F) No plaque formation was observed in aortic tissues from wt +HFD mice. (G, H, I) No plaque formation was observed in aortic tissues from APOE KO -HFD mice. (J, K) H/E staining showed that plaque was formed at the arch and thoracic aorta from APOE KO +HFD, however no plaque was visible in abdominal aorta from the same mice (L). NC, necrotic core. Haematoxylin stained dark purple/blue the nuclei, eosin stained pink the cytoplasm.

EVs were visualised and quantified using a Nanosight LM14 (Figure 5-4). An example Nanosight trace for serum EVs showed that the majority of EVs quantified had a size range 30-120 nm (Figure 5-4 A). NTA analysis of mean particle size revealed no difference between the size of EV population within the 4 groups of mice. Serum EVs from wt -HFD mice had average particle size 94.6±3.3 nm, serum EVs from wt +HFD mice had average particle size 91.6±1.4 nm, serum EVs from APOE KO -HFD mice had average particle size 110.4±5.4 nm and serum EVs from APOE KO +HFD mice had average particle size of 96.7±4.1 nm (Figure 5-4 B). Serum EVs from APOE KO -FD mice had larger sizes (110.4±5.4 nm) compared to EVs from wt -HFD mice (94.6±3.3 nm), but no statistical significance was detected. In both mice strains, HFD had no effect on circulating serum EV size (P_{diet}=0.10). Two-way ANOVA statistical analysis showed that the phenotype of mice had an effect on mean particle size ($P_{phenoype}$=0.0462). Quantification of the mode size of serum EVs revealed that EVs had a size range 75-80 nm with no statistical significance being detected (Figure 5-4 C). Two-way ANOVA analysis showed that phenotype, diet or interaction (interaction of diet x phenotype) had no effect on mode size of serum EVs as seen by non-significant $P_{phenotype}$, P_{diet} and $P_{interaction}$. $P_{interaction}$ refers to interaction of these two factors: diet vs phenotype in chapter 5.

Statistical analysis, based on the Two-way ANOVA, of serum EV concentration showed that the phenotype of mice (wt or APOE KO) has great effect on EV size ($P_{phenotype}$=0.0005). Moreover, the diet that the mice were fed affected the EV size (P_{diet}=0.0034). Moreover, the interaction of phenotype vs diet had an effect on EV size ($P_{interaction}$=0.0038). Serum EVs from wt -HFD mice had an average concentration of $9.2x10^{12}$±$1.9x10^{12}$ particles/mL and serum EVs from wt +HFD mice had an average concentration of $9.9x10^{12}$±$8.1x10^{11}$ particles/mL (Figure 5-4 D). Serum EVs from APOE KO +HFD mice were found to have significantly increased concentration (~6-fold), average particle concentration of $1.2x10^{14}$±$2.1x10^{13}$ particles/mL, compared to serum EV from APOE KO -HFD mice with average concentration of $2.2x10^{13}$±$3.3x10^{12}$ particles/mL (Figure 5-4 D, ****p<0.0001). Serum EVs from APOE KO +HFD mice were found to be significantly elevated (12-fold) compared to serum EVs from wt +HFD mice (***p<0.001) and serum EVs from wt -HFD (***p<0.001) indicating that HFD alone was not responsible for increased serum EV concentration in APOE KO +HFD mice. Serum EVs from APOE KO -HFD mice (Concentration: $2.2x10^{13}$±$3.3x10^{12}$ particles/mL) had elevated concentration

from wt -HFD mice ($9.2x10^{12}$±$1.9x10^{12}$ particles/mL) with no statistical significance detected.

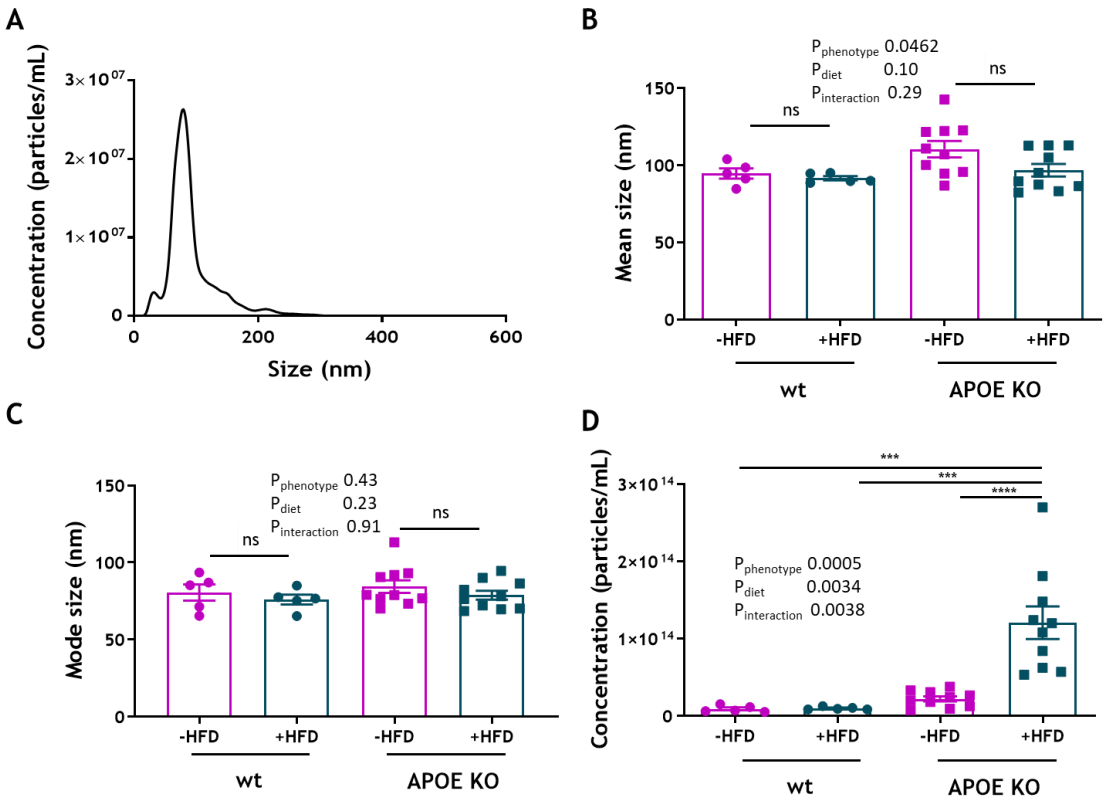

Figure 5-4 NTA analysis of serum EVs from wt and APOE KO mice

EV samples were analysed using a NanoSight LM14. (A) Representative trace of serum EVs produced by Nanosight showing particle size vs particle concentration. (B) NTA analysis of mean particle size of serum EVs from wt mice (-HFD n=5, +HFD n=5) and APOE KO mice (-HFD n=10, +HFD n=10). (C) NTA analysis of mode size of serum EVs from wt mice (-HFD n=5, +HFD n=5) and APOE KO mice (-HFD n=10, +HFD n=10). (D) NTA analysis of particle concentration of serum EVs from wt mice (-HFD n=5, +HFD n=5) and APOE KO mice (-HFD n=10, +HFD n=10). Statistical probability of differences was calculated using Two-way ANOVA with post-hoc Tukey's test (ns= nonsignificant, ***p<0.001, ****p<0.0001). Data are expressed as the mean ±SEM.

The data were re-analysed in a paired manner (Figure 5-5) to depict NTA analysis for serum EVs, for each individual mouse strain +/- HFD separately. Paired analysis did not reveal any other differences in terms of EV size or EV concentration.

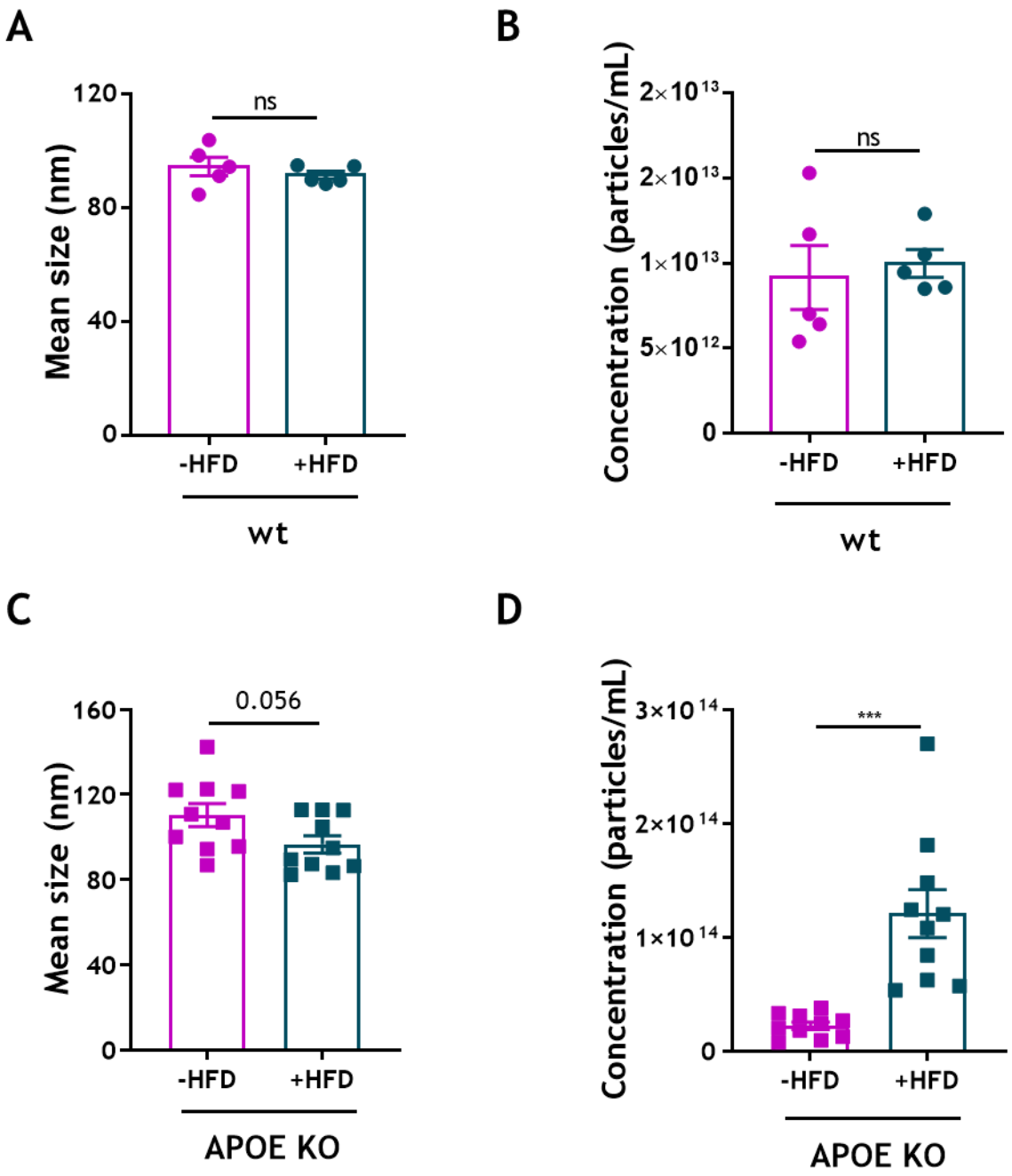

Figure 5-5 NTA analysis of serum EVs from wt and APOE KO mice

NTA analysis of particle size of serum EVs from wt mice (-HFD n=5, +HFD n=5) (A) and APOE mice (-HFD n=10, +HFD n=10) (B). NTA analysis of particle concentration of serum EVs from wt KO mice (-HFD n=5, +HFD n=5) (C) and APOE KO mice (-HFD n=10, +HFD n=10) (D). Statistical probability of differences was calculated using unpaired Student's t-test, vs -HFD group (ns= nonsignificant, ***p<0.001). Data are expressed as the mean ±SEM.

Next, microBCA assay was used to determine protein concentration for EVs derived from serum of wt and APOE KO mice ±HFD and EV marker detection was performed using western immunoblotting. TSG101, CD63, CD81 and Annexin 11 were investigated in serum from wt and APOE KO ±HFD (Figure 5-6). TSG101 was detected in all 4 groups of mice at an apparent molecular weight of 50 kDa. However, the manufacturer's guidance suggests that the antibody detected a band of 47 kDa and a band of 52 kDa. The detection of only one band of 50 kDa according to the manufacturer's guidance indicates an impure sample. The reason for this observation is not clear. CD63 was detected in EVs from all 4 groups of mice at 30-60 kDa agreeing with its predicted detected size per the manufacturer's suggestion which ranges from 30-60 kDa. CD81 was found to be enriched in all serum EV populations. The expected molecular weight of CD81 per manufacturer's guidance is 22-26 kDa whereas in these studies it was detected at an apparent molecular weight of 20 kDa. Finally, Annexin 11 was also detected in EVs from wt and APOE KO mice at an apparent molecular weight of 50 kDa. The manufacturer's predicted size for Annexin 11 antibody ranges from 50-55 kDa.

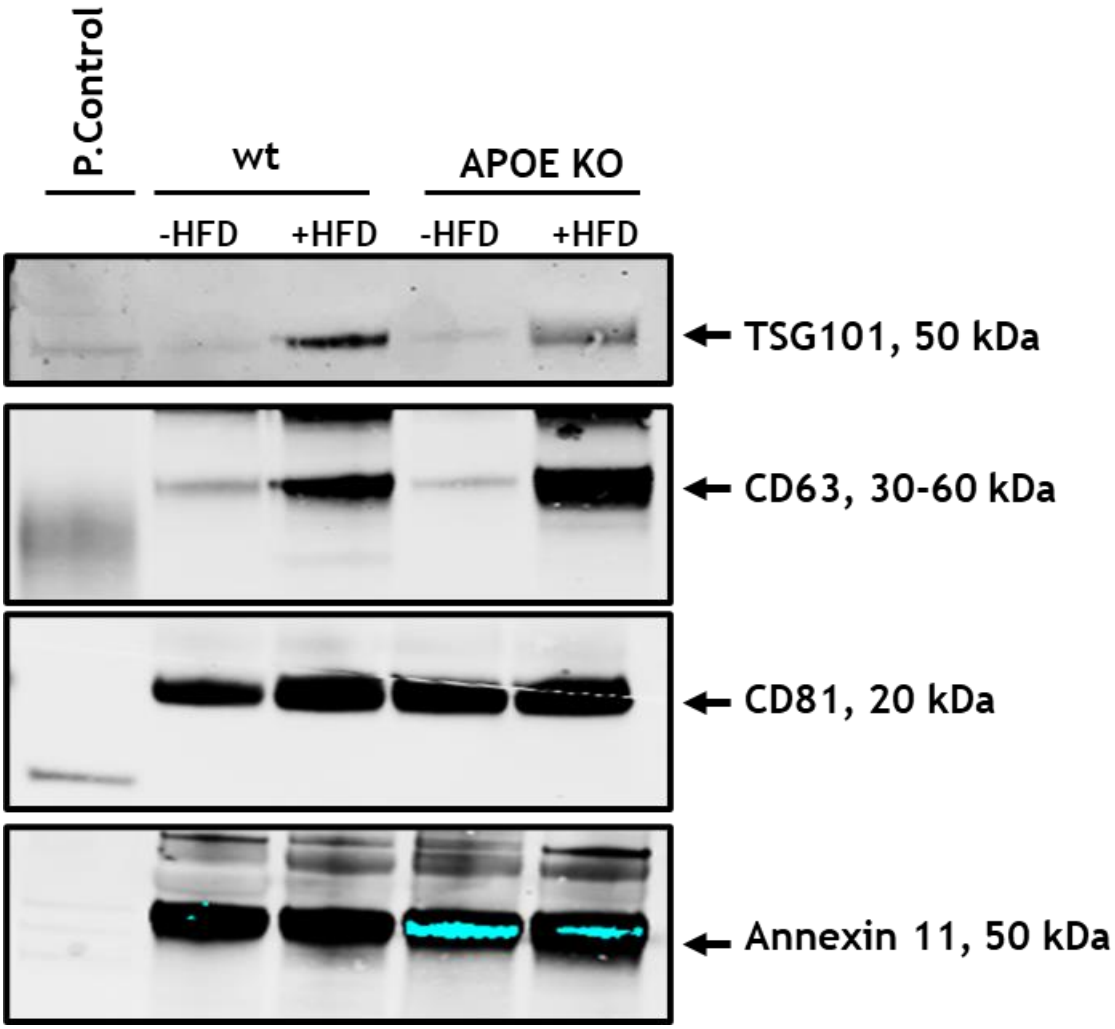

Figure 5-6 Characterisation of EV populations isolated from serum of wt and APOE KO mice

Detection of EV marker TSG101, CD63, CD81 and Annexin 11 on serum EVs from wt and APOE KO mice confirms the isolation of EVs from these mice. 10 µg of protein was loaded for each sample (wt -HFD n=1, wt +HFD n=1, APOE KO –HFD n=1, APOE KO +HFD n=1).

5.2.2 Profiling EVs secreted from aortic tissue from wt and APOE KO mice

During dissection, the whole aorta was isolated and separated into 3 distinct anatomic parts: aortic arch or arch, thoracic aorta, and abdominal aorta. The PVAT was not separated from aorta during dissection as it has been suggested that can regulate atherosclerosis progression (Qi et al., 2018). Tissues were then incubated overnight in Mitochondrial Respiration Medium at 37^{o}C to allow EV secretion. Aortic tissue secreted EVs were characterised using NTA analysis. The novelty of the methods relies on the fact that only the secreted EVs from the cultured vascular tissues were isolated whereas current methods of isolating tissue derived EVs aim to isolate all EVs encapsulated in tissue cells or extracellular space. In this study, only EVs which potentially would be secreted from vascular cells and would be taken up by other cells, meaning they would participate in cellular communication, were studied.

Arch secreted EVs were visualised and quantified using Nanosight (Figure 5-7). An example Nanosight trace for arch-EVs showed that the majority of arch-EVs quantified had a size range 30-120 nm (Figure 5-7 A). Phenotype of mice or diet or the interaction of diet vs mice phenotype had no impact on arch-EV size as seen by non-significant $P_{phenotype}$, P_{diet} and $P_{interaction}$. NTA analysis of mean particle size of arch secreted EVs showed that arch-EVs did not differ in terms of size across the 4 groups of mice (Figure 5-7 B). Arch-EVs isolated from wt -HFD mice had average particle size of 106.8±4.5 nm, arch-EVs isolated from wt +HFD mice had average particle size of 109.3±10.2 nm, arch-EVs isolated from APOE KO -HFD mice had average particle size of 103±4.6 nm and arch-EVs isolated from APOE KO +HFD mice had average particle size of 107.3±3.8 nm (Figure 5-7 B). Phenotype of mice or diet had no impact on arch-EV mode size as seen by non-significant $P_{phenotype}$ and P_{diet}. Moreover, interaction of genotype vs diet had an impact on arch EV-mode size ($P_{interaction}$=0.0234). NTA analysis of mode size of arch secreted EVs showed arch-EVs from wt -HFD mice had significantly larger mode size (96.1±3.8 nm) compared to arch-EVs from APOE KO -HFD mice (78.7±3.5 nm) (*p<0.05), while the mode size of arch-EVs from wt +HFD mice (88.0±2.8 nm) was similar to the mode size of APOE KO +HFD mice (89.1±3.2 nm) (Figure5-7 C).

NTA analysis of particle concentration showed that arch-EVs isolated from wt -HFD mice had average concentration of $1.4x10^{12}$±$5.4x10^{11}$ particles/mL, arch-EVs

isolated from wt +HFD mice had average concentration of $5.4x10^{11}\pm1.3x10^{11}$ particles/mL, arch-EVs isolated from APOE KO -HFD mice had average concentration of $1.3x10^{12}\pm2.9x10^{11}$ particles/mL and arch-EVs isolated from APOE KO +HFD mice had average concentration of $1x10^{12}\pm2.6x10^{11}$ particles/mL (Figure 5-7 D). Phenotype of mice or diet or the interaction between them had no impact on concentration of arch-EVs. Particle concentration and particle size analysis as obtained from NTA data suggested that arch-EV concentration or size did not change across the 4 groups of mice indicating that HFD had no effect on the size or concentration of arch secreted EVs.

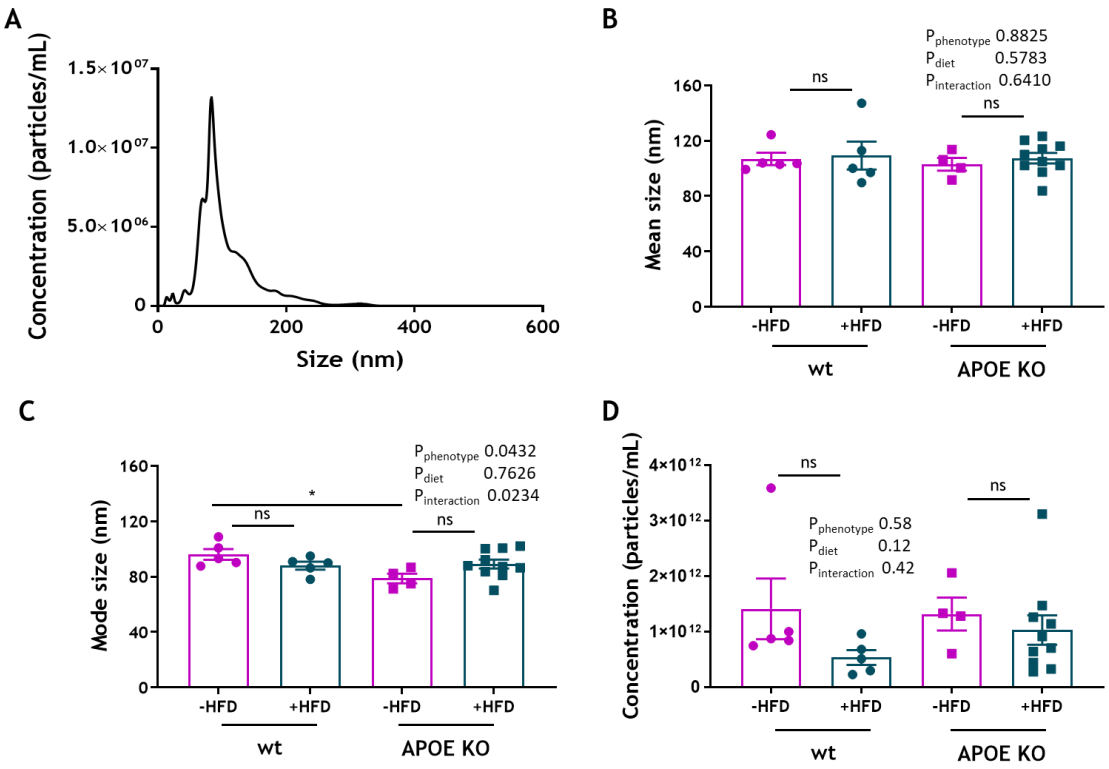

Figure 5-7 NTA analysis of arch-EVs from wt and APOE KO mice

EV samples were analysed using a NanoSight LM14. (A) Representative trace of arch-EVs produced by Nanosight showing particle size vs particle concentration. (B) NTA analysis of particle size of arch-EVs from wt mice (-HFD n=5, +HFD n=5) and APOE KO mice (-HFD n=4, +HFD n=10). (C) Modal size of arch-EVs from wt mice (-HFD n=5, +HFD n=5) and APOE KO mice (-HFD n=4, +HFD n=10). (D) NTA analysis of particle concentration of arch-EVs from wt mice (-HFD n=5, +HFD n=5) and APOE KO mice (-HFD n=4, +HFD n=10). Statistical probability of differences was calculated using Two-way ANOVA with post-hoc Tukey's test (ns= nonsignificant, *p<0.05). Data are expressed as the mean ±SEM.

Thoracic secreted EVs were visualised and quantified using Nanosight (Figure 5-8). An example Nanosight trace for thoracic-EVs showed that the majority of thoracic-EVs quantified had a size range of 30-120 nm (Figure 5-8 A). NTA analysis of mean particle size of thoracic secreted EVs showed that thoracic-EVs did not differ in terms of size across the 4 groups of mice (Figure 5-8 B). Thoracic-EVs isolated from wt -HFD mice had average particle size of 113.3±4.7 nm, thoracic-EVs isolated from wt +HFD mice had average particle size of 114.3±5.2 nm, thoracic-EVs isolated from APOE KO -HFD mice had average particle size of 112.9±2.6 nm and thoracic-EVs isolated from APOE KO +HFD mice had average particle size of 108.8±4.1 nm (Figure 5-8 B). NTA analysis of mode size revealed no difference in mode size of thoracic-EVs from wt and APOE KO mice (Figure 5-8 C). NTA analysis of particle concentration showed that thoracic-EVs isolated from wt -HFD mice had an average concentration of $2.0x10^{12}±1.8x10^{11}$ particles/mL, thoracic-EVs isolated from wt +HFD mice had average concentration of $1.6x10^{12}±3.9x10^{11}$ particles/mL, thoracic-EVs isolated from APOE KO -HFD mice had an average concentration of $1.5x10^{12}±4.1x10^{11}$ particles/mL and thoracic-EVs isolated from APOE KO +HFD mice had average concentration of $9.3x10^{11}±2.1x10^{11}$ particles/mL (Figure 5-8 D). Two-way ANOVA analysis showed that the phenotype of mice or diet or the interaction of phenotype vs diet had no impact on the size, mode and concentration of thoracic-EVs as seen by non-significant $P_{phenotype}$, P_{diet} and $P_{interaction}$. Particle concentration and particle size analysis as obtained from NTA data suggested that thoracic-EV concentration or size did not change across the 4 groups of mice indicating that HFD had no effect on size or concentration of thoracic secreted EVs.

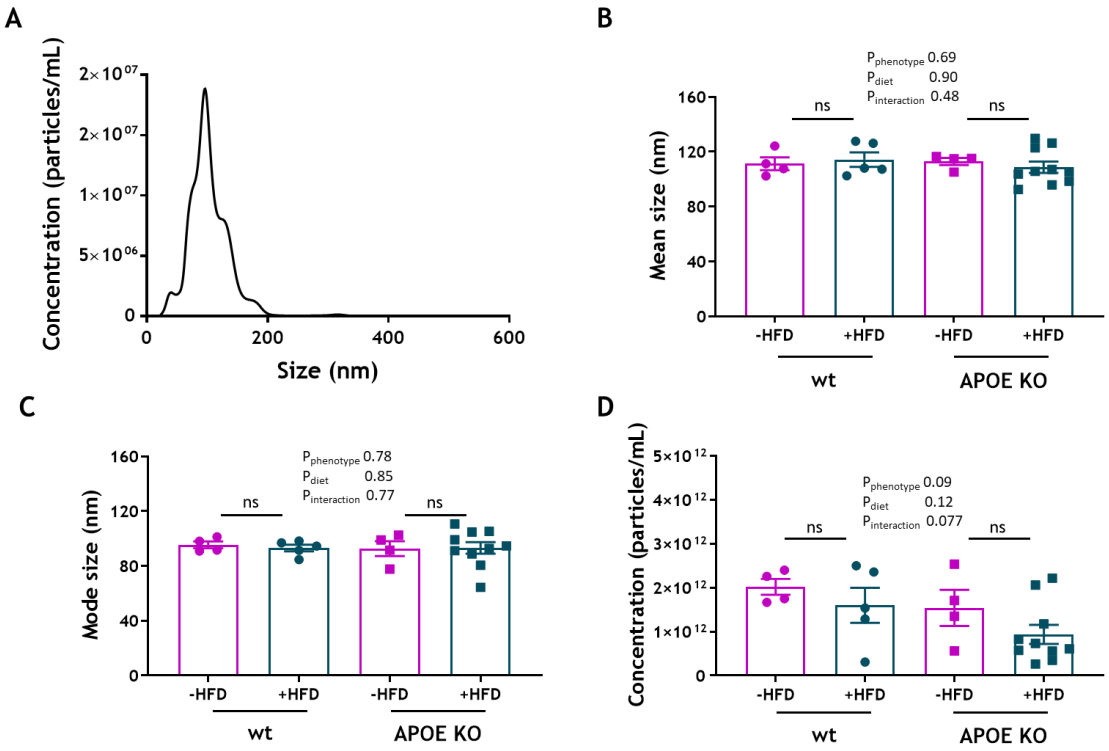

Figure 5-8 NTA analysis of thoracic-EVs from wt and APOE KO mice

EV samples were analysed using a NanoSight LM14. (A) Representative trace of thoracic-EVs produced by Nanosight showing particle size vs particle concentration. (B) NTA analysis of particle size of thoracic-EVs from wt mice (-HFD n=4, +HFD n=5) and APOE KO mice (-HFD n=4, +HFD n=10). (C) Modal size of thoracic-EVs from wt mice (-HFD n=4, +HFD n=5) and APOE KO mice (-HFD n=4, +HFD n=10). (D) NTA analysis of particle concentration of thoracic-EVs from wt mice (-HFD n=4, +HFD n=5) and APOE KO mice (-HFD n=4, +HFD n=10). Statistical probability of differences was calculated using Two-way ANOVA. Data are expressed as the mean ±SEM.

Abdominal secreted EVs from 4 groups of mice were characterised regarding their particle size and concentration. EVs were visualised and quantified using Nanosight (Figure 5-9). An example Nanosight trace for abdominal-EVs showed that the majority of abdominal-EVs quantified had a size range of 30-120 nm (Figure 5-9 A). Two-way ANOVA analysis showed the phenotype of mice or diet or interaction of phenotype vs diet have no impact on the size, mode and concentration of abdominal-EVs as seen by non-significant $P_{phenotype}$, P_{diet} and $P_{interaction}$. Analysis of NTA data showed that abdominal-EVs isolated from wt -HFD mice had average particle size of 104.1±2.8 nm, abdominal-EVs isolated from wt +HFD had average particle size of 113.3±6.0 nm, abdominal-EVs isolated from APOE KO -HFD mice had average size of 106.3±5.7 nm and abdominal-EVs isolated from APOE KO +HFD mice had average size of 106.8±3.3 nm (Figure 5-9 B). Moreover, NTA analysis of mode size showed no difference in mode size of abdominal-EVs secreted from wt and APOE KO mice (Figure 5-9 C). Regarding particle concentration of secreted abdominal EVs, NTA analysis revealed no major differences in EV concentration from 4 groups of mice (Figure 5-9 D). NTA analysis showed that abdominal-EVs isolated from wt -HFD had average concentration of $1.8x10^{12}$±$1.7x10^{11}$ particles/mL, abdominal-EVs isolated from wt +HFD mice had average concentration of $1.8x10^{12}$±$7.7x10^{11}$ particles/mL, abdominal-EVs isolated from APOE KO -HFD mice had average concentration of $1.8x10^{12}$±$7.7x10^{11}$ particles/mL and abdominal-EVs isolated from APOE KO +HFD mice found to have average concentration of $9.1x10^{11}$±$1.5x10^{11}$ particles/mL.

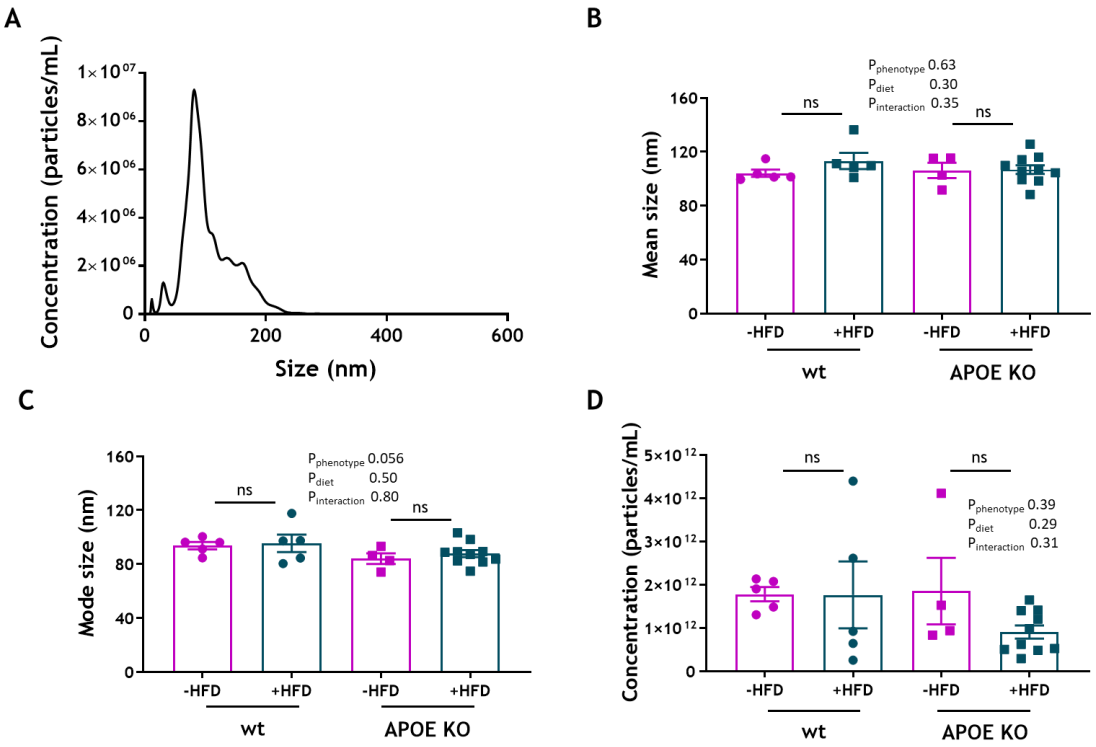

Figure 5-9 NTA analysis of abdominal-EVs from wt and APOE KO mice

EV samples were analysed using a NanoSight LM14. (A) Representative trace of abdominal-EVs produced by Nanosight showing particle size vs particle concentration. (B) NTA analysis of particle size of abdominal-EVs from wt mice (-HFD n=5, +HFD n=5) and APOE KO mice (-HFD n=4, +HFD n=10). (C) Modal size of abdominal-EVs from wt mice (-HFD n=5, +HFD n=5) and APOE KO mice (-HFD n=4, +HFD n=10). (D) NTA analysis of particle concentration of abdominal-EVs from wt mice (-HFD n=5, +HFD n=5) and APOE KO mice (-HFD n=4, +HFD n=10). Statistical probability of differences was calculated using Two-way ANOVA with post-hoc Tukey's test (ns= nonsignificant). Data are expressed as the mean ±SEM.

5.2.3 miR-125b-5p detection in serum and aortic tissue EVs from wt and APOE KO mice

After serum circulating EVs were characterised by NTA, the levels of miR-125b-5p in serum EVs from wt and APOE KO mice was quantified. In Chapter 4, miR-125b-5p was previously identified by RNA sequencing to be downregulated in SMC-derived EVs after oxLDL treatment. Serum and secreted aortic tissue EVs were spiked with a known amount of a synthetic miRNA as described in 2.4.3.1. RT-qPCR was used to quantify the levels of miR-125b-5p in serum and aortic tissue EVs.

Relative quantification revealed that HFD resulted in decreased EV-miR-125b-5p levels in serum of wt mice on high fat diet (RQ=0.30±0.73) compared to EV-miR-125b-5p levels in serum of wt mice on normal chow diet (RQ=1.0±0.43), however, no statistical significance was detected due to variability among groups (Figure 5-10 A). Regarding APOE KO mice, relative quantification showed that HFD resulted in no difference in EV-miR-125b-5p levels (RQ=0.16±0.45) compared to serum EV-miR-125b-5p levels from APOE KO -HFD mice (RQ=0.18±0.73) (Figure 5-10 A). EV-miR-125p-5p level in APOE KO mice -HFD (RQ=0.18±0.73) were reduced compared to EV-miR levels in wt mice -HFD (RQ=1.0±0.43), however no statistical significance was detected. Serum EV-miR-125b-5p levels in APOE KO mice +HFD mice were significantly reduced compared to EV-miR-125b-5p levels in wt mice on normal chow diet (*$p<0.05$). Figure 5-10 depicts relative quantification of EV-miR-125-5p levels in the 4 groups of mice normalised vs to wt -HFD group of mice. Two-way ANOVA analysis showed the phenotype of mice (as seen by $P_{pheotype}$) had an impact on the EV-miR125b-5p levels while diet and interaction of phenotype and diet had no impact on EV-miR-125b-5p levels as seen by Two-way ANOVA analysis.

The data were re-analysed in a paired manner to EV-miR-125b-5p analysis for serum EVs, for each individual mouse strain +/- HFD separately (Figure 5-10 B, C). No significant change between EV-miR-125b-5p levels in wt mice was observed (Figure 5-10 B). Moreover, high fat diet slightly reduced EV-miR-125b-5p levels in APOE KO mice (RQ=0.89±0.45) compared to APOE KO mice under chow diet (RQ=1.0±0.73), although this did not reach statistical significance (Figure 5-10 C). Overall, high fat seemed to reduce EV-miR-125b-5p levels in both mice strains, but due to variability no significance was detected.

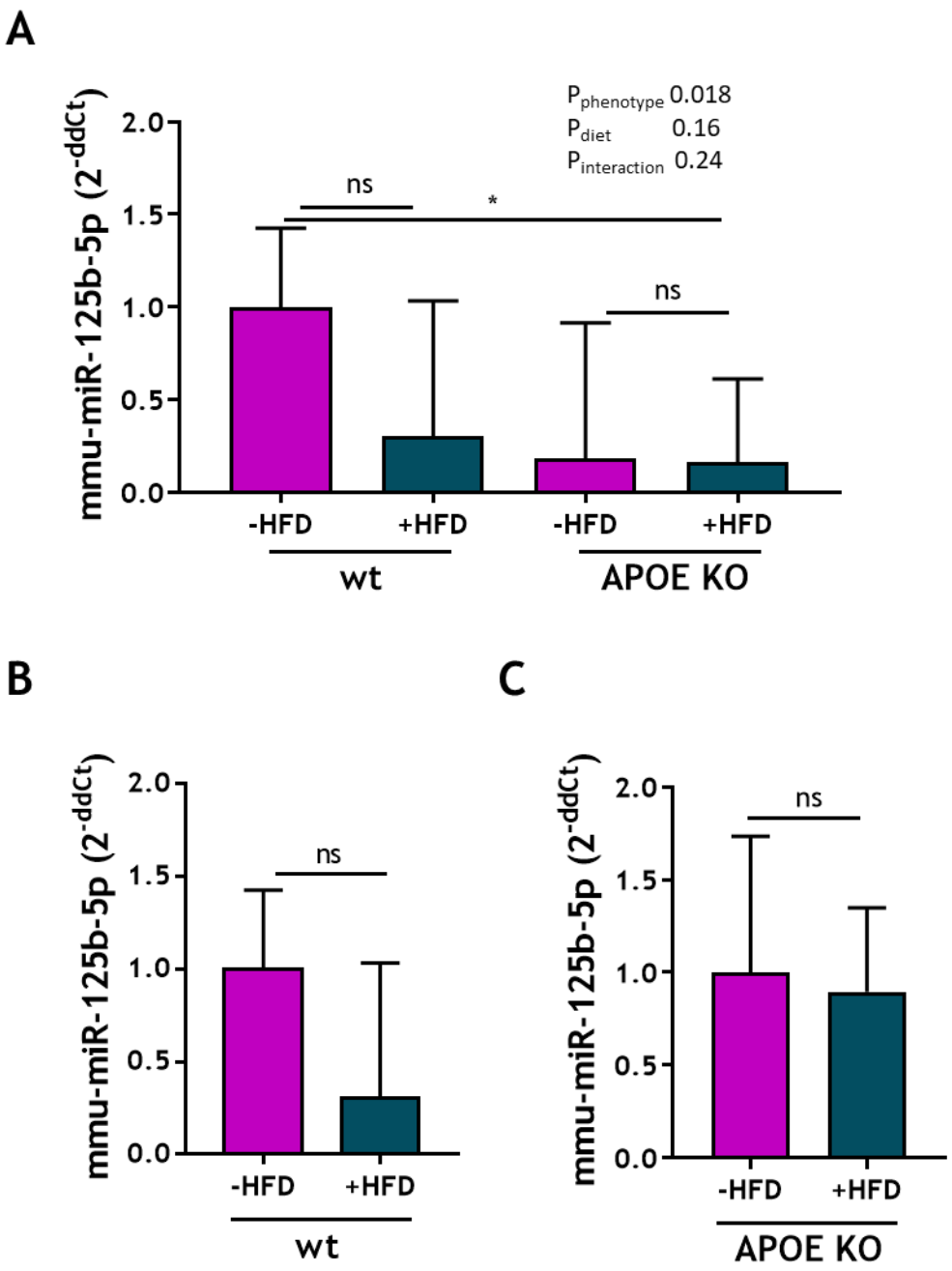

Figure 5-10 miR-125b-5p levels of serum EVs from wt and APOE KO mice

(A) miR-125b-5p levels in serum EVs from wt and APOE KO mice normalised to serum EVs from wt -HFD mice. qPCR analysis showed that in wt mice, HFD diet induced a reduction in miRNA levels on serum EVs, but no statistical significance was detected. HFD diet slightly reduced levels of EV-miR-125b-5p in APOE KO mice with no statistical significance detected. (B) miR-125b-5p levels on serum EVs from wt mice. (D) miR-125b-5p levels on serum EVs from APOE KO mice. Ct values were normalised to a spike housekeeper miRNA, cel-miR-39. Statistical probability of differences in expression observed were calculated using Two-way ANOVA with post-hoc Tukey's test (*$p<0.05$ wt -HFD vs APOE KO +HFD, ns= nonsignificant). Data are shown as RQ values ±SEM (wt -HFD n=5, wt +HFD n=5, APOE KO –HFD n=9, APOE KO +HFD n=9).

Previously, it was found that circulating EV concentration was significantly elevated in APOE KO mice under HFD. Another quantification method was used where miR-125-5p levels were normalised to the particle concentration of each sample. The analysis process is summarised in Figure 5-11. First, miR-125b-5p levels and cel-miR39-3p were measured for each sample. The particle concentration of each sample was logged, and that value was subtracted from the actual Ct value for miR-125b-5p from each sample generating a new "normalised Ct value". For RQ value quantification, the 2^{-ddCt} method was followed where the "normalised Ct" value of miR-125b-5p for each sample was used. The dCt for each sample was calculated and next the average dCt for each group was calculated e.g., wt -HFD mice.

Ct values of each sample were normalised to particle concentration as seen in Figure 5-11. The new values were plotted as seen Figure 5-12. Phenotype or diet or interaction of phenotype and diet had no effect on EV-miR-125b-5p levels (when normalised to particle concentration as seen by not significant $P_{phenotype}$, P_{diet} and $P_{interaction}$. HFD in wt mice resulted in reduced circulating levels of EV-miR-125b-5p (RQ=0.30±0.75) compared to wt mice -HFD (RQ=1.0±0.37) although this did not reach statistical significance (Figure 5-12 A, B), agreeing with previous analysis (Figure 5-10 B). When normalised to particle concentration APOE KO mice +HFD showed increased EV-miR-125b-5p levels (RQ=0.36±0.48) compared to APOE KO mice -HFD (RQ=0.24±0.73), however again this did not reach statistical significance (Figure 5-12 A). That change in EV-miR-125b-5p levels is clearly seen in Figure 5-12 C when paired comparison of APOE KO -HFD vs APOE KO +HFD mice is performed (APOE KO -HFD RQ=1.0±0.73, APOE KO +HFD RQ=1.53±0.48).

		A Concentration (particles/mL)	B Logged concentration Log (column A)	C Ct miR-125b-5p	D Ct-log C-B
wt -HFD	nr 1	15	1.2	28	26.8
	nr 2	6.4	0.8	28.2	27.4
wt +HFD	nr 3	8.5	0.9	30	29.1
	nr 4	8.4	0.9	30.2	29.3

		E Ct cel-miR-39-3p	F dCT D-F	G dCt Av Average (wt -HFD, G)	H ddCt
wt -HFD	nr 1	18	8.8	9.1	0.0
	nr 2	18	9.4		
wt +HFD	nr 3	18	11.1	11.2	2.1
	nr 4	18	11.3		

Figure 5-11 Schematic representation of data analysis process

Ct values of miR-125b-5p (column C) and cel-miR-39-39 (column E) were calculated. The concentration of each sample was included in the analysis (column A). The particle concentration of each sample was logged (column B). Then, the logged value (column B) was subtracted from the miR-125b-5p Ct value (column C), generating the "normalised Ct value" found in column D. The dCt (found in column F) was calculated by subtracting the Ct cel-miR-39-3p from Ct value in column D. The average dCt for each group of mice was calculated (column G) and RQ was generated using the 2^{-ddCt} method. No experimental values were used for the generation of this graph. These data are artificial arbitrary values purely to demonstrate the normalisation process.

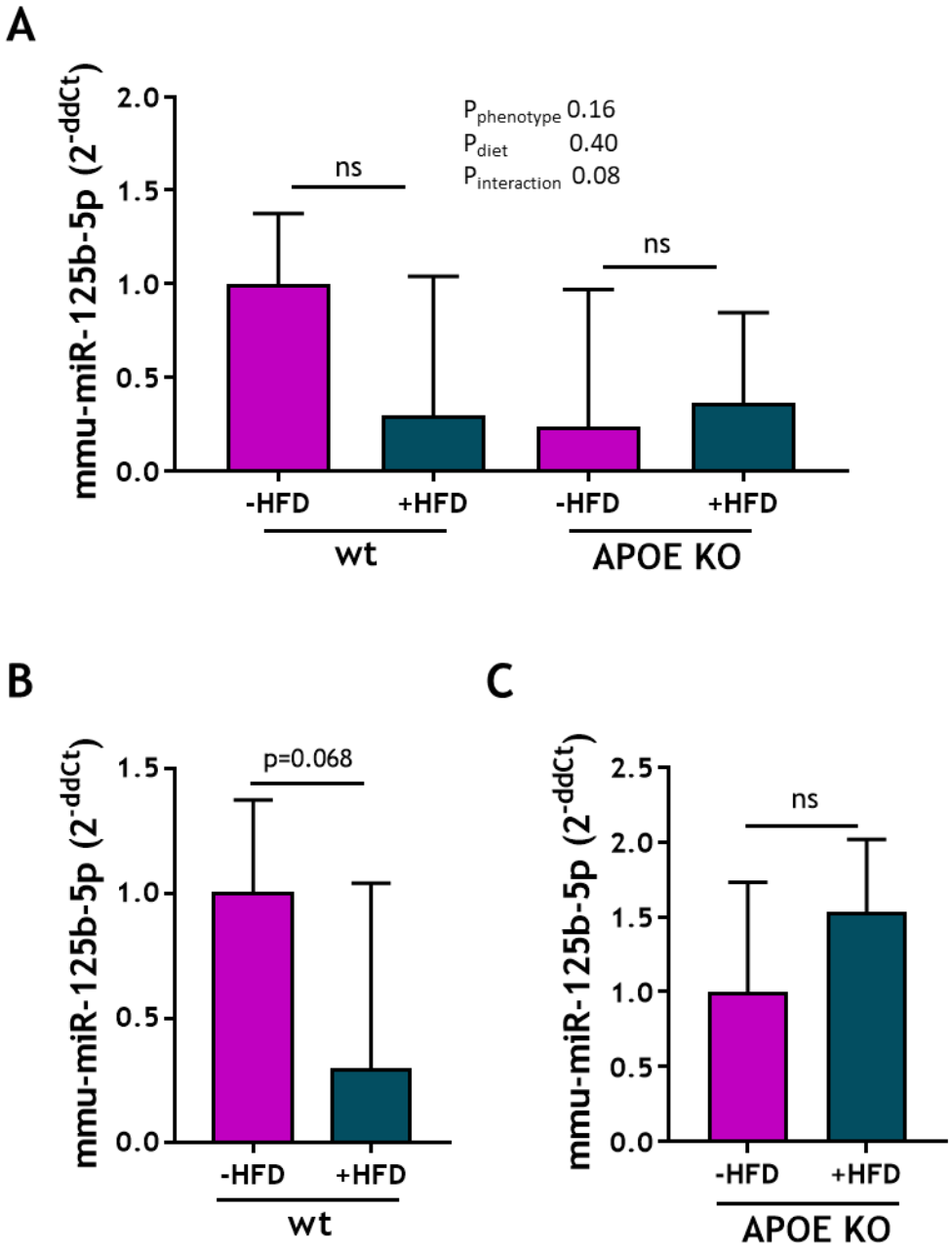

Figure 5-12 miR-125b-5p levels normalised vs particles/mL of serum EVs from wt and APOE KO mice

In this graph, the Ct values were normalised vs the particle/mL concentration of each sample. Normalised concentrations were logged and subtracted from the original Ct value of the sample. Then, normal process to quantify RQ values following the 2^{-ddCt} method was followed. (A) miR-125b-5p levels on serum EVs from wt and APOE KO mice normalised to serum EVs from wt -HFD mice. (B) miR-125b-5p levels on serum EVs from wt mice. (C) miR-125b-5p levels on serum EVs from APOE KO mice. Ct values were normalised to a spike housekeeper miRNA, cel-miR-39. Statistical probability of differences in expression observed were calculated using Two-way ANOVA with post-hoc Tukey's test (ns= nonsignificant). Data are shown as RQ values ±SEM (wt -HFD n=5, wt +HFD n=5, APOE KO –HFD n=9, APOE KO +HFD n=9).

Relative quantification of arch-EVs isolated from wt mice and APOE KO mice showed that HFD did not affect the EV-miR-125b-5p levels in wt and APOE KO mice fed either normal chow or high fat diet (Figure 5-13 A). In EVs isolated from the arch, phenotype of mice had an impact on the levels of EV-miR-125b-5p ($P_{phenotype}$=0.01). Two-way ANOVA analysis showed that diet or interaction of phenotype vs diet had no effect on EV-miR-125b-5p levels from arch-EVs. The levels of miR-125b-5p were significantly increased in APOE KO mice +HFD (RQ=7.66±0.69) compared to wt -HFD mice (RQ=1.0±0.85) (Figure 5-13 A). In EVs isolated from the thoracic aorta, only the phenotype of mice had an impact on the levels of EV-miR-125b-5p ($P_{phenotype}$=0.003). High fat diet did not significantly alter EV-miR-125b-5p levels in wt and APOE KO mice (Figure 5-13 B). Thoracic EV-miR-125b-5p levels were found significantly elevated in APOE KO +HFD mice (RQ=9.23±0.56) compared to wt -HFD mice (RQ=1.0±0.69) (*p<0.05). Regarding abdominal EVs, phenotype, diet or interaction of phenotype vs diet had no effect on EV-miR-125b-5p levels (when normalised to particle concentration as seen by not significant $P_{phenotype}$, P_{diet} and $P_{interaction}$. Relative quantification of miRNA levels in abdominal EVs shows that high fat diet did not significantly alter EV-miR-125b-5p levels in wt and APOE KO mice (Figure 5-13 C).

Finally, the levels of miR-125b-5p in arch, thoracic and abdominal EVs from APOE KO mice fed a high fat diet were examined separately (Figure 5-13 D). It was found that EV-miR-125b-5p levels did not alter between arch and abdominal secreted EVs (arch EVs RQ=1.0±0.69, abdominal EVs RQ=0.91±0.66), whereas EV-miR-125b-5p thoracic levels were found slightly elevated (thoracic EVs RQ=1.78±0.56) compared to arch and abdominal EV-miR-125b-5p levels, but this did not reach statistical significance (Figure 5-13 D).

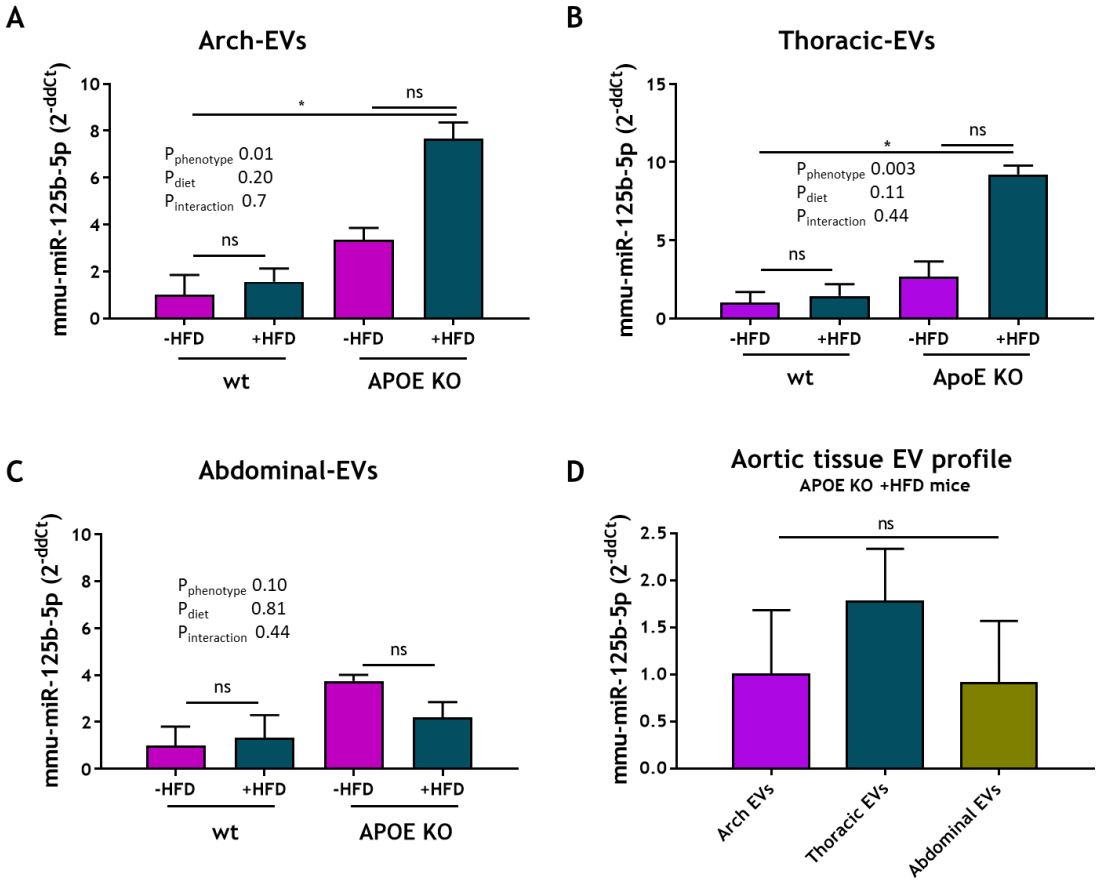

Figure 5-13 miR-125b-5p levels on secreted aortic tissue EVs from wt and APOE KO mice

(A) qPCR analysis shows that in wt mice +HFD diet does not affect the miR-125b-5p levels in arch-EVs. APOE KO +HFD mice showed increased levels of miRNA in arch–EVs with no statistical significance. (B) qPCR analysis revealed no difference in miR-125b-5p levels in thoracic-EVs in wt mice. APOE KO +HFD mice showed increased levels of miR-125b-5p in thoracic-EVs compared to –HFD group, but no statistical significance was detected. (C) qPCR analysis showed no difference in miR-125b-5p abdominal-EV levels to wt and APOE KO mice. (D) qPCR analysis of arch, thoracic and abdominal miR-125b-5p-EV level from APOE KO +HFD mice. MiR-125b-5p levels found increased in EVs secreted from thoracic aorta of APOE KO mice compared to arch and abdominal secreted EVs but no statistical significance was detected. Ct values were normalised to a spike housekeeper miRNA, cel-miR-39. Statistical probability of differences in expression observed were calculated using Two-way ANOVA with post-hoc Tukey's test (*p<0.05, wt -HFD vs APOE +HFD, ns= nonsignificant). Data are shown as RQ values ±SEM (wt -HFD n=5, wt +HFD n=5, APOE –HFD n=4, APOE +HFD n=6).

5.3 Discussion

In this chapter, circulating serum EVs from wt and APOE KO mice ±HFD were characterised. APOE KO mice under HFD had significantly increased serum EV concentration compared to APOE KO -HFD mice, wt +HFD mice and wt -HFD mice. The size of circulating EVs was not different between the 4 groups of mice. Analysis of mode size confirmed no differences in EV size across the 4 groups of mice. Secreted aortic tissue EVs were isolated from cultured aortic arch, thoracic aorta and abdominal aorta. No differences were observed regarding the size or concentration of aortic tissue EVs from wt or APOE KO mice in normal chow or high fat diet groups. Next, miR-125b-5p which was previously identified from the small RNA sequencing experiment, was analysed in serum and aortic tissue EVs. Lower expression levels of miR-125b-5p in serum EVs in both wt and APOE KO mice after HFD was observed but due to variability within the measurements no statistical significance was detected. MiR-125b-5p was also successfully detected in secreted aortic tissue EVs suggesting that cells in the vasculature may secrete EVs containing miR-125b-5p into the circulation. No changes were observed in expression levels in aortic tissue EVs between the 4 groups of mice. However, arch EV-miR-125b-5p and thoracic EV-miR-125b-5p levels were found significantly elevated in APOE KO +HFD mice compared to wt -HFD mice.

The APOE KO mouse model has been widely used to study atherosclerosis as it can spontaneously develop lesions which resemble human lesions when mice are fed standard chow diet (Nakashima et al., 1994). Female and male APOE KO mice develop lesions and can be used to study atherosclerosis (Marek et al., 2017). Marek et al., found that at 12 weeks of age both male and female APOE KO mice fed chow diet developed lesions with females having a higher percentage of lesions in the aortic arch compared to male mice (Marek et al., 2017). Another study examined the effect of age and sex on APOE KO mice fed chow diet and their ability to develop lesions (Liu et al., 2016). Interestingly, the study showed that at early age (1-2 months) sex had no impact on aortic lesion but as mice grew older (>3 months), more lesions were observed in male compared to female APOE KO mice (Liu et al., 2016). However, despite their phenotypic differences, mice of both sexes have been used in pharmacological studies for atherosclerosis treatment and studies unravelling the mechanism of the disease. Female APOE KO mice fed high fat diet have been successfully used to study the anti-inflammatory and anti-atherothrombotic properties of rosuvastatin (Monetti et al., 2007).

Another study examined the plaque stabilising effects of simvastatin on male APOE KO mice fed normal chow diet (Bea et al., 2002). Although there are some contradictory evidence regarding lesion properties between female and male APOE KO mice, research suggests that female mice can be successfully used as a mouse model for atherosclerosis.

Studies have looked at circulating levels of EVs in mice with or without atherosclerosis. Kang et al., characterised circulating EVs from C57BL/6N wt male mice under normal and HFD conditions for six months and showed that circulating EV concentration with average sizes 211.5–222.5 nm was higher in mice with atherosclerosis and suggested that EV concentration could be used as a tool for atherosclerosis detection (Kang et al., 2019). Increased circulating EV concentration was observed in mice with atherosclerosis in this study indicating that EV concentration could be used as a biomarker for disease detection. In the study presented here, the fat fed C57BL/6J APOE KO mouse model was used as the mouse model for atherosclerosis whereas Kang et al., used C57BL/6N wt male mice which were fed a HFD for 6 months (Kang et al., 2019). The findings from the study in this thesis showed that HFD did not affect the concentration of circulating EVs in wt mice, however the circulating EV concentration from APOE KO +HFD mice was significantly increased. Moreover, the average sizes of EVs isolated from the four groups of mice were between 90 and 120 nm. These differences could arise either from different isolation protocols (UC vs precipitation in our study) or maybe from the length of the diet (3 months HFD vs 6 months HFD (Kang et al., 2019)). Another difference is the substrain of mice used in two studies and that could account for some of the differences observed. Kern et al., compared the two substrains of mice, C57BL/6JRj and C57BL/6NTac, and showed that the C57BL/6J strain was protected against high fat diet induced obesity compared to C57BL/6N strain (Kern et al., 2012). Authors also observed genetic disparity between the two strains of mice which could explain the phenotypic alteration (Kern et al., 2012).

Comparison of EV concentration from wt mice and APOE KO mice under chow diet, showed that APOE KO mice had higher average EV concentration compared to wt mice. Deletion of the APOE gene affects lipid metabolism in APOE KO mice (Kuipers et al., 1996). Specifically, plasma cholesterol is reported to be 10 times higher in APOE KO mice compared to wt mice and mRNA levels and activity of

HMG-CoA reductase, a key enzyme in cholesterol biosynthesis is approximately 50% reduced in APOE KO mice (Kuipers et al., 1996). The reason for the novel observation that EV concentration is elevated in APOE KO mice fed normal chow or HFD compared to wt mice is unknown and is speculated that the difference could be due to APOE gene deletion.

Studies have focused on EVs secreted from diseased tissues as diagnostic tools or to better understand the disease pathology. The study of tissue derived EVs has gain a lot of scientific interest with studies aiming to optimise EV isolation protocols by extracting EVs from tissues (Hurwitz et al., 2019). In this study, aortic tissues were not dissected or lysed by enzymes, whereas they were cultured in media to allow EV secretion from vascular cells. A similar protocol was published where authors studied liver secreted EVs from intact cultured mouse liver or dissected liver small pieces after 48 hour incubation with culture media (Matejovič et al., 2021). Although the published protocol and the one used in this study have similarities, authors used UC for further EV isolation from cultured media whereas here SEC was used for aortic tissue EV isolation (Matejovič et al., 2021). In this study, no difference in size of secreted aortic tissue EVs was observed with EVs from aortic tissue having average sizes ranging from 90-120 nm. However, Matejovič et al., observed larger size isolated liver derived EVs (>200 nm) isolating EVs from cultured livers and smaller EVs (100-200 nm) only when liver-EVs were isolated from digested tissues (Matejovič et al., 2021). The novelty of this method as well as the one published by Matejovič et al., is that aortic tissues can be cultured *ex vivo* secreting EVs which can be characterised by NTA.

NTA analysis showed no difference in concentration of aortic tissue EVs of wt and APOE KO mice fed either chow or high fat diet. These data indicate that aortic tissue EVs release may not be disease related. One study, quantified the number of EVs present in the lymph nodes from atherosclerotic mice and showed that higher number of EVs was present in lymph nodes, isolated from lymph tissue, from mice with atherosclerosis indicating that EVs could be used as biomarkers of lymphatic dysfunction and/or for inflammatory disease progression (Milasan et al., 2016). In the paper the atherosclerotic mouse model used was female LDLR knockout mice on a C57BL/6 background fed HFD for eight weeks and compared to female C57BL/6 wt mice fed on a regular chow diet. EVs isolated from visceral adipose tissue from HFD-induced obese mice and wt mice were taken up by

macrophages and caused foam cell formation while EVs isolated from subcutaneous adipose tissue had no effect on macrophage foam cell formation (Xie et al., 2018). It was also shown that visceral adipose tissue cultures from HFD-obese mice released more EVs after 12 hours compared to subcutaneous adipose tissue cultures from lean mice (Xie et al., 2018). Another interesting finding of this study was that the systemic administration of EVs from visceral adipose tissue from HFD-induced obese mice in APOE KO atherosclerotic mice aggravated atherosclerosis by increasing lipid deposition and macrophage migration to the plaque area (Xie et al., 2018). These studies highlight the role of tissue EVs as contributors to disease pathology.

MiR-125b-5p levels were examined in serum EVs from wt and APOE mice and it was observed that HFD induced a reduction in serum EV-miR-125b-5p levels in both wt and APOE KO mice. Yerlikaya et al, showed that a 4 week HFD and high sucrose diet in male Wistar rats resulted in abnormal miRNA expression profile in the plasma with 19 miRNAs downregulated (miR-130a-3p, miR-320-3p, miR-17-5p, miR-16-5p, miR-144-3p, miR-93-5p, miR-192-5p, miR-532-5p, miR-106b-5p, miR-26b-5p, miR-208b-3p, miR-23a-3p, miR-25-3p, miR-15b-5p, miR-195-5p, miR-103-3p, miR-122-5p, miR-29b-3p and miR-30a-3p)(Yerlikaya and Öz, 2019). MiR-125b-5p was not one of the miRNAs studied. The rats were placed on HFD and high glucose diet as this contributes to hyperlipidaemia, glucose intolerance and atherosclerosis and the authors suggested that these findings would be used as diagnostic and treatment tools for HFD and high glucose related diseases (Yerlikaya and Öz, 2019). A direct comparison with the results presented here is not possible as the authors used male rats and put them under HFD and high glucose diet whereas this study used female mice which were out under HFD for 12 weeks. Another study examined the miRNA expression levels in adipose tissue from C57BL/6J wt male mice after 5 months of ±HFD (Chartoumpekis et al., 2012). Authors reported upregulation and downregulation of several miRNAs, however miR-125b-5p was not detected in that study (Chartoumpekis et al., 2012). Takanabe et al., examined the levels of miR-143 in male C57BL/6J mice under chow or HFD in mesenteric fat tissues (Takanabe et al., 2008). Authors reported significantly elevated levels of miR-143 in mesenteric fat tissues in correlation with elevated obesity parameters in mice fed HFD (Takanabe et al., 2008).A transcriptomic analysis study profiled the miRNA expression of adipocytes during adipogenesis in C57BL/6J mice under chow or HFD and found eight miRNAs

including miR-125b to be upregulated (miR-422b, miR-148a, miR-99b, miR-103, miR-30c, miR-30a-5p, miR-125b, and miR-143) and two miRNAs to be downregulated (miR-221 and miR-222) (Xie et al., 2009). These studies offer clear examples on how high fat diet may alter miRNA expression, including miR-125b, as regulators of disease development.

An interesting observation is that APOE KO -HFD mice had reduced, but no statistically significant, serum EV-miR-125b-5p levels compared to EV-miR-125b-5p levels from wt -HFD mice. NTA analysis showed that APOE KO -HFD mice had higher concentration (~ 3-fold) of serum EVs compared to wt -HFD mice. Interestingly, when normalised Ct values were used in the analysis (particle concentration of each sample was included in the 2^{-ddCt} analysis), EV-miR-125b-5p levels were still reduced in APOE KO -HFD mice, which almost reached statistical significance (p=0.068). EV-miR-125b-5p levels in APOE KO +HFD mice were also reduced compared to miRNA serum levels of wt +HFD mice, but no statistacally significant. NTA analysis of EV concentration showed increased EV concentration (12-fold) in serum of APOE KO +HFD mice compared to wt +HFD mice. When the normalised Ct values were used in the analysis, EV-miR-125b-5p serum levels of APOE KO mice were found to be higher. EV-miR-125b-5p levels were found reduced in APOE KO +HFD mice compared to APOE -HFD mice. Again, EV concentration of APOE KO +HFD was found significantly increased (~6-fold) compared to APOE KO -HFD mice and when the data was normalised to particle concentration, increased EV-miR-125b-5p levels in APOE KO +HFD mice compared to miRNA levels from APOE KO-HFD mice remained. It seems that in some comparisons, the method of quantification could affect the data interpretation, however there is no clear reason why the method of data quantification altered the miR-125b-5p expression levels in serum EVs from APOE KO +HFD mice and did not affect miR-125b-5p expression in APOE KO -HFD mice. One possible explanation could be the fold change in EV concentration. When the EV concentration exhibits 3-fold change, it seems that EV concentration does not affect EV-miR-125b-5p levels. However, when the changes in EV concentration between groups are ≥ 6-fold, Ct value normalisation to particle concentration seems to affect EV-miR-125b-5p expression levels. However, a more detailed mathematical model is required to support this observation. It is evident that some other factor apart from particle concentration may contribute to the change of miR-125-p expression pattern but this requires further investigation.

MiR-125b-5p levels from aortic tissue EVs were also examined. EV-miR-125b-5p expression had a tendency to increase after HFD in wt mice, however there were no statistically significant differences. In APOE KO mice, HFD showed increased levels of miR-125b-5p in arch and thoracic EVs, but again this was not statistically significant. In abdominal EVs, miR-125b-5p was found to be reduced in abdominal EVs of APOE KO +HFD mice compared to miRNA levels from APOE KO -HFD mice, but no statistically significant. Although no significant differences were observed in miR-125b-5p expression of aortic tissue EVs, these studies suggest that a cell type or cell types in the vasculature package miR-125b-5p into EVs which are secreted from vascular tissues. Mir-125b-5p is highly expressed in vascular cells such as murine ECs and SMCs (Li et al., 2010)(Hueso et al., 2022). MiR-125b-5p expression in murine aortas has been confirmed too (Hueso et al., 2016). Qiao et al., showed that EVs isolated from supernatant of KLF2 transduced HUVECs were enriched in miR-125b-5p (Qiao et al., 2020). Another study profiled the miRNA cargo of EVs isolated from HCASMCs from atherosclerotic plaque segments and non-atherosclerotic areas of coronary artery media layers from patients undergoing cardiac transplantation (de Gonzalo-Calvo et al., 2017). Among other miRNAs, authors confirmed that HCASMC derived EVs were packaging miR-125b-5p (de Gonzalo-Calvo et al., 2017). A study profiled miRNA cargo of MSCs-EVs derived from cord blood and adipose tissue and identified miR-125b-5p to be packaged in EVs derived from adipose tissue (Nazari-Shafti et al., 2020). These data support our observations that miR125b-5p is secreted from the vasculature packaged into EVs.

MiR-125b-5p levels in aortic tissue EVs from APOE KO +HFD mice were plotted separately. MiR-125b-5p levels from thoracic EVs appeared increased compared to miR-125b-5p levels from arch and abdominal EVs with no statistical significance being detected. EV-miRNAs have been studied as mediators of disease progression. MiRNA sequencing profiles of EVs isolated from abdominal aortic aneurysm tissues have been found to be enriched in miRNAs which were involved in cellular signalling of aneurysm progression (Botts et al., 2022). A cohort study examined the effects of adipose-tissue-derived EVs from obese and lean subjects on cholesterol efflux from macrophages *in vitro* (Barberio et al., 2019). The study showed that EVs from obese subjects showed reduced cholesterol efflux and identified six miRNAs (miR-3129-5p, miR-20b, miR-320d, miR9-5p, miR301a-5pm and miR-155-5p) in adipocyte serum EVs that participate in cholesterol efflux via

ABCA1 regulation (Barberio et al., 2019). These studies highlight the importance of tissue EV-miRNAs in the disease pathology.

5.4 Summary

The findings presented here show that APOE KO mice, with experimental atherosclerosis, had significantly increased EV concentration compared to APOE KO -HFD mice, wt +HFD mice and wt -HFD mice. These data indicate, possibly, that cells from plaques release higher number of EVs. However in this thesis, serum EVs were examined instead of EVs directly secreted from plaques. Further experiments directly characterising EVs released from plaques are required to support this hypothesis. The size of circulating EVs was unchanged among the 4 groups of mice. NTA size and EV concentration of aortic tissue EVs (arch, thoracic and abdominal EVs) revealed no differences regarding their size or concentration. Detection of miR-125b-5p in serum EVs showed that HFD induced lower expression of miR-125b-5p, although no statistically significant, in wt and APOE KO mice. A different approach where Ct values were normalised to particle concentration was used and it was found that in wt mice, HFD induced lower expression of EV-miR-125b-5p levels, but it was shown that in APOE KO mice, HFD induced higher expression levels of EV-miR-125b-5p, but no statistically significant. MiR-125b-5p was also detected in EVs secreted from cultured aortic tissue suggesting that miR125 is packaged into EVs from cells in the vasculature but no significant changes in miRNA expression levels in the tissue EVs from the 4 groups of mice were observed.

Chapter 6 Investigating the functional role of miR-125b-5p in SMCs and ECs

6.1 Introduction

Research focuses on finding new therapies for atherosclerosis and miRNA and anti-miRNA based therapies have been studied extensively. For example, tail vein injections of miR-181b-5p twice a week for 4 weeks or once a week for 12 weeks to APOE KO mice fed a HFD produced a 25% reduction in lesion size at the aortic sinus and approximately 40% reduction of lesion size in the descending thoracic and abdominal aorta (Sun et al., 2014). Authors suggested that miR-181b-5p systemic delivery inhibited gene expression of importin-α3 resulting in reduced nuclear translocation of NF-κB in vascular endothelium and thus reducing the expression of pro-inflammatory genes (Sun et al., 2014). A transfection agent, lipofectamine™, was used for the purpose of that study which allows the formation of liposome around the nucleic acid and allowing them to be taken up by the cells. Another study used synthetic lipid nanoparticles coated with cationic lipids and a peptide VHPK to target VCAM1, as vectors for successful delivery of an anti-miRNA (Kheirolomoom et al., 2015). Cationic coating was used to enhance the escape of anti-miRNA from the lysosomal compartment and efficient anti-miRNA delivery to ECs *in vitro* and *in vivo* (Gujrati et al., 2014)(Kheirolomoom et al., 2015). Nanoparticles loaded with anti-miR-712 were injected intravenously to a partial carotid ligation model of atherosclerosis using APOE KO mice fed a HFD (Kheirolomoom et al., 2015). Partial ligation of left carotid artery (LCA) involved the ligation of 3 out 4 branches of the LCA including the external carotid artery, internal carotid artery, and occipital artery while the superior thyroid artery remained open (Nam et al., 2009). This model leads to disturbed flow and shear stress in the artery wall resulting in endothelial dysfunction and atherosclerosis in the LCA (Nam et al., 2009). Authors observed that mice treated with anti-miR-712 loaded nanoparticles showed significant downregulation of miR-172 in the LCA which was previously upregulated due to disturbed flow in the artery, reduced expression of mR-172 target genes in the vascular endothelium, including tissue inhibitor of metalloproteinase 3 (TIMP3) and reversion-inducing-cysteine-rich protein with kazal motifs (RECK), and significant reduction in lesion development (Kheirolomoom et al., 2015). Another study showed that intravenous delivery of miR-126-5p loaded nanoparticles attenuated atherosclerosis progression in APOE KO mice fed a HFD via the inhibition of delta like non-canonical Notch ligand 1 (DLK1) and rescued EC proliferation caused by disturbed flow in the artery wall (Schober et al., 2014).

EVs, as natural occurring particles, have gained a lot of attention as drug delivery systems. Electroporation is a popular method of loading EVs with potential therapeutic cargo including nucleic acids and drugs. An electric pulse creates small pores in the EV membrane and enhances permeability (Fu et al., 2020). The efficiency of electroporation can be affected by the use of voltage, the length of the pulse or the amount of EVs being electroporated (Pomatto et al., 2019). Wahlgren et al., showed that plasma EVs could be successfully loaded with a siRNA via electroporation and could deliver the siRNA to recipient monocytes and lymphocytes with the result of silencing the mitogen-activated protein kinase 1 gene (Wahlgren et al., 2012).

Pathway hypothesis, (Chapter 4), suggested that miR-125b-5p regulates cell survival and proliferation via transcriptional regulation of target genes including TP53, STAT3, ERBB2, ERBB3, SP1 and PPP1CA. Cell death and proliferation are processes associated with atherosclerosis development (Bennett et al., 2016). SMC phenotypic switching towards a proliferative and migrating phenotype, or a pro-atherogenic phenotype, has been considered a fundamental step during early atherogenesis (Bennett et al., 2016). Increased SMC cell proliferation has been observed in early atherosclerosis and upon vascular injury (Bennett et al., 2016). Lineage tracking studies have shown that the majority of plaque cells are derived from proliferating local SMCs (Majesky, 2007). The presence of SMCs in the fibrous cap suggested that SMC migration is an important factor in disease progression (Bennett et al., 2016). Cell apoptosis in atherosclerotic plaques has been studied extensively, with studies suggesting increased cell death in advanced lesions (Bennett et al., 1995)(Lutgens et al., 1999)(Bennett et al., 2016). Increased SMC apoptosis has been also implicated in plaque rupture (Clarke et al., 2008). Clarke et al., showed that SMC apoptosis during early atherogenesis or advanced plaques resulted in acceleration of disease progression (Clarke et al., 2008). Chronic apoptosis also induced calcification in early and advanced plaques (Clarke et al., 2008).

Cell death of ECs also contributes to atherosclerosis progression (Choy et al., 2001). Such events would have detrimental effects on the disease pathology by increasing endothelial permeability to molecules and cells including lipids and monocytes and advancing the plaque development (Choy et al., 2001).

Furthermore, increased EC apoptosis has been observed in atheroprone areas of the vasculature (Gerrity et al., 1977)(Heo et al., 2011).

In the present study, modulation of miR-125b-5p levels in SMC-EVs through electroporation was investigated to examine if miR-125b-5p transfer via EVs could affect recipient HCASMC cell viability, proliferation and migration through transcriptional regulation of target pathway genes. A wider role for miR-125b-5p delivered by EVs was explored in studying recipient HCAEC cell viability. Small RNA sequencing (Chapter 4) revealed the downregulation of miR-125b-5p in SMC-EVs after oxLDL treatment. For these studies, the increase of miR-125b-5p levels loaded into EVs was chosen to force the expression pattern in the opposite way.

6.1.1 Aims

- Optimise miRNA loading into EVs and delivery to recipient cells.
- Characterise miR-125b-5p loaded EVs after electroporation.
- Investigate the effects of miR-125b-5p-EVs on recipient HCASMC cell viability and serum induced HCASMC proliferation.
- Investigate the effects of miR-125b-5p-EVs on recipient serum induced HCASMC migration.
- Investigate if miR-125b-5p-EVs regulate gene expression of genes identified by the bioinformatic analysis.
- Investigate the effects of miR-125b-5p-EVs on recipient HCAEC cell viability.

6.2 Methods

6.2.1 Working EV concentrations

The initial EV working concentration for all electroporation experiments was devised by Antoniya Pashova (University of Glasgow) while optimising the miRNA loading in EVs via electroporation. For a 24 well plate, $5.7x10^9$ particles per well were used. Using $5.7x10^9$ particles as a reference concentration, the amount of particles per cm^2 of surface area was calculated ($3x10^9$ particles per cm^2) and was used to calculated EV concentration for future experiments.

In all experiments in this chapter EV treatment was performed in SF media unless co-stimulation with FCS was stated.

Table 6-1 Working EV concentrations for electroporated EVs

Plate	EV concentration (Particles/well)	Particles per cm^2
96 well plate	$1x10^9$	
24 well plate	$5.7x10^9$	$3x10^9/cm^2$
12 well plate	$1.5x10^{10}$	

6.2.2 Data normalisation method

A method to normalise data was suggested by statistician Dr John McClure (School of Cardiovascular and Metabolic Heath, University of Glasgow) to reduce donor to donor variability. Experimental data regarding MTT cell viability and BrdU cell proliferation were normalised via this method. The analysis process is summarised in Figure 6-1. Figure 6-1 depicts triplicate absorbance values for each group for one experiment (each OD value corresponds to one well of the group). First, the average value of the blank sample was calculated (column B) and that value was subtracted from the OD value from each group (column C). The average of all absorbance values from all groups except the blank was calculated (column D). The average absorbance per group was calculated in column E. The normalised absorbance value (column F) generated from the 3 wells per condition was calculated by dividing the average absorbance of each group (column E) with the average of all absorbance values for all groups (column D). The normalised absorbance value or OD value was used to graph cell viability and cell proliferation assays in this chapter.

	A			B	C			D	E	F
	OD			Av Blank	OD-BL			Average of C Av of all OD-BL	Average of each sample	Normalised OD values E/D
	A1	A2	A3		A1-B	A2-B	A3-B			
Control	0.5	0.5	0.5		0.4	0.4	0.4	0.4	0.4	1
10% FCS	0.8	0.8	0.8		0.7	0.7	0.7		0.7	1.75
Naive-EVs	0.4	0.4	0.4		0.3	0.3	0.3		0.3	0.75
miR-125b-5p-EVs	0.3	0.3	0.3		0.2	0.2	0.2		0.2	0.5
Blank	0.1	0.1	0.1	0.1						

Figure 6-1 Schematic representation of data normalisation process

Triplicate absorbance or OD values per group are presented here. The average value for blank sample was calculated (column B). The average blank value was subtracted from all the absorbance values (column C). Column D represents the average of all absorbance values from all the groups. The average absorbance value for each group (column E) was calculated using the triplicate values in column C. The normalised absorbance or OD value was generated by dividing the value in column E by the value in column D. No experimental values were used for the generation of this graph. These data are artificial arbitrary values purely to demonstrate the normalisation process.

6.3 Results

6.3.1 Optimisation of miRNA loading in EVs and miRNA-EV transfer to recipient HCASMCs

MiRNA loading in EVs via electroporation was performed as described in 2.5.5. EVs were generated from HCASMCs as described in 2.5.1. For the purposes of these experiments, only Control-EVs were generated and isolated as described previously. EV populations were electroporated as described previously in 2.5.5 and two new EV populations generated, Naive-EVs and cel-miR-39-3p-EVs. A miRNA originating from Caenorhabditis elegans was chosen for optimisation studies as it would be easier to follow the miRNA loading into EVs and uptake in recipient cells without confounding factors of endogenous levels of miRNA. NTA was used to estimate size and concentration of EV populations. To validate the success of the electroporation, levels of cel-miR-39-3p were measured in Naïve and cel-miR-39-3p-EVs by qPCR. qPCR analysis showed that electroporation was successful as cel-miR-39-3p levels were 2684.6 higher fold in cel-miR-39-3p-EVs compared to Naïve-EVs (Figure 6-2).

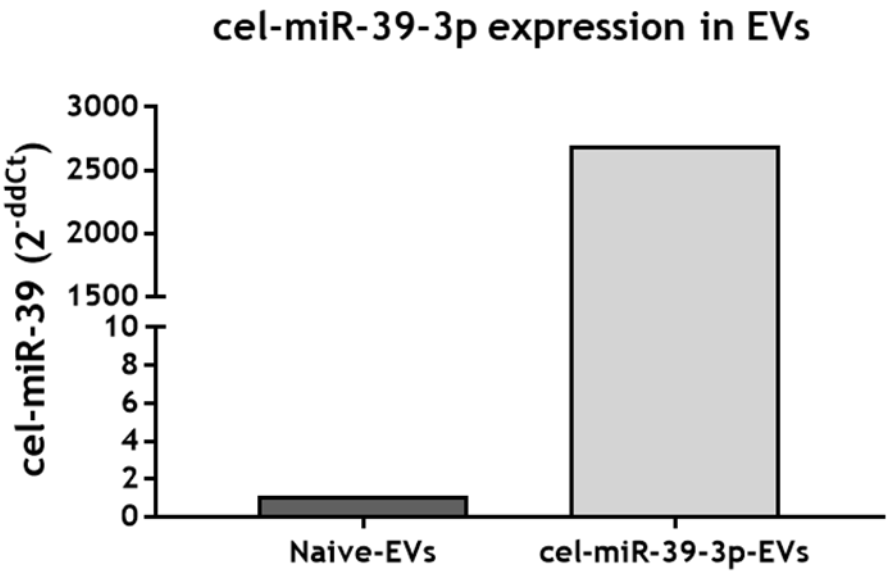

Figure 6-2 Loading of EVs with cel-miR-39-3p via electroporation

qPCR analysis confirms that cel-miR-39-3p is overexpressed in EVs after electroporation. Ct values were normalised to a spike housekeeper miRNA, ath-miR159a. Data are shown as RQ values ± SEM (n=1 patient).

HCASMCs were seeded into a 24 well plate cultured until confluent, and then quiesced for 48 hours in SF media. Next, they were treated with Naïve-EVs and cel-miR-39-3p-EVs ($5.7x10^9$ particles per well) for 6 hours and 24 hours, respectively. Cel-miR-39-3p transfer to recipient HCASMCs was examined by RT-qPCR, as described in 2.4.3. After 6 hr cel-miR-39-39-EV treatment, cel-miR-39-3p expression in recipient cells was increased (RQ=23.56±0.53) compared to Naïve-EV treated cells (RQ=1.0±0.63), indicating that EVs could transfer cel-miR-39-3p to recipient HCASMCs (Figure 6-3 A). After 24 hr cel-miR-125b-3p-EV treatment, cel-miR-39-3p expression remained increased (RQ=12.81±0.13) compared to Naïve-EV treated cells (RQ=1.0±0.02), indicating that cel-miR-39-3p was stably expressed for at least 24 hours following EV transfer (Figure 6-3 B).

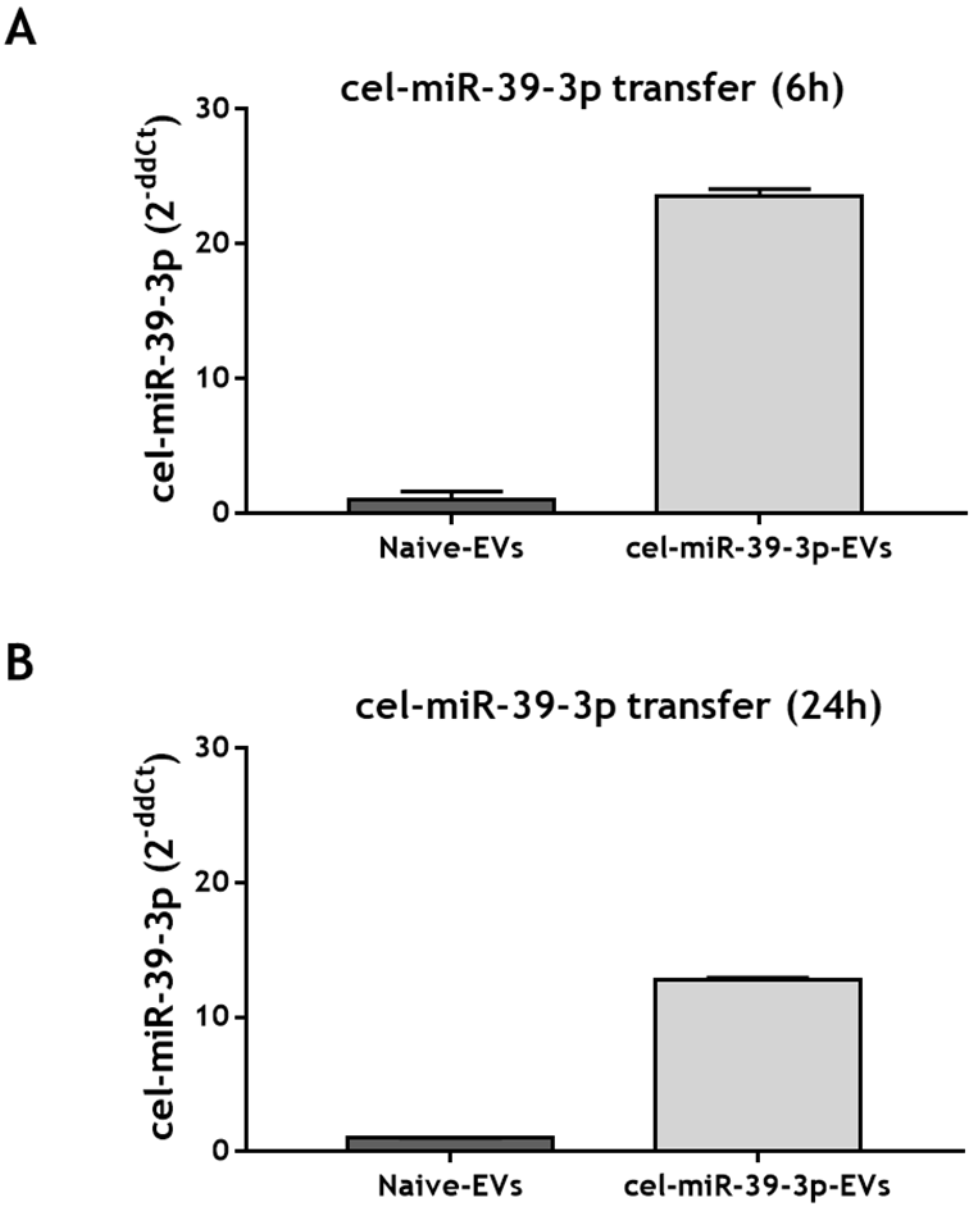

Figure 6-3 Transfer of cel-miR-39 via EVs to recipient HCASMCs

HCASMCs were quiesced for 48 hours before EV treatment. (A) qPCR analysis detected increased expression of cel-miR-39-3p to cells treated with cel-miR-39-EVs compared to cells treated with Naïve-EVs after 6 hours. (B) qPCR analysis detected increased expression of cel-miR-39-3p to cells treated with cel-miR-39-EVs compared to cells treated with Naïve-EVs after 24 hours. Ct values were normalised to an endogenous housekeeper miRNA, RNU48. Data are shown as RQ values ± SEM (n=2 replicates, 1 patient).

Next, the same approach was used to assess whether miR-125b-5p could be loaded into SMC-EVs via electroporation (Figure 6-4). QPCR analysis showed that miR-125b-5p was successfully loaded into EVs via electroporation as miR-125b-5p levels were significantly elevated by 2232-fold in miR-125b-5p-EVs (RQ=2232.03±0.44) compared to Naïve-EVs (RQ=1.0±0.56) (Figure 6-4).

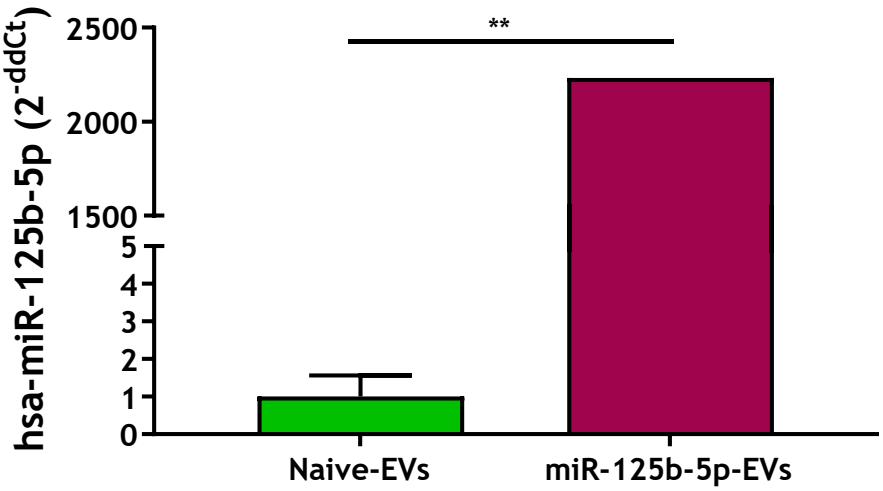

Figure 6-4 miR-125-5p loading in SMC-EVs

QPCR analysis confirmed that miR-125b-5p was overexpressed in miR-125b-5p-EVs. Ct values were normalised to a spike housekeeper miRNA, ath-miR159a. Statistical probability of differences in expression observed were calculated using paired Student's t-test (n=3 patients, vs Naive-EVs **p<0.01). Data are shown as RQ values ±SEM.

6.3.2 Characterisation of miR-125b-5p loaded EVs

Next, Naive-EVs and miR-125b-5p-EVs, were characterised in terms of size and concentration using NTA analysis, total protein quantification and EV markers were detected in EV populations by western immunoblotting.

An example NTA trace for Control-EVs before electroporation showed that the majority of EVs had a size range 30-150 nm and concentration of $2x10^7$ particles/mL (Figure 6-5 A). Next, Control-EV sample was divided into two equal fractions for electroporation (Naïve-EVs, miR-125b-5p-EVs). A NTA trace for Naive-EVs showed that the majority of EVs quantified had a size range 30-150 nm and concentration of $6x10^6$ particles/mL (Figure 6-5 A). An example Nanosight trace for miR-125b-5p-EVs showed that the majority of EVs quantified had a size range 30-150 nm and concentration of $6x10^6$ particles/mL (Figure 6-5 A). NTA traces of Naïve-EVs and miR-125b-5p-EVs had half the particle concentration compared to Control-EVs indicating that electroporation did not reduce the expected concentration of EVs. NTA analysis of mean particle size showed that electroporation had no significant effect on the size of EVs (Naive-EVs: 137.8±12.7 nm, miR-125b-5p-EVs: 134.5±7.2 nm) (Figure 6-5 B). NTA analysis of mode size confirmed there were no significant differences in size (Naïve-EVs: 116.2±6.4 nm, miR-125b-5p-EVs: 112.2±8.4 nm) (Figure 6-5 C). NTA analysis of particle concentration showed no significant difference in particle concentration; Naive-EVs: $3.3x10^{11}$±$1.4x10^{10}$ particles/mL, miR-125b-5p-EVs: $3.3x10^{11}$±$7.3x10^{10}$ particles/mL (Figure 6-5 D).

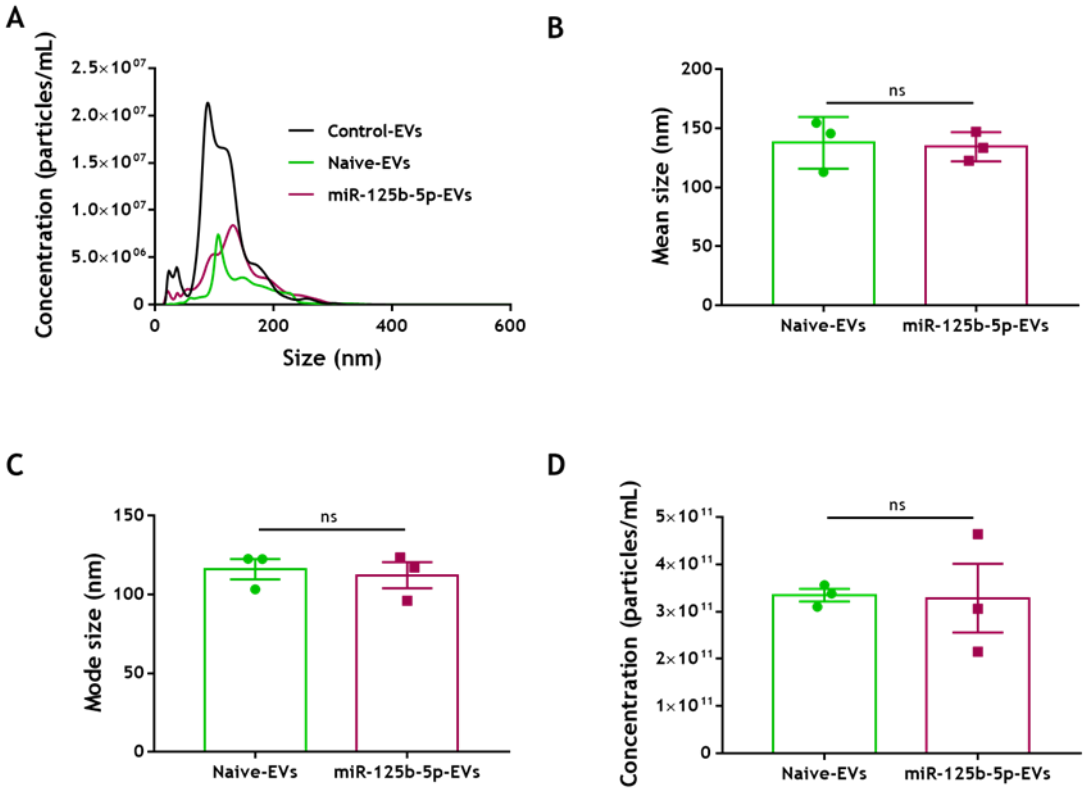

Figure 6-5 NTA Characterization of EV populations derived from HCASMC after electroporation

(A) Representative NTA trace for Control-EVs before electroporation, Naïve-EVs and miR-125b-5p-EVs after electroporation, produced by NTA showing particle size vs particle concentration. The black line corresponds to a representative trace for Control-EVs, the green line corresponds to a representative trace for Naïve-EVs, and the purple line corresponds to a representative trace for miR-125b-5p-EVs. (D) NTA analysis of particle size of EV samples (n=3 patients). (C) NTA analysis of mode size of EV samples (n=3 patients). (D) NTA analysis of particle concentration (n=3 patients). Statistical probability of differences was calculated using paired Student's t-test (ns= nonsignificant). Data are expressed as the mean ±SEM.

Micro BCA assay was used to determine protein concentration for Naive-EVs and miR-125b-5p-EVs derived from HCASMCs (Figure 6-6 A). Naïve-EVs were found to have an average concentration of 285.8±11.0 µg/mL whereas miR-125b-5p-EVs were found to have an average concentration of 604.4±10.9 µg/mL. The reason for this observation is not clear. Next, EV marker detection was performed using western immunoblotting with HCASMC lysate used as a positive control. CD81 was found to be enriched in both Naive and miR-125b-5p-EVs with an apparent molecular mass of 20 kDa (compared to manufacturer's guidance of 22-26 kDa) (Figure 6-6 B). In both EV populations, Annexin A2 was also detected with a molecular weight of 35 kDa (Manufacturer's guidance: 34-26 kDa) and CD63 was detected with an apparent molecular weight of 30-60 kDa (Manufacturer's guidance: 30-60 kDa) (Figure 6-6 B).

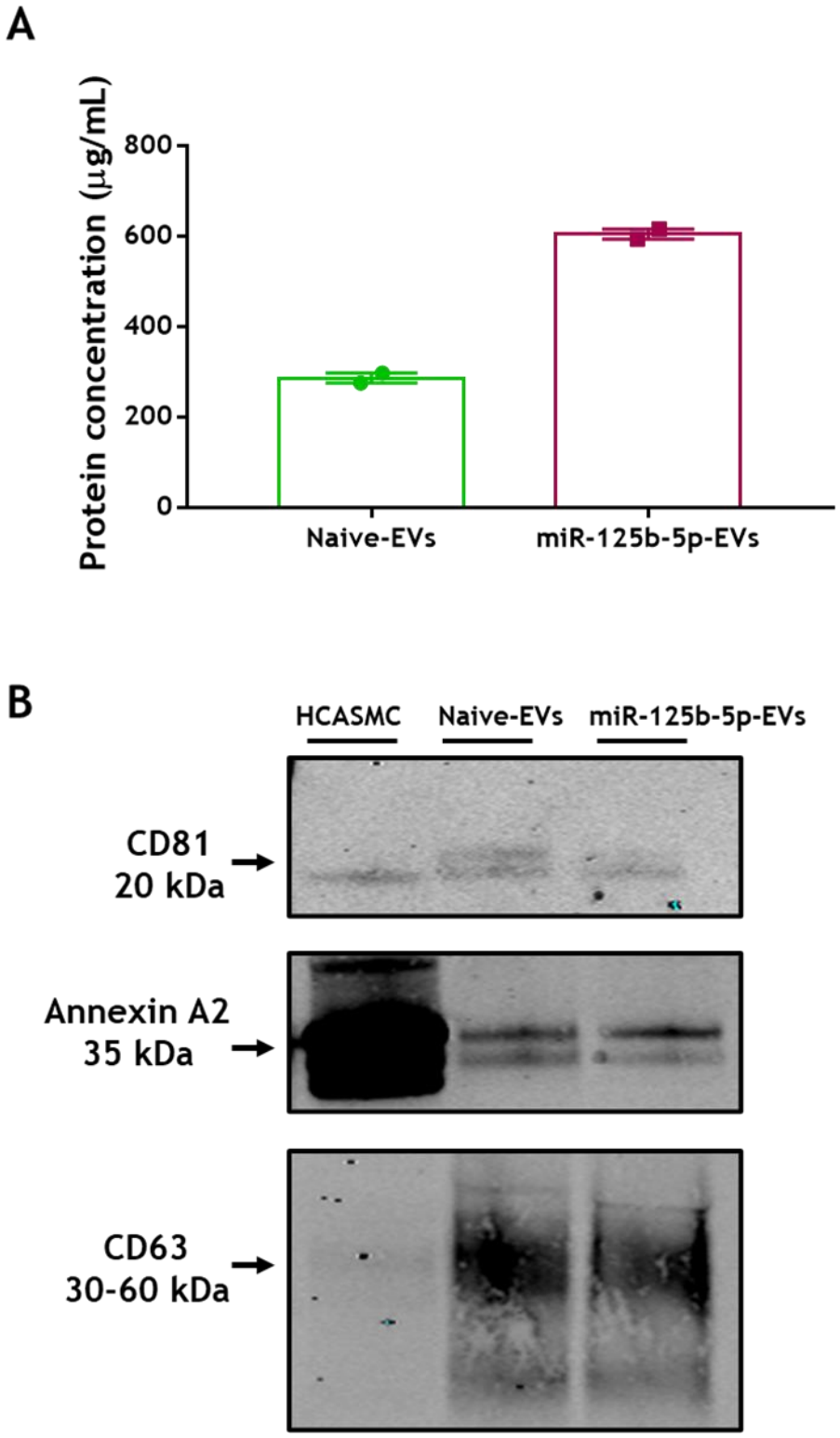

Figure 6-6 Analysis of electroporated SMC-EV protein by western immunoblotting

(A) Comparison of protein concentration of Naïve and miR-125b-5p-EVs (n=2 patients). (B) Detection of EV-markers CD81, Annexin A2 and CD63 on electroporated EV population derived from HCASMC (n=1 patient for all EV markers). HCASMC cell lysate was used as positive control. Data are expressed as the mean ±SEM.

6.3.3 Effects of miR-125b-5p-EVs isolated from SMCs on recipient SMC cell viability and serum induced HCASMC proliferation

MiR-125b-5p-EV effect on recipient HCASMC cell viability was investigated. HCASMCs were seeded into a 96 well plate, quiesced for 48 hours in SF media and then treated either with SF media (control), 10% FCS, Naïve-EVs or miR-125b-5p-EVs ($1x10^9$ particles per well) for 24 hours and cell viability measured using the CyQUANT™ MTT Cell Viability Assay. Significantly increased cell viability was observed after the 10% FCS treatment (% viable cells 181.2±0.1) compared to all groups (control cells: % viable cells 100.0±0.1, **p<0.01, Naïve-EVs: % viable cells 112.7±0.1, *p<0.05, miR125b-5p-EVs: % viable cells 116.5±0.1, *p<0.05).. No difference in cell viability following either Naïve or miR-125b-5p-EV treatment was detected (Figure 6-7). Since MTT Assay does not directly measure proliferation, next BRdU assay was investigated.

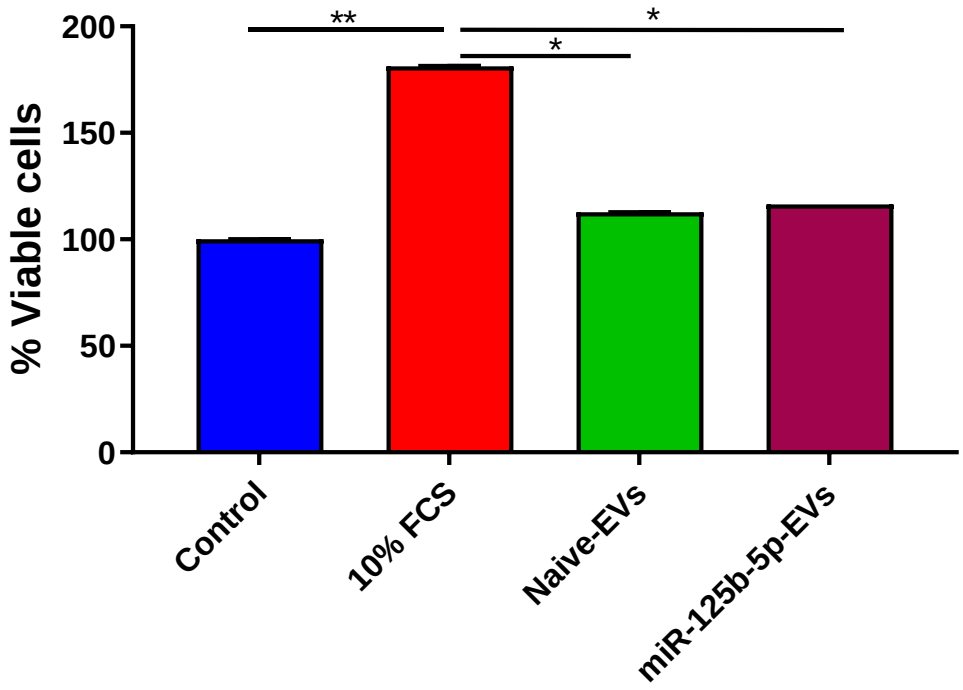

Figure 6-7 Effect of miR-125b-5p-EVs on HCASMC cell viability

HCASMCs were quiesced for 48 hours and then treated with 10% FCS or Naïve-EVs or miR-125b-5p-EVs in SF media for 24 hours. Cell viability was measured using the CyQUANT™ MTT Cell Viability Assay. Statistical probability of differences was calculated using RM One-way ANOVA with post-hoc Tukey's test (n=3 patients, **p<0.01 Control vs 10% FCS, *p<0.05 10% FCS vs Naïve-EVs, *p<0.05 10% FCS vs miR-125b-5p-EVs). Data are expressed as the mean of % Viable cells ±SEM.

HCASMCs were seeded into a 96 well plate and quiesced for 48 hours in SF media. A lower concentration of FCS stimulation was chosen to enable assessment of whether miR-125b-5p treatment would stimulate or inhibit proliferation induced by 5% FCS. Cells were stimulated with 5% FCS, or Naïve-EVs + 5% FCS or miR-125b-5p-EV + 5% FCS (in SF media for 24 hours). The 5% FCS treatment displayed significantly increased BrdU incorporation (1.4±0.08) compared to control treated cells (0.5±0.1) indicating enhanced cell proliferation (***$p<0.001$)(Figure 6-8). Naïve-EVs + 5% FCS treated cells showed significant increasing BrdU incorporation (1.3±0.0.08) compared to control treated cells (**$p<0.01$), indicating increased cell proliferation. Naïve-EVs + 5% FCS treated cells also displayed similar BrdU incorporation levels compared to 5% FCS treated cells. MiR-125b-5p-EVs + 5% FCS treated cells displayed significant reduced BrdU incorporation (0.7±0.3) compared to 5% FCS treatment (*$p<0.05$), indicating that miR-125b-5p-EVs treatment reduced serum induced cell proliferation (Figure 6-8). However, miR125b-5p-EVs + 5% FCS treatment showed no difference in BrdU incorporation compared to Naïve-EVs + 5% FCS.

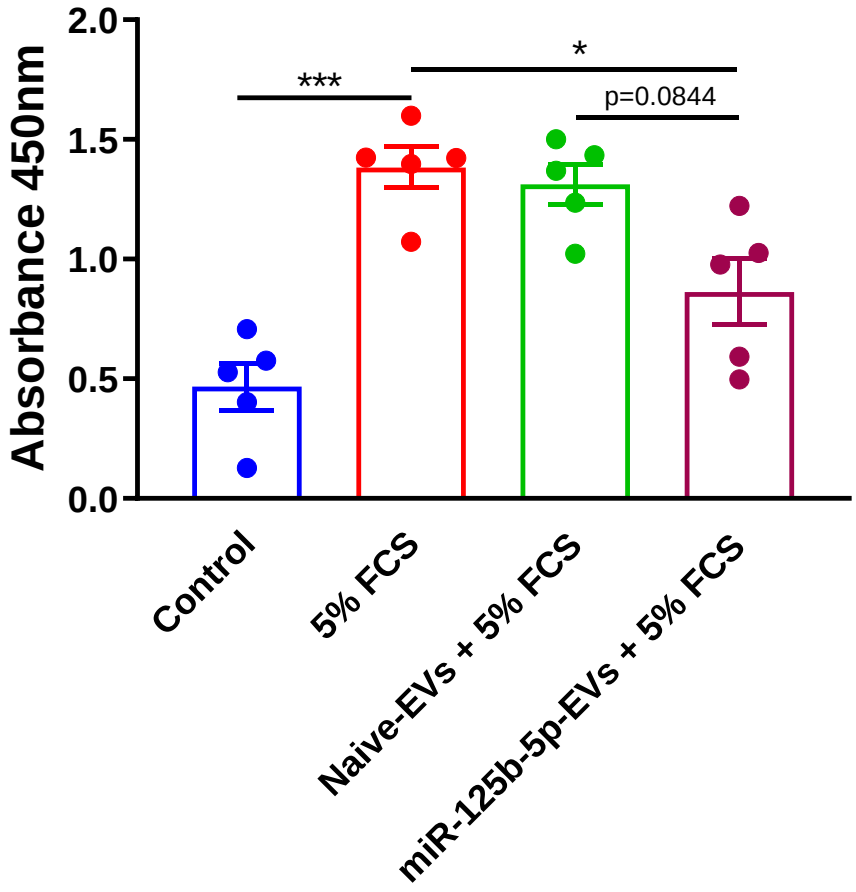

Figure 6-8 Effect of miR-125b-5p-EVs on serum induced HCASMC proliferation

HCASMCs were quiesced for 48 hours and then treated with 5% FCS or Naïve-EVs + 5% FCS or miR-125b-5p-EVs + 5% FCS in SF media for 24 hours. Cell proliferation was measured using the Cell Proliferation ELISA, BrdU (colorimetric). Statistical probability of differences was calculated using RM One-way ANOVA with post-hoc Tukey's test (n=5 replicates, 3 patients, ***p<0.001 Control vs 5% FCS, **p<0.01 Control vs Naïve-EVs + 5% FCS, *p<0.05 5% FCS s miR-125b-5pEVs + 5% FCS). Data are expressed as the mean ±SEM.

6.3.4 Effects of miR-125b-5p-EVs isolated from HCASMCs on recipient serum induced HCASMC migration

Next, the effects of miR-125b-5p-EVs on serum induced migration was studied. HCASMCs were seeded into a 12 well plate and quiesced for 48 hours in SF media. Next cells were stimulated with 5% FCS, Naïve-EVs + 5% FCS or miR-125b-5p-EVs + 5% FCS in SF media. Quiesced control HCASMCs showed 27.4±2.3% scratch closure in the absence of serum or any other treatment (Figure 6-9 and Figure 6-10). The 5% FCS condition demonstrated 72.4±4.1 scratch closure (Figure 6-9 and Figure 6-10). Naïve-EVs + 5% FCS treatment showed 72.9±3.5% scratch closure (Figure 6-9 and Figure 6-10), comparable to the effect observed with 5% FCS alone. MiR-125b-5p-EVs + 5% FCS treatment demonstrated 64.4±5.4% scratch closure (Figure 6-9 and Figure 6-10) which although not significant was lower compared to the oercentage scratch closure observed with Naïve-EV treatment (Figure 6-9 and Figure 6-10).

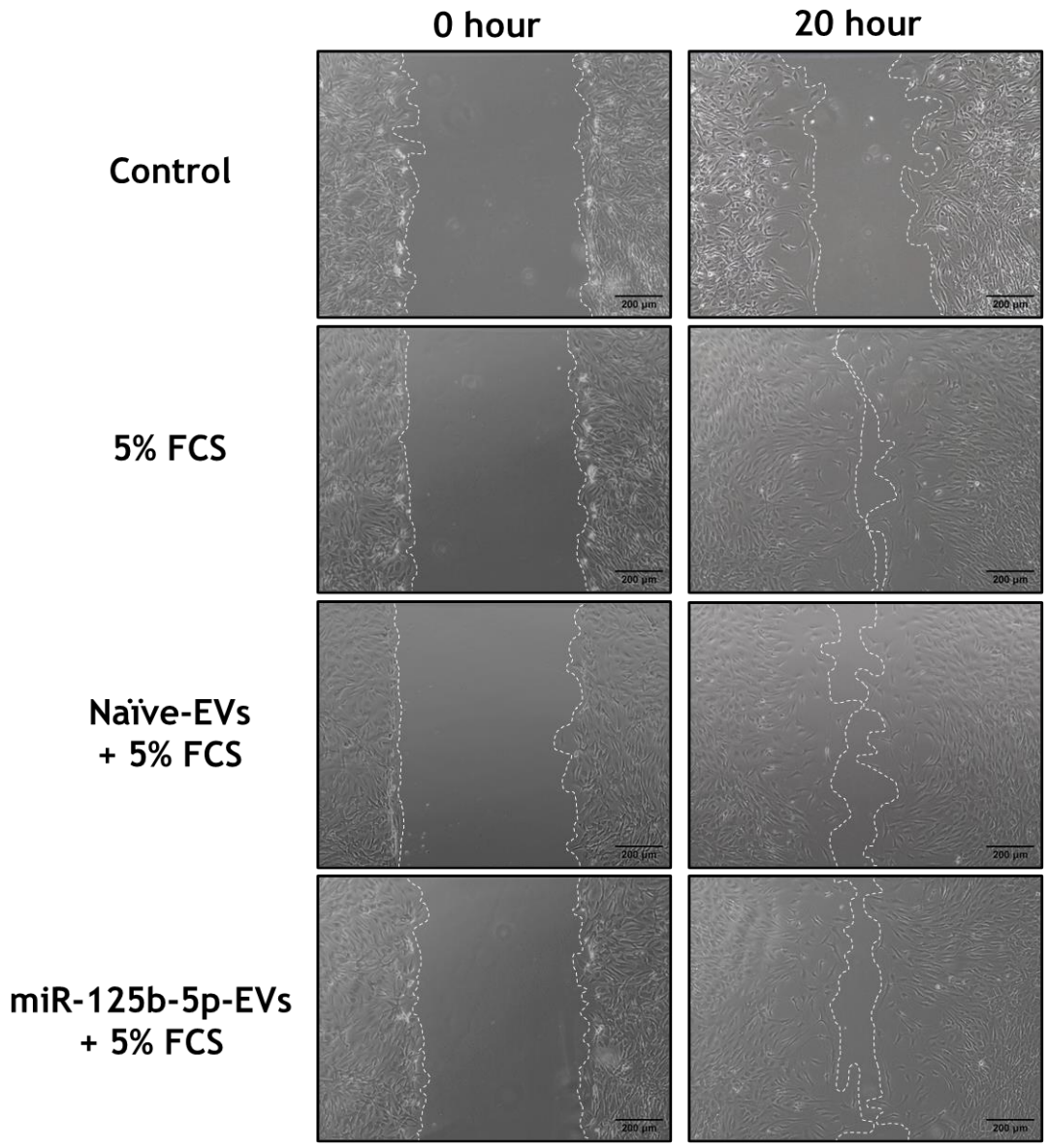

Figure 6-9 Effect of miR-125b-5p-EVs on serum induced primary HCASMC-driven scratch closure

Cells were seeded into 12-well plates ($1.5x10^5$ cells/mL), upon reaching confluence, cells were quiesced for 48 hours in SF media. Cells were horizontally scratched with a sterile 1000 µL pipette tip. Scratches were imaged at 10x magnification using the EVOS XL Core microscope (left panel). The scratches were imaged again at 20 hours at 10x magnification (right panel). White dotted lines indicate scratch edges. Scale bar: 200 µm.

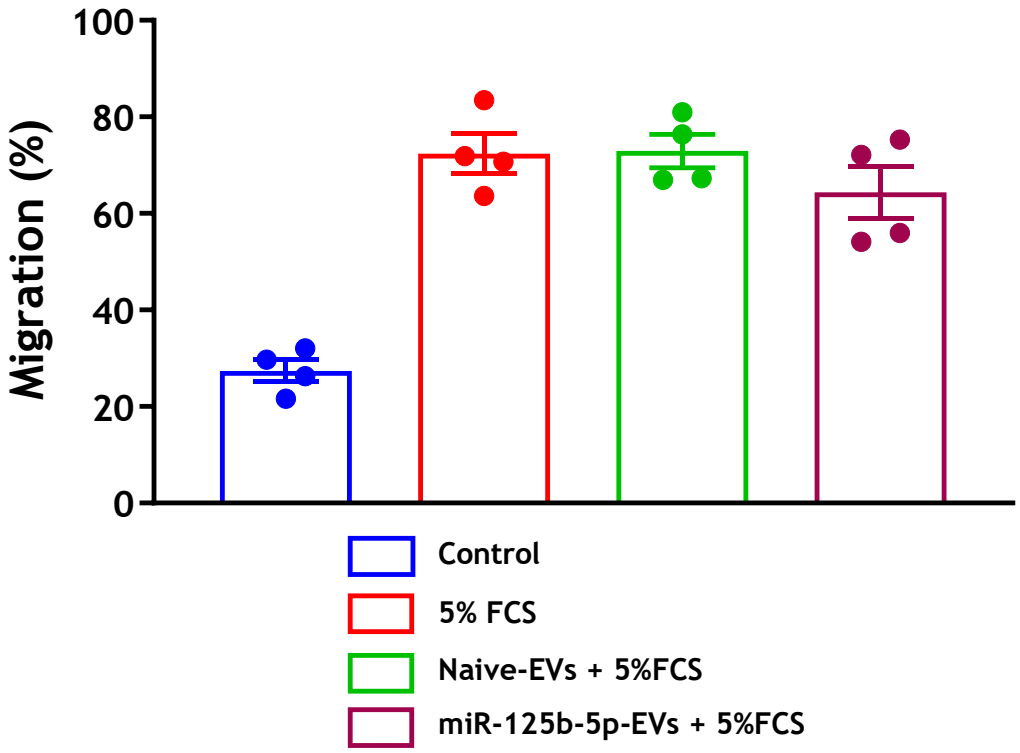

Figure 6-10 Quantification of anti-migratory effect of miR-125b-5p-EVs on serum induced primary HCASMC-driven scratch closure

Scratches were imaged at 0 hour and 20 hour at 10x magnification using the EVOS XL Core microscope. The image J software was used to quantify the scratch percentage closure. Data are expressed as the mean ±SEM (n=4 replicates, 2 patients).

6.3.5 Effects of miR-125b-5p-EVs isolated from SMCs on recipient SMC gene expression

The bioinformatic analysis (Chapter 4) identified 6 genes that could potentially be targets of miR-125b-5p. The pathway hypothesis formed in Chapter 4 suggested that miR-125b-5p may regulate cell survival and proliferation via transcriptional regulation of TP53, STAT3, ERBB2, ERBB3, SP1 and PPP1CA. Next, using the same experimental conditions it was investigated if uptake of miR-125b-5p-EV into HCASMCs invoked transcriptional regulation of these genes.

HCASMCs were seeded into 24 wells plates and upon reaching confluence, cells were quiesced for 48 hours in SF media. Cells were stimulated with 5% FCS or Naïve-EVs + 5% FCS or miR-125b-5p-EVs + 5% FCS for 6 hours and 12 hours. Gene expression was examined by RT-qPCR, as described in Section 2.4.3.

TP53 mRNA expression after 6 hours showed no differences in 5% FCS treated cells and miR-125b-5p-EVs + 5% FCS treated cells (Control RQ= 1.0±0.06, 5% FCS RQ= 0.65±0.18, miR-125b-5p-EVs + 5% FCS RQ= 0.63±0.30, Figure 6-11 A). However, Naïve-EVs + 5% FCS treatment reduced TP53 mRNA expression compared to control cells (RQ= 0.60±0.13). TP53 mRNA expression levels at 12 hours showed no differences in all 5% FCS groups ± each EVs (Control RQ=1.0±0.16, 5% FCS RQ=0.89±0.29, Naïve-EVs + 5% FCS RQ=0.92±0.34, miR-125b-5p-EVs + 5% FCS RQ=1.08±0.12, Figure 6-12 A).

STAT3 mRNA expression at 6 hours showed no differences in all 5% FCS groups ± each EVs (Control RQ=1.0±0.17, 5% FCS RQ=1.21±0.13, Naïve-EVs + 5% FCS RQ= 1.14±0.17, miR-125b-5p-EVs + 5% FCS RQ= 1.35±0.58, Figure 6-11 B). STAT3 mRNA expression at 12 hours showed no differences in 5% FCS treated cells and miR-125b-5p-EVs + 5% FCS treated cells (Control RQ=1.0±0.3, 5% FCS RQ=0.74±0.29, miR-125b-5p-EVs + 5% FCS RQ=0.68±0.18, Figure 6-12 B). Reduced STAT3 mRNA expression was observed after Naïve-EVs + 5% FCS treatment (RQ=0.6±0.32) compared to control cells.

ERBB2 mRNA expression at 6 hours did not change after 5% FCS treatment ± each EVs (Control RQ=1.0±0.25, 5% FCS RQ=1.05±0.29, Naïve-EVs + 5% FCS RQ=0.77±0.17, miR-125b-5p-EVs + 5% FCS RQ=0.83±0.28) Figure 6-11 C). . At 12 hours, ERBB2 mRNA expression levels showed a reduced expression in all 5% FCS treated cells and miR-125b-5p-EVs + 5% FCS treated cells (Control RQ=1.0±0.04,

5% FCS RQ= 0.77±0.11, miR-125b-5p-EVs + 5% FCS RQ= 0.79±0.11, Figure 6-12 C). Naïve-EVs + 5% FCS treatment (RQ=0.66±0.21) resulted in significant reduction of ERBB2 mRNA levels compared to control cell (*p<0.05).

ERRB3 mRNA expression levels demonstrated no alterations in all 5% FCS groups +/- each EVs (Control RQ=1.0±0.47, 5% FCS RQ= 1.18±0.33, Naïve-EVs + 5% FCS RQ=0.95±0.40, miR-125b-5p-EVs + 5% FCS RQ= 0.87±0.34, Figure 6-11 D). After 12 hour treatment, ERBB3 mRNA expression showed no differences in all 5% FCS groups +/- each EVs (Control RQ=1.0±0.3, 5% FCS RQ=0.72±0.71, Naïve-EV + 5% FCS RQ=0.30±0.48, miR-125b-5p-EV + 5% FCS RQ=0.48±0.31, Figure 6-12 D).

SP1 mRNA expression levels at 6 hours revealed no differences in all 5% FCS groups +/- each EVs (Control RQ= 1.0±0.02, 5% FCS RQ=1.15±0.15, Naïve-EVs + 5% FCS RQ= 0.94±0.16, miR125b-5p-EVs + 5% FCS RQ= 0.90±0.28, Figure 6-11 E). Again, SP1 mRNA expression at 12 hours showed no differences in all 5% FCS groups +/- EVs (Control RQ=1.0±0.21, 5% FCS RQ=0.93±0.16, Naïve-EVs + 5% FCS RQ= 0.87±0.21, miR-125b-5p-EVs + 5% FCS RQ=1.0±0.15, Figure 6-12 E).

PPP1CA mRNA expression levels at 6 hours showed no alterations in all 5% FCS groups +/- each EVs (Control RQ=1.0±0.04, 5% FCS RQ= 1.19±0.13, Naïve-EVs + 5% FCS RQ=1.11±0.12, miR-125b-5p-EVs + 5% FCS RQ=1.02±0.21, Figure 6-11 F). An increase in PPP1CA mRNA levels at 12 hours was observed in all 5% groups +/- each EVs (5% FCS treatment RQ=1.58±0.14; vs Control, Naive-EVs + 5% FCS RQ= 1.56±0.06,, miR-125b-5p-EVs + 5% FCS RQ=1.55±0.03) compared to Control treated cells (RQ=1.0±0.07, Figure 6-12 F).

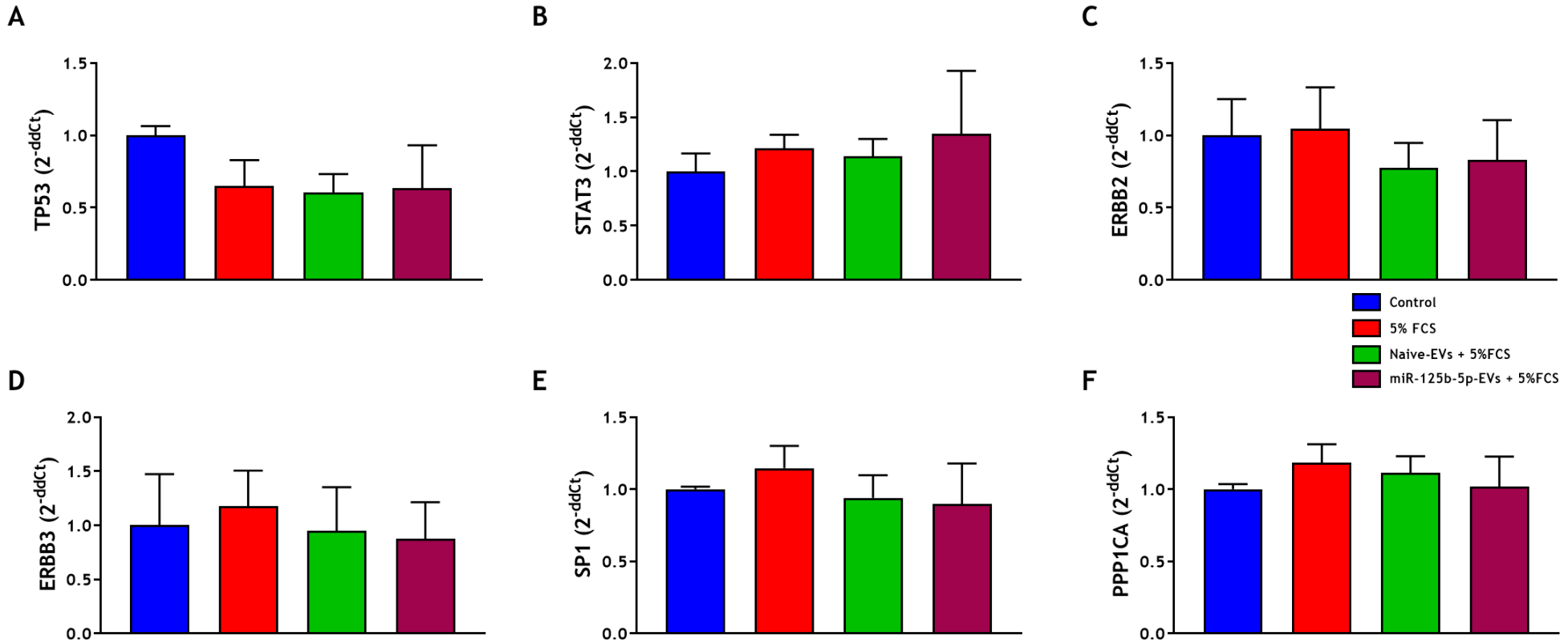

Figure 6-11 MiR-125b-5p-EV effect on recipient HCASMC gene expression after 6 hour treatment

HCASMCs were seeded into a 24 well plate, upon reaching confluence, cells were quiesced for 48 hours and were treated with EVs for 6 hours. Data are shown as RQ values ±SEM (n=4 replicates, 2 patients).

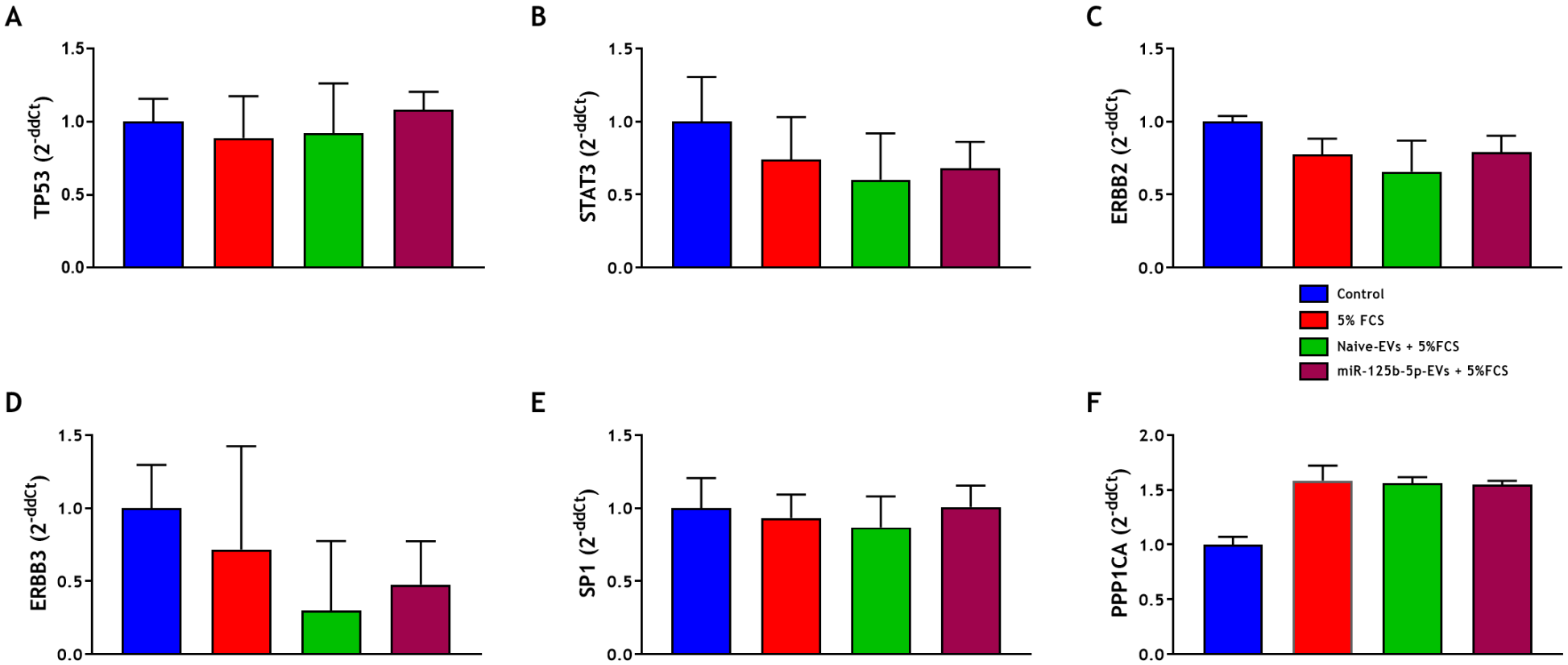

Figure 6-12 MiR-125b-5p-EV effect on recipient HCASMC gene expression after 12-hour treatment

HCASMCs were seeded into a 24 well plate, upon reaching confluence, cells were quiesced for 48 hours and were treated with EVs for 12 hours. Data are shown as RQ values ±SEM (n=4 replicates, 2 patients).

6.3.6 Effects of miR-125b-5p-EVs isolated from SMCs on recipient EC cell death and viability

MiR-125b-5p is expressed in ECs and has been previously reported to regulate vascular homeostasis by rescuing ECs by endothelin-1 upregulation after oxLDL stimulation (Li et al., 2010). It was of interest to investigate the effect of miR-125b-5p-EVs from SMCs on recipient HCAECs. HCAECs were seeded into a 96 well plate. Cells were not quiesced as quiescence in low serum media caused significant cell death (data not shown). To address these challenges, cells were instead treated with EVs in 2% EV depleted serum or in the presence of complete serum media (5% FCS). Cells were treated either with serum containing 2% EV-depleted serum or complete media containing 5% FCS and/or Naïve-EVs or miR-125b-5p-EVs for 4 hours and HCAEC viability was measured using the CyQUANT™ MTT Cell Viability Assay.

In the presence of media containing 2% EV depleted serum, 10% FCS treatment resulted in increased cell viability (% viable cells 125.2±0.1) compared to control treated cells (% viable cells 100.0±0.1, Figure 6-13 A), however no statistically significant. No change in cell viability was observed after Naive-EV treatment (106.8±0.1) or miR-125b-5p-EV treatment (104.9±0.1, Figure 6-13 A). In the presence of complete media (5% FCS), 10% FCS treatment did not alter the HCAEC cell viability (% viable cells 108.0±0.1) compared to Control treated cells in complete media containing 5% FCS (% viable cells 100.0±0.1, Figure 6-13 B). MiR-125b-5p-EV treatment resulted in no difference in HCAEC cell viability (% viable cells 93.0±0.1), similar to Naive-EV treatment (% viable cells 100.9±0.1, Figure 6-13 B).

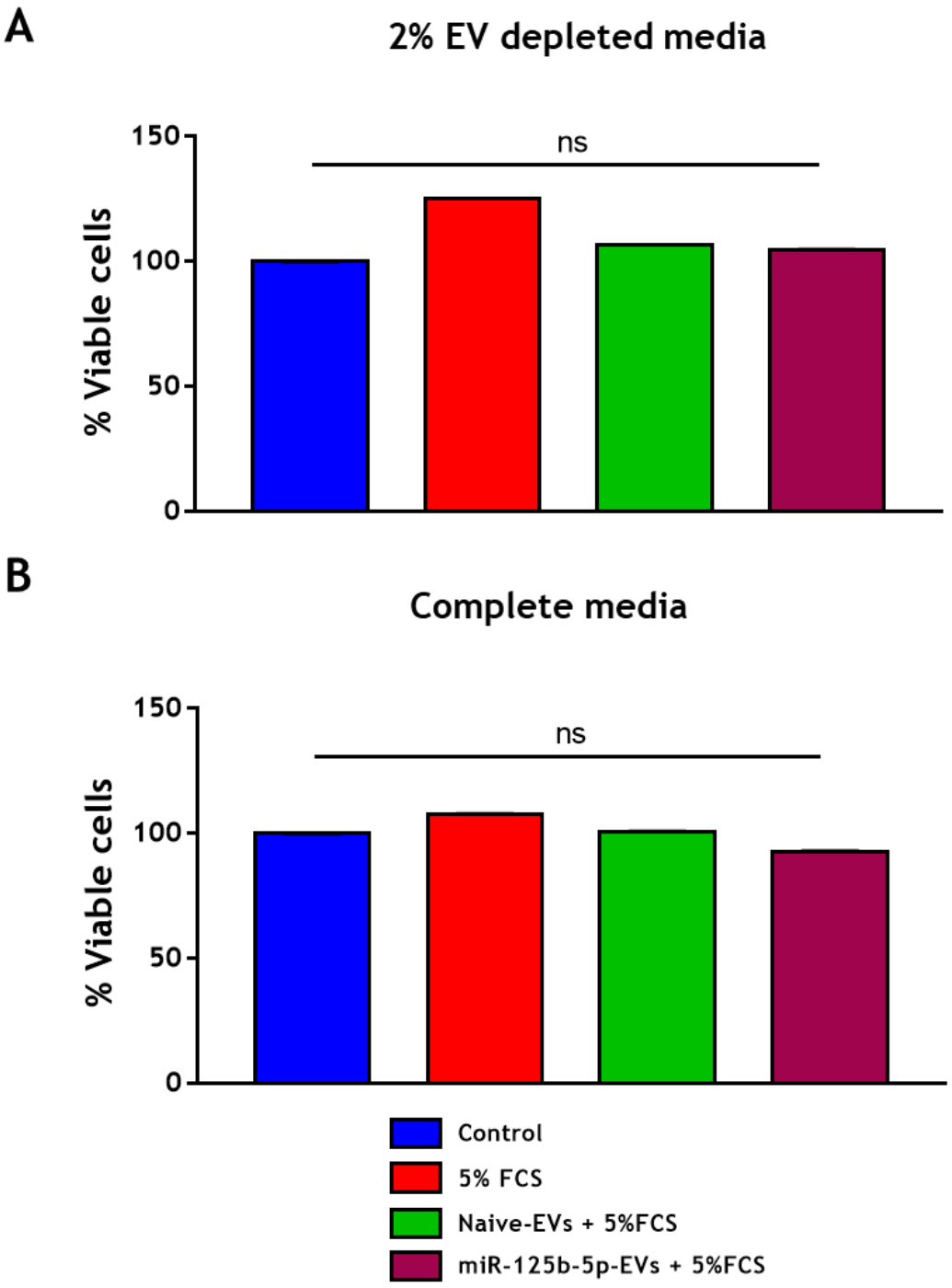

Figure 6-13 Effect of miR-125b-5p-EVs on recipient HCAEC cell viability

HCAECs were seeded into a 96 well ($4x10^4$ cells/mL). Cells were not quiesced. Cells were treated for 4 hours with EVs. Cell viability was measured using the CyQUANT™ MTT Cell Viability Assay. (A) HCAEC cell viability of cells treated with 10% FCS, Naive-EVs and miR-125b-5p-EVs in 2% EV depleted media (low serum media). (B) HCAEC cell viability of cells treated with 10% FCS, Naive-EVs and miR-125b-5p-EVs in complete HCAEC media (Endothelial Cell Growth Medium MV). Statistical probability of differences was calculated using RM One-way ANOVA with post-hoc Tukey's test (n=3 patients, ns= nonsignificant). Data are expressed as the mean of % viable cells ±SEM.

6.4 Discussion

In this chapter, successful cel-miR-39-3p loading in EVs via electroporation and successful cel-miR-39-3p-EV transfer to recipient HCASMCs was shown. MiR-125b-5p loaded EVs were characterised and no difference in terms of size or concentration was observed after electroporation. MiR-125b-5p-EVs did not affect recipient HCASMC cell viability or serum induced HCASMC migration. MiR-125b-5p-EVs significantly reduced recipient HCASMC serum induced proliferation but no difference in cell proliferation was observed between Naïve-EV and miR-125b-5p-EV treatment. Gene expression of target genes was examined after 6 hour and 12 hour treatment and no differences in mRNA expression was observed after 5% FCS treatment or 5% FCS +/- Naïve or miR-125b-5p-EV treatment. Finally, miR-125b-5p-EV treatment had no effect on recipient HCAEC cell viability.

Mimic concentration for electroporation experiments was optimised by Antoniya Pashova based on the protocol provided from Dr Work's group (both University of Glasgow). Although mimic concentration was optimised no other electroporation parameters were optimised as similar electroporation cuvettes and electroporator had been used in other studies in Dr Work's group. Published studies have suggested poor cargo loading in EVs of approximately 25% (meaning 25% of initial amount of mimic was loaded into EVs) with one study demonstrating 50% miRNA loading into EVs (Kooijmans et al., 2013)(Momen-Heravi et al., 2014). Unfortunately, the percentage of mimic loaded into EVs was not calculated in this study, however qPCR analysis confirmed highly elevated levels of cel-miR-39-3p into EVs after electroporation and significantly elevated levels of miR-125b-5p into EVs after electroporation. In these studies, cel-miR-39-3p, a non-human miRNA, was used to detect miRNA levels in EVs after electroporation and uptake of miRNA into cells without confounding effects of endogenous levels of the same miRNA. RT-qPCR analysis showed increased cel-miR-39-3p levels in EVs after electroporation and the efficiency of miRNA-EV transfer to recipient HCASMC was also examined. After 6 hours, cel-miR-39-3p levels were increased 20 times in HCASMCs and after 24 hours cel-miR-39-3p signal was lower indicating miRNA degradation. The cel-miR-39-3p mimic was chosen to assess miRNA delivery via EVs to cells as a method without confounding effects of endogenous miRNAs. Unfortunately, background contamination was detected in these studies. Cel-miR-39-3p signal was detected in Naïve-EVs and Naïve-EV treated cells where it should not be detected and was also detected in H_2O negative controls during cDNA

synthesis. However, this contamination was a lab issue as other members within groups using cel-miR-39-3p in their studies faced the same background contamination. Due to limited material, the experiment could not be repeated. Pomatto et al., showed successful cel-miR-39-3p transfer in recipient cells after 24 hour EV treatment (Pomatto et al., 2019). In that study only one timepoint of miRNA transfer was examined, different voltages of electroporation were used (500 V, 750 V, 1000V) and higher number of pulses (10 pulses) whereas in our study 400 mV and 1 pulse were used to electroporate EVs (Pomatto et al., 2019).

Characterisation of miR-125b-5p loaded EVs showed that electroporation did not affect size of EVs (Naïve-EVs 137.8±12.7 nm, miR-125b-5p-EVs 134.5±7.2 nm). In Chapter 3, it was shown that secreted EVs from HCASMCs had similar sizes (Control-EVs 116.9±5.8 nm, oxLDL-EVs 130.9±5.3 nm). These findings agree with those of Johnsen et al., who showed that electroporation did not alter the size of electroporated adipose-derived stem cell EVs isolated with UC (Johnsen et al., 2016). Protein EV markers like CD81, Annexin A2 and CD63, were also detected on both Naïve and miR-125b-5p-EVs as they were detected on freshly secreted SMC-EVs not subjected to electroporation as shown in chapter 3.2.3.

The pathway hypothesis formed upon the bioinformatic analysis suggested that miR-125b-5p might control transcriptional regulation of TP53, STAT3, ERBB2, ERBB3, SP1 and PPP1CA in HCAMSCs and thus affect pathways involved in cell proliferation, migration, and viability of HCASMCs or HCAECs. In this study, miR-125b-5p-EV treatment for 24 hours did not affect HCASMC cell viability. This is in contrast to findings where bone marrow mesenchymal stem cell (BMSC)-miR-125b-EVs induced significantly increased cell viability following ischemia reperfusion injury in rat cardiomyocytes (isolated from ventricular tissue of rats after ischemia reperfusion injury) after 24 hours, 48 hours and 72 hours treatment (Chen et al., 2020). In that study, BMSCs were transfected with lentiviral vector (LV)-miR-125b mimic using Lipofectamine 2000 and EVs were isolated 48 hours later (Chen et al., 2020). Some key differences in that study and the one reported here, is first of all the different cell type of that the EVs were derived from, the stimulus to the cells, the method of miRNA overexpression and finally in Chen et al., they do not mention which mature strand of miR-125b-2 they overexpressed in BMSC-EVs (Chen et al., 2020). In this study, no difference in cell viability between Naïve-EV treatment and miR-125b-5p-EV treatment was observed. One explanation could

be that miR-125b-5p-EVs did not affect HCASMC cell viability or different experimental design should be followed such as higher or lower EV dose or stimulation of cells with FCS and EVs or stimulation with a different molecule or examination of the effect of miR-125b-5p-EVs in induced cell death. Another reason could be the low sensitivity of MTT assay. The detection of cell viability in this assay is based on the MTT conversion by viable or proliferating cells which can be affected by numerous factors such the culture medium exhaustion, which could lead to false positive or negative signals (Hu et al., 2021).

Since no difference in cell viability between Naïve and miR-125b-5p-EV treatment was detected, it was decided to investigate the effect of miR-125b-5p-EVs in serum induced proliferation of HCASMCs. MiR-125b-5p-EVs reduced serum induced proliferation of HCASMCs in contrast to Naïve-EVs. Baldari et al., showed that treatment of hepatocellular carcinoma cells with human adipose tissue-derived mesenchymal stromal cell (ASC)-EVs overexpressing miR-125b-5p resulted in reduced proliferation of recipient cells (Baldari et al., 2019). Cell proliferation in that study was estimated in a different cell model, with different cell derived EVs and miR-125b-5p overexpression was performed using a lentiviral vector (recombinant vesicular stomatitis virus-pseudotyped lentiviral vector XMIRXpress miR125-5p)(Baldari et al., 2019). Another study showed that MSC-EVs which were found to be enriched in miR-125b-5p, promoted proliferation of tubular epithelial cells *in vitro* and *in vivo* (using an ischemia/reperfusion induced acute kidney injury mouse model) (Cao et al., 2021). Other studies have shown that miR-125b-5p inhibits proliferation of various cell types (Ouyang et al., 2015)(Hua et al., 2019). All the above indicate that the outcome of miR-125-5p biological function could either be cell type dependent.

MiR-125b-5p-EV treatment had no effect in serum HCASMC migration after 20 hours. Naïve-EV treatment had similar effect on HCASMC migration as the 5% FCS treatment. Wu et al., showed that EVs derived from highly invasive pancreatic cancer -1.0 (PC-1.0) cells promoted migration and invasion of the weakly invasive PC-1 cells via miR-125b-5p transfer from PC-1.0 EVs to weakly invasive PC-1 cells (Wu et al., 2020). They also showed that miR-125b-5p cell overexpression promoted migration of PC-1.0 cells while miR-125b-5p inhibition resulted in reduced cell migration (Wu et al., 2020). In this study, the effect on miR-125-5p-EV treatment was observed while cells were co-stimulated with 5% FCS. Other

studies observed low levels of miR-125b-5p in different types of cancer and showed that miR-125b-5p overexpression inhibited cell migration (Mei et al., 2017)(Hua et al., 2019). Another study examined the pre-operative serum levels of miR-125b-5p showing that low levels of miR-125b-5p were significantly correlated with microvascular invasion in patients with hepatocellular carcinoma and could serve as an independent biomarker (Liu et al., 2016). It is important to mention that scratch assays were performed for two sets of donor cells (n=4 replicates, 2 donor patients). Perhaps, increasing the number of donor cells examined would result in a clear result as to whether miR-125b-5p-EVs inhibit HCASMC serum induced migration. Furthermore, the scratch assay is not the most efficient assay as it cannot properly distinguish between proliferation-and/or migration-driven scratch closure as both migration and proliferation participate in wound closure with studies showing that over time proliferative mechanisms contribute to wound closure (Varankar and Bapat, 2018)(Ammann et al., 2019). However, the use of a proliferation inhibitor mitomycin C and low serum concentration is advised to remove confounding proliferation in migration studies (Grada et al., 2017). Hence, Boyden chamber migration analysis should be added to this data set in the future. Preliminary studies regarding the functional effect of miR-125b-5p-EVs in serum induced proliferation and migration suggest that future studies with miR-125b-5p loaded EVs and anti-miR-125b-5p-EVs are required to decipher whether miR-125b-5p may exert anti-proliferative and anti-migratory effects in HCASMCs.

Gene expression of TP53, STAT3, ERBB2, ERBB3, SP1 and PPP1CA was examined in HCASMCs after 6 and 12 hours of treatment. No differences were observed regarding gene expression of these genes at the two timepoints. All of the 6 genes were validated gene targets of miR-125b-5p in different tissues or cell types. The most efficient way to validate that miR-125b-5p-EV transfer to recipient HCASMCs targets the pathway genes would be using a luciferase reporter assay, but due to the time required to optimise and validate a protocol for examining all 6 genes, that method was not chosen. Another reason explaining the negative results collected could be the design of the experiment itself, the EV concentration used or that these genes are not regulated by miR-125b-5p in SMCs. In a preliminary study, the expression of TP53, STAT3, ERBB2 and SP1 was examined after 18-hour EV treatment and 5% FCS co-stimulation (data are not shown). No difference in gene expression between Naïve-EV and miR-125b-5p-EV treatment was detected

so it was decided that maybe an earlier timepoint should be checked. The pathway hypothesis was formed based on 6 genes out of 303 predicted and validated gene targets generated from the bioinformatic analysis, so there are 297 potential targets of miR-125b-5p to be investigated in future studies.

A study by Zhang et al., showed that in mouse embryonic fibroblasts mechanistic target of rapamycin complex 1 (mTORC1) upregulated STAT3 expression via miR-125b-5p downregulation and luciferase activity assay confirmed that STAT3 is a miR-125b-5p target (Zhang et al., 2020). Moreover, miR-125b-5p overexpression resulted in reduced cell proliferation in cells with increased mTORC1 activity (Zhang et al., 2020). MSC-EVs were found enriched in miR-125b-5p reduced epithelial cell apoptosis *in vitro* and *in vivo* via miR-125b-5p targeting of TP53 gene (Cao et al., 2021). Another study showed that hyperglycaemia in ARPE-19 cells resulted in SP1 upregulation and miR-125b-5p downregulation in these cells (Gong et al., 2019). MiR-125b-5p overexpression in ARPE-19 cells reduced hyperglycaemia-induced SP1 upregulation with luciferase activity assay confirming that SP1 is a target of miR-125b-5p (Gong et al., 2019). Moreover, ERRB2 has been reported as a miR-125b-5p target in small cell lung cancer cells (Yagishita et al., 2015). Another study reported ERBB3 and ERBB2 as targets of miR-125b with miR-125b overexpression resulting in reduced ERBB2, ERBB3 gene expression, inhibition of ERK1/2 signalling pathway and aggravating migration of the breast cancer cell line SKBR3 (Scott et al., 2007). PPP1CA has been identified as a target of miR-125b-5p among the p53 network regulating apoptosis (Le et al., 2011). All the above studies reported that STAT3, TP53, SP1, ERBB2, ERBB3 and PPP1CA are validated targets of miR-125b-5p in various cell models.

Cell viability of HCAEC was examined after miR-125b-5p-EV treatment. HCAECs were not quiesced as low serum media caused significant cell death (data not shown). For this purpose, no quiescence was performed and the effect of miR-125b-5p-EVs in cells undergoing cell death was estimated (cells in 2% EV depleted FCS containing media) and in proliferating cells (cells in complete media). MiR-125b-5p-EVs did not induce or inhibit cell death of recipient HCAECs and showed no difference in cell viability when compared with Naïve-EVs. Since cells were not quiesced and no synchronisation of cell cycle was established, it is difficult to draw conclusions regarding the effect of miR-125b-5p-EVs and Naïve-EVs on recipient HCAEC cell viability in these studies. Umbilical cord MSC-EVs under

hypoxia after skin injury *in vitro* were found enriched in miR-125b-5p and miR-125b-5p was responsible for promoting cell viability and proliferation of recipient ECs via targeting tumor protein p53 inducible nuclear protein 1 (TP53INP1) and rescuing the hypoxia induced apoptosis in ECs (Zhang et al., 2021). Human placental microvascular ECs (HPMECs) were subjected to hypoxia followed by reoxygenation (H/R) to establish pregnancy-induced hypertension cellular model and miR-125b-5p expression was found significantly reduced after H/R treatment (Zheng et al., 2022). Overexpression of miR-125b-5p ameliorated the H/R induced apoptosis in HPMECs via targeting of Bcl2 Modifying Factor gene (Zheng et al., 2022).

6.5 Summary

Successful loading of cel-miR-39-3p and miR-125b-5p mimic in SMC-EVs and transfer of cel-miR-39 to recipient HCASMCs was shown in this chapter. MiR-125b-5p was successfully overexpressed in SMC-EVs and characterisation of Naïve-EVs and miR-125b-5p-EVs showed that electroporation did not cause any change in the size of EVs. MiR-125b-5p-EVs did not alter recipient HCASMC or HCAEC cell viability. Encouragingly, miR-125b-5p-EVs significantly suppressed HCASMC serum induced proliferation but no difference compared to Naïve-EV treatment was observed. Moreover, miR-125b-5p-EV treatment did not alter in serum induced HCASMC migration. Gene expression analysis showed no difference in mRNA levels of target genes after miR-125b-5p-EV treatment compared to Naïve-EV treatment. However, with more time to optimise the experimental conditions and/or a different pathway hypothesis, EV transfer of miR-125b-5p could be investigated further for its effects on vascular cell phenotype and ultimately against atherosclerosis progression.

Chapter 7 General discussion

7.1 Overall Summary

Atherosclerosis is the most frequent underlying cause of death worldwide. The disease does not cause death but disease complications including MI, stroke, or ACS due to plaque rupture and that can be fatal. Current pharmacological approaches including statins and PSCK9 inhibitors have resulted in reduced LDL-C levels. Mitigation of other cardiovascular risk factors such as obesity, smoking and hypertension has contributed to the reduction of the burden of the disease, but not completely. Therefore, the need for new and effective therapeutic interventions is urgent. The primary aims of the work presented in this thesis are to investigate and characterise EVs and their cargo, from vascular cells integral to the development of atherosclerosis. EVs were isolated from both physiological conditions and following exposure to pro-atherogenic stimuli to extrapolate these findings and compare them to relevant models of atherosclerosis. EVs are key players in the development of atherosclerosis as summarised in Figure 7-1.

Initially, the potential of isolating EVs from HCASMCs was assessed. The previous method used for EV isolation in our lab was UC, but studies have shown that despite the distinct advantage the method offers, including removal of lipoprotein/protein contaminants, it comes with its limitations including EV aggregation and lower EV yield (Takov et al., 2019). A recent study showed that SEC can better preserve EV integrity and their biological effects compared to UC (Takov et al., 2019). Before starting EV isolation with SEC, the elution profile of SMC-EVs isolated from CCM was assessed to enable optimisation of isolation. The SEC column was optimised by the manufacturer for EV isolation from plasma samples. In these experiments, it was found that the void volume and the first 3 fractions contained pure EVs based on EV purity ratio. Therefore, collecting and combining them was worthwhile despite the manufacturer's protocol suggestions for serum/plasma EV isolation where it was recommended to exclude the void volume. Overall, characterising and optimising the EV elution profile for EVs isolated from cultured cells was worthwhile for both evidence of the SEC method and also to maximise the EV yield for downstream experimentation. Gaspar et al., reported an optimised protocol with alterations compared to the manufacturer's protocol using SEC to isolate EVs from plasma (Gaspar et al., 2020). Authors reported higher EV and RNA yield, reduced cellular contamination in the isolated samples and higher purity of the isolated EV samples while using their optimised SEC protocol (Gaspar et al., 2020). Next, an appropriate dose of oxLDL for HCASMC

stimulation was determined. A range of oxLDL doses (10 µg/mL, 40 µg/mL and 60 µg/mL) were examined. The lower oxLDL working concentration 10 µg/mL, was chosen as cell imaging data confirmed sufficient oxLDL uptake by HCASMCs and no cell death was observed according to the MTT data. Published evidence also suggests that high oxLDL concentration (>40 µg/mL) can result in cell death (Kataoka et al., 2001)(John Liu et al., 2014). The lower oxLDL dose was used for all other experiments. More importantly, results suggest that oxLDL stimulation did not alter EV release from HCASMC in terms of size, morphology, or concentration. Furthermore, no functional response, regarding cell death, was observed in recipient HCASMCs and HCAECs while exposed to either control or oxLDL-EVs. In contrast, a publication reported that EVs secreted from macrophages, after oxLDL treatment, can induce an anti-migratory effect on recipient macrophages (Nguyen et al., 2018). This highlights the effects of EVs isolated from oxLDL-stimulated SMCs in other cell types may have revealed effects and is worth investigating. Next, the EV internalisation by recipient HCAEC was examined. Control and oxLDL-EVs were labelled with PKH67 with significantly lower uptake of oxLDL-EVs compared to Control-EVs. The results were analysed in recipient HCAECs. However, it is important to interpret results carefully as although PKH67 is a popular fluorescence stain for EV imaging and is associated with limitations such as staining lipoprotein particles or protein contaminants of the samples. This can result in detection of non-EV stained particles (Takov et al., 2017)(Pužar Dominkuš et al., 2018).

Nguyen et al., investigated cel-miR-54-EV transfer from +/- oxLDL treated macrophages to recipient naïve macrophages, and found that EVs from oxLDL treated macrophages can transfer higher number of cel-miR-54 copies to recipient cells (Nguyen et al., 2018). Uptake of EVs by recipient cells was not quantified in the study. However, this study provides evidence that oxLDL treatment can alter miRNA-EV transfer (Nguyen et al., 2018).

The next studies investigated the effect of oxLDL treatment on the small RNA cargo of SMC-EVs. Small RNA sequencing of SMC-EVs revealed small RNA species packaged into SMC-EVs. Of the 112 miRNAs, which were profiled in SMC-EVs, a differential expression analysis identified only miR-125b-5p to be downregulated after oxLDL treatment. Interestingly, miR-125b-5p was also found to be expressed in oxLDL-EVs by a different method of analysis of the RNA sequencing experiment.

In that approach, the counts were normalised to the total genetic material within the sample. Furthermore, two other miRNAs, miR-199b-5p and miR-199a-5p, were identified to be downregulated after oxLDL treatment. OxLDL is a potent stimulating agent and other studies have reported its effect on small RNA cargo of EVs (Nguyen et al., 2018)(He et al., 2018). He et al, showed that 24 hr oxLDL stimulation (50 μg/mL) of HUVECs could result in an increase miR-155 expression in secreted EVs (24hr EV secretion) (He et al., 2018). Mouse peritoneal macrophages and mouse bone-marrow derived macrophage (BMDM) secreted EVs (24 hr EV secretion) showed increased expression of miR-146a, miR-128, miR-185, miR-365, and miR-503 after 24 hr oxLDL (50 μg/mL) stimulation (Nguyen et al., 2018). MiR-125b-5p levels in HCASMCs were also investigated in response to oxLDL treatment. It was shown that oxLDL treatment (24 hr) resulted in increased cellular miR-125-5p levels in contrast with downregulation of miR-125b-5p in HCASMCs after 48 hr EV secretion. Another study showed that oxLDL treatment (24 hr) induced a reduction in miR-125b-5p expression in recipient HAVSMCs (Li et al., 2015). The different expression patterns in response to oxLDL could be attributed to the different cell model used for each study. HAVSMCs used by Li et al., were isolated from aorta, while HCASMCs, used in these studies, were isolated from coronary arteries. A genetic lineage tracing study showed that postnatal coronary vessels in neonatal mouse arise de novo instead of expanding from pre-existing embryonic vasculature. This indicates that SMCs populating coronary arteries come from a different source from SMCs, which populate the aorta as they arise from mesoderm (Tian et al., 2014). MiR-125b-5p has been implicated in atherosclerosis development. Studies have examined levels of miR-125b-5p and observed increased miRNA levels in patients with ACS (Jia et al., 2016). Other studies have localised miR-125b-5p expression in human aortas from CAD patients and also in murine aortas (Hueso et al., 2016)(Hueso et al., 2022).

Further bioinformatic analysis for miR-125b-5p and pathway enrichment analysis suggests thatmiR-125b-5p may regulate cell survival and proliferation of recipient cells via transcriptional regulation of TP53, STAT3, SP1, ERBB2, ERBB3 and PPP1CA. Other studies report that miR-125b-5p/STAT3 pathway regulates cell proliferation in mouse embryonic fibroblasts and that miR-125b-5p overexpression can inhibit cell proliferation via targeting STAT3 (Zhang et al., 2020). STAT3 is an important regulator of vascular biology (Liao et al., 2015). Daniel et al., showed that in a mouse model of neointima lesion formation following wire-induced

injury, STAT3 activation was increased in the neointima lesion area (Daniel et al., 2012). STAT3 inhibition with WP1066, a highly potent inhibitor of STAT3 signalling, abolished STAT3 activation along with reduced proliferation and migration of SMCs in neointimal lesions (Daniel et al., 2012). The pathophysiologic mechanism of several vascular disease including atherosclerosis and neointima formation after stent placement is characterised by SMC proliferation and migration (Dzau et al., 2002). SMC apoptosis can also promote plaque instability, as SMCs make up the fibrous cap and their secreted collagen fibers are detrimental for the strength of the fibrous cap (Kockx and Herman, 2000). TP53 is another validated target of miR-125b-5p (Cenariu et al., 2021). P53-mediated SMC apoptosis has been implicated in the pathogenesis of abdominal aortic aneurysms (Holmes et al., 1996)(Mayr et al., 2002). Furthermore, activation of SP1 transcription factor has been suggested to promote SMC apoptosis (Kavurma et al., 2001). These studies highlight that miR125-5p and its gene targets regulate pathways, which are relevant to the role of VSMCs in atherosclerosis development.

Small RNA sequencing identified 3 U2 snRNAs, RNU2-7p, RNU2-29p, RNU2-57p, to be upregulated in oxLDL-EVs compared to Control-EVs. U2 snRNAs are part of the spliceosome which is responsible for splicing of more than 90% of human pre-mRNAs (Jia et al., 2012). Time was limited to further explore the function of these small RNAs in splicing processes. Alternative splicing could have detrimental effects for the progression or treatment of the disease and has been implicated previously in atherosclerosis. Medina et al., showed that an alternative spliced variant of the HMG-CoA reductase gene (HMGCR), HMGCRv_1, which was identified in lymphocytes isolated from participants in the Cholesterol and Pharmacogenetics study, demonstrated reduced sensitivity to statin-mediated inhibition of HMG-CoA resulting in a smaller reduction of plasma cholesterol levels (Medina et al., 2008). Furthermore, a study reported a change in VEGF-A splicing towards an atherogenic $VEGF_{165}$ in aortic ECs and macrophages from APOE KO mice under HFD suggesting that alternative splicing of VEGF-A may contribute to lesion development during atherosclerosis (Zhao and Zhang, 2018). In this particular study, increased aortic EC proliferation and apoptosis of aortic macrophages isolated from APOE KO mice fed with a HFD compared to APOE KO mice fed with a normal chow diet was observed. APOE KO mice fed HFD developed lesions while mice fed chow diet did not (Zhao and Zhang, 2018). SMCs and their phenotypic plasticity are key contributors to atherosclerosis development. Transcriptome-

wide studies have reported several alterations in alternative splicing of differentiated SMCs (Green et al., 2021). Xie e al., showed that serine/arginine splicing factor 1 (SRSF1) expression was upregulated in SMCs after vascular injury *in vivo* and proliferative stimuli *in vitro* (Xie et al., 2017). SRSF1 upregulation resulted in alternative splicing of p53 towards a proliferative isoform activating KLF5 and increasing SMC proliferation (Xie et al., 2017). Therapeutic targeting of alternative splicing in SMCs pathologies, like atherosclerosis, is therefore being explored as a new therapeutic target (Green et al., 2021).

Next, the effect of oxLDL on EV release from HCASMCs was investigated, and it was found that oxLDL treatment did not affect SMC-EV release or did alter the size or the concentration of EVs secreted from VSMCs. Several previous studies have shown increased systemic circulating levels of EVs in CAD, highlighting that EV profile can alter under various pathological conditions (Sinning et al., 2011)(Jansen et al., 2014). One reason for the difference in the findings could be that while the circulating EVs are secreted from a number of cells and organs, including immune cells, platelets and ECs this thesis examined EVs released from HCASMCs. However, to extrapolate the findings to the in vivo setting, a further investigation is needed to understand the EV profile from female wt and APOE KO mice under normal chow or high fat diet for 12 weeks. It was found that APOE KO mice with experimental atherosclerosis had a higher number of circulating EVs compared to APOE KO mice fed chow diet and wt mice under both diets. A previous study examined the effect of high fat diet, (6 months) on C57BL/6N wt male mice, and found elevated circulating EV concentrations, suggesting that circulating EVs could be used as a diagnostic tool for atherosclerosis detection (Kang et al., 2019). In the studies presented in this thesis, the data was in agreement since increased circulating numbers of EVs were observed in female ApoE KO mice fed a high fat diet indicating that EV concentration may be elevated in mice with experimental atherosclerosis of both sexes. However, a difference between the two studies is that in the studies presented here the APOE KO mouse model (under high fat diet for 3 months) was used to establish atherosclerosis while authors used wt mice fed a prolonged high fat diet (6 months) (Kang et al., 2019). Next, a novel method was used to isolate EVs secreted from cultured aortic tissues, including the aortic arch, thoracic aorta and abdominal aorta, from wt and APOE KO mice fed either chow diet or HFD. Although no difference in size or concentration was observed between the EVs secreted from these different vascular tissues, this method of isolation

indicated that intact cultured vascular tissues secreted EVs. Further, experiments such as flow cytometry could enable the identification of the cellular source of these secreted EVs. However, it needs to be mentioned that EVs were secreted from cultured tissues *ex vivo* and thus interpretation of the results should be performed with caution with regard to extrapolation to the *in vivo* setting. In previous publications, secreted EVs were successfully isolated from cultured mouse liver using a similar protocol to the one used in this study as an effort to directly collect EVs from tissues and improve the use of EVs as diagnostic tools (Matejovič et al., 2021). A further difference was that the authors used UC for isolation of secreted EVs from liver (Matejovič et al., 2021), while SEC was used in this thesis. Matejovič et al., observed that EVs isolated from liver had larger sizes (>200 nm) when isolated from cultured intact livers compared to smaller EVs with size range of 100-200 nm, isolated from digested liver tissues (Matejovič et al., 2021). These latter EVs were similar in size to the aortic tissue EVs isolated in these studies. After miR-125b-5p was found to be packaged into SMC-EVs and oxLDL treatment was responsible for its differential expression, EV-miR-125b-5p expression in serum of wt and APOE KO mice was examined. It was found that HFD resulted in lower miR-125b-5p levels, however, not statistically significant, in the serum EVs for both wt and APOE KO mice. Circulating levels of miR-125b-5p have also been reported to be increased in patients with ACS compared to healthy subjects (Jia et al., 2016). Other studies have highlighted that increased plasma miR-125b-5p expression was associated with unfavourable outcomes in stroke patients (He et al., 2019). Overall, these studies support the translational significance of further exploring the use of miR-125b-5p as a biomarker for atherosclerosis progression. EV-miR-125b-5p levels were also examined in secreted EVs from cultured aortic tissues. No significant change in EV-miR-125b-5p levels was observed in aortic tissue EVs from wt and APOE KO mice. However, secreted EVs from aortic tissues which could participate in cell-cell communication were successfully isolated and it was shown that miR-125b-5p is packaged in EVs from vascular cells.

MiR-25b-5p was identified to be endogenous cargo in SMC-EVs and it was shown that EVs with endogenous miR-125b-5p did not affected cell viability of recipient HCASMCs and HCAECs. Next key aspect of the thesis was the investigation of exogenous miR-125b-5p loading into EVs as to whether miR-125b-5p loaded EVs (miR-125b-5p-EVs) would regulate recipient cell viability, proliferation and

migration based on the pathway hypothesis formed previously. Electroporation was chosen to load EVs with miR-125b-5p. Although previous studies have suggested poor performance of the method (when comparing the number of copies of miRNA initially and the number of copies of miRNA being loaded into EVs) (Kooijmans et al., 2013), sufficient loading of cel-miR-39-3p and transfer of cel-miR-39-39-EV to HCASMCs was shown. Alternative methods of miRNA modulation in EVs allow the delivery and expression of high levels of miRNA in cells of interest and subsequent secretion of EVs encapsulating the over-expressed molecule. MiRNA modulation methods include genetic modification of EV-producing cells by transfection with miRNA-expressing plasmids or viral vectors loaded with pri-miRNA mimic or miRNA mimic or cell transfection with miRNA mimic using a transfection agent like lipofectamine. This approach can offer the advantage of accurate dosing of miRNAs incorporated into EVs (Martellucci et al., 2020). Electroporation also offers accurate loading dose of miRNA electroporated into EVs, however, leakage of cargo while EV pores are still open is a limitation associated with the process (Munir et al., 2020). Phenotypic switching of SMCs towards a proliferative and migrating phenotype has been considered as a key step during early atherogenesis (Bennett et al., 2016). SMC migration into the intima, during lesion formation, as well as, neointima formation following angioplasty, is common in humans (Allahverdian et al., 2018). Treatment with miR-125b-5p-EVs did not affect recipient HCASMC cell viability, as measured with MTT assay, however MTT assay may not be the best tool to study cell viability due to its low sensitivity (Hu et al., 2021). Preliminary evidence suggested that miR-125b-5p-EVs altered serum-induced proliferation of recipient HCASMCs and lower cell migration was observed after miR-125b-5p-EV treatment. However the data collected did not reach a statistical significance. Increasing the number of donor cells in future experiments could provide a robust conclusions. Further studies suggested that miR-125b-5p-EVs did not regulate gene expression of TP53, STAT3, SP1, PPP1CA, ERBB2 and ERRB3 at the EV dosage and timepoints used for these studies. Further studies are required to fully determine whether miR-125b-5p loaded EVs regulate cell proliferation and migration of vascular SMCs.

It was also observed that oxLDL treatment induced miR-125b-5p upregulation in HCASMCs and 48 hours later miR-125b-5p levels were found reduced. This initial miR-125b-5p upregulation could be a protective mechanism by HCASMCs against atherogenic stimulation. However, miR-125b-5p downregulation and decreased

levels of miR-125b-5p packaged into SMC-EVs could aggravate early atherosclerosis via a paracrine method of communication. This is a hypothesis which would require further investigation with *in vitro* experiments and *in vivo* studies. *In vitro* experiments could examine the effect of EVs loaded with antagomiR-125-5p and miR-125b-5p in disease related processes (cell proliferation, migration and SMC differentiation) in SMCs. Furthermore, *in vivo* studies of mice with atherosclerosis treated with the modulated EVs, described previously, could examine the effect of miR-125b-5p modulation in the progression of atherosclerosis. A similar observation was suggested by Nguyen et al., where authors reported that macrophages exposed to oxLDL secreted EVs which modulated macrophage migration (Nguyen et al., 2018). MSC-derived nanovesicles (artificially produced vesicles by serial extrusion through filters) were found enriched in miR-125b-5p (2-fold increase) and miR-100-5p (1.5 fold increase) and treatment with MSC-nanovesicles inhibited PDGF-induced proliferation, migration, and phenotype switching of pulmonary artery SMCs (PASMCs) (Hu et al., 2022). In this thesis, electroporation resulted in a 2000-fold increase of miR125b-5p levels in SMC-EVs. However since the relative expression levels were measured in these studies and in the studies by Hu et al., and not the copy number of miR-125b-5p, so it is not possible to determine if there is difference between the levels of miR-125b-5p in SMC-EVs and the published data on MSC-nanovesicles. All these studies support the idea that miR-125b-5p loaded EVs or anti-miR-125b-5p-EVs are worthwhile to investigate further regarding their potential for atherosclerosis treatment.

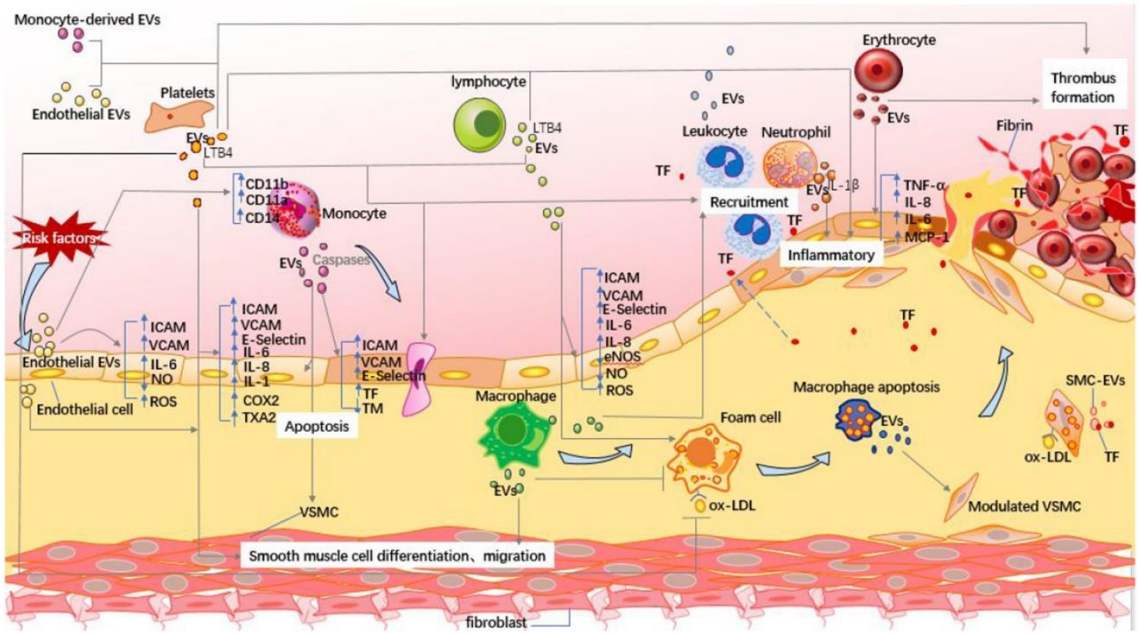

Figure 7-1 Overview of EVs in atherosclerosis

EVs participate in all stages of atherosclerosis progression, from early fatty streak to plaque destabilisation and thrombus formation. Adapted from ((Deng et al., 2019) published under a Creative Commons CC-BY license).

7.2 Future Perspectives

The initial aims of this thesis to understand if SMC-EV release would alter under an atherogenic environment and later study the EVs regarding their contribution to atherosclerosis development (Figure 7-1). Characterisation of EVs, mainly involved NTA analysis of particle size and particle concentration, analysis of protein concentration using Micro BCA™ Protein Assay and EV protein marker detection by western immunoblotting and finally imaging of EV structure using TEM, all of which are recommended methods of characterisation by ISEV (Théry et al., 2018). However, the MISEV 2018 guidelines suggest the use of EV markers ranging from 3-5 categories, and also including the detection of non-EV marker proteins, such as albumin or apolipoproteins often co-isolated with EVs as negative markers (Théry et al., 2018). In these studies, three EV markers (CD81, CD63 and Annexin A2) were detected, while the detection of a non-EV marker was not examined. However, it was found that oxLDL was not co-isolated with EVs or it was not encapsulated in SMC-EVs. Future studies would benefit from further EV characterisation via western blotting including investigation of non-EV markers. However, there are some limitations associated with this method of characterisation. The majority of EV isolation protocols will isolate a mixture of EV populations and there is not an established protein marker to distinguish them (Ramirez et al., 2018). More recent, studies have reported that the method of isolation can also impact the EV marker protein content (Gámez-Valero et al., 2016)(Allelein et al., 2021). There are other methods of EV marker detection gaining popularity and offering advantages like flow cytometry or ELISA (Serrano-Pertierra et al., 2020). ELISA is commonly used for protein, peptide or antibody detection and quantification of an antibody used to detect the target molecule (Serrano-Pertierra et al., 2020). Regarding EV research, ELISA can offer detection and quantification of cellular markers to identify the cellular source of EVs or functional EV proteins (Serrano-Pertierra et al., 2020). However, this method is not suitable for EV quantification due to EV heterogeneity, with EV subtypes demonstrating different membrane proteins (Serrano-Pertierra et al., 2020). Flow cytometry is a single cell analysis technique allowing detection and quantification where one or more fluorescent antibodies are used for target detection (Serrano-Pertierra et al., 2020). By attaching EVs to microbeads, proteins markers on EVs can be qualitatively and quantitatively studied, as well as enable identification of

proteins related to the cellular source of EVs, or proteins related to their function (Serrano-Pertierra et al., 2020).

HCASMCs stimulated with oxLDL were used to mimic the early atherogenic environment in the vessel wall. A low concentration of oxLDL was chosen so as to prevent cell death, however purchasing commercially oxidised LDL for this scale of experiments comes at a cost (John Liu et al., 2014). Even though oxLDL is a potent stimulator and key molecule involved in atherosclerosis progression, it had no effect on the EV release from HCASMCs, although oxLDL stimulation did alter the small RNA cargo of SMC-EVs. Future studies might benefit from either a slightly increased oxLDL concentration (e.g., 20 μg/mL) or an alternatively less costly stimulus. The higher oxLDL concentration (20 μg/mL) was not investigated to determine if it would cause cell death to recipient HCASMCs or other phenotypic changes. Perhaps a higher oxLDL concentration would alter the SMC-EV release and would result in an increased number of differentially expressed miRNAs. An alternative stimuli able to mimic early atherogenic conditions can be other lipids such as oxidised lipids, lipoprotein or shear stress (Reusch et al., 1996)(Ichikawa et al., 2002)(Pidkovka et al., 2007). Moreover, potentially less costly stimulus would involve cytokines like transforming growth factor ß (TGFß), PDGF, TNF-a or IL-6 that could be used in future studies and compare their effect on SMC-EV release to that of oxLDL (Tousoulis et al., 2016)(Lian et al., 2020)(Zhu et al., 2021). Moreover, comparison studies among the different pro-atherogenic stimuli mentioned above would potentially lead to different miRNAs being differentially expressed in EVs and identify specific miRNAs being induced or not by certain stimuli.

Small RNA sequencing of SMC-EVs after oxLDL stimulation identified miR-125b-5p, and 3 snRNAs, RNU2-7p, RNU2-29p and RNU2-57p to be upregulated. In these studies, the role of miR-125b-5p-EV transfer to recipient cells and its potential anti-migratory and anti-proliferative role was investigated. Future studies would explore the role of the previously identified U2 snRNAs and their implication in the disease progression. Small RNAs have gained a lot of interest as biomarkers for several pathologies. Research suggest that Ro-associated non-coding RNAs (RNYs) could be used as an independent diagnostic biomarker for CAD and atherosclerotic burden (Repetto et al., 2015). Furthermore, a different method to analyse data from the RNAseq experiment also identified two other miRNAs, miR-199b-5p and

miR-199a-5p, which were also found to be downregulated in SMC-EVs after oxLDL stimulation. Future studies could investigate the role of miR-199b-5p and miR-199a-5p (loaded EVs) in atherosclerosis progression. MiR-199a-5p has been suggested to regulate the NOS/NO pathway in the endothelium. MiRNA inhibition, with an antagomir, resulted in increased NO signalling and improved function of the endothelium (Joris et al., 2018). Another study reported that miR-199a is implicated in cardiac hypertrophy (Song et al., 2010). Authors showed increased miR-199a expression in rat hypertrophic hearts, whereas downregulation of miR-199a expression in cardiomyocytes (neonatal rat ventricular myocytes) reduced cell size in phenylephrine-stimulated cardiomyocytes (Song et al., 2010). A recent study examined the role of miR-199b-5p in EC apoptosis (Cui et al., 2022). Authors reported that oxLDL stimulation in HUVECs induced miR-199b-5p downregulation and apoptosis, while miR-199b-5p reversed the effect of oxLDL (Cui et al., 2022). Furthermore, miR-199a-3p and miR-199b-3p (tissue-specific miRNAs derived from internal thoracic artery of CAD patients undergoing coronary artery bypass grafting (CABG)) have been reported to significantly correlate with cardiovascular risk factors such as hypertension and hypercholesterolemia (Neiburga et al., 2021). The role of miR-199b and miR-199a encapsulated in EVs has also been studied. Circulating serum levels of EV-miR-199 have been examined in patients with acute-graft-versus-host disease (reaction of donor immune cells against host tissues after hematopoietic stem cell transplant). The EV-miR-199 levels at 14 days for post-transplant were found reduced compared to 0 days. The authors suggested that the role of EV-miR-199 in the acute-graft-versus-host disease biology required further investigation (Crossland et al., 2016b). Another study showed that treatment of APOE KO mice fed a HFD with EVs derived from oxLDL-induced THP-1 macrophages, which encapsulated miR-199a-5p, exacerbated atherosclerosis promotion. Increased plaque size in mice treated with EVs encapsulating miR-199a-5p was observed and authors suggested that miR-199a-5p could be a new target for treatment of arthrosclerosis, (Liang et al., 2022).

The results obtained from the analysis of serum EVs from wt and APOE KO mice suggest that HFD in APOE KO mice, which is a mouse model of experimental atherosclerosis, resulted in increased numbers of circulating particles is in agreement with the literature (Kang et al., 2019). Characterisation of serum EVs involved NTA analysis of particle size and particle concentration, analysis of protein concentration using Micro BCA™ Protein Assay and EV protein marker

detection by western immunoblotting, all of which are recommended methods of characterisation by ISEV (Théry et al., 2018). Further EV characterisation could involve analysis of EV structure by TEM and detection of the cellular source of isolated EVs from serum using flow cytometry. Characterisation of aortic tissue secreted EVs was performed only with NTA. Future studies would benefit from EV characterisation involving EV marker detection, imaging of EV structure using TEM, and finally detect the cellular origin of secreted tissue EVs. Moreover, it was found that HFD lowered EV-miR-125b-5p expression in serum from wt and from APOE KO mice, agreeing to a certain extent with the RNAseq data. Nonetheless, serum EVs contain a mixture of EVs from multiple cells/tissues and therefore likely a limited number of SMC-EVs can be found (Li et al., 2020). MiR-125b-5p expression in serum EVs was examined based on RNAseq data and showed that miR-125b-5p was packaged into SMC-EVs. Advantageous to the research could also be a further investigation from either a higher number of animals being studied, so that conclusive results can be derived for miR-125b-5p levels or alternatively microarray studies analysing the miRNA profile of serum EVs from wt and APOE KO mice. Moreover, a modified plan regarding high fat diet over a longer time frame could be used to investigate if that further modified miR-125b-5p levels. Based on the findings further future studies could benefit from the examination of the EV profile in other experimental models of atherosclerosis such as the LDLR KO mouse model fed a high fat diet or the AVV-mediated PCSK9-overexpression mouse model under a high fat diet (Ilyas et al., 2022)(Gisterå et al., 2022).

Studies regarding the aortic tissue secreted EVs from wt and APOE KO mice did not find any difference in EV profile or alterations in miR-125b-5p-EV levels. Characterisation of aortic tissue secreted EVs was performed only with NTA. Future studies would benefit from EV characterisation involving EV marker detection, imaging of EV structure using TEM, and finally detect the cellular origin of the vascular tissue secreted EVs. Identifying the cellular origin of aortic tissue EVs would help correlate the RNAseq data with our findings, suggesting that miR-125b-5p is packaged into EVs originating from cells in the vasculature.

These studies also analysed the functional effects of miR-125b-5p loaded VSMC-EVs *in vitro*. Although, no significant changes were observed, this could be attributed to many reasons which could be further investigated in future studies. MiR-125b-5p-EV treatment induced a significant reduction in cell proliferation (vs

control cells, not Naïve-EV treated cells) and did not alter migration of recipient HCASMCs. Potentially, increasing the concentration of mimic being loaded into the EVs, could induce a clearer response in recipient cells (Pomatto et al., 2019). Due to time commitments, only one dose of loaded EVs was tested to study cell viability, cell proliferation, migration and gene expression responses in recipient cells. A dose response and timepoint study could be beneficial for future studies. Another option would be to perform a pre-treatment with EVs before adding 5% FCS + EVs, as 5% FCS is a strong stimulus and would mask the effect of EV treatment. The scratch assay studies were performed in two sets of donor cells (n=4 replicates, 2 donor patients) and in addition increasing the number of donor cells would produce a clear result to determine whether miR-125b-5p-EVs inhibit HCASMC serum induced migration. Another limitation of using replicates of donor cells instead of increasing the number of donors, is that statistical analysis when using replicates is not possible. Moreover, one limitation of the scratch assay is that it cannot properly distinguish between proliferation-and/or migration-driven scratch closure (Vang Mouritzen and Jenssen, 2018). Future studies would also benefit from Boyden chamber migration analysis, where confounding effects of cell proliferation are not considered (Chen, 2005). In addition, future studies where all the previous parameters are optimised would benefit from the inclusion of miR-125b-5p inhibition via antagomir-loading into EVs and investigation of the functional effect of miR-125b-5p and anti-miR-125b-5p loaded EVs. These studies investigated the effect of miR125b-5p loaded EVs as the RNAseq identified miR-125b-5p was downregulated after oxLDL treatment. Therefore we forced the miRNA expression in the opposite direction. Moreover, miRNA mimic loading into EVs via electroporation was already optimised by Dr Lorraine Work's group (University of Glasgow). It would also be of interest to determine any downstream signalling of miR-125b-5p-EV treatment, since preliminary studies indicated that miR-125b-5p may not regulate gene expression of TP53, STAT3, SP1, PPP1CA, ERBB2 and ERRB3. Most importantly, the pathway hypothesis was formed based on 6 out of 303 gene targets generated by the bioinformatic analysis, so there are 297 potential gene targets of miR-125b-5p to be investigated. Moreover, a new bioinformatic analysis using a commercial pathway analysis software like ingenuity pathway analysis (IPA), could be helpful to offer more relevant enriched pathways. These tools could provide an interesting approach to from a pathway hypothesis. Another limitation of these studies was the inability to quiesce HCAECs as it caused

significant cell death. HCAECs were chosen as they are the other main cell type of the coronary arteries and are in intimate contact with VSMCs and therefore an appropriate cell type to investigate cell-cell communication with the HCASMC (Lakota et al., 2009). Another option would be the use of another endothelial cell type like HUVECs, however that would diminish the translational value of the studies. Finally, the preliminary *in vitro* studies would benefit from *in vivo* studies examining the effect of miR-125b-5p-EV modulation (antagomiR-125b-5p and miR-125b-5p mimic) in mice with experimental atherosclerosis.

One general limitation of this thesis was the use of replicates of donor cells instead of n=3 or more number of donor cells in some experiments. The caveat of not using n=3 or 4 number of donor cells did not allow statistical analysis of these experiments, thus diminishing the translational value of these experiments. These types of experiments are worth repeating with the appropriate n number of donor cells. Another limitation using donor cells, which has already been discussed, was the heterogeneity that introduced in results as EVs isolated from different donors showed heterogenous cell response to recipient cells.

The translational significance of the studies would be improved by the examination of serum miR-125b-5p-EV levels in patients with CAD or ACS vs healthy participants One limitation of these studies was that *in vitro* results were extrapolated to an animal model but not to clinical human samples. The mouse model of atherosclerosis offers a degree of relevance to humans but examining EV-miR-125b-5p levels in human samples would add greater value to translational perspectives of this study. Another set of experiments that would add translational value to this thesis, would be the examination of EVs isolated or secreted from atherosclerotic plaque specimens vs EVs isolated from non-atherosclerotic vessels. Healthy and diseased vessels could be cultured ex vivo similarly to animal aortic tissues in chapter 5 and EV characterisation and miR-125b-5p EV level detection could performed. These studies would offer insight into whether miR-125b-5p-EV levels could be considered for use as a future biomarker for the evaluation of CAD progression, or the detection of a coronary event in CAD patients.

7.3 Conclusions

In summary, the data in this thesis showed that oxLDL stimulation of HCASMCs did not alter SMC-EV release profiles, but did alter the small RNA cargo of secreted EVs with miR-125b-5p found to be downregulated and RNU2-7p, RNU2-29p, RNU2-57p found to be upregulated in EVs after oxLDL stimulation. Moreover, APOE KO mice with experimental atherosclerosis, demonstrated lower levels of miR-125b-5p in serum EVs, complementing the *in vitro* findings. Preliminary *in vitro* data of SMC-EVs loaded with miR-125b-5p suggested that serum-induced cell proliferation of vascular SMCs was significantly reduced (when compared to untreated cells and to Naïve-EV treated cells), although serum-induced cell migration was not altered after miR-125b-5p-EV treatment. Future studies are needed to elucidate the functional role of miR-125b-5p loaded EVs in the setting of atherosclerosis and answer the over-arching hypothesis of this thesis, that SMC-EVs during atherogenesis is a cell-controlled response.

References

't Hoen, P.A., Friedländer, M.R., Almlöf, J., Sammeth, M., Pulyakhina, I., Anvar, S.Y., Laros, J.F.J., Buermans, H.P.J., Karlberg, O., Brännvall, M., van Ommen, G.-J.B., Estivill, X., Guigó, R., Syvänen, A.-C., Gut, I.G., Dermitzakis, E.T., Antonarakis, S.E., Brazma, A., Flicek, P., Schreiber, S., Rosenstiel, P., Meitinger, T., Strom, T.M., Lehrach, H., Sudbrak, R., Carracedo, A., 't Hoen, P.A.C., Pulyakhina, I., Anvar, S.Y., Laros, J.F.J., Buermans, H.P.J., van Iterson, M., Friedländer, M.R., Monlong, J., Lizano, E., Bertier, G., Ferreira, P.G., Sammeth, M., Almlöf, J., Karlberg, O., Brännvall, M., Ribeca, P., Griebel, T., Beltran, S., Gut, M., Kahlem, K., Lappalainen, T., Giger, T., Ongen, H., Padioleau, I., Kilpinen, H., Gonzàlez-Porta, M., Kurbatova, N., Tikhonov, A., Greger, L., Barann, M., Esser, D., Häsler, R., Wieland, T., Schwarzmayr, T., Sultan, M., Amstislavskiy, V., den Dunnen, J.T., van Ommen, G.-J.B., Gut, I.G., Guigó, R., Estivill, X., Syvänen, A.-C., Dermitzakis, E.T., Lappalainen, T., Consortium, T.G., 2013. Reproducibility of high-throughput mRNA and small RNA sequencing across laboratories. Nat. Biotechnol. 31, 1015–1022.

Aaronson, S., Behrens, U., Orner, R., Haines, T.H., 1971. Ultrastructure of intracellular and extracellular vesicles, membranes, and myelin figures produced by Ochromonas danica. J. Ultrastruct. Res. 35, 418–430.

Abid Hussein, M.N., Nieuwland, R., Hau, C.M., Evers, L.M., Meesters, E.W., Sturk, A., 2005. Cell-derived microparticles contain caspase 3 in vitro and in vivo. J. Thromb. Haemost. 3, 888–896.

Abuzaid, A., Saad, M., Addoumieh, A., Ha, L.D., Elbadawi, A., Mahmoud, A.N., Elgendy, A., Abdelaziz, H.K., Barakat, A.F., Mentias, A., Adeola, O., Elgendy, I.Y., Qasim, A., Budoff, M., 2021. Coronary artery calcium score and risk of cardiovascular events without established coronary artery disease: a systemic review and meta-analysis. Coron. Artery Dis. 32, 317–328.

Afonyushkin, T., Binder, C.J., 2018. Extracellular Vesicles Act as Messengers of Macrophages Sensing Atherogenic Stimuli. Arterioscler. Thromb. Vasc. Biol. 38, 2–3.

Aharon, A., Tamari, T., Brenner, B., 2008. Monocyte-derived microparticles and exosomes induce procoagulant and apoptotic effects on endothelial cells.

Thromb. Haemost. 100, 878–885.

Akers, J.C., Gonda, D., Kim, R., Carter, B.S., Chen, C.C., 2013. Biogenesis of extracellular vesicles (EV): exosomes, microvesicles, retrovirus-like vesicles, and apoptotic bodies. J. Neurooncol. 113, 1–11.

Al-Nedawi, K., Meehan, B., Micallef, J., Lhotak, V., May, L., Guha, A., Rak, J., 2008. Intercellular transfer of the oncogenic receptor EGFRvIII by microvesicles derived from tumour cells. Nat. Cell Biol. 10, 619–624.

Allahverdian, S., Chaabane, C., Boukais, K., Francis, G.A., Bochaton-Piallat, M.-L., 2018. Smooth muscle cell fate and plasticity in atherosclerosis. Cardiovasc. Res. 114, 540–550.

Allahverdian, S., Chehroudi, A.C., McManus, B.M., Abraham, T., Francis, G.A., 2014. Contribution of Intimal Smooth Muscle Cells to Cholesterol Accumulation and Macrophage-Like Cells in Human Atherosclerosis. Circulation 129, 1551–1559.

Allelein, S., Medina-Perez, P., Lopes, A.L.H., Rau, S., Hause, G., Kölsch, A., Kuhlmeier, D., 2021. Potential and challenges of specifically isolating extracellular vesicles from heterogeneous populations. Sci. Rep. 11, 11585.

Amabile, N., Cheng, S., Renard, J.M., Larson, M.G., Ghorbani, A., McCabe, E., Griffin, G., Guerin, C., Ho, J.E., Shaw, S.Y., Cohen, K.S., Vasan, R.S., Tedgui, A., Boulanger, C.M., Wang, T.J., 2014. Association of circulating endothelial microparticles with cardiometabolic risk factors in the Framingham Heart Study. Eur. Heart J. 35, 2972–2979.

Ammann, K.R., DeCook, K.J., Li, M., Slepian, M.J., 2019. Migration versus proliferation as contributor to in vitro wound healing of vascular endothelial and smooth muscle cells. Exp. Cell Res. 376, 58–66.

Andreou, I., Sun, X., Stone, P.H., Edelman, E.R., Feinberg, M.W., 2015. miRNAs in atherosclerotic plaque initiation, progression, and rupture. Trends Mol. Med. 21, 307–318.

Aronow, H.D., Topol, E.J., Roe, M.T., Houghtaling, P.L., Wolski, K.E., Lincoff, A.M., Harrington, R.A., Califf, R.M., Ohman, E.M., Kleiman, N.S., Keltai, M., Wilcox, R.G., Vahanian, A., Armstrong, P.W., Lauer, M.S., 2001. Effect of lipid-lowering therapy on early mortality after acute coronary syndromes: an

observational study. Lancet 357, 1063–1068.

Arteaga, R.B., Chirinos, J.A., Soriano, A.O., Jy, W., Horstman, L., Jimenez, J.J., Mendez, A., Ferreira, A., de Marchena, E., Ahn, Y.S., 2006. Endothelial microparticles and platelet and leukocyte activation in patients with the metabolic syndrome. Am. J. Cardiol. 98, 70–74.

Asea, A., Jean-Pierre, C., Kaur, P., Rao, P., Linhares, I.M., Skupski, D., Witkin, S.S., 2008. Heat shock protein-containing exosomes in mid-trimester amniotic fluids. J. Reprod. Immunol. 79, 12–17.

Ásgeirsdóttir, S.A., van Solingen, C., Kurniati, N.F., Zwiers, P.J., Heeringa, P., van Meurs, M., Satchell, S.C., Saleem, M.A., Mathieson, P.W., Banas, B., Kamps, J.A.A.M., Rabelink, T.J., van Zonneveld, A.J., Molema, G., 2012. MicroRNA-126 contributes to renal microvascular heterogeneity of VCAM-1 protein expression in acute inflammation. Am. J. Physiol. Physiol. 302, F1630–F1639. https://doi.org/1

Asuka, N., Eri, K., Ryuji, Y., Hironori, Y., 2013. Exosomes Derived from Epstein-Barr Virus-Infected Cells Are Internalized via Caveola-Dependent Endocytosis and Promote Phenotypic Modulation in Target Cells. J. Virol. 87, 10334–10347.

Atienzar-Aroca, S., Flores-Bellver, M., Serrano-Heras, G., Martinez-Gil, N., Barcia, J.M., Aparicio, S., Perez-Cremades, D., Garcia-Verdugo, J.M., Diaz-Llopis, M., Romero, F.J., Sancho-Pelluz, J., 2016. Oxidative stress in retinal pigment epithelium cells increases exosome secretion and promotes angiogenesis in endothelial cells. J. Cell. Mol. Med. 20, 1457–1466.

Atkins, B.G., Jain, M.K., 2007. Role of Krüppel-Like Transcription Factors in Endothelial Biology. Circ. Res. 100, 1686–1695.

Auge, N., Garcia, V., Maupas-Schwalm, F., Levade, T., Salvayre, R., Negre-Salvayre, A., 2002. Oxidized LDL-Induced Smooth Muscle Cell Proliferation Involves the EGF Receptor/PI-3 Kinase/Akt and the Sphingolipid Signaling Pathways. Arterioscler. Thromb. Vasc. Biol. 22, 1990–1995.

Bäck, M., Hansson, G.K., 2015. Anti-inflammatory therapies for atherosclerosis. Nat. Rev. Cardiol. 12, 199–211.

Badimon, L., Padró, T., Vilahur, G., 2012. Atherosclerosis, platelets and thrombosis in acute ischaemic heart disease. Eur. Hear. journal. Acute

Cardiovasc. care 1, 60–74.

Baig, S., Lim, J.Y., Fernandis, A.Z., Wenk, M.R., Kale, A., Su, L.L., Biswas, A., Vasoo, S., Shui, G., Choolani, M., 2013. Lipidomic analysis of human placental syncytiotrophoblast microvesicles in adverse pregnancy outcomes. Placenta 34, 436–442.

Baigent, C., Blackwell, L., Emberson, J., Holland, L.E., Reith, C., Bhala, N., Peto, R., Barnes, E.H., Keech, A., Simes, J., Collins, R., 2010. Efficacy and safety of more intensive lowering of LDL cholesterol: a meta-analysis of data from 170,000 participants in 26 randomised trials. Lancet (London, England) 376, 1670–1681.

Baldari, S., Di Rocco, G., Magenta, A., Picozza, M., Toietta, G., 2019. Extracellular Vesicles–Encapsulated MicroRNA-125b Produced in Genetically Modified Mesenchymal Stromal Cells Inhibits Hepatocellular Carcinoma Cell Proliferation. Cells 8, 1560.

Bao, Q., Gong, L., Wang, J., Wen, J., Shen, Y., Zhang, W., 2018. Extracellular Vesicle RNA Sequencing Reveals Dramatic Transcriptomic Alterations Between Metastatic and Primary Osteosarcoma in a Liquid Biopsy Approach. Ann. Surg. Oncol. 25, 2642–2651.

Barberio, M.D., Kasselman, L.J., Playford, M.P., Epstein, S.B., Renna, H.A., Goldberg, M., DeLeon, J., Voloshyna, I., Barlev, A., Salama, M., Ferrante, S.C., Nadler, E.P., Mehta, N., Reiss, A.B., Freishtat, R.J., 2019. Cholesterol efflux alterations in adolescent obesity: role of adipose-derived extracellular vesical microRNAs. J. Transl. Med. 17, 232.

Barillari, G., Albonici, L., Incerpi, S., Bogetto, L., Pistritto, G., Volpi, A., Ensoli, B., Manzari, V., 2001. Inflammatory cytokines stimulate vascular smooth muscle cells locomotion and growth by enhancing alpha5beta1 integrin expression and function. Atherosclerosis 154, 377–385.

Barrett, T.J., 2020. Macrophages in Atherosclerosis Regression. Arterioscler. Thromb. Vasc. Biol. 40, 20–33.

Bea, F., Blessing, E., Bennett, B., Levitz, M., Wallace, E.P., Rosenfeld, M.E., 2002. Simvastatin Promotes Atherosclerotic Plaque Stability in ApoE-Deficient Mice Independently of Lipid Lowering. Arterioscler. Thromb. Vasc. Biol. 22, 1832–

1837.

Beery, A.K., 2018. Inclusion of females does not increase variability in rodent research studies. Curr. Opin. Behav. Sci. 23, 143–149.

Bell, C.R., Jones, L.B., Crenshaw, B.J., Kumar, S., Rowe, G.C., Sims, B., Javan, G.T., Matthews, Q.L., 2019. The Role of Lipopolysaccharide-Induced Extracellular Vesicles in Cardiac Cell Death. Biology (Basel). 8, 69.

Benedikter, B.J., Bouwman, F.G., Heinzmann, A.C.A., Vajen, T., Mariman, E.C., Wouters, E.F.M., Savelkoul, P.H.M., Koenen, R.R., Rohde, G.G.U., van Oerle, R., Spronk, H.M., Stassen, F.R.M., 2019. Proteomic analysis reveals procoagulant properties of cigarette smoke-induced extracellular vesicles. J. Extracell. Vesicles 8, 1585163.

Benedikter, B.J., Bouwman, F.G., Vajen, T., Heinzmann, A.C.A., Grauls, G., Mariman, E.C., Wouters, E.F.M., Savelkoul, P.H., Lopez-Iglesias, C., Koenen, R.R., Rohde, G.G.U., Stassen, F.R.M., 2017. Ultrafiltration combined with size exclusion chromatography efficiently isolates extracellular vesicles from cell culture media for compositional and functional studies. Sci. Rep. 7, 15297.

Bennett, M.R., Evan, G.I., Schwartz, S.M., 1995. Apoptosis of human vascular smooth muscle cells derived from normal vessels and coronary atherosclerotic plaques. J. Clin. Invest. 95, 2266–2274.

Bennett, M.R., Sanjay, S., Owens, G.K., 2016. Vascular Smooth Muscle Cells in Atherosclerosis. Circ. Res. 118, 692–702.

Bentzon, J.F., Otsuka, F., Virmani, R., Falk, E., 2014. Mechanisms of Plaque Formation and Rupture. Circ. Res. 114, 1852–1866.

Bergheanu, S.C., Bodde, M.C., Jukema, J.W., 2017. Pathophysiology and treatment of atherosclerosis. Netherlands Hear. J. 25, 231–242.

Bernal-Mizrachi, L., Jy, W., Jimenez, J.J., Pastor, J., Mauro, L.M., Horstman, L.L., de Marchena, E., Ahn, Y.S., 2003. High levels of circulating endothelial microparticles in patients with acute coronary syndromes. Am. Heart J. 145, 962–970.

BHF, 2021. No Title [WWW Document]. URL https://www.bhf.org.uk/what-we-do/our-research/heart-statistics

Bi, S., Wang, C., Jin, Y., Lv, Z., Xing, X., Lu, Q., 2015. Correlation between serum exosome derived miR-208a and acute coronary syndrome. Int. J. Clin. Exp. Med. 8, 4275–4280.

Biasucci, L.M., Porto, I., Di Vito, L., De Maria, G.L., Leone, A.M., Tinelli, G., Tritarelli, A., Di Rocco, G., Snider, F., Capogrossi, M.C., Crea, F., 2012. Differences in microparticle release in patients with acute coronary syndrome and stable angina. Circ. J. 76, 2174–2182.

Bissig, C., Gruenberg, J., 2014. ALIX and the multivesicular endosome: ALIX in Wonderland. Trends Cell Biol. 24, 19–25.

Blaser, M.C., Buffolo, F., Halu, A., Schlotter, F., Higashi, H., Pantano, L., Saddic, L.A., Atkins, S.K., Rogers, M.A., Pham, T., Shvartz, E., Sukhova, G.K., Monticone, S., Camussi, G., Body, S.C., Muehlschlegel, J.D., Singh, S.A., Aikawa, M., Aikawa, E., 2020. Conserved and Divergent Modulation of Calcification in Atherosclerosis and Aortic Valve Disease by Tissue Extracellular Vesicles. bioRxiv 2020.04.02.022525.

Bobryshev, Y. V, Killingsworth, M.C., Orekhov, A.N., 2013. Increased shedding of microvesicles from intimal smooth muscle cells in athero-prone areas of the human aorta: implications for understanding of the predisease stage. Pathobiology 80, 24–31.

Bohula, E.A., Giugliano, R.P., Leiter, L.A., Verma, S., Park, J.-G., Sever, P.S., Lira Pineda, A., Honarpour, N., Wang, H., Murphy, S.A., Keech, A., Pedersen, T.R., Sabatine, M.S., 2018. Inflammatory and Cholesterol Risk in the FOURIER Trial. Circulation 138, 131–140.

Böing, A.N., Hau, C.M., Sturk, A., Nieuwland, R., 2008. Platelet microparticles contain active caspase 3. Platelets 19, 96–103.

Böing, A.N., van der Pol, E., Grootemaat, A.E., Coumans, F.A.W., Sturk, A., Nieuwland, R., 2014. Single-step isolation of extracellular vesicles by size-exclusion chromatography. J. Extracell. Vesicles 3, 23430.

Bonetti, P.O., Lerman, L.O., Lerman, A., 2003. Endothelial Dysfunction. Arterioscler. Thromb. Vasc. Biol. 23, 168–175.

Bonucci, E., 1970. Fine structure and histochemistry of “calcifying globules” in epiphyseal cartilage. Zeitschrift für Zellforsch. und Mikroskopische Anat. 103,

192–217.

Boon, R.A., Seeger, T., Heydt, S., Fischer, A., Hergenreider, E., Horrevoets, A.J.G., Vinciguerra, M., Rosenthal, N., Sciacca, S., Pilato, M., van Heijningen, P., Essers, J., Brandes, R.P., Zeiher, A.M., Dimmeler, S., 2011. MicroRNA-29 in Aortic Dilation: Implications for Aneurysm Formation. Circ. Res. 109, 1115–1119.

Borén, J., Chapman, M.J., Krauss, R.M., Packard, C.J., Bentzon, J.F., Binder, C.J., Daemen, M.J., Demer, L.L., Hegele, R.A., Nicholls, S.J., Nordestgaard, B.G., Watts, G.F., Bruckert, E., Fazio, S., Ference, B.A., Graham, I., Horton, J.D., Landmesser, U., Laufs, U., Masana, L., Pasterkamp, G., Raal, F.J., Ray, K.K., Schunkert, H., Taskinen, M.-R., van de Sluis, B., Wiklund, O., Tokgozoglu, L., Catapano, A.L., Ginsberg, H.N., 2020. Low-density lipoproteins cause atherosclerotic cardiovascular disease: pathophysiological, genetic, and therapeutic insights: a consensus statement from the European Atherosclerosis Society Consensus Panel. Eur. Heart J. 41, 2313–2330.

Boström, K.I., Yao, J., Guihard, P.J., Blazquez-Medela, A.M., Yao, Y., 2016. Endothelial-mesenchymal transition in atherosclerotic lesion calcification. Atherosclerosis 253, 124–127.

Botts, S.R., Raju, S., Prajapati, K., Breda, L.C.D., Fish, J.E., Howe, K.L., 2022. Extracellular Vesicle-derived MicroRNAs From Human Abdominal Aortic Aneurysm Associate With Proaneurysmal Cell Signaling and Senescence Pathways. J. Vasc. Surg. 75, e247.

Boulanger, C.M., Loyer, X., Rautou, P.-E., Amabile, N., 2017. Extracellular vesicles in coronary artery disease. Nat. Rev. Cardiol. 14, 259–272.

Brautbar, A., Leary, E., Rasmussen, K., Wilson, D.P., Steiner, R.D., Virani, S., 2015. Genetics of Familial Hypercholesterolemia. Curr. Atheroscler. Rep. 17, 20.

Briot, A., Jaroszewicz, A., Warren, C.M., Lu, J., Touma, M., Rudat, C., Hofmann, J.J., Airik, R., Weinmaster, G., Lyons, K., Wang, Y., Kispert, A., Pellegrini, M., Iruela-Arispe, M.L., 2014. Repression of Sox9 by Jag1 is continuously required to suppress the default chondrogenic fate of vascular smooth muscle cells. Dev. Cell 31, 707–721.

Brodsky, S. V, Zhang, F., Nasjletti, A., Goligorsky, M.S., 2004. Endothelium-derived microparticles impair endothelial function in vitro. Am. J. Physiol. Heart Circ. Physiol. 286, H1910-5.

Bronisz, A., Godlewski, J., Chiocca, E.A., 2016. Extracellular Vesicles and MicroRNAs: Their Role in Tumorigenicity and Therapy for Brain Tumors. Cell. Mol. Neurobiol. 36, 361–376.

Brümmer, A., Hausser, J., 2014. MicroRNA binding sites in the coding region of mRNAs: extending the repertoire of post-transcriptional gene regulation. Bioessays 36, 617–626.

Brzozowski, J.S., Jankowski, H., Bond, D.R., McCague, S.B., Munro, B.R., Predebon, M.J., Scarlett, C.J., Skelding, K.A., Weidenhofer, J., 2018. Lipidomic profiling of extracellular vesicles derived from prostate and prostate cancer cell lines. Lipids Health Dis. 17, 211.

Budoff, M.J., Shaw, L.J., Liu, S.T., Weinstein, S.R., Mosler, T.P., Tseng, P.H., Flores, F.R., Callister, T.Q., Raggi, P., Berman, D.S., 2007. Long-term prognosis associated with coronary calcification: observations from a registry of 25,253 patients. J. Am. Coll. Cardiol. 49, 1860–1870.

Buendía, P., Montes de Oca, A., Madueño, J.A., Merino, A., Martín-Malo, A., Aljama, P., Ramírez, R., Rodríguez, M., Carracedo, J., 2015. Endothelial microparticles mediate inflammation-induced vascular calcification. FASEB J. 29, 173–181.

Bukhari, S.I.A., Truesdell, S.S., Lee, S., Kollu, S., Classon, A., Boukhali, M., Jain, E., Mortensen, R.D., Yanagiya, A., Sadreyev, R.I., Haas, W., Vasudevan, S., 2016. A Specialized Mechanism of Translation Mediated by FXR1a-Associated MicroRNP in Cellular Quiescence. Mol. Cell 61, 760–773.

Buschow, S.I., Liefhebber, J.M.P., Wubbolts, R., Stoorvogel, W., 2005. Exosomes contain ubiquitinated proteins. Blood Cells. Mol. Dis. 35, 398–403.

Buschow, S.I., Nolte-‘t Hoen, E.N.M., Van Niel, G., Pols, M.S., Ten Broeke, T., Lauwen, M., Ossendorp, F., Melief, C.J.M., Raposo, G., Wubbolts, R., Wauben, M.H.M., Stoorvogel, W., 2009. MHC II in Dendritic Cells is Targeted to Lysosomes or T Cell-Induced Exosomes Via Distinct Multivesicular Body Pathways. Traffic 10, 1528–1542.

Byrne, P., Demasi, M., Smith, S.M., 2021. NICE guidance on inclisiran should be reconsidered. BMJ 375, n2462.

Cai, J., Han, Y., Ren, H., Chen, C., He, D., Zhou, L., Eisner, G.M., Asico, L.D., Jose, P.A., Zeng, C., 2013. Extracellular vesicle-mediated transfer of donor genomic DNA to recipient cells is a novel mechanism for genetic influence between cells. J. Mol. Cell Biol. 5, 227–238.

Canault, M., Leroyer, A.S., Peiretti, F., Lesèche, G., Tedgui, A., Bonardo, B., Alessi, M.-C., Boulanger, C.M., Nalbone, G., 2007. Microparticles of human atherosclerotic plaques enhance the shedding of the tumor necrosis factor-alpha converting enzyme/ADAM17 substrates, tumor necrosis factor and tumor necrosis factor receptor-1. Am. J. Pathol. 171, 1713–1723.

Cannon, C.P., Cariou, B., Blom, D., McKenney, J.M., Lorenzato, C., Pordy, R., Chaudhari, U., Colhoun, H.M., 2015. Efficacy and safety of alirocumab in high cardiovascular risk patients with inadequately controlled hypercholesterolaemia on maximally tolerated doses of statins: the ODYSSEY COMBO II randomized controlled trial. Eur. Heart J. 36, 1186–1194.

Cao, J.Y., Wang, B., Tang, T.T., Wen, Y., Li, Z.L., Feng, S.T., Wu, M., Liu, D., Yin, D., Ma, K.L., Tang, R.N., Wu, Q.L., Lan, H.Y., Lv, L.L., Liu, B.C., 2021. Exosomal miR-125b-5p deriving from mesenchymal stem cells promotes tubular repair by suppression of p53 in ischemic acute kidney injury. Theranostics 11, 5248–5266.

Carbonetti, G., Wilpshaar, T., Kroonen, J., Studholme, K., Converso, C., D'Oelsnitz, S., Kaczocha, M., 2019. FABP5 coordinates lipid signaling that promotes prostate cancer metastasis. Sci. Rep. 9, 18944.

Cenariu, D., Zimta, A.-A., Munteanu, R., Onaciu, A., Moldovan, C.S., Jurj, A., Raduly, L., Moldovan, A., Florea, A., Budisan, L., Pop, L.A., Magdo, L., Albu, M.T., Tonea, R.B., Muresan, M.-S., Ionescu, C., Petrut, B., Buiga, R., Irimie, A., Gulei, D., Berindan-Neagoe, I., 2021. Hsa-miR-125b Therapeutic Role in Colon Cancer Is Dependent on the Mutation Status of the TP53 Gene. Pharmaceutics 13, 664.

Cha, D.J., Franklin, J.L., Dou, Y., Liu, Q., Higginbotham, J.N., Demory Beckler, M., Weaver, A.M., Vickers, K., Prasad, N., Levy, S., Zhang, B., Coffey, R.J., Patton, J.G., 2015. KRAS-dependent sorting of miRNA to exosomes. Elife 4,

e07197.

Chairoungdua, A., Smith, D.L., Pochard, P., Hull, M., Caplan, M.J., 2010. Exosome release of ß-catenin: a novel mechanism that antagonizes Wnt signaling. J. Cell Biol. 190, 1079–1091.

Chang, Y.-J., Li, Y.-S., Wu, C.-C., Wang, K.-C., Huang, T.-C., Chen, Z., Chien, S., 2019. Extracellular MicroRNA-92a Mediates Endothelial Cell-Macrophage Communication. Arterioscler. Thromb. Vasc. Biol. 39, 2492–2504.

Chao, C.-T., Yeh, H.-Y., Yuan, T.-H., Chiang, C.-K., Chen, H.-W., 2019. MicroRNA-125b in vascular diseases: An updated systematic review of pathogenetic implications and clinical applications. J. Cell. Mol. Med. 23, 5884–5894.

Charla, E., Mercer, J., Maffia, P., Nicklin, S.A., 2020. Extracellular vesicle signalling in atherosclerosis. Cell. Signal. 75, 109751.

Charo, I.F., Taub, R., 2011. Anti-inflammatory therapeutics for the treatment of atherosclerosis. Nat. Rev. Drug Discov. 10, 365–376.

Chartoumpekis, D. V, Zaravinos, A., Ziros, P.G., Iskrenova, R.P., Psyrogiannis, A.I., Kyriazopoulou, V.E., Habeos, I.G., 2012. Differential expression of microRNAs in adipose tissue after long-term high-fat diet-induced obesity in mice. PLoS One 7, e34872.

Chattopadhyay, A., Kwartler, C.S., Kaw, K., Li, Y., Kaw, A., Chen, J., LeMaire, S.A., Shen, Y.H., Milewicz, D.M., 2021. Cholesterol-Induced Phenotypic Modulation of Smooth Muscle Cells to Macrophage/Fibroblast–like Cells Is Driven by an Unfolded Protein Response. Arterioscler. Thromb. Vasc. Biol. 41, 302–316.

Chellan, B., Rojas, E., Zhang, C., Hofmann Bowman, M.A., 2018. Enzyme-modified non-oxidized LDL (ELDL) induces human coronary artery smooth muscle cell transformation to a migratory and osteoblast-like phenotype. Sci. Rep. 8, 11954.

Chen, H.-C., 2005. Boyden Chamber Assay BT - Cell Migration: Developmental Methods and Protocols, in: Guan, J.-L. (Ed.), . Humana Press, Totowa, NJ, pp. 15–22.

Chen, J., Tung, C.-H., Mahmood, U., Ntziachristos, V., Gyurko, R., Fishman, M.C.,

Huang, P.L., Weissleder, R., 2002. In Vivo Imaging of Proteolytic Activity in Atherosclerosis. Circulation 105, 2766–2771.

Chen, N.X., O'Neill, K.D., Moe, S.M., 2018. Matrix vesicles induce calcification of recipient vascular smooth muscle cells through multiple signaling pathways. Kidney Int. 93, 343–354.

Chen, P.-Y., Qin, L., Baeyens, N., Li, G., Afolabi, T., Budatha, M., Tellides, G., Schwartz, M.A., Simons, M., 2015. Endothelial-to-mesenchymal transition drives atherosclerosis progression. J. Clin. Invest. 125, 4514–4528.

Chen, Q., Liu, Y., Ding, X., Li, Q., Qiu, F., Wang, M., Shen, Z., Zheng, H., Fu, G., 2020. Bone marrow mesenchymal stem cell-secreted exosomes carrying microRNA-125b protect against myocardial ischemia reperfusion injury via targeting SIRT7. Mol. Cell. Biochem. 465, 103–114.

Chen, Q., Lv, J., Yang, W., Xu, B., Wang, Z., Yu, Z., Wu, J., Yang, Y., Han, Y., 2019. Targeted inhibition of STAT3 as a potential treatment strategy for atherosclerosis. Theranostics 9, 6424–6442.

Chen, Y., Wang, X., 2020. miRDB: an online database for prediction of functional microRNA targets. Nucleic Acids Res. 48, D127–D131.

Cherepanova, O.A., Pidkovka, N.A., Sarmento, O.F., Yoshida, T., Gan, Q., Adiguzel, E., Bendeck, M.P., Berliner, J., Leitinger, N., Owens, G.K., 2009. Oxidized Phospholipids Induce Type VIII Collagen Expression and Vascular Smooth Muscle Cell Migration. Circ. Res. 104, 609–618.

Chettimada, S., Lorenz, D.R., Misra, V., Wolinsky, S.M., Gabuzda, D., 2020. Small RNA sequencing of extracellular vesicles identifies circulating miRNAs related to inflammation and oxidative stress in HIV patients. BMC Immunol. 21, 57.

Chevallier, J., Chamoun, Z., Jiang, G., Prestwich, G., Sakai, N., Matile, S., Parton, R.G., Gruenberg, J., 2008. Lysobisphosphatidic acid controls endosomal cholesterol levels. J. Biol. Chem. 283, 27871–27880.

Chevillet, J.R., Kang, Q., Ruf, I.K., Briggs, H.A., Vojtech, L.N., Hughes, S.M., Cheng, H.H., Arroyo, J.D., Meredith, E.K., Gallichotte, E.N., Pogosova-Agadjanyan, E.L., Morrissey, C., Stirewalt, D.L., Hladik, F., Yu, E.Y., Higano, C.S., Tewari, M., 2014. Quantitative and stoichiometric analysis of the microRNA content of exosomes. Proc. Natl. Acad. Sci. U. S. A. 111, 14888–

14893.

Chiabotto, G., Gai, C., Deregibus, M.C., Camussi, G., 2019. Salivary Extracellular Vesicle-Associated exRNA as Cancer Biomarker. Cancers (Basel). 11, 891.

Chistiakov, D.A., Melnichenko, A.A., Grechko, A. V, Myasoedova, V.A., Orekhov, A.N., 2018. Potential of anti-inflammatory agents for treatment of atherosclerosis. Exp. Mol. Pathol. 104, 114–124.

Chistiakov, D.A., Orekhov, A.N., Bobryshev, Y. V, 2015. Vascular smooth muscle cell in atherosclerosis. Acta Physiol. 214, 33–50.

Chong, S.Y., Lee, C.K., Huang, C., Ou, Y.H., Charles, C.J., Richards, A.M., Neupane, Y.R., Pavon, M. V, Zharkova, O., Pastorin, G., Wang, J.-W., 2019. Extracellular Vesicles in Cardiovascular Diseases: Alternative Biomarker Sources, Therapeutic Agents, and Drug Delivery Carriers. Int. J. Mol. Sci.

Choy, J.C., Granville, D.J., Hunt, D.W.C., McManus, B.M., 2001. Endothelial Cell Apoptosis: Biochemical Characteristics and Potential Implications for Atherosclerosis. J. Mol. Cell. Cardiol. 33, 1673–1690.

Cipollone, F., Felicioni, L., Sarzani, R., Ucchino, S., Spigonardo, F., Mandolini, C., Malatesta, S., Bucci, M., Mammarella, C., Santovito, D., de Lutiis, F., Marchetti, A., Mezzetti, A., Buttitta, F., 2011. A unique microRNA signature associated with plaque instability in humans. Stroke 42, 2556–2563.

Clague, M.J., Liu, H., Urbé, S., 2012. Governance of endocytic trafficking and signaling by reversible ubiquitylation. Dev. Cell 23, 457–467.

Clarke, M.C.H., Littlewood, T.D., Figg, N., Maguire, J.J., Davenport, A.P., Goddard, M., Bennett, M.R., 2008. Chronic Apoptosis of Vascular Smooth Muscle Cells Accelerates Atherosclerosis and Promotes Calcification and Medial Degeneration. Circ. Res. 102, 1529–1538.

Climent, M., Quintavalle, M., Miragoli, M., Chen, J., Condorelli, G., Elia, L., 2015. TGFß Triggers miR-143/145 Transfer From Smooth Muscle Cells to Endothelial Cells, Thereby Modulating Vessel Stabilization. Circ. Res. 116, 1753–1764.

Collaboration*, T.E.R.F., 2012. Lipid-Related Markers and Cardiovascular Disease Prediction. JAMA 307, 2499–2506.

Collins, R.F., Touret, N., Kuwata, H., Tandon, N.N., Grinstein, S., Trimble, W.S.,

2009. Uptake of oxidized low density lipoprotein by CD36 occurs by an actin-dependent pathway distinct from macropinocytosis. J. Biol. Chem. 284, 30288–30297.

Colombo, M., Moita, C., van Niel, G., Kowal, J., Vigneron, J., Benaroch, P., Manel, N., Moita, L.F., Théry, C., Raposo, G., 2013. Analysis of ESCRT functions in exosome biogenesis, composition and secretion highlights the heterogeneity of extracellular vesicles. J. Cell Sci. 126, 5553–5565.

Colombo, M., Raposo, G., Théry, C., 2014. Biogenesis, secretion, and intercellular interactions of exosomes and other extracellular vesicles. Annu. Rev. Cell Dev. Biol. 30, 255–289.

Cordes, K.R., Sheehy, N.T., White, M.P., Berry, E.C., Morton, S.U., Muth, A.N., Lee, T.-H., Miano, J.M., Ivey, K.N., Srivastava, D., 2009. miR-145 and miR-143 regulate smooth muscle cell fate and plasticity. Nature 460, 705–710.

Cory, G., 2011. Scratch-wound assay. Methods Mol. Biol. 769, 25–30.

Crane, A.M., Bhattacharya, S.K., 2013. The use of bromodeoxyuridine incorporation assays to assess corneal stem cell proliferation. Methods Mol. Biol. 1014, 65–70.

Crossland, R.E., Norden, J., Bibby, L.A., Davis, J., Dickinson, A.M., 2016a. Evaluation of optimal extracellular vesicle small RNA isolation and qRT-PCR normalisation for serum and urine. J. Immunol. Methods 429, 39–49.

Crossland, R.E., Norden, J., Pearce, K.F., Kralj Juric, M., Lendrem, C., Bibby, L.A., Collin, M., Greinix, H.T., Dickinson, A.M., 2016b. Serum and Extracellular Vesicle Micrornas MiR-423, MiR-199 and MiR-93* As Biomarkers for Acute Graft Versus Host Disease. Blood 128, 4545.

Cui, R.-R., Li, S.-J., Liu, L.-J., Yi, L., Liang, Q.-H., Zhu, X., Liu, G.-Y., Liu, Y., Wu, S.-S., Liao, X.-B., Yuan, L.-Q., Mao, D.-A., Liao, E.-Y., 2012. MicroRNA-204 regulates vascular smooth muscle cell calcification in vitro and in vivo. Cardiovasc. Res. 96, 320–329.

Cui, X., Tian, Y., Zhao, Y., Gao, H., Yao, D., Liu, L., Li, Y., 2022. miR-199b-5p-AKAP1-DRP1 Pathway Plays a Key Role in ox-LDL-induced Mitochondrial Fission and Endothelial Apoptosis. Curr. Pharm. Biotechnol. 23, 1612–1622.

Cushing, S.D., Berliner, J.A., Valente, A.J., Territo, M.C., Navab, M., Parhami, F., Gerrity, R., Schwartz, C.J., Fogelman, A.M., 1990. Minimally modified low density lipoprotein induces monocyte chemotactic protein 1 in human endothelial cells and smooth muscle cells. Proc. Natl. Acad. Sci. U. S. A. 87, 5134–5138.

Cybulsky, M.I., Gimbrone, M.A.J., 1991. Endothelial expression of a mononuclear leukocyte adhesion molecule during atherogenesis. Science 251, 788–791.

Daniel, J.-M., Dutzmann, J., Bielenberg, W., Widmer-Teske, R., Gündüz, D., Hamm, C.W., Sedding, D.G., 2012. Inhibition of STAT3 signaling prevents vascular smooth muscle cell proliferation and neointima formation. Basic Res. Cardiol. 107, 261.

Davignon, J., Ganz, P., 2004. Role of Endothelial Dysfunction in Atherosclerosis. Circulation 109, III-27-III–32.

de Gonzalo-Calvo, D., Cenarro, A., Garlaschelli, K., Pellegatta, F., Vilades, D., Nasarre, L., Camino-Lopez, S., Crespo, J., Carreras, F., Leta, R., Catapano, A.L., Norata, G.D., Civeira, F., Llorente-Cortes, V., 2017. Translating the microRNA signature of microvesicles derived from human coronary artery smooth muscle cells in patients with familial hypercholesterolemia and coronary artery disease. J. Mol. Cell. Cardiol. 106, 55–67.

Del Turco, S., Basta, G., Mazzarisi, A., Battaglia, D., Navarra, T., Coceani, M., Bianchi, M., Schlueter, M., Marraccini, P., 2014. Procoagulant activity of circulating microparticles is associated with the presence of moderate calcified plaque burden detected by multislice computed tomography. J. Geriatr. Cardiol. 11, 13–19.

Deng, S., Wang, H., Jia, C., Zhu, S., Chu, X., Ma, Q., Wei, J., Chen, E., Zhu, W., Macon, C.J., Jayaweera, D.T., Dykxhoorn, D.M., Dong, C., 2017. MicroRNA-146a Induces Lineage-Negative Bone Marrow Cell Apoptosis and Senescence by Targeting Polo-Like Kinase 2 Expression. Arterioscler. Thromb. Vasc. Biol. 37, 280–290.

Deng, W., Tang, T., Hou, Y., Zeng, Q., Wang, Y., Fan, W., Qu, S., 2019. Extracellular vesicles in atherosclerosis. Clin. Chim. Acta 495, 109–117.

Densmore, J.C., Signorino, P.R., Ou, J., Hatoum, O.A., Rowe, J.J., Shi, Y., Kaul,

S., Jones, D.W., Sabina, R.E., Pritchard, K.A.J., Guice, K.S., Oldham, K.T., 2006. Endothelium-derived microparticles induce endothelial dysfunction and acute lung injury. Shock 26, 464–471.

Desai, M.Y., Nasir, K., Braunstein, J.B., Rumberger, J.A., Post, W.S., Budoff, M.J., Blumenthal, R.S., 2004. Underlying risk factors incrementally add to the standard risk estimate in detecting subclinical atherosclerosis in low- and intermediate-risk middle-aged asymptomatic individuals. Am. Heart J. 148, 871–877.

Dharap, A., Pokrzywa, C., Murali, S., Pandi, G., Vemuganti, R., 2013. MicroRNA miR-324-3p Induces Promoter-Mediated Expression of RelA Gene. PLoS One 8, e79467.

Di Gregoli, K., Jenkins, N., Salter, R., White, S., Newby, A.C., Johnson, J.L., 2014. MicroRNA-24 Regulates Macrophage Behavior and Retards Atherosclerosis. Arterioscler. Thromb. Vasc. Biol. 34, 1990–2000.

Di Pietro, N., Formoso, G., Pandolfi, A., 2016. Physiology and pathophysiology of oxLDL uptake by vascular wall cells in atherosclerosis. Vascul. Pharmacol. 84, 1–7.

Dignat-George, F., Boulanger, C.M., 2011. The many faces of endothelial microparticles. Arterioscler. Thromb. Vasc. Biol. 31, 27–33.

Ding, Y., Sun, Z., Zhang, S., Han, X., Li, Y., Xu, Q., Zhou, L., Xu, H., Bai, Y., Xu, C., Ding, H., Ge, Y., Wang, W., 2020. Down-regulation of small nuclear RNA (snRNA) RNU5E-1 in hepatocellular carcinoma presents with vital clinical significance. J. Gastrointest. Oncol. 11, 738–746.

Distler, J.H.W., Huber, L.C., Hueber, A.J., Reich, C.F. 3rd, Gay, S., Distler, O., Pisetsky, D.S., 2005. The release of microparticles by apoptotic cells and their effects on macrophages. Apoptosis 10, 731–741.

Dolz, S., Górriz, D., Tembl, J.I., Sánchez, D., Fortea, G., Parkhutik, V., Lago, A., 2017. Circulating MicroRNAs as Novel Biomarkers of Stenosis Progression in Asymptomatic Carotid Stenosis. Stroke 48, 10–16.

Donners, M.M.P.C., Wolfs, I.M.J., Stöger, L.J., van der Vorst, E.P.C., Pöttgens, C.C.H., Heymans, S., Schroen, B., Gijbels, M.J.J., de Winther, M.P.J., 2012. Hematopoietic miR155 deficiency enhances atherosclerosis and decreases

plaque stability in hyperlipidemic mice. PLoS One 7, e35877.

Dores, M.R., Grimsey, N.J., Mendez, F., Trejo, J., 2016. ALIX Regulates the Ubiquitin-Independent Lysosomal Sorting of the P2Y1 Purinergic Receptor via a YPX3L Motif. PLoS One 11, e0157587.

Du, F., Yu, F., Wang, Y., Hui, Y., Carnevale, K., Fu, M., Lu, H., Fan, D., 2014. MicroRNA-155 deficiency results in decreased macrophage inflammation and attenuated atherogenesis in apolipoprotein E-deficient mice. Arterioscler. Thromb. Vasc. Biol. 34, 759–767.

Durak-Kozica, M., Baster, Z., Kubat, K., Stępień, E., 2018. 3D visualization of extracellular vesicle uptake by endothelial cells. Cell. Mol. Biol. Lett. 23, 57.

Dzau, V.J., Braun-Dullaeus, R.C., Sedding, D.G., 2002. Vascular proliferation and atherosclerosis: New perspectives and therapeutic strategies. Nat. Med. 8, 1249–1256.

Edgar, J.R., Eden, E.R., Futter, C.E., 2014. Hrs- and CD63-Dependent Competing Mechanisms Make Different Sized Endosomal Intraluminal Vesicles. Traffic 15, 197–211.

El-Khoury, V., Pierson, S., Kaoma, T., Bernardin, F., Berchem, G., 2016. Assessing cellular and circulating miRNA recovery: the impact of the RNA isolation method and the quantity of input material. Sci. Rep. 6, 19529.

Elmén, J., Lindow, M., Schütz, S., Lawrence, M., Petri, A., Obad, S., Lindholm, M., Hedtjärn, M., Hansen, H.F., Berger, U., Gullans, S., Kearney, P., Sarnow, P., Straarup, E.M., Kauppinen, S., 2008. LNA-mediated microRNA silencing in non-human primates. Nature 452, 896–899.

Emini Veseli, B., Perrotta, P., De Meyer, G.R.A., Roth, L., Van der Donckt, C., Martinet, W., De Meyer, G.R.Y., 2017. Animal models of atherosclerosis. Eur. J. Pharmacol. 816, 3–13.

Esau, C., Davis, S., Murray, S.F., Yu, X.X., Pandey, S.K., Pear, M., Watts, L., Booten, S.L., Graham, M., McKay, R., Subramaniam, A., Propp, S., Lollo, B.A., Freier, S., Bennett, C.F., Bhanot, S., Monia, B.P., 2006. miR-122 regulation of lipid metabolism revealed by in vivo antisense targeting. Cell Metab. 3, 87–98.

Evrard, S.M., Lecce, L., Michelis, K.C., Nomura-Kitabayashi, A., Pandey, G., Purushothaman, K.-R., D'Escamard, V., Li, J.R., Hadri, L., Fujitani, K., Moreno, P.R., Benard, L., Rimmele, P., Cohain, A., Mecham, B., Randolph, G.J., Nabel, E.G., Hajjar, R., Fuster, V., Boehm, M., Kovacic, J.C., 2016. Endothelial to mesenchymal transition is common in atherosclerotic lesions and is associated with plaque instability. Nat. Commun. 7, 11853.

Fabrice, S., K., S.G., Masanori, A., James, C., Norbert, G., Timothy, T.S.-M., Guo-Ping, S., S., A.S., Peter, L., 2008. Matrix Metalloproteinase-14 Deficiency in Bone Marrow–Derived Cells Promotes Collagen Accumulation in Mouse Atherosclerotic Plaques. Circulation 117, 931–939.

Faccini, J., Ruidavets, J.-B., Cordelier, P., Martins, F., Maoret, J.-J., Bongard, V., Ferrières, J., Roncalli, J., Elbaz, M., Vindis, C., 2017. Circulating miR-155, miR-145 and let-7c as diagnostic biomarkers of the coronary artery disease. Sci. Rep. 7, 42916.

Falati, S., Liu, Q., Gross, P., Merrill-Skoloff, G., Chou, J., Vandendries, E., Celi, A., Croce, K., Furie, B.C., Furie, B., 2003. Accumulation of tissue factor into developing thrombi in vivo is dependent upon microparticle P-selectin glycoprotein ligand 1 and platelet P-selectin. J. Exp. Med. 197, 1585–1598.

Falk, E., Shah, P.K., Fuster, V., 1995. Coronary Plaque Disruption. Circulation 92, 657–671.

Fang, Y., Shi, C., Manduchi, E., Civelek, M., Davies, P.F., 2010. MicroRNA-10a regulation of proinflammatory phenotype in athero-susceptible endothelium in vivo and in vitro. Proc. Natl. Acad. Sci. 107, 13450–13455.

Feinberg, M.W., Moore, K.J., 2016. MicroRNA Regulation of Atherosclerosis. Circ. Res. 118, 703–720.

Ference, B.A., Yoo, W., Alesh, I., Mahajan, N., Mirowska, K.K., Mewada, A., Kahn, J., Afonso, L., Williams, K.A.S., Flack, J.M., 2012. Effect of long-term exposure to lower low-density lipoprotein cholesterol beginning early in life on the risk of coronary heart disease: a Mendelian randomization analysis. J. Am. Coll. Cardiol. 60, 2631–2639.

Fernández-Messina, L., Rodríguez-Galán, A., de Yébenes, V.G., Gutiérrez-Vázquez, C., Tenreiro, S., Seabra, M.C., Ramiro, A.R., Sánchez-Madrid, F.,

2020. Transfer of extracellular vesicle-microRNA controls germinal center reaction and antibody production. EMBO Rep. 21, e48925.

Fernando, M.R., Jiang, C., Krzyzanowski, G.D., Ryan, W.L., 2017. New evidence that a large proportion of human blood plasma cell-free DNA is localized in exosomes. PLoS One 12, e0183915.

Février, B., Raposo, G., 2004. Exosomes: endosomal-derived vesicles shipping extracellular messages. Curr. Opin. Cell Biol. 16, 415–421.

Fichtlscherer, S., De Rosa, S., Fox, H., Schwietz, T., Fischer, A., Liebetrau, C., Weber, M., Hamm, C.W., Röxe, T., Müller-Ardogan, M., Bonauer, A., Zeiher, A.M., Dimmeler, S., 2010. Circulating MicroRNAs in Patients With Coronary Artery Disease. Circ. Res. 107, 677–684.

Fischer, S., Cornils, K., Speiseder, T., Badbaran, A., Reimer, R., Indenbirken, D., Grundhoff, A., Brunswig-Spickenheier, B., Alawi, M., Lange, C., 2016. Indication of Horizontal DNA Gene Transfer by Extracellular Vesicles. PLoS One 11, e0163665.

Fishbein, M.C., 2010. The vulnerable and unstable atherosclerotic plaque. Cardiovasc. Pathol. 19, 6–11.

Fiskaa, T., Knutsen, E., Nikolaisen, M.A., Jørgensen, T.E., Johansen, S.D., Perander, M., Seternes, O.M., 2016. Distinct Small RNA Signatures in Extracellular Vesicles Derived from Breast Cancer Cell Lines. PLoS One 11, e0161824.

Foers, A.D., Chatfield, S., Dagley, L.F., Scicluna, B.J., Webb, A.I., Cheng, L., Hill, A.F., Wicks, I.P., Pang, K.C., 2018. Enrichment of extracellular vesicles from human synovial fluid using size exclusion chromatography. J. Extracell. vesicles 7, 1490145.

Folsom, A.R., Kronmal, R.A., Detrano, R.C., O'Leary, D.H., Bild, D.E., Bluemke, D.A., Budoff, M.J., Liu, K., Shea, S., Szklo, M., Tracy, R.P., Watson, K.E., Burke, G.L., 2008. Coronary Artery Calcification Compared With Carotid Intima-Media Thickness in the Prediction of Cardiovascular Disease Incidence: The Multi-Ethnic Study of Atherosclerosis (MESA). Arch. Intern. Med. 168, 1333–1339.

Forrester, S.J., Kawai, T., O'Brien, S., Thomas, W., Harris, R.C., Eguchi, S., 2016.

Epidermal Growth Factor Receptor Transactivation: Mechanisms, Pathophysiology, and Potential Therapies in the Cardiovascular System. Annu. Rev. Pharmacol. Toxicol. 56, 627–653.

Franco, M., Cooper, R.S., Bilal, U., Fuster, V., 2011. Challenges and Opportunities for Cardiovascular Disease Prevention. Am. J. Med. 124, 95–102.

Frid, M.G., Kale, V.A., Stenmark, K.R., 2002. Mature Vascular Endothelium Can Give Rise to Smooth Muscle Cells via Endothelial-Mesenchymal Transdifferentiation. Circ. Res. 90, 1189–1196.

Friedman, R.C., Farh, K.K.-H., Burge, C.B., Bartel, D.P., 2009. Most mammalian mRNAs are conserved targets of microRNAs. Genome Res. 19, 92–105.

Fu, S., Wang, Y., Xia, X., Zheng, J.C., 2020. Exosome engineering: Current progress in cargo loading and targeted delivery. NanoImpact 20, 100261.

Fujita, K., Kume, H., Matsuzaki, K., Kawashima, A., Ujike, T., Nagahara, A., Uemura, M., Miyagawa, Y., Tomonaga, T., Nonomura, N., 2017. Proteomic analysis of urinary extracellular vesicles from high Gleason score prostate cancer. Sci. Rep. 7, 42961.

Gai, C., Camussi, F., Broccoletti, R., Gambino, A., Cabras, M., Molinaro, L., Carossa, S., Camussi, G., Arduino, P.G., 2018. Salivary extracellular vesicle-associated miRNAs as potential biomarkers in oral squamous cell carcinoma. BMC Cancer 18, 439.

Galkina, E., Kadl, A., Sanders, J., Varughese, D., Sarembock, I.J., Ley, K., 2006. Lymphocyte recruitment into the aortic wall before and during development of atherosclerosis is partially L-selectin dependent. J. Exp. Med. 203, 1273–1282.

Gámez-Valero, A., Monguió-Tortajada, M., Carreras-Planella, L., Franquesa, M., Beyer, K., Borràs, F.E., 2016. Size-Exclusion Chromatography-based isolation minimally alters Extracellular Vesicles' characteristics compared to precipitating agents. Sci. Rep. 6, 33641.

Gao, W., Liu, H., Yuan, J., Wu, C., Huang, D., Ma, Y., Zhu, J., Ma, L., Guo, J., Shi, H., Zou, Y., Ge, J., 2016. Exosomes derived from mature dendritic cells increase endothelial inflammation and atherosclerosis via membrane TNF-α mediated NF-κB pathway. J. Cell. Mol. Med. 20, 2318–2327.

Gardiner, C., Ferreira, Y.J., Dragovic, R.A., Redman, C.W.G., Sargent, I.L., 2013. Extracellular vesicle sizing and enumeration by nanoparticle tracking analysis. J. Extracell. vesicles 2.

Gaspar, L.S., Santana, M.M., Henriques, C., Pinto, M.M., Ribeiro-Rodrigues, T.M., Girão, H., Nobre, R.J., Pereira de Almeida, L., 2020. Simple and Fast SEC-Based Protocol to Isolate Human Plasma-Derived Extracellular Vesicles for Transcriptional Research. Mol. Ther. Methods Clin. Dev. 18, 723–737.

Geovanini, G.R., Libby, P., 2018. Atherosclerosis and inflammation: overview and updates. Clin. Sci. (Lond). 132, 1243–1252.

Gerrity, R.G., Richardson, M., Somer, J.B., Bell, F.P., Schwartz, C.J., 1977. Endothelial cell morphology in areas of in vivo Evans blue uptake in the aorta of young pigs: II. Ultrastructure of the intima in areas of differing permeability to proteins. Am. J. Pathol. 89, 313.

Getz, G.S., Reardon, C.A., 2012. Animal models of atherosclerosis. Arterioscler. Thromb. Vasc. Biol. 32, 1104–1115.

Gézsi, A., Kovács, Á., Visnovitz, T., Buzás, E.I., 2019. Systems biology approaches to investigating the roles of extracellular vesicles in human diseases. Exp. Mol. Med. 51, 1–11.

Gimbrone, M.A.J., García-Cardeña, G., 2016. Endothelial Cell Dysfunction and the Pathobiology of Atherosclerosis. Circ. Res. 118, 620–636.

Gisterå, A., Ketelhuth, D.F.J., Malin, S.G., Hansson, G.K., 2022. Animal Models of Atherosclerosis–Supportive Notes and Tricks of the Trade. Circ. Res. 130, 1869–1887.

Gleissner, C.A., Leitinger, N., Ley, K., 2007. Effects of Native and Modified Low-Density Lipoproteins on Monocyte Recruitment in Atherosclerosis. Hypertension 50, 276–283.

Goedeke, L., Rotllan, N., Canfrán-Duque, A., Aranda, J.F., Ramírez, C.M., Araldi, E., Lin, C.-S., Anderson, N.N., Wagschal, A., de Cabo, R., Horton, J.D., Lasunción, M.A., Näär, A.M., Suárez, Y., Fernández-Hernando, C., 2015. MicroRNA-148a regulates LDL receptor and ABCA1 expression to control circulating lipoprotein levels. Nat. Med. 21, 1280–1289.

Goettsch, C., Hutcheson, J.D., Aikawa, E., 2013. MicroRNA in Cardiovascular Calcification. Circ. Res. 112, 1073–1084.

Goettsch, C., Rauner, M., Pacyna, N., Hempel, U., Bornstein, S.R., Hofbauer, L.C., 2011. miR-125b regulates calcification of vascular smooth muscle cells. Am. J. Pathol. 179, 1594–1600.

Goetzl, E.J., Schwartz, J.B., Mustapic, M., Lobach, I. V, Daneman, R., Abner, E.L., Jicha, G.A., 2017. Altered cargo proteins of human plasma endothelial cell-derived exosomes in atherosclerotic cerebrovascular disease. FASEB J. 31, 3689–3694.

Goicoechea, M., de Vinuesa, S.G., Lahera, V., Cachofeiro, V., Gómez-Campderá, F., Vega, A., Abad, S., Luño, J., 2006. Effects of atorvastatin on inflammatory and fibrinolytic parameters in patients with chronic kidney disease. J. Am. Soc. Nephrol. 17, S231-5.

Gomez, D., Shankman, L.S., Nguyen, A.T., Owens, G.K., 2013. Detection of histone modifications at specific gene loci in single cells in histological sections. Nat. Methods 10, 171–177.

Gong, Q., Xie, J., Li, Y., Liu, Y., Su, G., 2019. Enhanced ROBO4 is mediated by up-regulation of HIF-1α/SP1 or reduction in miR-125b-5p/miR-146a-5p in diabetic retinopathy. J. Cell. Mol. Med. 23, 4723–4737. https://doi.org/https://doi.org/10.1111/jcmm.14369

Gough, P.J., Gomez, I.G., Wille, P.T., Raines, E.W., 2006. Macrophage expression of active MMP-9 induces acute plaque disruption in apoE-deficient mice. J. Clin. Invest. 116, 59–69.

Grada, A., Otero-Vinas, M., Prieto-Castrillo, F., Obagi, Z., Falanga, V., 2017. Research Techniques Made Simple: Analysis of Collective Cell Migration Using the Wound Healing Assay. J. Invest. Dermatol. 137, e11–e16.

Green, I.D., Liu, R., Wong, J.J.L., 2021. The Expanding Role of Alternative Splicing in Vascular Smooth Muscle Cell Plasticity. Int. J. Mol. Sci.

Greenland, P., Blaha, M.J., Budoff, M.J., Erbel, R., Watson, K.E., 2018. Coronary Calcium Score and Cardiovascular Risk. J. Am. Coll. Cardiol. 72, 434–447.

Griffith, T.M., 2004. Endothelium-dependent smooth muscle hyperpolarization: do

gap junctions provide a unifying hypothesis? Br. J. Pharmacol. 141, 881–903.

Griffith, T.M., Chaytor, A.T., Edwards, D.H., 2004. The obligatory link: role of gap junctional communication in endothelium-dependent smooth muscle hyperpolarization. Pharmacol. Res. 49, 551–564.

Grootaert, M.O.J., Roth, L., Schrijvers, D.M., De Meyer, G.R.Y., Martinet, W., 2018. Defective Autophagy in Atherosclerosis: To Die or to Senesce? Oxid. Med. Cell. Longev. 2018, 7687083.

Gu, W., Xu, Y., Xie, X., Wang, T., Ko, J.-H., Zhou, T., 2014. The role of RNA structure at 5' untranslated region in microRNA-mediated gene regulation. RNA 20, 1369–1375.

Gudbergsson, J.M., Johnsen, K.B., Skov, M.N., Duroux, M., 2016. Systematic review of factors influencing extracellular vesicle yield from cell cultures. Cytotechnology 68, 579–592.

Gujrati, M., Malamas, A., Shin, T., Jin, E., Sun, Y., Lu, Z.-R., 2014. Multifunctional Cationic Lipid-Based Nanoparticles Facilitate Endosomal Escape and Reduction-Triggered Cytosolic siRNA Release. Mol. Pharm. 11, 2734–2744.

Guo, H., Ingolia, N.T., Weissman, J.S., Bartel, D.P., 2010. Mammalian microRNAs predominantly act to decrease target mRNA levels. Nature 466, 835–840.

Guo, Y., Yu, H., Wang, J., Sheng, Q., Zhao, S., Zhao, Y.-Y., Lehmann, B.D., 2018. The Landscape of Small Non-Coding RNAs in Triple-Negative Breast Cancer. Genes (Basel). 9, 29.

Guyton, J.R., Lenz, M.L., Mathews, B., Hughes, H., Karsan, D., Selinger, E., Smith, C. V, 1995. Toxicity of oxidized low density lipoproteins for vascular smooth muscle cells and partial protection by antioxidants. Atherosclerosis 118, 237–249.

Ha, J.M., Yun, S.J., Kim, Y.W., Jin, S.Y., Lee, H.S., Song, S.H., Shin, H.K., Bae, S.S., 2015. Platelet-derived growth factor regulates vascular smooth muscle phenotype via mammalian target of rapamycin complex 1. Biochem. Biophys. Res. Commun. 464, 57–62.

Ha, M., Kim, V.N., 2014. Regulation of microRNA biogenesis. Nat. Rev. Mol. Cell Biol. 15, 509–524.

Han, J., Hajjar, D.P., Febbraio, M., Nicholson, A.C., 1997. Native and Modified Low Density Lipoproteins Increase the Functional Expression of the Macrophage Class B Scavenger Receptor, CD36 *. J. Biol. Chem. 272, 21654–21659.

Han, J., Lee, Y., Yeom, K.-H., Kim, Y.-K., Jin, H., Kim, V.N., 2004. The Drosha-DGCR8 complex in primary microRNA processing. Genes Dev. 18, 3016–3027.

Harding, C., Heuser, J., Stahl, P., 1983. Receptor-mediated endocytosis of transferrin and recycling of the transferrin receptor in rat reticulocytes. J. Cell Biol. 97, 329–339.

Harmati, M., Gyukity-Sebestyen, E., Dobra, G., Janovak, L., Dekany, I., Saydam, O., Hunyadi-Gulyas, E., Nagy, I., Farkas, A., Pankotai, T., Ujfaludi, Z., Horvath, P., Piccinini, F., Kovacs, M., Biro, T., Buzas, K., 2019. Small extracellular vesicles convey the stress-induced adaptive responses of melanoma cells. Sci. Rep. 9, 15329.

Hartjes, T.A., Mytnyk, S., Jenster, G.W., van Steijn, V., van Royen, M.E., 2019. Extracellular Vesicle Quantification and Characterization: Common Methods and Emerging Approaches. Bioeng. (Basel, Switzerland) 6, 7.

Hasimbegovic, E., Schweiger, V., Kastner, N., Spannbauer, A., Traxler, D., Lukovic, D., Gyöngyösi, M., Mester-Tonczar, J., 2021. Alternative Splicing in Cardiovascular Disease—A Survey of Recent Findings. Genes (Basel).

He, S., Wu, C., Xiao, J., Li, D., Sun, Z., Li, M., 2018. Endothelial extracellular vesicles modulate the macrophage phenotype: Potential implications in atherosclerosis. Scand. J. Immunol. 87, e12648.

He, X.-W., Shi, Y.-H., Liu, Y.-S., Li, G.-F., Zhao, R., Hu, Y., Lin, C.-C., Zhuang, M.-T., Su, J.-J., Liu, J.-R., 2019. Increased plasma levels of miR-124-3p, miR-125b-5p and miR-192-5p are associated with outcomes in acute ischaemic stroke patients receiving thrombolysis. Atherosclerosis 289, 36–43.

Heijnen, H.F.G., Schiel, A.E., Fijnheer, R., Geuze, H.J., Sixma, J.J., 1999. Activated Platelets Release Two Types of Membrane Vesicles: Microvesicles by Surface Shedding and Exosomes Derived From Exocytosis of Multivesicular Bodies and □-Granules. Blood 94, 3791–3799.

Henne, W.M., Buchkovich, N.J., Emr, S.D., 2011. The ESCRT Pathway. Dev. Cell

21, 77–91.

Heo, K.-S., Fujiwara, K., Abe, J., 2011. Disturbed-flow-mediated vascular reactive oxygen species induce endothelial dysfunction. Circ. J. 75, 2722–2730.

Hergenreider, E., Heydt, S., Tréguer, K., Boettger, T., Horrevoets, A.J.G., Zeiher, A.M., Scheffer, M.P., Frangakis, A.S., Yin, X., Mayr, M., Braun, T., Urbich, C., Boon, R.A., Dimmeler, S., 2012. Atheroprotective communication between endothelial cells and smooth muscle cells through miRNAs. Nat. Cell Biol. 14, 249–256.

Hermansson, A., Ketelhuth, D.F.J., Strodthoff, D., Wurm, M., Hansson, E.M., Nicoletti, A., Paulsson-Berne, G., Hansson, G.K., 2010. Inhibition of T cell response to native low-density lipoprotein reduces atherosclerosis. J. Exp. Med. 207, 1081–1093.

Herrington, W., Lacey, B., Sherliker, P., Armitage, J., Lewington, S., 2016. Epidemiology of Atherosclerosis and the Potential to Reduce the Global Burden of Atherothrombotic Disease. Circ. Res. 118, 535–546.

Hildebrandt, A., Kirchner, B., Nolte-'t Hoen, E.N.M., Pfaffl, M.W., 2021. miREV: An Online Database and Tool to Uncover Potential Reference RNAs and Biomarkers in Small-RNA Sequencing Data Sets from Extracellular Vesicles Enriched Samples. J. Mol. Biol. 433, 167070.

Hogg, N., Kalyanaraman, B., Joseph, J., Struck, A., Parthasarathy, S., 1993. Inhibition of low-density lipoprotein oxidation by nitric oxide Potential role in atherogenesis. FEBS Lett. 334, 170–174.

Holdt, L.M., Teupser, D., 2013. From genotype to phenotype in human atherosclerosis--recent findings. Curr. Opin. Lipidol. 24, 410–418.

Holmes, D.R., Lopez-Candales, A., Liao, S., Thompson, R.W., 1996. Smooth Muscle Cell Apoptosis and p53 Expression in Human Abdominal Aortic Aneurysmsa. Ann. N. Y. Acad. Sci. 800, 286–287.

Hosseinkhani, B., van den Akker, N., D'Haen, J., Gagliardi, M., Struys, T., Lambrichts, I., Waltenberger, J., Nelissen, I., Hooyberghs, J., Molin, D.G.M., Michiels, L., 2017. Direct detection of nano-scale extracellular vesicles derived from inflammation-triggered endothelial cells using surface plasmon resonance. Nanomedicine 13, 1663–1671.

Hsieh, C.-C., Yen, M.-H., Yen, C.-H., Lau, Y.-T., 2001. Oxidized low density lipoprotein induces apoptosis via generation of reactive oxygen species in vascular smooth muscle cells. Cardiovasc. Res. 49, 135–145.

Hu, L., Wang, J., Lin, D., Shen, Y., Huang, H., Cao, Y., Li, Y., Li, K., Yu, Yanfang, Yu, Youjia, Chu, C., Qin, L., Wang, X., Zhang, H., Fulton, D., Chen, F., 2022. Mesenchymal Stem Cell-derived Nanovesicles as a Credible Agent for Therapy of Pulmonary Hypertension. Am. J. Respir. Cell Mol. Biol. 67, 61–75.

Hu, Q., Su, H., Li, J., Lyon, C., Tang, W., Wan, M., Hu, T.Y., 2020. Clinical applications of exosome membrane proteins. Precis. Clin. Med. 3, 54–66.

Hu, X., Li, Z., Lin, R., Shan, J., Yu, Q., Wang, R., Liao, L., Yan, W., Wang, Z., Shang, L., Huang, Y., Zhang, Q., Xiong, K., 2021. Guidelines for Regulated Cell Death Assays: A Systematic Summary, A Categorical Comparison, A Prospective. Front. Cell Dev. Biol.

Hu, Y.-B., Dammer, E.B., Ren, R.-J., Wang, G., 2015. The endosomal-lysosomal system: from acidification and cargo sorting to neurodegeneration. Transl. Neurodegener. 4, 18.

Hua, S., Quan, Y., Zhan, M., Liao, H., Li, Y., Lu, L., 2019. miR-125b-5p inhibits cell proliferation, migration, and invasion in hepatocellular carcinoma via targeting TXNRD1. Cancer Cell Int. 19, 203.

Huang, D.W., Sherman, B.T., Lempicki, R.A., 2009. Systematic and integrative analysis of large gene lists using DAVID bioinformatics resources. Nat. Protoc. 4, 44–57.

Huang, D.W., Sherman, B.T., Tan, Q., Kir, J., Liu, D., Bryant, D., Guo, Y., Stephens, R., Baseler, M.W., Lane, H.C., Lempicki, R.A., 2007. DAVID Bioinformatics Resources: expanded annotation database and novel algorithms to better extract biology from large gene lists. Nucleic Acids Res. 35, W169–W175.

Huber, J., Vales, A., Mitulovic, G., Blumer, M., Schmid, R., Witztum, J.L., Binder, B.R., Leitinger, N., 2002. Oxidized Membrane Vesicles and Blebs From Apoptotic Cells Contain Biologically Active Oxidized Phospholipids That Induce Monocyte-Endothelial Interactions. Arterioscler. Thromb. Vasc. Biol. 22, 101–107.

Huber, L.C., Jüngel, A., Distler, J.H.W., Moritz, F., Gay, R.E., Michel, B.A., Pisetsky, D.S., Gay, S., Distler, O., 2007. The role of membrane lipids in the induction of macrophage apoptosis by microparticles. Apoptosis 12, 363–374.

Hueso, M., De Ramon, L., Navarro, E., Ripoll, E., Cruzado, J.M., Grinyo, J.M., Torras, J., 2016. Silencing of CD40 in vivo reduces progression of experimental atherogenesis through an NF-κB/miR-125b axis and reveals new potential mediators in the pathogenesis of atherosclerosis. Atherosclerosis 255, 80–89.

Hueso, M., Griñán, R., Mallen, A., Navarro, E., Purqueras, E., Gomá, M., Sbraga, F., Blasco-Lucas, A., Revilla, G., Santos, D., Canyelles, M., Julve, J., Escolà-Gil, J.C., Rotllan, N., 2022. MiR-125b downregulates macrophage scavenger receptor type B1 and reverse cholesterol transport. Biomed. Pharmacother. 146, 112596.

Hurd, P.J., Nelson, C.J., 2009. Advantages of next-generation sequencing versus the microarray in epigenetic research. Brief. Funct. Genomics 8, 174–183.

Hurwitz, S.N., Olcese, J.M., Meckes Jr., D.G., 2019. Extraction of Extracellular Vesicles from Whole Tissue. JoVE e59143.

Hutcheson, J.D., Goettsch, C., Bertazzo, S., Maldonado, N., Ruiz, J.L., Goh, W., Yabusaki, K., Faits, T., Bouten, C., Franck, G., Quillard, T., Libby, P., Aikawa, M., Weinbaum, S., Aikawa, E., 2016. Genesis and growth of extracellular-vesicle-derived microcalcification in atherosclerotic plaques. Nat. Mater. 15, 335–343.

Ichikawa, T., Unoki, H., Sun, H., Shimoyamada, H., Marcovina, S., Shikama, H., Watanabe, T., Fan, J., 2002. Lipoprotein(a) promotes smooth muscle cell proliferation and dedifferentiation in atherosclerotic lesions of human apo(a) transgenic rabbits. Am. J. Pathol. 160, 227–236.

Ihling, C., Haendeler, J., Menzel, G., Hess, R.D., Fraedrich, G., Schaefer, H.E., Zeiher, A.M., 1998. Co-expression of p53 and MDM2 in human atherosclerosis: implications for the regulation of cellularity of atherosclerotic lesions. J. Pathol. 185, 303–312.

Ilyas, I., Little, P.J., Liu, Z., Xu, Y., Kamato, D., Berk, B.C., Weng, J., Xu, S., 2022. Mouse models of atherosclerosis in translational research. Trends Pharmacol. Sci. 43, 920–939.

Jabalee, J., Towle, R., Garnis, C., 2018. The Role of Extracellular Vesicles in Cancer: Cargo, Function, and Therapeutic Implications. Cells 7, 93.

Janiszewski, M., Do Carmo, A.O., Pedro, M.A., Silva, E., Knobel, E., Laurindo, F.R.M., 2004. Platelet-derived exosomes of septic individuals possess proapoptotic NAD(P)H oxidase activity: A novel vascular redox pathway. Crit. Care Med. 32, 818–825.

Jansen, F., Yang, X., Baumann, K., Przybilla, D., Schmitz, T., Flender, A., Paul, K., Alhusseiny, A., Nickenig, G., Werner, N., 2015. Endothelial microparticles reduce ICAM-1 expression in a microRNA-222-dependent mechanism. J. Cell. Mol. Med. 19, 2202–2214.

Jansen, F., Yang, X., Franklin, B.S., Hoelscher, M., Schmitz, T., Bedorf, J., Nickenig, G., Werner, N., 2013. High glucose condition increases NADPH oxidase activity in endothelial microparticles that promote vascular inflammation. Cardiovasc. Res. 98, 94–106.

Jansen, F., Yang, X., Proebsting, S., Hoelscher, M., Przybilla, D., Baumann, K., Schmitz, T., Dolf, A., Endl, E., Franklin, B.S., Sinning, J.-M., Vasa-Nicotera, M., Nickenig, G., Werner, N., 2014. MicroRNA expression in circulating microvesicles predicts cardiovascular events in patients with coronary artery disease. J. Am. Heart Assoc. 3, e001249.

Jayachandran, M., Litwiller, R.D., Owen, W.G., Heit, J.A., Behrenbeck, T., Mulvagh, S.L., Araoz, P.A., Budoff, M.J., Harman, S.M., Miller, V.M., 2008. Characterization of blood borne microparticles as markers of premature coronary calcification in newly menopausal women. Am. J. Physiol. Circ. Physiol. 295, H931–H938.

Jenjaroenpun, P., Kremenska, Y., Nair, V.M., Kremenskoy, M., Joseph, B., Kurochkin, I. V, 2013. Characterization of RNA in exosomes secreted by human breast cancer cell lines using next-generation sequencing. PeerJ 1, e201.

Jia, K., Shi, P., Han, X., Chen, T., Tang, H., Wang, J., 2016. Diagnostic value of miR-30d-5p and miR-125b-5p in acute myocardial infarction. Mol. Med. Rep. 14, 184–194.

Jia, Y., Mu, J.C., Ackerman, S.L., 2012. Mutation of a U2 snRNA Gene Causes Global Disruption of Alternative Splicing and Neurodegeneration. Cell 148,

296–308.

Jian, W., Wei, C.-M., Guan, J.-H., Mo, C.-H., Xu, Y.-T., Zheng, W.-B., Li, L., Gui, C., 2020. Association between serum HER2/ErbB2 levels and coronary artery disease: a case–control study. J. Transl. Med. 18, 124.

Johnsen, K.B., Gudbergsson, J.M., Skov, M.N., Christiansen, G., Gurevich, L., Moos, T., Duroux, M., 2016. Evaluation of electroporation-induced adverse effects on adipose-derived stem cell exosomes. Cytotechnology 68, 2125–2138.

Johnstone, R.M., Adam, M., Hammond, J.R., Orr, L., Turbide, C., 1987. Vesicle formation during reticulocyte maturation. Association of plasma membrane activities with released vesicles (exosomes). J. Biol. Chem. 262, 9412–9420.

Johnstone, R.M., Mathew, A., Mason, A.B., Teng, K., 1991. Exosome formation during maturation of mammalian and avian reticulocytes: Evidence that exosome release is a major route for externalization of obsolete membrane proteins. J. Cell. Physiol. 147, 27–36.

Joris, V., Gomez, E.L., Menchi, L., Lobysheva, I., Di Mauro, V., Esfahani, H., Condorelli, G., Balligand, J.-L., Catalucci, D., Dessy, C., 2018. MicroRNA-199a-3p and MicroRNA-199a-5p Take Part to a Redundant Network of Regulation of the NOS (NO Synthase)/NO Pathway in the Endothelium. Arterioscler. Thromb. Vasc. Biol. 38, 2345–2357.

Kahlert, C., Kalluri, R., 2013. Exosomes in tumor microenvironment influence cancer progression and metastasis. J. Mol. Med. (Berl). 91, 431–437.

Kalluri, R., LeBleu, V.S., 2020. The biology, function, and biomedical applications of exosomes. Science 367, eaau6977.

Kang, S., Yang, J.W., Jeong, J.Y., Park, J., An, H.J., Koh, H.M., Jang, S.M., Lee, Y.J., Song, D.H., 2019. Size distribution of serum extracellular vesicles in mice with atherosclerosis. Pathol. - Res. Pract. 215, 152574.

Kapustin, A.N., Chatrou, M.L., Drozdov, I., Zheng, Y., Davidson, S.M., Soong, D., Furmanik, M., Sanchis, P., De Rosales, R.T., Alvarez-Hernandez, D., Shroff, R., Yin, X., Muller, K., Skepper, J.N., Mayr, M., Reutelingsperger, C.P., Chester, A., Sergio, B., Schurgers, L.J., Shanahan, C.M., 2015. Vascular Smooth Muscle Cell Calcification Is Mediated by Regulated Exosome Secretion.

Circ. Res. 116, 1312–1323.

Kapustin, A.N., Davies, J.D., Reynolds, J.L., McNair, R., Jones, G.T., Sidibe, A., Schurgers, L.J., Skepper, J.N., Proudfoot, D., Mayr, M., Shanahan, C.M., 2011. Calcium regulates key components of vascular smooth muscle cell-derived matrix vesicles to enhance mineralization. Circ. Res. 109, e1-12.

Karagkouni, D., Paraskevopoulou, M.D., Chatzopoulos, S., Vlachos, I.S., Tastsoglou, S., Kanellos, I., Papadimitriou, D., Kavakiotis, I., Maniou, S., Skoufos, G., Vergoulis, T., Dalamagas, T., Hatzigeorgiou, A.G., 2018. DIANA-TarBase v8: a decade-long collection of experimentally supported miRNA-gene interactions. Nucleic Acids Res. 46, D239–D245.

Karel, M.F.A., Hechler, B., Kuijpers, M.J.E., Cosemans, J., 2020. Atherosclerotic plaque injury-mediated murine thrombosis models: advantages and limitations. Platelets 31, 439–446.

Karlöf, E., Seime, T., Dias, N., Lengquist, M., Witasp, A., Almqvist, H., Kronqvist, M., Gådin, J.R., Odeberg, J., Maegdefessel, L., Stenvinkel, P., Matic, L.P., Hedin, U., 2019. Correlation of computed tomography with carotid plaque transcriptomes associates calcification with lesion-stabilization. Atherosclerosis 288, 175–185.

Kasikara, C., Schilperoort, M., Gerlach, B., Xue, C., Wang, X., Zheng, Z., Kuriakose, G., Dorweiler, B., Zhang, H., Fredman, G., Saleheen, D., Reilly, M.P., Tabas, I., 2021. Deficiency of macrophage PHACTR1 impairs efferocytosis and promotes atherosclerotic plaque necrosis. J. Clin. Invest. 131, e145275.

Kataoka, H., Kume, N., Miyamoto, S., Minami, M., Morimoto, M., Hayashida, K., Hashimoto, N., Kita, T., 2001. Oxidized LDL Modulates Bax/Bcl-2 Through the Lectinlike Ox-LDL Receptor-1 in Vascular Smooth Muscle Cells. Arterioscler. Thromb. Vasc. Biol. 21, 955–960.

Kattoor, A.J., Pothineni, N.V.K., Palagiri, D., Mehta, J.L., 2017. Oxidative Stress in Atherosclerosis. Curr. Atheroscler. Rep. 19, 42.

Katzmann, D.J., Odorizzi, G., Emr, S.D., 2002. Receptor downregulation and multivesicular-body sorting. Nat. Rev. Mol. Cell Biol. 3, 893–905.

Kavurma, M.M., Santiago, F.S., Bonfoco, E., Khachigian, L.M., 2001. Sp1

Phosphorylation Regulates Apoptosis via Extracellular FasL-Fas Engagement*. J. Biol. Chem. 276, 4964–4971.

Keller, S., König, A.-K., Marmé, F., Runz, S., Wolterink, S., Koensgen, D., Mustea, A., Sehouli, J., Altevogt, P., 2009. Systemic presence and tumor-growth promoting effect of ovarian carcinoma released exosomes. Cancer Lett. 278, 73–81.

Kern, M., Knigge, A., Heiker, J.T., Kosacka, J., Stumvoll, M., Kovacs, P., Blüher, M., Klöting, N., 2012. C57BL/6JRj mice are protected against diet induced obesity (DIO). Biochem. Biophys. Res. Commun. 417, 717–720.

Kettunen, S., Ruotsalainen, A.-K., Ylä-Herttuala, S., 2022. RNA interference-based therapies for the control of atherosclerosis risk factors. Curr. Opin. Cardiol. 37, 364–371.

Keup, C., Mach, P., Aktas, B., Tewes, M., Kolberg, H.-C., Hauch, S., Sprenger-Haussels, M., Kimmig, R., Kasimir-Bauer, S., 2018. RNA Profiles of Circulating Tumor Cells and Extracellular Vesicles for Therapy Stratification of Metastatic Breast Cancer Patients. Clin. Chem. 64, 1054–1062.

Keyel, P.A., Tkacheva, O.A., Larregina, A.T., Salter, R.D., 2012. Coordinate Stimulation of Macrophages by Microparticles and TLR Ligands Induces Foam Cell Formation. J. Immunol. 189, 4621 LP – 4629.

Khalaj, K., Miller, J.E., Lingegowda, H., Fazleabas, A.T., Young, S.L., Lessey, B.A., Koti, M., Tayade, C., 2019. Extracellular vesicles from endometriosis patients are characterized by a unique miRNA-lncRNA signature. JCI insight 4.

Khan, B. V, Parthasarathy, S.S., Alexander, R.W., Medford, R.M., 1995. Modified low density lipoprotein and its constituents augment cytokine-activated vascular cell adhesion molecule-1 gene expression in human vascular endothelial cells. J. Clin. Invest. 95, 1262–1270.

Kheirolomoom, A., Kim, C.W., Seo, J.W., Kumar, S., Son, D.J., Gagnon, M.K.J., Ingham, E.S., Ferrara, K.W., Jo, H., 2015. Multifunctional Nanoparticles Facilitate Molecular Targeting and miRNA Delivery to Inhibit Atherosclerosis in ApoE–/– Mice. ACS Nano 9, 8885–8897.

Khurana, S., Gupta, S., Bhalla, H., Nandwani, S., Gupta, V., 2015. Comparison of anti-inflammatory effect of atorvastatin with rosuvastatin in patients of acute

coronary syndrome. J. Pharmacol. Pharmacother. 6, 130–135.

Khvorova, A., Reynolds, A., Jayasena, S.D., 2003. Functional siRNAs and miRNAs exhibit strand bias. Cell 115, 209–216.

Kinlay, S., Schwartz, G.G., Olsson, A.G., Rifai, N., Leslie, S.J., Sasiela, W.J., Szarek, M., Libby, P., Ganz, P., 2003. High-dose atorvastatin enhances the decline in inflammatory markers in patients with acute coronary syndromes in the MIRACL study. Circulation 108, 1560–1566.

Kinoshita, T., Yip, K.W., Spence, T., Liu, F.-F., 2017. MicroRNAs in extracellular vesicles: potential cancer biomarkers. J. Hum. Genet. 62, 67–74.

Kinscherf, R., Claus, R., Wagner, M., Gehrke, C., Kamencic, H., Hou, D., Nauen, O., Schmiedt, W., Kovacs, G., Pill, J., Metz, J., Deigner, H.P., 1998. Apoptosis caused by oxidized LDL is manganese superoxide dismutase and p53 dependent. FASEB J. 12, 461–467.

Kobayashi, T., Beuchat, M.H., Lindsay, M., Frias, S., Palmiter, R.D., Sakuraba, H., Parton, R.G., Gruenberg, J., 1999. Late endosomal membranes rich in lysobisphosphatidic acid regulate cholesterol transport. Nat. Cell Biol. 1, 113–118.

Kobayashi, Toshihide, Beuchat, M.-H., Chevallier, J., Makino, A., Mayran, N., Escola, J.-M., Lebrand, C., Cosson, P., Kobayashi, Tetsuyuki, Gruenberg, J., 2002. Separation and characterization of late endosomal membrane domains. J. Biol. Chem. 277, 32157–32164.

Kockx, M.M., Herman, A.G., 2000. Apoptosis in atherosclerosis: beneficial or detrimental? Cardiovasc. Res. 45, 736–746.

Kong, L., Li, K., Gao, L., Yin, A., Zhou, L., Teng, G., Huang, P., 2020. Mediating effects of platelet-derived extracellular vesicles on PM2.5-induced vascular endothelial injury. Ecotoxicol. Environ. Saf. 198, 110652.

Kooijmans, S.A.A., Stremersch, S., Braeckmans, K., de Smedt, S.C., Hendrix, A., Wood, M.J.A., Schiffelers, R.M., Raemdonck, K., Vader, P., 2013. Electroporation-induced siRNA precipitation obscures the efficiency of siRNA loading into extracellular vesicles. J. Control. Release 172, 229–238.

Kowal, J., Arras, G., Colombo, M., Jouve, M., Morath, J.P., Primdal-Bengtson, B.,

Dingli, F., Loew, D., Tkach, M., Théry, C., 2016. Proteomic comparison defines novel markers to characterize heterogeneous populations of extracellular vesicle subtypes. Proc. Natl. Acad. Sci. 113, E968 LP-E977.

Kraiss, L.W., 2005. Distinct Endothelial Phenotypes Evoked by Arterial Waveforms Derived from Atherosclerosis-Susceptible and -Resistant Regions of Human Vasculature. Perspect. Vasc. Surg. Endovasc. Ther. 17, 268–269.

Krenning, G., Moonen, J.-R.A.J., van Luyn, M.J.A., Harmsen, M.C., 2008. Vascular smooth muscle cells for use in vascular tissue engineering obtained by endothelial-to-mesenchymal transdifferentiation (EnMT) on collagen matrices. Biomaterials 29, 3703–3711.

Krohn, J.B., Hutcheson, J.D., Martínez-Martínez, E., Aikawa, E., 2016. Extracellular vesicles in cardiovascular calcification: expanding current paradigms. J. Physiol. 594, 2895–2903.

Kubota, S., Chiba, M., Watanabe, M., Sakamoto, M., Watanabe, N., 2015. Secretion of small/microRNAs including miR-638 into extracellular spaces by sphingomyelin phosphodiesterase 3. Oncol. Rep. 33, 67–73.

Kuhlmann, J.D., Baraniskin, A., Hahn, S.A., Mosel, F., Bredemeier, M., Wimberger, P., Kimmig, R., Kasimir-Bauer, S., 2014. Circulating U2 Small Nuclear RNA Fragments as a Novel Diagnostic Tool for Patients with Epithelial Ovarian Cancer. Clin. Chem. 60, 206–213.

Kühnast, S., van der Hoorn, J.W.A., Pieterman, E.J., van den Hoek, A.M., Sasiela, W.J., Gusarova, V., Peyman, A., Schäfer, H.-L., Schwahn, U., Jukema, J.W., Princen, H.M.G., 2014. Alirocumab inhibits atherosclerosis, improves the plaque morphology, and enhances the effects of a statin. J. Lipid Res. 55, 2103–2112.

Kuipers, F., van Ree, J.M., Hofker, M.H., Wolters, H., Veld, G.I., Havinga, R., Vonk, R.J., Princen, H.M., Havekes, L.M., 1996. Altered lipid metabolism in apolipoprotein E–deficient mice does not affect cholesterol balance across the liver. Hepatology 24, 241–247.

Kwok, Z.H., Wang, C., Jin, Y., 2021. Extracellular Vesicle Transportation and Uptake by Recipient Cells: A Critical Process to Regulate Human Diseases. Process. (Basel, Switzerland) 9, 273.

Kyotani, Y., Ota, H., Itaya-Hironaka, A., Yamauchi, A., Sakuramoto-Tsuchida, S., Zhao, J., Ozawa, K., Nagayama, K., Ito, S., Takasawa, S., Kimura, H., Uno, M., Yoshizumi, M., 2013. Intermittent hypoxia induces the proliferation of rat vascular smooth muscle cell with the increases in epidermal growth factor family and erbB2 receptor. Exp. Cell Res. 319, 3042–3050.

Laffont, B., Corduan, A., Rousseau, M., Duchez, A.-C., Lee, C.H.C., Boilard, E., Provost, P., 2016. Platelet microparticles reprogram macrophage gene expression and function. Thromb. Haemost. 115, 311–323.

Laffont, B., Rayner, K.J., 2017. MicroRNAs in the Pathobiology and Therapy of Atherosclerosis. Can. J. Cardiol. 33, 313–324.

Lakota, K., Mrak-Poljsak, K., Rozman, B., Sodin-Semrl, S., 2009. Increased responsiveness of human coronary artery endothelial cells in inflammation and coagulation. Mediators Inflamm. 2009, 146872.

Langmead, B., Trapnell, C., Pop, M., Salzberg, S.L., 2009. Ultrafast and memory-efficient alignment of short DNA sequences to the human genome. Genome Biol. 10, R25.

Lässer, C., Alikhani, V.S., Ekström, K., Eldh, M., Paredes, P.T., Bossios, A., Sjöstrand, M., Gabrielsson, S., Lötvall, J., Valadi, H., 2011a. Human saliva, plasma and breast milk exosomes contain RNA: uptake by macrophages. J. Transl. Med. 9, 9.

Lässer, C., O'Neil, S.E., Ekerljung, L., Ekström, K., Sjöstrand, M., Lötvall, J., 2011b. RNA-containing exosomes in human nasal secretions. Am. J. Rhinol. Allergy 25, 89–93.

Lázaro-Ibáñez, E., Sanz-Garcia, A., Visakorpi, T., Escobedo-Lucea, C., Siljander, P., Ayuso-Sacido, A., Yliperttula, M., 2014. Different gDNA content in the subpopulations of prostate cancer extracellular vesicles: apoptotic bodies, microvesicles, and exosomes. Prostate 74, 1379–1390.

Le, M.T.N., Shyh-Chang, N., Khaw, S.L., Chin, L., Teh, C., Tay, J., O'Day, E., Korzh, V., Yang, H., Lal, A., Lieberman, J., Lodish, H.F., Lim, B., 2011. Conserved regulation of p53 network dosage by microRNA-125b occurs through evolving miRNA-target gene pairs. PLoS Genet. 7, e1002242.

Lee, H., Groot, M., Pinilla-Vera, M., Fredenburgh, L.E., Jin, Y., 2019.

Identification of miRNA-rich vesicles in bronchoalveolar lavage fluid: Insights into the function and heterogeneity of extracellular vesicles. J. Control. Release 294, 43–52.

Lee, I., Ajay, S.S., Yook, J.I., Kim, H.S., Hong, S.H., Kim, N.H., Dhanasekaran, S.M., Chinnaiyan, A.M., Athey, B.D., 2009. New class of microRNA targets containing simultaneous 5'-UTR and 3'-UTR interaction sites. Genome Res. 19, 1175–1183.

Lee, R.C., Feinbaum, R.L., Ambros, V., 1993. The C. elegans heterochronic gene lin-4 encodes small RNAs with antisense complementarity to lin-14. Cell 75, 843–854.

Lee, R.T., Yamamoto, C., Feng, Y., Potter-Perigo, S., Briggs, W.H., Landschulz, K.T., Turi, T.G., Thompson, J.F., Libby, P., Wight, T.N., 2001. Mechanical strain induces specific changes in the synthesis and organization of proteoglycans by vascular smooth muscle cells. J. Biol. Chem. 276, 13847–13851.

Lee, T.H., Chennakrishnaiah, S., Audemard, E., Montermini, L., Meehan, B., Rak, J., 2014. Oncogenic ras-driven cancer cell vesiculation leads to emission of double-stranded DNA capable of interacting with target cells. Biochem. Biophys. Res. Commun. 451, 295–301. https://doi.org/10.1016/j.bbrc.2014.07.109

Lee, Y., Jeon, K., Lee, J.-T., Kim, S., Kim, V.N., 2002. MicroRNA maturation: stepwise processing and subcellular localization. EMBO J. 21, 4663–4670.

Lee, Y., Kim, M., Han, J., Yeom, K.-H., Lee, S., Baek, S.H., Kim, V.N., 2004. MicroRNA genes are transcribed by RNA polymerase II. EMBO J. 23, 4051–4060.

Lendon, C., Davies, M.J., Born, G. V, Richardson, P.D., 1991. Atherosclerotic plaque caps are locally weakened when macrophages density is increased. Atherosclerosis 87, 87–90.

Leroyer, A.S., Isobe, H., Lesèche, G., Castier, Y., Wassef, M., Mallat, Z., Binder, B.R., Tedgui, A., Boulanger, C.M., 2007. Cellular origins and thrombogenic activity of microparticles isolated from human atherosclerotic plaques. J. Am. Coll. Cardiol. 49, 772–777.

Li, C.-J., Liu, Y., Chen, Y., Yu, D., Williams, K.J., Liu, M.-L., 2013. Novel

proteolytic microvesicles released from human macrophages after exposure to tobacco smoke. Am. J. Pathol. 182, 1552–1562.

Li, D., Yang, P., Xiong, Q., Song, X., Yang, X., Liu, L., Yuan, W., Rui, Y.-C., 2010. MicroRNA-125a/b-5p inhibits endothelin-1 expression in vascular endothelial cells. J. Hypertens. 28, 1646–1654.

Li, H., Cybulsky, M.I., Gimbrone, M.A.J., Libby, P., 1993. An atherogenic diet rapidly induces VCAM-1, a cytokine-regulatable mononuclear leukocyte adhesion molecule, in rabbit aortic endothelium. Arterioscler. Thromb. a J. Vasc. Biol. 13, 197–204.

Li, L., Wang, H., Zhang, J., Chen, X., Zhang, Z., Li, Q., 2021. Effect of endothelial progenitor cell-derived extracellular vesicles on endothelial cell ferroptosis and atherosclerotic vascular endothelial injury. Cell Death Discov. 7, 235.

Li, L., Wang, Z., Hu, X., Wan, T., Wu, H., Jiang, W., Hu, R., 2016. Human aortic smooth muscle cell-derived exosomal miR-221/222 inhibits autophagy via a PTEN/Akt signaling pathway in human umbilical vein endothelial cells. Biochem. Biophys. Res. Commun. 479, 343–350.

Li, M., Qian, M., Kyler, K., Xu, J., 2018. Endothelial-Vascular Smooth Muscle Cells Interactions in Atherosclerosis. Front. Cardiovasc. Med. 5, 151.

Li, X., Yao, N., Zhang, J., Liu, Z., 2015. MicroRNA-125b is involved in atherosclerosis obliterans in vitro by targeting podocalyxin. Mol. Med. Rep. 12, 561–568.

Li, Yuchen, He, X., Li, Q., Lai, H., Zhang, H., Hu, Z., Li, Yan, Huang, S., 2020. EV-origin: Enumerating the tissue-cellular origin of circulating extracellular vesicles using exLR profile. Comput. Struct. Biotechnol. J. 18, 2851–2859.

Lian, C., Wang, Z., Qiu, J., Jiang, B., Lv, J., He, R., Liu, R., Li, W., Wang, J., Wang, S., 2020. TIM-3 inhibits PDGF-BB-induced atherogenic responses in human artery vascular smooth muscle cells. Mol. Med. Rep. 22, 886–894.

Liang, L.-G., Kong, M.-Q., Zhou, S., Sheng, Y.-F., Wang, P., Yu, T., Inci, F., Kuo, W.P., Li, L.-J., Demirci, U., Wang, S., 2017. An integrated double-filtration microfluidic device for isolation, enrichment and quantification of urinary extracellular vesicles for detection of bladder cancer. Sci. Rep. 7, 46224.

Liang, W., Chen, J., Zheng, H., Lin, A., Li, J., Wu, W., Jie, Q., 2022. MiR-199a-5p-containing macrophage-derived extracellular vesicles inhibit SMARCA4 and alleviate atherosclerosis by reducing endothelial cell pyroptosis. Cell Biol. Toxicol.

Liao, J.K., Bettmann, M.A., Sandor, T., Tucker, J.I., Coleman, S.M., Creager, M.A., 1991. Differential impairment of vasodilator responsiveness of peripheral resistance and conduit vessels in humans with atherosclerosis. Circ. Res. 68, 1027–1034.

Liao, X.-H., Wang, N., Zhao, D.-W., Zheng, D.-L., Zheng, L., Xing, W.-J., Ma, W.-J., Bao, L.-Y., Dong, J., Zhang, T.-C., 2015. STAT3 Protein Regulates Vascular Smooth Muscle Cell Phenotypic Switch by Interaction with Myocardin. J. Biol. Chem. 290, 19641–19652.

Libby, P., 2005. The forgotten majority: unfinished business in cardiovascular risk reduction. J. Am. Coll. Cardiol. 46, 1225–1228.

Libby, P., Hansson, G.K., 2019. From Focal Lipid Storage to Systemic Inflammation. J. Am. Coll. Cardiol. 74, 1594–1607.

Libby, P., Ridker, P.M., Hansson, G.K., 2011. Progress and challenges in translating the biology of atherosclerosis. Nature 473, 317–325.

Libby, P., Theroux, P., 2005. Pathophysiology of coronary artery disease. Circulation 111, 3481–3488.

Lidster, K., Owen, K., Browne, W.J., Prescott, M.J., 2019. Cage aggression in group-housed laboratory male mice: an international data crowdsourcing project. Sci. Rep. 9, 15211.

Lin, S., Gregory, R.I., 2015. MicroRNA biogenesis pathways in cancer. Nat. Rev. Cancer 15, 321–333.

Lin, X., He, Y., Hou, X., Zhang, Z., Wang, R., Wu, Q., 2016. Endothelial Cells Can Regulate Smooth Muscle Cells in Contractile Phenotype through the miR-206/ARF6&NCX1/Exosome Axis. PLoS One 11, e0152959.

Liu, John, Ren, Y., Kang, L., Zhang, L., 2014. Oxidized low-density lipoprotein increases the proliferation and migration of human coronary artery smooth muscle cells through the upregulation of osteopontin. Int J Mol Med 33, 1341–

7.

Liu, Jan, Ren, Y., Kang, L., Zhang, L., 2014. Oxidized low-density lipoprotein increases the proliferation and migration of human coronary artery smooth muscle cells through the upregulation of osteopontin. Int J Mol Med 33, 1341–7.

Liu, Mei, Wang, L., Zhu, H., Rong, W., Wu, F., Liang, S., Xu, N., Wu, J., 2016. A Preoperative Measurement of Serum MicroRNA-125b May Predict the Presence of Microvascular Invasion in Hepatocellular Carcinomas Patients. Transl. Oncol. 9, 167–172.

Liu, Mengyang, Zhang, W., Li, X., Han, J., Chen, Y., Duan, Y., 2016. Impact of age and sex on the development of atherosclerosis and expression of the related genes in apoE deficient mice. Biochem. Biophys. Res. Commun. 469, 456–462.

Liu, X., Cheng, Y., Yang, J., Xu, L., Zhang, C., 2012. Cell-specific effects of miR-221/222 in vessels: Molecular mechanism and therapeutic application. J. Mol. Cell. Cardiol. 52, 245–255.

Liu, X., Cheng, Y., Zhang, S., Lin, Y., Yang, J., Zhang, C., 2009. A Necessary Role of miR-221 and miR-222 in Vascular Smooth Muscle Cell Proliferation and Neointimal Hyperplasia. Circ. Res. 104, 476–487.

Liu, Y., Li, Q., Hosen, M.R., Zietzer, A., Flender, A., Levermann, P., Schmitz, T., Frühwald, D., Goody, P., Nickenig, G., Werner, N., Jansen, F., 2019. Atherosclerotic Conditions Promote the Packaging of Functional MicroRNA-92a-3p Into Endothelial Microvesicles. Circ. Res. 124, 575–587.

Livak, K.J., Schmittgen, T.D., 2001. Analysis of relative gene expression data using real-time quantitative PCR and the 2(-Delta Delta C(T)) Method. Methods 25, 402–408.

Livshits, M.A., Khomyakova, E., Evtushenko, E.G., Lazarev, V.N., Kulemin, N.A., Semina, S.E., Generozov, E. V, Govorun, V.M., 2015. Isolation of exosomes by differential centrifugation: Theoretical analysis of a commonly used protocol. Sci. Rep. 5, 17319.

Lobb, R.J., Becker, M., Wen, S.W., Wong, C.S.F., Wiegmans, A.P., Leimgruber, A., Möller, A., 2015. Optimized exosome isolation protocol for cell culture supernatant and human plasma. J. Extracell. vesicles 4, 27031.

Loftus, I.M., Naylor, A.R., Goodall, S., Crowther, M., Jones, L., Bell, P.R., Thompson, M.M., 2000. Increased matrix metalloproteinase-9 activity in unstable carotid plaques. A potential role in acute plaque disruption. Stroke 31, 40–47.

Love, M.I., Huber, W., Anders, S., 2014. Moderated estimation of fold change and dispersion for RNA-seq data with DESeq2. Genome Biol. 15, 550.

Lovren, F., Pan, Y., Quan, A., Singh, K.K., Shukla, P.C., Gupta, N., Steer, B.M., Ingram, A.J., Gupta, M., Al-Omran, M., Teoh, H., Marsden, P.A., Verma, S., 2012. MicroRNA-145 Targeted Therapy Reduces Atherosclerosis. Circulation 126, S81–S90.

Lozito, T.P., Tuan, R.S., 2012. Endothelial cell microparticles act as centers of matrix metalloproteinsase-2 (MMP-2) activation and vascular matrix remodeling. J. Cell. Physiol. 227, 534–549.

Lu, M., Yuan, S., Li, S., Li, L., Liu, M., Wan, S., 2019. The Exosome-Derived Biomarker in Atherosclerosis and Its Clinical Application. J. Cardiovasc. Transl. Res. 12, 68–74.

Lu, Y., Thavarajah, T., Gu, W., Cai, J., Xu, Q., 2018. Impact of miRNA in Atherosclerosis. Arterioscler. Thromb. Vasc. Biol. 38, e159–e170.

Ludmer, P.L., Selwyn, A.P., Shook, T.L., Wayne, R.R., Mudge, G.H., Alexander, R.W., Ganz, P., 1986. Paradoxical vasoconstriction induced by acetylcholine in atherosclerotic coronary arteries. N. Engl. J. Med. 315, 1046–1051.

Luo, Y., Duan, H., Qian, Y., Feng, L., Wu, Z., Wang, F., Feng, J., Yang, D., Qin, Z., Yan, X., 2017. Macrophagic CD146 promotes foam cell formation and retention during atherosclerosis. Cell Res. 27, 352–372.

Lusis, A.J., 2000. Atherosclerosis. Nature 407, 233–241.

Lutgens, E., de Muinck, E.D., Kitslaar, P.J., Tordoir, J.H., Wellens, H.J., Daemen, M.J., 1999. Biphasic pattern of cell turnover characterizes the progression from fatty streaks to ruptured human atherosclerotic plaques. Cardiovasc. Res. 41, 473–479.

Macfarlane, L.-A., Murphy, P.R., 2010. MicroRNA: Biogenesis, Function and Role in Cancer. Curr. Genomics 11, 537–561.

Mach, F., Baigent, C., Catapano, A.L., Koskinas, K.C., Casula, M., Badimon, L., Chapman, M.J., De Backer, G.G., Delgado, V., Ference, B.A., Graham, I.M., Halliday, A., Landmesser, U., Mihaylova, B., Pedersen, T.R., Riccardi, G., Richter, D.J., Sabatine, M.S., Taskinen, M.-R., Tokgozoglu, L., Wiklund, O., 2020. 2019 ESC/EAS Guidelines for the management of dyslipidaemias: lipid modification to reduce cardiovascular risk: The Task Force for the management of dyslipidaemias of the European Society of Cardiology (ESC) and European Atherosclerosis Society (EAS). Eur. Heart J. 41, 111–188.

Majesky, M.W., 2007. Developmental basis of vascular smooth muscle diversity. Arterioscler. Thromb. Vasc. Biol. 27, 1248–1258.

Marek, I., Canu, M., Cordasic, N., Rauh, M., Volkert, G., Fahlbusch, F.B., Rascher, W., Hilgers, K.F., Hartner, A., Menendez-Castro, C., 2017. Sex differences in the development of vascular and renal lesions in mice with a simultaneous deficiency of Apoe and the integrin chain Itga8. Biol. Sex Differ. 8, 19.

Marín, R.M., Sulc, M., Vanícek, J., 2013. Searching the coding region for microRNA targets. RNA 19, 467–474.

Martellucci, S., Orefice, N.S., Angelucci, A., Luce, A., Caraglia, M., Zappavigna, S., 2020. Extracellular Vesicles: New Endogenous Shuttles for miRNAs in Cancer Diagnosis and Therapy? Int. J. Mol. Sci. 21, 6486.

Martin, M., 2011. Cutadapt removes adapter sequences from high-throughput sequencing reads. EMBnet.journal; Vol 17, No 1 Next Gener. Seq. Data Anal.

Martínez de Lizarrondo, S., Roncal, C., Calvayrac, O., Rodríguez, C., Varo, N., Purroy, A., Lorente, L., Rodríguez, J.A., Doeuvre, L., Hervás-Stubbs, S., Angles-Cano, E., Páramo, J.A., Martínez-González, J., Orbe, J., 2012. Synergistic effect of thrombin and CD40 ligand on endothelial matrix metalloproteinase-10 expression and microparticle generation in vitro and in vivo. Arterioscler. Thromb. Vasc. Biol. 32, 1477–1487.

Matejovič, A., Wakao, S., Kitada, M., Kushida, Y., Dezawa, M., 2021. Comparison of separation methods for tissue-derived extracellular vesicles in the liver, heart, and skeletal muscle. FEBS Open Bio 11, 482–493.

Matoba, T., Sato, K., Egashira, K., 2013. Mouse models of plaque rupture. Curr. Opin. Lipidol. 24, 419–425.

Matsuura, E., Hughes, G.R. V, Khamashta, M.A., 2008. Oxidation of LDL and its clinical implication. Autoimmun. Rev. 7, 558–566.

Mause, S.F., von Hundelshausen, P., Zernecke, A., Koenen, R.R., Weber, C., 2005. Platelet microparticles: a transcellular delivery system for RANTES promoting monocyte recruitment on endothelium. Arterioscler. Thromb. Vasc. Biol. 25, 1512–1518.

Mayers, J.R., Audhya, A., 2012. Vesicle formation within endosomes: An ESCRT marks the spot. Commun. Integr. Biol. 5, 50–56.

Mayr, M., Hu, Y., Hainaut, P., Xu, Q., 2002. Mechanical Stress-induced DNA damage and rac-p38MAPK Signal Pathways Mediate p53-dependent Apoptosis in Vascular Smooth Muscle Cells. FASEB J. 16, 1423–1425.

Mayr, M., Xu, Q., 2001. Smooth muscle cell apoptosis in arteriosclerosis. Exp. Gerontol. 36, 969–987.

Mazière, C., Alimardani, G., Dantin, F., Dubois, F., Conte, M.-A., Mazière, J.-C., 1999. Oxidized LDL activates STAT1 and STAT3 transcription factors: possible involvement of reactive oxygen species. FEBS Lett. 448, 49–52.

McCormick, K.P., Willmann, M.R., Meyers, B.C., 2011. Experimental design, preprocessing, normalization and differential expression analysis of small RNA sequencing experiments. Silence 2, 2.

Medina, M.W., Gao, F., Ruan, W., Rotter, J.I., Krauss, R.M., 2008. Alternative splicing of 3-hydroxy-3-methylglutaryl coenzyme A reductase is associated with plasma low-density lipoprotein cholesterol response to simvastatin. Circulation 118, 355–362.

Mei, L.-L., Wang, W.-J., Qiu, Y.-T., Xie, X.-F., Bai, J., Shi, Z.-Z., 2017. miR-125b-5p functions as a tumor suppressor gene partially by regulating HMGA2 in esophageal squamous cell carcinoma. PLoS One 12, e0185636.

Meijer, H.A., Smith, E.M., Bushell, M., 2014. Regulation of miRNA strand selection: follow the leader? Biochem. Soc. Trans. 42, 1135–1140.

Meir, K.S., Leitersdorf, E., 2004. Atherosclerosis in the Apolipoprotein E–Deficient Mouse. Arterioscler. Thromb. Vasc. Biol. 24, 1006–1014.

Menghini, R., Casagrande, V., Cardellini, M., Martelli, E., Terrinoni, A., Amati, F.,

Vasa-Nicotera, M., Ippoliti, A., Novelli, G., Melino, G., Lauro, R., Federici, M., 2009. MicroRNA 217 Modulates Endothelial Cell Senescence via Silent Information Regulator 1. Circulation 120, 1524–1532.

Mihaylova, B., Emberson, J., Blackwell, L., Keech, A., Simes, J., Barnes, E.H., Voysey, M., Gray, A., Collins, R., Baigent, C., 2012. The effects of lowering LDL cholesterol with statin therapy in people at low risk of vascular disease: meta-analysis of individual data from 27 randomised trials. Lancet (London, England) 380, 581–590.

Milasan, A., Tessandier, N., Tan, S., Brisson, A., Boilard, E., Martel, C., 2016. Extracellular vesicles are present in mouse lymph and their level differs in atherosclerosis. J. Extracell. Vesicles 5, 31427.

Mitchell, P.S., Parkin, R.K., Kroh, E.M., Fritz, B.R., Wyman, S.K., Pogosova-Agadjanyan, E.L., Peterson, A., Noteboom, J., O'Briant, K.C., Allen, A., Lin, D.W., Urban, N., Drescher, C.W., Knudsen, B.S., Stirewalt, D.L., Gentleman, R., Vessella, R.L., Nelson, P.S., Martin, D.B., Tewari, M., 2008. Circulating microRNAs as stable blood-based markers for cancer detection. Proc. Natl. Acad. Sci. U. S. A. 105, 10513–10518.

Mitra, R., Qiao, J., Madhavan, S., O'Neil, G.L., Ritchie, B., Kulkarni, P., Sridhar, S., van de Ven, A.L., Cherry Kemmerling, E.M., Ferris, C., Hamilton, J.A., Ebong, E.E., 2018. The comparative effects of high fat diet or disturbed blood flow on glycocalyx integrity and vascular inflammation. Transl. Med. Commun. 3, 10.

Molloy, K.J., Thompson, M.M., Jones, J.L., Schwalbe, E.C., Bell, P.R.F., Naylor, A.R., Loftus, I.M., 2004. Unstable Carotid Plaques Exhibit Raised Matrix Metalloproteinase-8 Activity. Circulation 110, 337–343.

Momen-Heravi, F., Bala, S., Bukong, T., Szabo, G., 2014. Exosome-mediated delivery of functionally active miRNA-155 inhibitor to macrophages. Nanomedicine 10, 1517–1527.

Momen-Heravi, F., Balaj, L., Alian, S., Trachtenberg, A.J., Hochberg, F.H., Skog, J., Kuo, W.P., 2012. Impact of biofluid viscosity on size and sedimentation efficiency of the isolated microvesicles. Front. Physiol. 3, 162.

Monetti, M., Canavesi, M., Camera, M., Parente, R., Paoletti, R., Tremoli, E.,

Corsini, A., Bellosta, S., 2007. Rosuvastatin displays anti-atherothrombotic and anti-inflammatory properties in apoE-deficient mice. Pharmacol. Res. 55, 441–449.

Monguió-Tortajada, M., Gálvez-Montón, C., Bayes-Genis, A., Roura, S., Borràs, F.E., 2019. Extracellular vesicle isolation methods: rising impact of size-exclusion chromatography. Cell. Mol. Life Sci. 76, 2369–2382.

Morelli, A.E., Larregina, A.T., Shufesky, W.J., Sullivan, M.L.G., Stolz, D.B., Papworth, G.D., Zahorchak, A.F., Logar, A.J., Wang, Z., Watkins, S.C., Falo Jr, L.D., Thomson, A.W., 2004. Endocytosis, intracellular sorting, and processing of exosomes by dendritic cells. Blood 104, 3257–3266.

Morhayim, J., van de Peppel, J., Braakman, E., Rombouts, E.W.J.C., ter Borg, M.N.D., Dudakovic, A., Chiba, H., van der Eerden, B.C.J., Raaijmakers, M.H., van Wijnen, A.J., Cornelissen, J.J., van Leeuwen, J.P., 2016. Osteoblasts secrete miRNA-containing extracellular vesicles that enhance expansion of human umbilical cord blood cells. Sci. Rep. 6, 32034.

Mulcahy, L.A., Pink, R.C., Carter, D.R.F., 2014. Routes and mechanisms of extracellular vesicle uptake. J. Extracell. vesicles 3, 10.3402/jev.v3.24641.

Munir, J., Yoon, J.K., Ryu, S., 2020. Therapeutic miRNA-Enriched Extracellular Vesicles: Current Approaches and Future Prospects. Cells 9, 2271.

Muralidharan-Chari, V., Clancy, J., Plou, C., Romao, M., Chavrier, P., Raposo, G., D'Souza-Schorey, C., 2009. ARF6-regulated shedding of tumor cell-derived plasma membrane microvesicles. Curr. Biol. 19, 1875–1885.

Nabhan, J.F., Hu, R., Oh, R.S., Cohen, S.N., Lu, Q., 2012. Formation and release of arrestin domain-containing protein 1-mediated microvesicles (ARMMs) at plasma membrane by recruitment of TSG101 protein. Proc. Natl. Acad. Sci. U. S. A. 109, 4146–4151.

Nadkarni, S.K., Bouma, B.E., de Boer, J., Tearney, G.J., 2009. Evaluation of collagen in atherosclerotic plaques: the use of two coherent laser-based imaging methods. Lasers Med. Sci. 24, 439–445.

Nakashima, Y., Plump, A.S., Raines, E.W., Breslow, J.L., Ross, R., 1994. ApoE-deficient mice develop lesions of all phases of atherosclerosis throughout the arterial tree. Arterioscler. Thromb. A J. Vasc. Biol. 14, 133–140.

Nam, D., Ni, C.-W., Rezvan, A., Suo, J., Budzyn, K., Llanos, A., Harrison, D., Giddens, D., Jo, H., 2009. Partial carotid ligation is a model of acutely induced disturbed flow, leading to rapid endothelial dysfunction and atherosclerosis. Am. J. Physiol. Circ. Physiol. 297, H1535–H1543.

Napoli, C., Quehenberger, O., De Nigris, F., Abete, P., Glass, C.K., Palinski, W., 2000. Mildly oxidized low density lipoprotein activates multiple apoptotic signaling pathways in human coronary cells. FASEB J. 14, 1996–2007.

Navab, M., Imes, S.S., Hama, S.Y., Hough, G.P., Ross, L.A., Bork, R.W., Valente, A.J., Berliner, J. axA, Drinkwater, D.C., Laks, H., 1991. Monocyte transmigration induced by modification of low density lipoprotein in cocultures of human aortic wall cells is due to induction of monocyte chemotactic protein 1 synthesis and is abolished by high density lipoprotein. J. Clin. Invest. 88, 2039–2046.

Nawaz, M., Shah, N., Zanetti, B.R., Maugeri, M., Silvestre, R.N., Fatima, F., Neder, L., Valadi, H., 2018. Extracellular Vesicles and Matrix Remodeling Enzymes: The Emerging Roles in Extracellular Matrix Remodeling, Progression of Diseases and Tissue Repair. Cells 7, 167.

Nazari-Shafti, T.Z., Neuber, S., Duran, A.G., Exarchos, V., Beez, C.M., Meyborg, H., Krüger, K., Wolint, P., Buschmann, J., Böni, R., Seifert, M., Falk, V., Emmert, M.Y., 2020. MiRNA Profiles of Extracellular Vesicles Secreted by Mesenchymal Stromal Cells—Can They Predict Potential Off-Target Effects? Biomolecules 10, 1353.

Neiburga, K.D., Vilne, B., Bauer, S., Bongiovanni, D., Ziegler, T., Lachmann, M., Wengert, S., Hawe, J.S., Güldener, U., Westerlund, A.M., Li, L., Pang, S., Yang, C., Saar, K., Huebner, N., Maegdefessel, L., Consortium, D.B., Lange, R., Krane, M., Schunkert, H., von Scheidt, M., 2021. Vascular Tissue Specific miRNA Profiles Reveal Novel Correlations with Risk Factors in Coronary Artery Disease. Biomolecules 11, 1683.

Németh, A., Orgovan, N., Sódar, B.W., Osteikoetxea, X., Pálóczi, K., Szabó-Taylor, K.É., Vukman, K. V, Kittel, Á., Turiák, L., Wiener, Z., Tóth, S., Drahos, L., Vékey, K., Horvath, R., Buzás, E.I., 2017. Antibiotic-induced release of small extracellular vesicles (exosomes) with surface-associated DNA. Sci. Rep. 7, 8202.

New, S.E.P., Goettsch, C., Aikawa, M., Marchini, J.F., Shibasaki, M., Yabusaki, K., Libby, P., Shanahan, C.M., Kevin, C., Elena, A., 2013. Macrophage-Derived Matrix Vesicles. Circ. Res. 113, 72–77.

Nguyen, M.-A., Karunakaran, D., Geoffrion, M., Cheng, H.S., Tandoc, K., Perisic Matic, L., Hedin, U., LMaegdefessel, L., Fish, J.E., Rayner, K.J., 2018. Extracellular Vesicles Secreted by Atherogenic Macrophages Transfer MicroRNA to Inhibit Cell Migration. Arterioscler. Thromb. Vasc. Biol. 38, 49–63.

Nidorf, S.M., Eikelboom, J.W., Budgeon, C.A., Thompson, P.L., 2013. Low-Dose Colchicine for Secondary Prevention of Cardiovascular Disease. J. Am. Coll. Cardiol. 61, 404–410.

Nielsen, T., Kristensen, A.F., Pedersen, S., Christiansen, G., Kristensen, S.R., 2018. Investigation of procoagulant activity in extracellular vesicles isolated by differential ultracentrifugation. J. Extracell. Vesicles 7, 1454777.

Nikpay, M., Goel, A., Won, H.-H., Hall, L.M., Willenborg, C., Kanoni, S., Saleheen, D., Kyriakou, T., Nelson, C.P., Hopewell, J.C., Webb, T.R., Zeng, L., Dehghan, A., Alver, M., Armasu, S.M., Auro, K., Bjonnes, A., Chasman, D.I., Chen, S., Ford, I., Franceschini, N., Gieger, C., Grace, C., Gustafsson, S., Huang, Jie, Hwang, S.-J., Kim, Y.K., Kleber, M.E., Lau, K.W., Lu, X., Lu, Y., Lyytikäinen, L.-P., Mihailov, E., Morrison, A.C., Pervjakova, N., Qu, L., Rose, L.M., Salfati, E., Saxena, R., Scholz, M., Smith, A. V, Tikkanen, E., Uitterlinden, A., Yang, X., Zhang, W., Zhao, W., de Andrade, M., de Vries, P.S., van Zuydam, N.R., Anand, S.S., Bertram, L., Beutner, F., Dedoussis, G., Frossard, P., Gauguier, D., Goodall, A.H., Gottesman, O., Haber, M., Han, B.-G., Huang, Jianfeng, Jalilzadeh, S., Kessler, T., König, I.R., Lannfelt, L., Lieb, W., Lind, L., Lindgren, C.M., Lokki, M.-L., Magnusson, P.K., Mallick, N.H., Mehra, N., Meitinger, T., Memon, F.-R., Morris, A.P., Nieminen, M.S., Pedersen, N.L., Peters, A., Rallidis, L.S., Rasheed, A., Samuel, M., Shah, S.H., Sinisalo, J., Stirrups, K.E., Trompet, S., Wang, L., Zaman, K.S., Ardissino, D., Boerwinkle, E., Borecki, I.B., Bottinger, E.P., Buring, J.E., Chambers, J.C., Collins, R., Cupples, L.A., Danesh, J., Demuth, I., Elosua, R., Epstein, S.E., Esko, T., Feitosa, M.F., Franco, O.H., Franzosi, M.G., Granger, C.B., Gu, D., Gudnason, V., Hall, A.S., Hamsten, A., Harris, T.B., Hazen, S.L., Hengstenberg, C., Hofman, A., Ingelsson, E., Iribarren, C., Jukema, J.W.,

Karhunen, P.J., Kim, B.-J., Kooner, J.S., Kullo, I.J., Lehtimäki, T., Loos, R.J.F., Melander, O., Metspalu, A., März, W., Palmer, C.N., Perola, M., Quertermous, T., Rader, D.J., Ridker, P.M., Ripatti, S., Roberts, R., Salomaa, V., Sanghera, D.K., Schwartz, S.M., Seedorf, U., Stewart, A.F., Stott, D.J., Thiery, J., Zalloua, P.A., O'Donnell, C.J., Reilly, M.P., Assimes, T.L., Thompson, J.R., Erdmann, J., Clarke, R., Watkins, H., Kathiresan, S., McPherson, R., Deloukas, P., Schunkert, H., Samani, N.J., Farrall, M., Consortium, the Cardi., 2015. A comprehensive 1000 Genomes–based genome-wide association meta-analysis of coronary artery disease. Nat. Genet. 47, 1121–1130.

Nishino, J., Kim, I., Chada, K., Morrison, S.J., 2008. Hmga2 Promotes Neural Stem Cell Self-Renewal in Young but Not Old Mice by Reducing p16Ink4a and p19Arf Expression. Cell 135, 227–239.

Niu, C., Wang, X., Zhao, M., Cai, T., Liu, P., Li, J., Willard, B., Zu, L., Zhou, E., Li, Y., Pan, B., Yang, F., Zheng, L., 2016. Macrophage Foam Cell-Derived Extracellular Vesicles Promote Vascular Smooth Muscle Cell Migration and Adhesion. J. Am. Heart Assoc. 5, e004099.

Nordin, J.Z., Lee, Y., Vader, P., Mäger, I., Johansson, H.J., Heusermann, W., Wiklander, O.P.B., Hällbrink, M., Seow, Y., Bultema, J.J., Gilthorpe, J., Davies, T., Fairchild, P.J., Gabrielsson, S., Meisner-Kober, N.C., Lehtiö, J., Smith, C.I.E., Wood, M.J.A., El Andaloussi, S., 2015. Ultrafiltration with size-exclusion liquid chromatography for high yield isolation of extracellular vesicles preserving intact biophysical and functional properties. Nanomedicine 11, 879–883.

Nording, H.M., Seizer, P., Langer, H.F., 2015. Platelets in inflammation and atherogenesis. Front. Immunol. 6, 98.

Nozaki, T., Sugiyama, S., Koga, H., Sugamura, K., Ohba, K., Matsuzawa, Y., Sumida, H., Matsui, K., Jinnouchi, H., Ogawa, H., 2009. Significance of a multiple biomarkers strategy including endothelial dysfunction to improve risk stratification for cardiovascular events in patients at high risk for coronary heart disease. J. Am. Coll. Cardiol. 54, 601–608.

O'Brien, J., Hayder, H., Zayed, Y., Peng, C., 2018. Overview of MicroRNA Biogenesis, Mechanisms of Actions, and Circulation. Front. Endocrinol.

(Lausanne).

Ochiai, A., Miyata, S., Iwase, M., Shimizu, M., Inoue, J., Sato, R., 2016. Kaempferol stimulates gene expression of low-density lipoprotein receptor through activation of Sp1 in cultured hepatocytes. Sci. Rep. 6, 24940.

Olayioye, M.A., 2001. Intracellular signaling pathways of ErbB2/HER-2 and family members. Breast Cancer Res. 3, 385.

Olivieri, F., Lazzarini, R., Recchioni, R., Marcheselli, F., Rippo, M.R., Di Nuzzo, S., Albertini, M.C., Graciotti, L., Babini, L., Mariotti, S., Spada, G., Abbatecola, A.M., Antonicelli, R., Franceschi, C., Procopio, A.D., 2013. MiR-146a as marker of senescence-associated pro-inflammatory status in cells involved in vascular remodelling. Age (Dordr). 35, 1157–1172.

Osterud, B., Bjorklid, E., 2003. Role of monocytes in atherogenesis. Physiol. Rev. 83, 1069–1112.

Otogenetics, 2023. RNA Sequencing VS Microarray [WWW Document]. URL https://www.otogenetics.com/ (accessed 1.8.23).

Ouyang, D., Ye, Y., Guo, D., Yu, X., Chen, J., Qi, J., Tan, X., Zhang, Y., Ma, Y., Li, Y., 2015. MicroRNA-125b-5p inhibits proliferation and promotes adipogenic differentiation in 3T3-L1 preadipocytes. Acta Biochim. Biophys. Sin. (Shanghai). 47, 355–361.

Owens, G.K., Kumar, M.S., Wamhoff, B.R., 2004. Molecular regulation of vascular smooth muscle cell differentiation in development and disease. Physiol. Rev. 84, 767–801.

Pahwa, R., Jialal, I., 2021. Atherosclerosis. Treasure Island (FL).

Parahuleva, M.S., Lipps, C., Parviz, B., Hölschermann, H., Schieffer, B., Schulz, R., Euler, G., 2018. MicroRNA expression profile of human advanced coronary atherosclerotic plaques. Sci. Rep. 8, 7823.

Pasquet, J.-M., Dachary-Prigent, J., Nurden, A.T., 1996. Calcium Influx is a Determining Factor of Calpain Activation and Microparticle Formation in Platelets. Eur. J. Biochem. 239, 647–654.

Paul, P., Chakraborty, A., Sarkar, D., Langthasa, M., Rahman, M., Bari, M., Singha, R.K.S., Malakar, A.K., Chakraborty, S., 2018. Interplay between miRNAs and

human diseases. J. Cell. Physiol. 233, 2007–2018.

Peeters, W., Moll, F.L., Vink, A., van der Spek, P.J., de Kleijn, D.P. V, de Vries, J.-P.P.M., Verheijen, J.H., Newby, A.C., Pasterkamp, G., 2011. Collagenase matrix metalloproteinase-8 expressed in atherosclerotic carotid plaques is associated with systemic cardiovascular outcome. Eur. Heart J. 32, 2314–2325.

Pereira-da-Silva, T., Coutinho Cruz, M., Carrusca, C., Cruz Ferreira, R., Napoleão, P., Mota Carmo, M., 2018. Circulating microRNA profiles in different arterial territories of stable atherosclerotic disease: a systematic review. Am. J. Cardiovasc. Dis. 8, 1–13.

Perrotta, I., Saveria, A., 2016. Exosomes in human atherosclerosis: An ultrastructural analysis study. Ultrastruct. Pathol. 40, 101–106.

Petersen, C.P., Bordeleau, M.-E., Pelletier, J., Sharp, P.A., 2006. Short RNAs repress translation after initiation in mammalian cells. Mol. Cell 21, 533–542.

Peterson, S., Thompson, J., Ufkin, M., Sathyanarayana, P., Liaw, L., Congdon, C.B., 2014. Common features of microRNA target prediction tools. Front. Genet.

Pidkovka, N.A., Cherepanova, O.A., Yoshida, T., Alexander, M.R., Deaton, R.A., Thomas, J.A., Leitinger, N., Owens, G.K., 2007. Oxidized Phospholipids Induce Phenotypic Switching of Vascular Smooth Muscle Cells In Vivo and In Vitro. Circ. Res. 101, 792–801.

Pienimaeki-Roemer, A., Konovalova, T., Musri, M.M., Sigruener, A., Boettcher, A., Meister, G., Schmitz, G., 2017. Transcriptomic profiling of platelet senescence and platelet extracellular vesicles. Transfusion 57, 144–156.

Pillai, R.S., Artus, C.G., Filipowicz, W., 2004. Tethering of human Ago proteins to mRNA mimics the miRNA-mediated repression of protein synthesis. RNA 10, 1518–1525.

Pinzón, N., Li, B., Martinez, L., Sergeeva, A., Presumey, J., Apparailly, F., Seitz, H., 2017. microRNA target prediction programs predict many false positives. Genome Res. 27, 234–245.

Pols, M.S., Klumperman, J., 2009. Trafficking and function of the tetraspanin

CD63. Exp. Cell Res. 315, 1584–1592.

Pomatto, M.A.C., Bussolati, B., D'Antico, S., Ghiotto, S., Tetta, C., Brizzi, M.F., Camussi, G., 2019. Improved Loading of Plasma-Derived Extracellular Vesicles to Encapsulate Antitumor miRNAs. Mol. Ther. Methods Clin. Dev. 13, 133–144.

Poznyak, A. V, Nikiforov, N.G., Starodubova, A. V, Popkova, T. V, Orekhov, A.N., 2021. Macrophages and Foam Cells: Brief Overview of Their Role, Linkage, and Targeting Potential in Atherosclerosis. Biomedicines 9, 1221.

Pradhan, A.D., Aday, A.W., Rose, L.M., Ridker, P.M., 2018. Residual Inflammatory Risk on Treatment With PCSK9 Inhibition and Statin Therapy. Circulation 138, 141–149.

Preston, R.A., Jy, W., Jimenez, J.J., Mauro, L.M., Horstman, L.L., Valle, M., Aime, G., Ahn, Y.S., 2003. Effects of Severe Hypertension on Endothelial and Platelet Microparticles. Hypertension 41, 211–217.

Pužar Dominkuš, P., Stenovec, M., Sitar, S., Lasič, E., Zorec, R., Plemenitaš, A., Žagar, E., Kreft, M., Lenassi, M., 2018. PKH26 labeling of extracellular vesicles: Characterization and cellular internalization of contaminating PKH26 nanoparticles. Biochim. Biophys. acta. Biomembr. 1860, 1350–1361.

Qi, X.-Y., Qu, S.-L., Xiong, W.-H., Rom, O., Chang, L., Jiang, Z.-S., 2018. Perivascular adipose tissue (PVAT) in atherosclerosis: a double-edged sword. Cardiovasc. Diabetol. 17, 134.

Qiao, L., Hu, S., Liu, S., Zhang, H., Ma, H., Huang, K., Li, Z., Su, T., Vandergriff, A., Tang, J., Allen, T., Dinh, P.-U., Cores, J., Yin, Q., Li, Y., Cheng, K., 2019. microRNA-21-5p dysregulation in exosomes derived from heart failure patients impairs regenerative potential. J. Clin. Invest. 129, 2237–2250.

Qiao, S., Zhang, W., Yin, Y., Wei, Z., Chen, F., Zhao, J., Sun, X., Mu, D., Xie, J., Xu, B., 2020. Extracellular vesicles derived from Krüppel-Like Factor 2-overexpressing endothelial cells attenuate myocardial ischemia-reperfusion injury by preventing Ly6C(high) monocyte recruitment. Theranostics 10, 11562–11579.

Quillard, T., Croce, K., Jaffer, F.A., Weissleder, R., Libby, P., 2011. Molecular imaging of macrophage protease activity in cardiovascular inflammation in vivo. Thromb. Haemost. 105, 828–836.

Quillet, A., Saad, C., Ferry, G., Anouar, Y., Vergne, N., Lecroq, T., Dubessy, C., 2020. Improving Bioinformatics Prediction of microRNA Targets by Ranks Aggregation. Front. Genet.

Quinlan, A.R., Hall, I.M., 2010. BEDTools: a flexible suite of utilities for comparing genomic features. Bioinformatics 26, 841–842.

Ramirez, M.I., Amorim, M.G., Gadelha, C., Milic, I., Welsh, J.A., Freitas, V.M., Nawaz, M., Akbar, N., Couch, Y., Makin, L., Cooke, F., Vettore, A.L., Batista, P.X., Freezor, R., Pezuk, J.A., Rosa-Fernandes, L., Carreira, A.C.O., Devitt, A., Jacobs, L., Silva, I.T., Coakley, G., Nunes, D.N., Carter, D., Palmisano, G., Dias-Neto, E., 2018. Technical challenges of working with extracellular vesicles. Nanoscale 10, 881–906.

Rautou, P.-E., Leroyer, A.S., Ramkhelawon, B., Devue, C., Duflaut, D., Vion, A.-C., Nalbone, G., Castier, Y., Leseche, G., Lehoux, S., Tedgui, A., Boulanger, C.M., 2011. Microparticles from human atherosclerotic plaques promote endothelial ICAM-1-dependent monocyte adhesion and transendothelial migration. Circ. Res. 108, 335–343.

Ray, K.K., Wright, R.S., Kallend, D., Koenig, W., Leiter, L.A., Raal, F.J., Bisch, J.A., Richardson, T., Jaros, M., Wijngaard, P.L.J., Kastelein, J.J.P., 2020. Two Phase 3 Trials of Inclisiran in Patients with Elevated LDL Cholesterol. N. Engl. J. Med. 382, 1507–1519.

Reddy, K.G., Nair, R.N., Sheehan, H.M., Hodgson, J.M., 1994. Evidence that selective endothelial dysfunction may occur in the absence of angiographic or ultrasound atherosclerosis in patients with risk factors for atherosclerosis. J. Am. Coll. Cardiol. 23, 833–843.

Rekker, K., Saare, M., Roost, A.M., Kubo, A.-L., Zarovni, N., Chiesi, A., Salumets, A., Peters, M., 2014. Comparison of serum exosome isolation methods for microRNA profiling. Clin. Biochem. 47, 135–138.

Rennenberg, R.J.M.W., Kessels, A.G.H., Schurgers, L.J., van Engelshoven, J.M.A., de Leeuw, P.W., Kroon, A.A., 2009. Vascular calcifications as a marker of increased cardiovascular risk: a meta-analysis. Vasc. Health Risk Manag. 5, 185–197.

Repetto, E., Lichtenstein, L., Hizir, Z., Tekaya, N., Benahmed, M., Ruidavets, J.-

B., Zaragosi, L.-E., Perret, B., Bouchareychas, L., Genoux, A., Lotte, R., Ruimy, R., Ferrières, J., Barbry, P., Martinez, L.O., Trabucchi, M., 2015. RNY-derived small RNAs as a signature of coronary artery disease. BMC Med. 13, 259.

Reusch, P., Wagdy, H., Reusch, R., Wilson, E., Ives, H.E., 1996. Mechanical Strain Increases Smooth Muscle and Decreases Nonmuscle Myosin Expression in Rat Vascular Smooth Muscle Cells. Circ. Res. 79, 1046–1053.

Reynolds, J.L., Skepper, J.N., McNair, R., Kasama, T., Gupta, K., Weissberg, P.L., Jahnen-Dechent, W., Shanahan, C.M., 2005. Multifunctional roles for serum protein fetuin-a in inhibition of human vascular smooth muscle cell calcification. J. Am. Soc. Nephrol. 16, 2920–2930.

Ridker, P.M., Danielson, E., Fonseca, F.A.H., Genest, J., Gotto, A.M., Kastelein, J.J.P., Koenig, W., Libby, P., Lorenzatti, A.J., MacFadyen, J.G., Nordestgaard, B.G., Shepherd, J., Willerson, J.T., Glynn, R.J., 2009. Reduction in C-reactive protein and LDL cholesterol and cardiovascular event rates after initiation of rosuvastatin: a prospective study of the JUPITER trial. Lancet 373, 1175–1182.

Ridker, P.M., Danielson, E., Fonseca, F.A.H., Genest, J., Gotto, A.M.J., Kastelein, J.J.P., Koenig, W., Libby, P., Lorenzatti, A.J., MacFadyen, J.G., Nordestgaard, B.G., Shepherd, J., Willerson, J.T., Glynn, R.J., 2008. Rosuvastatin to prevent vascular events in men and women with elevated C-reactive protein. N. Engl. J. Med. 359, 2195–2207.

Ridker, P.M., Everett, B.M., Thuren, T., MacFadyen, J.G., Chang, W.H., Ballantyne, C., Fonseca, F., Nicolau, J., Koenig, W., Anker, S.D., Kastelein, J.J.P., Cornel, J.H., Pais, P., Pella, D., Genest, J., Cifkova, R., Lorenzatti, A., Forster, T., Kobalava, Z., Vida-Simiti, L., Flather, M., Shimokawa, H., Ogawa, H., Dellborg, M., Rossi, P.R.F., Troquay, R.P.T., Libby, P., Glynn, R.J., 2017. Antiinflammatory Therapy with Canakinumab for Atherosclerotic Disease. N. Engl. J. Med. 377, 1119–1131.

Rizzacasa, B., Morini, E., Pucci, S., Murdocca, M., Novelli, G., Amati, F., 2017. LOX-1 and Its Splice Variants: A New Challenge for Atherosclerosis and Cancer-Targeted Therapies. Int. J. Mol. Sci. 18, 290.

Roche-Molina, M., Sanz-Rosa, D., Cruz, F.M., García-Prieto, J., López, S., Abia,

R., Muriana, F.J.G., Fuster, V., Ibáñez, B., Bernal, J.A., 2015. Induction of Sustained Hypercholesterolemia by Single Adeno-Associated Virus–Mediated Gene Transfer of Mutant hPCSK9. Arterioscler. Thromb. Vasc. Biol. 35, 50–59.

Rodriguez, A., Griffiths-Jones, S., Ashurst, J.L., Bradley, A., 2004. Identification of mammalian microRNA host genes and transcription units. Genome Res. 14, 1902–1910.

Romaine, S.P.R., Tomaszewski, M., Condorelli, G., Samani, N.J., 2015. MicroRNAs in cardiovascular disease: an introduction for clinicians. Heart 101, 921 LP – 928.

Ross, R., Glomset, J., Harker, L., 1977. Response to injury and atherogenesis. Am. J. Pathol. 86, 675–684.

Ross, R., Glomset, J.A., 1973. Atherosclerosis and the arterial smooth muscle cell: Proliferation of smooth muscle is a key event in the genesis of the lesions of atherosclerosis. Science 180, 1332–1339.

Roura, S., Gámez-Valero, A., Lupón, J., Gálvez-Montón, C., Borràs, F.E., Bayes-Genis, A., 2018. Proteomic signature of circulating extracellular vesicles in dilated cardiomyopathy. Lab. Investig. 98, 1291–1299.

Rzucidlo, E.M., Martin, K.A., Powell, R.J., 2007. Regulation of vascular smooth muscle cell differentiation. J. Vasc. Surg. 45, A25–A32.

Sabatine, M.S., Giugliano, R.P., Wiviott, S.D., Raal, F.J., Blom, D.J., Robinson, J., Ballantyne, C.M., Somaratne, R., Legg, J., Wasserman, S.M., Scott, R., Koren, M.J., Stein, E.A., 2015. Efficacy and Safety of Evolocumab in Reducing Lipids and Cardiovascular Events. N. Engl. J. Med. 372, 1500–1509.

Sadallah, S., Eken, C., Martin, P.J., Schifferli, J.A., 2011. Microparticles (ectosomes) shed by stored human platelets downregulate macrophages and modify the development of dendritic cells. J. Immunol. 186, 6543–6552.

Sampat, G.D., Rebecca, L., Mariola, K.-S., A., P.S., Narayanaswamy, B.K., 2012. MicroRNA-155 Is Required for Mycobacterium bovis BCG-Mediated Apoptosis of Macrophages. Mol. Cell. Biol. 32, 2239–2253.

Sansone, P., Savini, C., Kurelac, I., Chang, Q., Amato, L.B., Strillacci, A., Stepanova, A., Iommarini, L., Mastroleo, C., Daly, L., Galkin, A., Thakur,

B.K., Soplop, N., Uryu, K., Hoshino, A., Norton, L., Bonafé, M., Cricca, M., Gasparre, G., Lyden, D., Bromberg, J., 2017. Packaging and transfer of mitochondrial DNA via exosomes regulate escape from dormancy in hormonal therapy-resistant breast cancer. Proc. Natl. Acad. Sci. U. S. A. 114, E9066–E9075.

Sarkar, A., Mitra, S., Mehta, S., Raices, R., Wewers, M.D., 2009. Monocyte Derived Microvesicles Deliver a Cell Death Message via Encapsulated Caspase-1. PLoS One 4, e7140.

Sarlon-Bartoli, G., Bennis, Y., Lacroix, R., Piercecchi-Marti, M.D., Bartoli, M.A., Arnaud, L., Mancini, J., Boudes, A., Sarlon, E., Thevenin, B., Leroyer, A.S., Squarcioni, C., Magnan, P.E., Dignat-George, F., Sabatier, F., 2013. Plasmatic Level of Leukocyte-Derived Microparticles Is Associated With Unstable Plaque in Asymptomatic Patients With High-Grade Carotid Stenosis. J. Am. Coll. Cardiol. 62, 1436–1441.

Schober, A., Nazari-Jahantigh, M., Wei, Y., Bidzhekov, K., Gremse, F., Grommes, J., Megens, R.T.A., Heyll, K., Noels, H., Hristov, M., Wang, S., Kiessling, F., Olson, E.N., Weber, C., 2014. MicroRNA-126-5p promotes endothelial proliferation and limits atherosclerosis by suppressing Dlk1. Nat. Med. 20, 368–376.

Scholtes, V.P., Johnson, J.L., Jenkins, N., Sala-Newby, G.B., de Vries, J.P.M., de Borst, G.J., de Kleijn, D.P. V, Moll, F.L., Pasterkamp, G., Newby, A.C., 2012. Carotid Atherosclerotic Plaque Matrix Metalloproteinase-12–Positive Macrophage Subpopulation Predicts Adverse Outcome After Endarterectomy. J. Am. Heart Assoc. 1, e001040.

Schulte, C., Molz, S., Appelbaum, S., Karakas, M., Ojeda, F., Lau, D.M., Hartmann, T., Lackner, K.J., Westermann, D., Schnabel, R.B., Blankenberg, S., Zeller, T., 2016. miRNA-197 and miRNA-223 Predict Cardiovascular Death in a Cohort of Patients with Symptomatic Coronary Artery Disease. PLoS One 10, e0145930.

Schwarzenbach, H., da Silva, A.M., Calin, G., Pantel, K., 2015. Data Normalization Strategies for MicroRNA Quantification. Clin. Chem. 61, 1333–1342.

Schwenke, D.C., Carew, T.E., 1989a. Initiation of atherosclerotic lesions in cholesterol-fed rabbits. I. Focal increases in arterial LDL concentration

precede development of fatty streak lesions. Arterioscler. An Off. J. Am. Hear. Assoc. Inc. 9, 895–907.

Schwenke, D.C., Carew, T.E., 1989b. Initiation of atherosclerotic lesions in cholesterol-fed rabbits. II. Selective retention of LDL vs. selective increases in LDL permeability in susceptible sites of arteries. Arteriosclerosis 9, 908–918.

Scott, G.K., Goga, A., Bhaumik, D., Berger, C.E., Sullivan, C.S., Benz, C.C., 2007. Coordinate suppression of ERBB2 and ERBB3 by enforced expression of micro-RNA miR-125a or miR-125b. J. Biol. Chem. 282, 1479–1486.

Serrano-Pertierra, E., Oliveira-Rodríguez, M., Matos, M., Gutiérrez, G., Moyano, A., Salvador, M., Rivas, M., Blanco-López, M.C., 2020. Extracellular Vesicles: Current Analytical Techniques for Detection and Quantification. Biomolecules 10, 11585.

Shaalan, W.E., Cheng, H., Gewertz, B., McKinsey, J.F., Schwartz, L.B., Katz, D., Cao, D., Desai, T., Glagov, S., Bassiouny, H.S., 2004. Degree of carotid plaque calcification in relation to symptomatic outcome and plaque inflammation. J. Vasc. Surg. 40, 262–269.

Shankman, L.S., Gomez, D., Cherepanova, O.A., Salmon, M., Alencar, G.F., Haskins, R.M., Swiatlowska, P., Newman, A.A.C., Greene, E.S., Straub, A.C., Isakson, B., Randolph, G.J., Owens, G.K., 2015. KLF4-dependent phenotypic modulation of smooth muscle cells has a key role in atherosclerotic plaque pathogenesis. Nat. Med. 21, 628–637.

Shen, C.M., Mao, S.J., Huang, G.S., Yang, P.C., Chu, R.M., 2001. Stimulation of smooth muscle cell proliferation by ox-LDL- and acetyl LDL-induced macrophage-derived foam cells. Life Sci. 70, 443–452.

Shepherd, J., Blauw, G.J., Murphy, M.B., Bollen, E.L.E.M., Buckley, B.M., Cobbe, S.M., Ford, I., Gaw, A., Hyland, M., Jukema, J.W., Kamper, A.M., Macfarlane, P.W., Meinders, A.E., Norrie, J., Packard, C.J., Perry, I.J., Stott, D.J., Sweeney, B.J., Twomey, C., Westendorp, R.G.J., 2002. Pravastatin in elderly individuals at risk of vascular disease (PROSPER): a randomised controlled trial. Lancet (London, England) 360, 1623–1630.

Sherman, B.T., Hao, M., Qiu, J., Jiao, X., Baseler, M.W., Lane, H.C., Imamichi,

T., Chang, W., 2022. DAVID: a web server for functional enrichment analysis and functional annotation of gene lists (2021 update). Nucleic Acids Res. 50, W216-21.

Shin, S., Park, Y.H., Jung, S.-H., Jang, S.-H., Kim, M.Y., Lee, J.Y., Chung, Y., 2021. Urinary exosome microRNA signatures as a noninvasive prognostic biomarker for prostate cancer. npj Genomic Med. 6, 45.

Shurtleff, M.J., Yao, J., Qin, Y., Nottingham, R.M., Temoche-Diaz, M.M., Schekman, R., Lambowitz, A.M., 2017. Broad role for YBX1 in defining the small noncoding RNA composition of exosomes. Proc. Natl. Acad. Sci. U. S. A. 114, E8987–E8995.

Silverman, M.G., Ference, B.A., Im, K., Wiviott, S.D., Giugliano, R.P., Grundy, S.M., Braunwald, E., Sabatine, M.S., 2016. Association Between Lowering LDL-C and Cardiovascular Risk Reduction Among Different Therapeutic Interventions: A Systematic Review and Meta-analysis. JAMA 316, 1289–1297.

Singh, R.B., Mengi, S.A., Xu, Y.-J., Arneja, A.S., Dhalla, N.S., 2002. Pathogenesis of atherosclerosis: A multifactorial process. Exp. Clin. Cardiol. 7, 40–53.

Sinning, J.-M., Losch, J., Walenta, K., Böhm, M., Nickenig, G., Werner, N., 2011. Circulating CD31+/Annexin V+ microparticles correlate with cardiovascular outcomes. Eur. Heart J. 32, 2034–2041.

Skokos, D., Botros, H.G., Demeure, C., Morin, J., Peronet, R., Birkenmeier, G., Boudaly, S., Mécheri, S., 2003. Mast cell-derived exosomes induce phenotypic and functional maturation of dendritic cells and elicit specific immune responses in vivo. J. Immunol. 170, 3037–3045.

Skotland, T., Ekroos, K., Kauhanen, D., Simolin, H., Seierstad, T., Berge, V., Sandvig, K., Llorente, A., 2017. Molecular lipid species in urinary exosomes as potential prostate cancer biomarkers. Eur. J. Cancer 70, 122–132.

Sódar, B.W., Kittel, Á., Pálóczi, K., Vukman, K. V., Osteikoetxea, X., Szabó-Taylor, K., Németh, A., Sperlágh, B., Baranyai, T., Giricz, Z., Wiener, Z., Turiák, L., Drahos, L., Pállinger, É., Vékey, K., Ferdinandy, P., Falus, A., Buzás, E.I., 2016. Low-density lipoprotein mimics blood plasma-derived exosomes and microvesicles during isolation and detection. Sci. Rep. 6. https://doi.org/10.1038/srep24316

Soehnlein, O., Libby, P., 2021. Targeting inflammation in atherosclerosis — from experimental insights to the clinic. Nat. Rev. Drug Discov. 20, 589–610.

Song, P., Fang, Z., Wang, H., Cai, Y., Rahimi, K., Zhu, Y., Fowkes, F.G.R., Fowkes, F.J.I., Rudan, I., 2020. Global and regional prevalence, burden, and risk factors for carotid atherosclerosis: a systematic review, meta-analysis, and modelling study. Lancet. Glob. Heal. 8, e721–e729.

Song, X.W., Li, Q., Lin, L., Wang, X.C., Li, D.F., Wang, G.K., Ren, A.J., Wang, Y.R., Qin, Y.W., Yuan, W.J., Jing, Q., 2010. MicroRNAs are dynamically regulated in hypertrophic hearts, and miR-199a is essential for the maintenance of cell size in cardiomyocytes. J. Cell. Physiol. 225, 437–443.

Sorokin, V., Vickneson, K., Kofidis, T., Woo, C.C., Lin, X.Y., Foo, R., Shanahan, C.M., 2020. Role of Vascular Smooth Muscle Cell Plasticity and Interactions in Vessel Wall Inflammation. Front. Immunol.

Souilhol, C., Harmsen, M.C., Evans, P.C., Krenning, G., 2018. Endothelial–mesenchymal transition in atherosclerosis. Cardiovasc. Res. 114, 565–577.

Speer, M.Y., Yang, H.-Y., Brabb, T., Leaf, E., Look, A., Lin, W.-L., Frutkin, A., Dichek, D., Giachelli, C.M., 2009. Smooth muscle cells give rise to osteochondrogenic precursors and chondrocytes in calcifying arteries. Circ. Res. 104, 733–741.

Ståhl, A.-L., Johansson, K., Mossberg, M., Kahn, R., Karpman, D., 2019. Exosomes and microvesicles in normal physiology, pathophysiology, and renal diseases. Pediatr. Nephrol. 34, 11–30.

Stamatikos, A., Knight, E., Vojtech, L., Bi, L., Wacker, B.K., Tang, C., Dichek, D.A., 2019. Exosome-Mediated Transfer of Anti-miR-33a-5p from Transduced Endothelial Cells Enhances Macrophage and Vascular Smooth Muscle Cell Cholesterol Efflux. Hum. Gene Ther. 31, 219–232.

Steitz, S.A., Speer, M.Y., Curinga, G., Yang, H.-Y., Haynes, P., Aebersold, R., Schinke, T., Karsenty, G., Giachelli, C.M., 2001. Smooth Muscle Cell Phenotypic Transition Associated With Calcification. Circ. Res. 89, 1147–1154.

Stępień, E., Stankiewicz, E., Zalewski, J., Godlewski, J., Zmudka, K., Wybrańska, I., 2012. Number of microparticles generated during acute myocardial infarction and stable angina correlates with platelet activation. Arch. Med.

Res. 43, 31–35.

Sticht, C., De La Torre, C., Parveen, A., Gretz, N., 2018. miRWalk: An online resource for prediction of microRNA binding sites. PLoS One 13, e0206239.

Stocker, R., Keaney, J.F., 2004. Role of Oxidative Modifications in Atherosclerosis. Physiol. Rev. 84, 1381–1478.

Stranska, R., Gysbrechts, L., Wouters, J., Vermeersch, P., Bloch, K., Dierickx, D., Andrei, G., Snoeck, R., 2018. Comparison of membrane affinity-based method with size-exclusion chromatography for isolation of exosome-like vesicles from human plasma. J. Transl. Med. 16, 1.

Street, J.M., Barran, P.E., Mackay, C.L., Weidt, S., Balmforth, C., Walsh, T.S., Chalmers, R.T.A., Webb, D.J., Dear, J.W., 2012. Identification and proteomic profiling of exosomes in human cerebrospinal fluid. J. Transl. Med. 10, 5.

Stuffers, S., Sem Wegner, C., Stenmark, H., Brech, A., 2009. Multivesicular Endosome Biogenesis in the Absence of ESCRTs. Traffic 10, 925–937.

Suades, R., Padró, T., Vilahur, G., Badimon, L., 2012. Circulating and platelet-derived microparticles in human blood enhance thrombosis on atherosclerotic plaques. Thromb. Haemost. 108, 1208–1219.

Suárez, Y., Wang, C., Manes, T.D., Pober, J.S., 2010. Cutting edge: TNF-induced microRNAs regulate TNF-induced expression of E-selectin and intercellular adhesion molecule-1 on human endothelial cells: feedback control of inflammation. J. Immunol. 184, 21–25.

Subbotin, V.M., 2016. Excessive intimal hyperplasia in human coronary arteries before intimal lipid depositions is the initiation of coronary atherosclerosis and constitutes a therapeutic target. Drug Discov. Today 21, 1578–1595.

Subra, C., Laulagnier, K., Perret, B., Record, M., 2007. Exosome lipidomics unravels lipid sorting at the level of multivesicular bodies. Biochimie 89, 205–212.

Sun, X., He, S., Wara, A.K.M., Icli, B., Shvartz, E., Tesmenitsky, Y., Belkin, N., Li, D., Blackwell, T.S., Sukhova, G.K., Croce, K., Feinberg, M.W., 2014. Systemic Delivery of MicroRNA-181b Inhibits Nuclear Factor-κB Activation, Vascular Inflammation, and Atherosclerosis in Apolipoprotein E–Deficient Mice. Circ.

Res. 114, 32–40.

Svensson, K.J., Christianson, H.C., Wittrup, A., Bourseau-Guilmain, E., Lindqvist, E., Svensson, L.M., Mörgelin, M., Belting, M., 2013. Exosome uptake depends on ERK1/2-heat shock protein 27 signaling and lipid Raft-mediated endocytosis negatively regulated by caveolin-1. J. Biol. Chem. 288, 17713–17724.

Tabas, I., 2007. Apoptosis and efferocytosis in mouse models of atherosclerosis. Curr. Drug Targets 8, 1288–1296.

Tabas, I., Williams, K.J., Borén, J., 2007. Subendothelial Lipoprotein Retention as the Initiating Process in Atherosclerosis. Circulation 116, 1832–1844.

Takanabe, R., Ono, K., Abe, Y., Takaya, T., Horie, T., Wada, H., Kita, T., Satoh, N., Shimatsu, A., Hasegawa, K., 2008. Up-regulated expression of microRNA-143 in association with obesity in adipose tissue of mice fed high-fat diet. Biochem. Biophys. Res. Commun. 376, 728–732.

Takov, K., Yellon, D.M., Davidson, S.M., 2019. Comparison of small extracellular vesicles isolated from plasma by ultracentrifugation or size-exclusion chromatography: yield, purity and functional potential. J. Extracell. Vesicles 8, 1560809.

Takov, K., Yellon, D.M., Davidson, S.M., 2017. Confounding factors in vesicle uptake studies using fluorescent lipophilic membrane dyes. J. Extracell. vesicles 6, 1388731.

Tang, F., Barbacioru, C., Wang, Y., Nordman, E., Lee, C., Xu, N., Wang, X., Bodeau, J., Tuch, B.B., Siddiqui, A., Lao, K., Surani, M.A., 2009. mRNA-Seq whole-transcriptome analysis of a single cell. Nat. Methods 6, 377–382.

Tang, N., Sun, B., Gupta, A., Rempel, H., Pulliam, L., 2016. Monocyte exosomes induce adhesion molecules and cytokines via activation of NF-κB in endothelial cells. FASEB J. 30, 3097–3106.

Taraboletti, G., D'Ascenzo, S., Borsotti, P., Giavazzi, R., Pavan, A., Dolo, V., 2002. Shedding of the matrix metalloproteinases MMP-2, MMP-9, and MT1-MMP as membrane vesicle-associated components by endothelial cells. Am. J. Pathol. 160, 673–680.

Tardif, J.-C., Kouz, S., Waters, D.D., Bertrand, O.F., Diaz, R., Maggioni, A.P., Pinto, F.J., Ibrahim, R., Gamra, H., Kiwan, G.S., Berry, C., López-Sendón, J., Ostadal, P., Koenig, W., Angoulvant, D., Grégoire, J.C., Lavoie, M.-A., Dubé, M.-P., Rhainds, D., Provencher, M., Blondeau, L., Orfanos, A., L'Allier, P.L., Guertin, M.-C., Roubille, F., 2019. Efficacy and Safety of Low-Dose Colchicine after Myocardial Infarction. N. Engl. J. Med. 381, 2497–2505.

Tauro, B.J., Greening, D.W., Mathias, R.A., Ji, H., Mathivanan, S., Scott, A.M., Simpson, R.J., 2012. Comparison of ultracentrifugation, density gradient separation, and immunoaffinity capture methods for isolating human colon cancer cell line LIM1863-derived exosomes. Methods 56, 293–304.

Thakur, B.K., Zhang, H., Becker, A., Matei, I., Huang, Y., Costa-Silva, B., Zheng, Y., Hoshino, A., Brazier, H., Xiang, J., Williams, C., Rodriguez-Barrueco, R., Silva, J.M., Zhang, W., Hearn, S., Elemento, O., Paknejad, N., Manova-Todorova, K., Welte, K., Bromberg, J., Peinado, H., Lyden, D., 2014. Double-stranded DNA in exosomes: a novel biomarker in cancer detection. Cell Res.

Théry, C., Amigorena, S., Raposo, G., Clayton, A., 2006. Isolation and Characterization of Exosomes from Cell Culture Supernatants and Biological Fluids. Curr. Protoc. Cell Biol. 30, 3.22.1-3.22.29.

Théry, C., Witwer, K.W., Aikawa, E., Alcaraz, M.J., Anderson, J.D., Andriantsitohaina, R., Antoniou, A., Arab, T., Archer, F., Atkin-Smith, G.K., Ayre, D.C., Bach, J.-M., Bachurski, D., Baharvand, H., Balaj, L., Baldacchino, S., Bauer, N.N., Baxter, A.A., Bebawy, M., Beckham, C., Bedina Zavec, A., Benmoussa, A., Berardi, A.C., Bergese, P., Bielska, E., Blenkiron, C., Bobis-Wozowicz, S., Boilard, E., Boireau, W., Bongiovanni, A., Borràs, F.E., Bosch, S., Boulanger, C.M., Breakefield, X., Breglio, A.M., Brennan, M.Á., Brigstock, D.R., Brisson, A., Broekman, M.L., Bromberg, J.F., Bryl-Górecka, P., Buch, S., Buck, A.H., Burger, D., Busatto, S., Buschmann, D., Bussolati, B., Buzás, E.I., Byrd, J.B., Camussi, G., Carter, D.R.F., Caruso, S., Chamley, L.W., Chang, Y.-T., Chen, C., Chen, S., Cheng, L., Chin, A.R., Clayton, A., Clerici, S.P., Cocks, A., Cocucci, E., Coffey, R.J., Cordeiro-da-Silva, A., Couch, Y., Coumans, F.A.W., Coyle, B., Crescitelli, R., Criado, M.F., D'Souza-Schorey, C., Das, S., Datta Chaudhuri, A., de Candia, P., De Santana, E.F., De Wever, O., del Portillo, H.A., Demaret, T., Deville, S., Devitt, A., Dhondt, B., Di Vizio, D., Dieterich, L.C., Dolo, V., Dominguez Rubio, A.P., Dominici, M., Dourado,

M.R., Driedonks, T.A.P., Duarte, F. V, Duncan, H.M., Eichenberger, R.M., Ekström, K., EL Andaloussi, S., Elie-Caille, C., Erdbrügger, U., Falcón-Pérez, J.M., Fatima, F., Fish, J.E., Flores-Bellver, M., Försönits, A., Frelet-Barrand, A., Fricke, F., Fuhrmann, G., Gabrielsson, S., Gámez-Valero, A., Gardiner, C., Gärtner, K., Gaudin, R., Gho, Y.S., Giebel, B., Gilbert, C., Gimona, M., Giusti, I., Goberdhan, D.C.I., Görgens, A., Gorski, S.M., Greening, D.W., Gross, J.C., Gualerzi, A., Gupta, G.N., Gustafson, D., Handberg, A., Haraszti, R.A., Harrison, P., Hegyesi, H., Hendrix, A., Hill, A.F., Hochberg, F.H., Hoffmann, K.F., Holder, B., Holthofer, H., Hosseinkhani, B., Hu, G., Huang, Y., Huber, V., Hunt, S., Ibrahim, A.G.-E., Ikezu, T., Inal, J.M., Isin, M., Ivanova, A., Jackson, H.K., Jacobsen, S., Jay, S.M., Jayachandran, M., Jenster, G., Jiang, L., Johnson, S.M., Jones, J.C., Jong, A., Jovanovic-Talisman, T., Jung, S., Kalluri, R., Kano, S., Kaur, S., Kawamura, Y., Keller, E.T., Khamari, D., Khomyakova, E., Khvorova, A., Kierulf, P., Kim, K.P., Kislinger, T., Klingeborn, M., Klinke, D.J., Kornek, M., Kosanović, M.M., Kovács, Á.F., Krämer-Albers, E.-M., Krasemann, S., Krause, M., Kurochkin, I. V, Kusuma, G.D., Kuypers, S., Laitinen, S., Langevin, S.M., Languino, L.R., Lannigan, J., Lässer, C., Laurent, L.C., Lavieu, G., Lázaro-Ibáñez, E., Le Lay, S., Lee, M.-S., Lee, Y.X.F., Lemos, D.S., Lenassi, M., Leszczynska, A., Li, I.T.S., Liao, K., Libregts, S.F., Ligeti, E., Lim, R., Lim, S.K., Linē, A., Linnemannstöns, K., Llorente, A., Lombard, C.A., Lorenowicz, M.J., Lörincz, Á.M., Lötvall, J., Lovett, J., Lowry, M.C., Loyer, X., Lu, Q., Lukomska, B., Lunavat, T.R., Maas, S.L.N., Malhi, H., Marcilla, A., Mariani, J., Mariscal, J., Martens-Uzunova, E.S., Martin-Jaular, L., Martinez, M.C., Martins, V.R., Mathieu, M., Mathivanan, S., Maugeri, M., McGinnis, L.K., McVey, M.J., Meckes, D.G., Meehan, K.L., Mertens, I., Minciacchi, V.R., Möller, A., Møller Jørgensen, M., Morales-Kastresana, A., Morhayim, J., Mullier, F., Muraca, M., Musante, L., Mussack, V., Muth, D.C., Myburgh, K.H., Najrana, T., Nawaz, M., Nazarenko, I., Nejsum, P., Neri, C., Neri, T., Nieuwland, R., Nimrichter, L., Nolan, J.P., Nolte-'t Hoen, E.N.M., Noren Hooten, N., O'Driscoll, L., O'Grady, T., O'Loghlen, A., Ochiya, T., Olivier, M., Ortiz, A., Ortiz, L.A., Osteikoetxea, X., Østergaard, O., Ostrowski, M., Park, J., Pegtel, D.M., Peinado, H., Perut, F., Pfaffl, M.W., Phinney, D.G., Pieters, B.C.H., Pink, R.C., Pisetsky, D.S., Pogge von Strandmann, E., Polakovicova, I., Poon, I.K.H., Powell, B.H., Prada, I., Pulliam, L., Quesenberry, P., Radeghieri, A., Raffai, R.L.,

Raimondo, S., Rak, J., Ramirez, M.I., Raposo, G., Rayyan, M.S., Regev-Rudzki, N., Ricklefs, F.L., Robbins, P.D., Roberts, D.D., Rodrigues, S.C., Rohde, E., Rome, S., Rouschop, K.M.A., Rughetti, A., Russell, A.E., Saá, P., Sahoo, S., Salas-Huenuleo, E., Sánchez, C., Saugstad, J.A., Saul, M.J., Schiffelers, R.M., Schneider, R., Schøyen, T.H., Scott, A., Shahaj, E., Sharma, S., Shatnyeva, O., Shekari, F., Shelke, G.V., Shetty, A.K., Shiba, K., Siljander, P.R.-M., Silva, A.M., Skowronek, A., Snyder, O.L., Soares, R.P., Sódar, B.W., Soekmadji, C., Sotillo, J., Stahl, P.D., Stoorvogel, W., Stott, S.L., Strasser, E.F., Swift, S., Tahara, H., Tewari, M., Timms, K., Tiwari, S., Tixeira, R., Tkach, M., Toh, W.S., Tomasini, R., Torrecilhas, A.C., Tosar, J.P., Toxavidis, V., Urbanelli, L., Vader, P., van Balkom, B.W.M., van der Grein, S.G., Van Deun, J., van Herwijnen, M.J.C., Van Keuren-Jensen, K., van Niel, G., van Royen, M.E., van Wijnen, A.J., Vasconcelos, M.H., Vechetti, I.J., Veit, T.D., Vella, L.J., Velot, É., Verweij, F.J., Vestad, B., Viñas, J.L., Visnovitz, T., Vukman, K. V, Wahlgren, J., Watson, D.C., Wauben, M.H.M., Weaver, A., Webber, J.P., Weber, V., Wehman, A.M., Weiss, D.J., Welsh, J.A., Wendt, S., Wheelock, A.M., Wiener, Z., Witte, L., Wolfram, J., Xagorari, A., Xander, P., Xu, J., Yan, X., Yáñez-Mó, M., Yin, H., Yuana, Y., Zappulli, V., Zarubova, J., Žėkas, V., Zhang, J., Zhao, Z., Zheng, L., Zheutlin, A.R., Zickler, A.M., Zimmermann, P., Zivkovic, A.M., Zocco, D., Zuba-Surma, E.K., 2018. Minimal information for studies of extracellular vesicles 2018 (MISEV2018): a position statement of the International Society for Extracellular Vesicles and update of the MISEV2014 guidelines. J. Extracell. Vesicles 7, 1535750.

Tian, X., Hu, T., Zhang, H., He, Lingjuan, Huang, X., Liu, Q., Yu, W., He, Liang, Yang, Z., Yan, Y., Yang, X., Zhong, T.P., Pu, W.T., Zhou, B., 2014. Vessel formation. De novo formation of a distinct coronary vascular population in neonatal heart. Science 345, 90–94.

Tiberio, P., Callari, M., Angeloni, V., Daidone, M.G., Appierto, V., 2015. Challenges in using circulating miRNAs as cancer biomarkers. Biomed Res. Int. 2015, 731479.

Timmerman, N., Waissi, F., Dekker, M., de Borst, G.J., van Bennekom, J., de Winter, R.J., Hilvo, M., Jylhä, A., Pasterkamp, G., de Kleijn, D.P. V, Laaksonen, R., 2022. Ceramides and phospholipids in plasma extracellular vesicles are associated with high risk of major cardiovascular events after

carotid endarterectomy. Sci. Rep. 12, 5521.

Timmis, A., Townsend, N., Gale, C., Grobbee, R., Maniadakis, N., Flather, M., Wilkins, E., Wright, L., Vos, R., Bax, J., Blum, M., Pinto, F., Vardas, P., 2018. European Society of Cardiology: Cardiovascular Disease Statistics 2017. Eur. Heart J. 39, 508–579.

Tousoulis, D., Oikonomou, E., Economou, E.K., Crea, F., Kaski, J.C., 2016. Inflammatory cytokines in atherosclerosis: current therapeutic approaches. Eur. Heart J. 37, 1723–1732.

Trajkovic, K., Hsu, C., Chiantia, S., Rajendran, L., Wenzel, D., Wieland, F., Schwille, P., Brügger, B., Simons, M., 2008. Ceramide triggers budding of exosome vesicles into multivesicular endosomes. Science 319, 1244–1247.

Tricarico, C., Clancy, J., D'Souza-Schorey, C., 2017. Biology and biogenesis of shed microvesicles. Small GTPases 8, 220–232.

Trioulier, Y., Torch, S., Blot, B., Cristina, N., Chatellard-Causse, C., Verna, J.-M., Sadoul, R., 2004. Alix, a protein regulating endosomal trafficking, is involved in neuronal death. J. Biol. Chem. 279, 2046–2052.

Tripisciano, C., Weiss, R., Karuthedom George, S., Fischer, M.B., Weber, V., 2020. Extracellular Vesicles Derived From Platelets, Red Blood Cells, and Monocyte-Like Cells Differ Regarding Their Ability to Induce Factor XII-Dependent Thrombin Generation. Front. Cell Dev. Biol.

Truesdell, S.S., Mortensen, R.D., Seo, M., Schroeder, J.C., Lee, J.H., LeTonqueze, O., Vasudevan, S., 2012. MicroRNA-mediated mRNA Translation Activation in Quiescent Cells and Oocytes Involves Recruitment of a Nuclear microRNP. Sci. Rep. 2, 842.

Tyson, K.L., Reynolds, J.L., McNair, R., Zhang, Q., Weissberg, P.L., Shanahan, C.M., 2003. Osteo/chondrocytic transcription factors and their target genes exhibit distinct patterns of expression in human arterial calcification. Arterioscler. Thromb. Vasc. Biol. 23, 489–494.

Ueta, E., Tsutsumi, K., Kato, H., Matsushita, H., Shiraha, H., Fujii, M., Matsumoto, K., Horiguchi, S., Okada, H., 2021. Extracellular vesicle-shuttled miRNAs as a diagnostic and prognostic biomarker and their potential roles in gallbladder cancer patients. Sci. Rep. 11, 12298.

Vajen, T., Benedikter, B.J., Heinzmann, A.C.A., Vasina, E.M., Henskens, Y., Parsons, M., Maguire, P.B., Stassen, F.R., Heemskerk, J.W.M., Schurgers, L.J., Koenen, R.R., 2017. Platelet extracellular vesicles induce a pro-inflammatory smooth muscle cell phenotype. J. Extracell. vesicles 6, 1322454.

Valadi, H., Ekström, K., Bossios, A., Sjöstrand, M., Lee, J.J., Lötvall, J.O., 2007. Exosome-mediated transfer of mRNAs and microRNAs is a novel mechanism of genetic exchange between cells. Nat. Cell Biol. 9, 654–659.

Valinezhad Orang, A., Safaralizadeh, R., Kazemzadeh-Bavili, M., 2014. Mechanisms of miRNA-Mediated Gene Regulation from Common Downregulation to mRNA-Specific Upregulation. Int. J. Genomics 2014, 970607.

van Balkom, B.W.M., Eisele, A.S., Pegtel, D.M., Bervoets, S., Verhaar, M.C., 2015. Quantitative and qualitative analysis of small RNAs in human endothelial cells and exosomes provides insights into localized RNA processing, degradation and sorting. J. Extracell. vesicles 4, 26760. https://doi.org/10.3402/jev.v4.26760

Van der Donckt, C., Van Herck, J.L., Schrijvers, D.M., Vanhoutte, G., Verhoye, M., Blockx, I., Van Der Linden, A., Bauters, D., Lijnen, H.R., Sluimer, J.C., Roth, L., Van Hove, C.E., Fransen, P., Knaapen, M.W., Hervent, A.-S., De Keulenaer, G.W., Bult, H., Martinet, W., Herman, A.G., De Meyer, G.R.Y., 2015. Elastin fragmentation in atherosclerotic mice leads to intraplaque neovascularization, plaque rupture, myocardial infarction, stroke, and sudden death. Eur. Heart J. 36, 1049–1058.

van der Feltz, C., Hoskins, A.A., 2019. Structural and functional modularity of the U2 snRNP in pre-mRNA splicing. Crit. Rev. Biochem. Mol. Biol. 54, 443–465.

van Niel, G., Charrin, S., Simoes, S., Romao, M., Rochin, L., Saftig, P., Marks, M.S., Rubinstein, E., Raposo, G., 2011. The Tetraspanin CD63 Regulates ESCRT-Independent and -Dependent Endosomal Sorting during Melanogenesis. Dev. Cell 21, 708–721.

van Niel, G., D'Angelo, G., Raposo, G., 2018. Shedding light on the cell biology of extracellular vesicles. Nat. Rev. Mol. Cell Biol. 19, 213–228.

VanderLaan, P.A., Reardon, C.A., Getz, G.S., 2004. Site Specificity of Atherosclerosis. Arterioscler. Thromb. Vasc. Biol. 24, 12–22.

Vang Mouritzen, M., Jenssen, H., 2018. Optimized Scratch Assay for In Vitro Testing of Cell Migration with an Automated Optical Camera. J. Vis. Exp. 138, 57691.

VanHorn, S., Morris, S.A., 2021. Next-Generation Lineage Tracing and Fate Mapping to Interrogate Development. Dev. Cell 56, 7–21.

Varankar, S.S., Bapat, S.A., 2018. Migratory Metrics of Wound Healing: A Quantification Approach for in vitro Scratch Assays. Front. Oncol. 8, 633.

Vasina, E.M., Cauwenberghs, S., Feijge, M.A.H., Heemskerk, J.W.M., Weber, C., Koenen, R.R., 2011. Microparticles from apoptotic platelets promote resident macrophage differentiation. Cell Death Dis. 2, e211.

Vengrenyuk, Y., Carlier, S., Xanthos, S., Cardoso, L., Ganatos, P., Virmani, R., Einav, S., Gilchrist, L., Weinbaum, S., 2006. A hypothesis for vulnerable plaque rupture due to stress-induced debonding around cellular microcalcifications in thin fibrous caps. Proc. Natl. Acad. Sci. U. S. A. 103, 14678–14683.

Vengrenyuk, Y., Nishi, H., Long, X., Ouimet, M., Savji, N., Martinez, F.O., Cassella, C.P., Moore, K.J., Ramsey, S.A., Miano, J.M., Fisher, E.A., 2015. Cholesterol loading reprograms the microRNA-143/145-myocardin axis to convert aortic smooth muscle cells to a dysfunctional macrophage-like phenotype. Arterioscler. Thromb. Vasc. Biol. 35, 535–546.

Verweij, F.J., Bebelman, M.P., Jimenez, C.R., Garcia-Vallejo, J.J., Janssen, H., Neefjes, J., Knol, J.C., de Goeij-de Haas, R., Piersma, S.R., Baglio, S.R., Verhage, M., Middeldorp, J.M., Zomer, A., van Rheenen, J., Coppolino, M.G., Hurbain, I., Raposo, G., Smit, M.J., Toonen, R.F.G., van Niel, G., Pegtel, D.M., 2018. Quantifying exosome secretion from single cells reveals a modulatory role for GPCR signaling. J. Cell Biol. 217, 1129–1142.

Vickers, K.C., Landstreet, S.R., Levin, M.G., Shoucri, B.M., Toth, C.L., Taylor, R.C., Palmisano, B.T., Tabet, F., Cui, H.L., Rye, K.-A., Sethupathy, P., Remaley, A.T., 2014. MicroRNA-223 coordinates cholesterol homeostasis. Proc. Natl. Acad. Sci. 111, 14518–14523.

Vlachos, I.S., Paraskevopoulou, M.D., Karagkouni, D., Georgakilas, G., Vergoulis, T., Kanellos, I., Anastasopoulos, I.-L., Maniou, S., Karathanou, K., Kalfakakou, D., Fevgas, A., Dalamagas, T., Hatzigeorgiou, A.G., 2015. DIANA-TarBase v7.0: indexing more than half a million experimentally supported miRNA:mRNA interactions. Nucleic Acids Res. 43, D153-9.

Wagschal, A., Najafi-Shoushtari, S.H., Wang, L., Goedeke, L., Sinha, S., DeLemos, A.S., Black, J.C., Ramírez, C.M., Li, Y., Tewhey, R., Hatoum, I., Shah, N., Lu, Y., Kristo, F., Psychogios, N., Vrbanac, V., Lu, Y.-C., Hla, T., de Cabo, R., Tsang, J.S., Schadt, E., Sabeti, P.C., Kathiresan, S., Cohen, D.E., Whetstine, J., Chung, R.T., Fernández-Hernando, C., Kaplan, L.M., Bernards, A., Gerszten, R.E., Näär, A.M., 2015. Genome-wide identification of microRNAs regulating cholesterol and triglyceride homeostasis. Nat. Med. 21, 1290–1297.

Wahid, F., Shehzad, A., Khan, T., Kim, Y.Y., 2010. MicroRNAs: synthesis, mechanism, function, and recent clinical trials. Biochim. Biophys. Acta 1803, 1231–1243.

Wahlgren, C.-M., Zheng, W., Shaalan, W., Tang, J., Bassiouny, H.S., 2009. Human carotid plaque calcification and vulnerability. Relationship between degree of plaque calcification, fibrous cap inflammatory gene expression and symptomatology. Cerebrovasc. Dis. 27, 193–200.

Wahlgren, J., Karlson, T.D.L., Brisslert, M., Vaziri Sani, F., Telemo, E., Sunnerhagen, P., Valadi, H., 2012. Plasma exosomes can deliver exogenous short interfering RNA to monocytes and lymphocytes. Nucleic Acids Res. 40, e130–e130.

Wang, G., Dinkins, M., He, Q., Zhu, G., Poirier, C., Campbell, A., Mayer-Proschel, M., Bieberich, E., 2012. Astrocytes secrete exosomes enriched with proapoptotic ceramide and prostate apoptosis response 4 (PAR-4): potential mechanism of apoptosis induction in Alzheimer disease (AD). J. Biol. Chem. 287, 21384–21395.

Wang, J.-G., Williams, J.C., Davis, B.K., Jacobson, K., Doerschuk, C.M., Ting, J.P.-Y., Mackman, N., 2011. Monocytic microparticles activate endothelial cells in an IL-1ß-dependent manner. Blood 118, 2366–2374.

Wang, J.C., Bennett, M., 2012. Aging and Atherosclerosis. Circ. Res. 111, 245–259.

Wang, J.G., Williams, J.C., Davis, B.K., Jacobson, K., Doerschuk, C.M., Ting, J.P.-Y., Mackman, N., 2011. Monocytic microparticles activate endothelial cells in an IL-1ß-dependent manner. Blood 118, 2366–2374. https://doi.org/10.1182/blood-2011-01-330878

Wang, L., Huang, Z., Huang, W., Chen, X., Shan, P., Zhong, P., Khan, Z., Wang, J., Fang, Q., Liang, G., Wang, Y., 2017. Inhibition of epidermal growth factor receptor attenuates atherosclerosis via decreasing inflammation and oxidative stress. Sci. Rep. 7, 45917.

Wang, M., Li, W., Chang, G.-Q., Ye, C.-S., Ou, J.-S., Li, X.-X., Liu, Y., Cheang, T.-Y., Huang, X.-L., Wang, S.-M., 2011. MicroRNA-21 Regulates Vascular Smooth Muscle Cell Function via Targeting Tropomyosin 1 in Arteriosclerosis Obliterans of Lower Extremities. Arterioscler. Thromb. Vasc. Biol. 31, 2044–2053.

Wang, S., Kojima, K., Mobley, J.A., West, A.B., 2019. Proteomic analysis of urinary extracellular vesicles reveal biomarkers for neurologic disease. EBioMedicine 45, 351–361.

Wang, Y., Dubland, J.A., Allahverdian, S., Asonye, E., Sahin, B., Jaw, J.E., Sin, D.D., Seidman, M.A., Leeper, N.J., Francis, G.A., 2019. Smooth Muscle Cells Contribute the Majority of Foam Cells in ApoE (Apolipoprotein E)-Deficient Mouse Atherosclerosis. Arterioscler. Thromb. Vasc. Biol. 39, 876–887.

Wang, Y., Tan, J., Wang, L., Pei, G., Cheng, H., Zhang, Q., Wang, S., He, C., Fu, C., Wei, Q., 2021. MiR-125 Family in Cardiovascular and Cerebrovascular Diseases. Front. Cell Dev. Biol.

Wang, Y., Zeng, G., Jiang, Y., 2020. The Emerging Roles of miR-125b in Cancers. Cancer Manag. Res. 12, 1079–1088.

Wang, Y.T., Shi, T., Srivastava, S., Kagan, J., Liu, T., Rodland, K.D., 2020. Proteomic Analysis of Exosomes for Discovery of Protein Biomarkers for Prostate and Bladder Cancer. Cancers (Basel). 12, 2335.

Webber, J., Clayton, A., 2013. How pure are your vesicles? J. Extracell. Vesicles 2, 19861.

Weber, A., Köppen, H.O., Schrör, K., 2000. Platelet-derived microparticles stimulate coronary artery smooth muscle cell mitogenesis by a PDGF-

independent mechanism. Thromb. Res. 98, 461–466.

Wei, Y., Nazari-Jahantigh, M., Neth, P., Weber, C., Schober, A., 2013. MicroRNA-126, -145, and -155. Arterioscler. Thromb. Vasc. Biol. 33, 449–454.

Wei, Z., Batagov, A.O., Schinelli, S., Wang, J., Wang, Y., El Fatimy, R., Rabinovsky, R., Balaj, L., Chen, C.C., Hochberg, F., Carter, B., Breakefield, X.O., Krichevsky, A.M., 2017. Coding and noncoding landscape of extracellular RNA released by human glioma stem cells. Nat. Commun. 8, 1145.

Welsh, P., Grassia, G., Botha, S., Sattar, N., Maffia, P., 2017. Targeting inflammation to reduce cardiovascular disease risk: a realistic clinical prospect? Br. J. Pharmacol. 174, 3898–3913.

Werner, N., Wassmann, S., Ahlers, P., Kosiol, S., Nickenig, G., 2006. Circulating CD31+/annexin V+ apoptotic microparticles correlate with coronary endothelial function in patients with coronary artery disease. Arterioscler. Thromb. Vasc. Biol. 26, 112–116.

WHO, 2019. No Title [WWW Document].

Wightman, B., Ha, I., Ruvkun, G., 1993. Posttranscriptional regulation of the heterochronic gene lin-14 by lin-4 mediates temporal pattern formation in C. elegans. Cell 75, 855–862.

Willer, C.J., Schmidt, E.M., Sengupta, S., Peloso, G.M., Gustafsson, S., Kanoni, S., Ganna, A., Chen, J., Buchkovich, M.L., Mora, S., Beckmann, J.S., Bragg-Gresham, J.L., Chang, H.-Y., Demirkan, A., Den Hertog, H.M., Do, R., Donnelly, L.A., Ehret, G.B., Esko, T., Feitosa, M.F., Ferreira, T., Fischer, K., Fontanillas, P., Fraser, R.M., Freitag, D.F., Gurdasani, D., Heikkilä, K., Hyppönen, E., Isaacs, A., Jackson, A.U., Johansson, Å., Johnson, T., Kaakinen, M., Kettunen, J., Kleber, M.E., Li, X., Luan, J., Lyytikäinen, L.-P., Magnusson, P.K.E., Mangino, M., Mihailov, E., Montasser, M.E., Müller-Nurasyid, M., Nolte, I.M., O'Connell, J.R., Palmer, C.D., Perola, M., Petersen, A.-K., Sanna, S., Saxena, R., Service, S.K., Shah, S., Shungin, D., Sidore, C., Song, C., Strawbridge, R.J., Surakka, I., Tanaka, T., Teslovich, T.M., Thorleifsson, G., Van den Herik, E.G., Voight, B.F., Volcik, K.A., Waite, L.L., Wong, A., Wu, Y., Zhang, W., Absher, D., Asiki, G., Barroso, I., Been, L.F., Bolton, J.L., Bonnycastle, L.L., Brambilla, P., Burnett, M.S., Cesana, G., Dimitriou, M., Doney, A.S.F., Döring, A., Elliott, P., Epstein, S.E., Eyjolfsson,

G.I., Gigante, B., Goodarzi, M.O., Grallert, H., Gravito, M.L., Groves, C.J., Hallmans, G., Hartikainen, A.-L., Hayward, C., Hernandez, D., Hicks, A.A., Holm, H., Hung, Y.-J., Illig, T., Jones, M.R., Kaleebu, P., Kastelein, J.J.P., Khaw, K.-T., Kim, E., Klopp, N., Komulainen, P., Kumari, M., Langenberg, C., Lehtimäki, T., Lin, S.-Y., Lindström, J., Loos, R.J.F., Mach, F., McArdle, W.L., Meisinger, C., Mitchell, B.D., Müller, G., Nagaraja, R., Narisu, N., Nieminen, T.V.M., Nsubuga, R.N., Olafsson, I., Ong, K.K., Palotie, A., Papamarkou, T., Pomilla, C., Pouta, A., Rader, D.J., Reilly, M.P., Ridker, P.M., Rivadeneira, F., Rudan, I., Ruokonen, A., Samani, N., Scharnagl, H., Seeley, J., Silander, K., Stancáková, A., Stirrups, K., Swift, A.J., Tiret, L., Uitterlinden, A.G., van Pelt, L.J., Vedantam, S., Wainwright, N., Wijmenga, C., Wild, S.H., Willemsen, G., Wilsgaard, T., Wilson, J.F., Young, E.H., Zhao, J.H., Adair, L.S., Arveiler, D., Assimes, T.L., Bandinelli, S., Bennett, F., Bochud, M., Boehm, B.O., Boomsma, D.I., Borecki, I.B., Bornstein, S.R., Bovet, P., Burnier, M., Campbell, H., Chakravarti, A., Chambers, J.C., Chen, Y.-D.I., Collins, F.S., Cooper, R.S., Danesh, J., Dedoussis, G., de Faire, U., Feranil, A.B., Ferrières, J., Ferrucci, L., Freimer, N.B., Gieger, C., Groop, L.C., Gudnason, V., Gyllensten, U., Hamsten, A., Harris, T.B., Hingorani, A., Hirschhorn, J.N., Hofman, A., Hovingh, G.K., Hsiung, C.A., Humphries, S.E., Hunt, S.C., Hveem, K., Iribarren, C., Järvelin, M.-R., Jula, A., Kähönen, M., Kaprio, J., Kesäniemi, A., Kivimaki, M., Kooner, J.S., Koudstaal, P.J., Krauss, R.M., Kuh, D., Kuusisto, J., Kyvik, K.O., Laakso, M., Lakka, T.A., Lind, L., Lindgren, C.M., Martin, N.G., März, W., McCarthy, M.I., McKenzie, C.A., Meneton, P., Metspalu, A., Moilanen, L., Morris, A.D., Munroe, P.B., Njølstad, I., Pedersen, N.L., Power, C., Pramstaller, P.P., Price, J.F., Psaty, B.M., Quertermous, T., Rauramaa, R., Saleheen, D., Salomaa, V., Sanghera, D.K., Saramies, J., Schwarz, P.E.H., Sheu, W.H.-H., Shuldiner, A.R., Siegbahn, A., Spector, T.D., Stefansson, K., Strachan, D.P., Tayo, B.O., Tremoli, E., Tuomilehto, J., Uusitupa, M., van Duijn, C.M., Vollenweider, P., Wallentin, L., Wareham, N.J., Whitfield, J.B., Wolffenbuttel, B.H.R., Ordovas, J.M., Boerwinkle, E., Palmer, C.N.A., Thorsteinsdottir, U., Chasman, D.I., Rotter, J.I., Franks, P.W., Ripatti, S., Cupples, L.A., Sandhu, M.S., Rich, S.S., Boehnke, M., Deloukas, P., Kathiresan, S., Mohlke, K.L., Ingelsson, E., Abecasis, G.R., Consortium, G.L.G., 2013. Discovery and refinement of loci associated with lipid levels. Nat. Genet. 45, 1274–1283.

Williams, K.J., Tabas, I., 1995. The response-to-retention hypothesis of early atherogenesis. Arterioscler. Thromb. Vasc. Biol. 15, 551–561.

Willms, E., Johansson, H.J., Mäger, I., Lee, Y., Blomberg, K.E.M., Sadik, M., Alaarg, A., Smith, C.I.E., Lehtiö, J., EL Andaloussi, S., Wood, M.J.A., Vader, P., 2016. Cells release subpopulations of exosomes with distinct molecular and biological properties. Sci. Rep. 6, 22519.

Wood, D., 2001. Established and emerging cardiovascular risk factors. Am. Heart J. 141, S49–S57.

Wouters, K., Shiri-Sverdlov, R., van Gorp, P.J., van Bilsen, M., Hofker, M.H., 2005. Understanding hyperlipidemia and atherosclerosis: lessons from genetically modified apoe and ldlr mice. Clinical Chemistry and Laboratory Medicine (CCLM) 43, 470–479.

Wu, M., Tan, X., Liu, P., Yang, Y., Huang, Y., Liu, X., Meng, X., Yu, B., Wu, Y., Jin, H., 2020. Role of exosomal microRNA-125b-5p in conferring the metastatic phenotype among pancreatic cancer cells with different potential of metastasis. Life Sci. 255, 117857.

Xiang, Y., Duan, Y., Peng, Z., Huang, H., Ding, W., Chen, E., Liu, Z., Dou, C., Li, J., Ou, J., Wan, Q., Yang, B., He, Z., 2022. Microparticles from Hyperphosphatemia-Stimulated Endothelial Cells Promote Vascular Calcification Through Astrocyte-Elevated Gene-1. Calcif. Tissue Int. 111, 73–86.

Xie, H., Lim, B., Lodish, H.F., 2009. MicroRNAs induced during adipogenesis that accelerate fat cell development are downregulated in obesity. Diabetes 58, 1050–1057.

Xie, N., Chen, M., Dai, R., Zhang, Y., Zhao, H., Song, Z., Zhang, L., Li, Z., Feng, Y., Gao, H., Wang, L., Zhang, T., Xiao, R.-P., Wu, J., Cao, C.-M., 2017. SRSF1 promotes vascular smooth muscle cell proliferation through a Δ133p53/EGR1/KLF5 pathway. Nat. Commun. 8, 16016.

Xie, Z., Wang, X., Liu, X., Du, H., Sun, C., Shao, X., Tian, Jiangtian, Gu, X., Wang, H., Tian, Jinwei, Yu, B., 2018. Adipose-Derived Exosomes Exert Proatherogenic Effects by Regulating Macrophage Foam Cell Formation and Polarization. J. Am. Heart Assoc. 7, e007442.

Xu, F., Zhong, J.-Y., Lin, X., Shan, S.-K., Guo, B., Zheng, M.-H., Wang, Y., Li, F., Cui, R.-R., Wu, F., Zhou, E., Liao, X.-B., Liu, Y.-S., Yuan, L.-Q., 2020. Melatonin alleviates vascular calcification and ageing through exosomal miR-204/miR-211 cluster in a paracrine manner. J. Pineal Res. 68, e12631.

Xu, H., Ni, Y.-Q., Liu, Y.-S., 2021. Mechanisms of Action of MiRNAs and LncRNAs in Extracellular Vesicle in Atherosclerosis. Front. Cardiovasc. Med. 8, 733985.

Yagishita, S., Fujita, Y., Kitazono, S., Ko, R., Nakadate, Y., Sawada, T., Kitamura, Y., Shimoyama, T., Maeda, Y., Takahashi, F., Takahashi, K., Tamura, T., Koizumi, F., 2015. Chemotherapy-Regulated microRNA-125–HER2 Pathway as a Novel Therapeutic Target for Trastuzumab-Mediated Cellular Cytotoxicity in Small Cell Lung Cancer. Mol. Cancer Ther. 14, 1414–1423.

Yang, C.M., Chien, C.S., Hsiao, L.D., Pan, S.L., Wang, C.C., Chiu, C.T., Lin, C.C., 2001. Mitogenic effect of oxidized low-density lipoprotein on vascular smooth muscle cells mediated by activation of Ras/Raf/MEK/MAPK pathway. Br. J. Pharmacol. 132, 1531–1541.

Yang, F., Du, Y., Zhang, J., Jiang, Z., Wang, L., Hong, B., 2016. Low-density lipoprotein upregulate SR-BI through Sp1 Ser702 phosphorylation in hepatic cells. Biochim. Biophys. Acta 1861, 1066–1075. https://doi.org/1

Yang, J.-S., Maurin, T., Robine, N., Rasmussen, K.D., Jeffrey, K.L., Chandwani, R., Papapetrou, E.P., Sadelain, M., O'Carroll, D., Lai, E.C., 2010. Conserved vertebrate mir-451 provides a platform for Dicer-independent, Ago2-mediated microRNA biogenesis. Proc. Natl. Acad. Sci. U. S. A. 107, 15163–15168.

Yerlikaya, F.H., Öz, M., 2019. Aberrant expression of miRNA profiles in high-fat and high-sucrose fed rats. Clin. Nutr. Exp. 27, 1–8.

Yoda, M., Kawamata, T., Paroo, Z., Ye, X., Iwasaki, S., Liu, Q., Tomari, Y., 2010. ATP-dependent human RISC assembly pathways. Nat. Struct. Mol. Biol. 17, 17–23.

Young, M.D., Wakefield, M.J., Smyth, G.K., Oshlack, A., 2010. Gene ontology analysis for RNA-seq: accounting for selection bias. Genome Biol. 11, R14.

Zampetaki, A., Mayr, M., 2012. Analytical challenges and technical limitations in assessing circulating miRNAs. Thromb. Haemost. 108, 592–598.

Zand, T., Majno, G., Nunnari, J.J., Hoffman, A.H., Savilonis, B.J., MacWilliams, B., Joris, I., 1991. Lipid deposition and intimal stress and strain. A study in rats with aortic stenosis. Am. J. Pathol. 139, 101–113.

Zhang, C., Wan, X., Tang, S., Li, K., Wang, Y., Liu, Yujie, Sha, Q., Zha, X., Liu, Yehai, 2020. miR-125b-5p/STAT3 Pathway Regulated by mTORC1 Plays a Critical Role in Promoting Cell Proliferation and Tumor Growth. J. Cancer 11, 919–931.

Zhang, C., Zhang, K., Huang, F., Feng, W., Chen, J., Zhang, H., Wang, J., Luo, P., Huang, H., 2018. Exosomes, the message transporters in vascular calcification. J. Cell. Mol. Med. 22, 4024–4033.

Zhang, M.M., Bahal, R., Rasmussen, T.P., Manautou, J.E., Zhong, X., 2021. The growth of siRNA-based therapeutics: Updated clinical studies. Biochem. Pharmacol. 189, 114432.

Zhang, X.F., Wang, T., Wang, Z.-X., Huang, K.-P., Zhang, Y.-W., Wang, G.-L., Zhang, H.-J., Chen, Z.-H., Wang, C.-Y., Zhang, J.-X., Wang, H., 2021. Hypoxic ucMSC-secreted exosomal miR-125b promotes endothelial cell survival and migration during wound healing by targeting TP53INP1. Mol. Ther. - Nucleic Acids 26, 347–359.

Zhang, Y., Liu, D., Chen, X., Li, J., Li, L., Bian, Z., Sun, F., Lu, J., Yin, Y., Cai, X., Sun, Q., Wang, K., Ba, Y., Wang, Q., Wang, D., Yang, J., Liu, P., Xu, T., Yan, Q., Zhang, J., Zen, K., Zhang, C.-Y., 2010. Secreted monocytic miR-150 enhances targeted endothelial cell migration. Mol. Cell 39, 133–144.

Zhao, N., Zhang, J., 2018. Role of alternative splicing of VEGF-A in the development of atherosclerosis. Aging (Albany. NY). 10, 2695–2708.

Zhao, T., Li, J., Chen, A.F., 2010. MicroRNA-34a induces endothelial progenitor cell senescence and impedes its angiogenesis via suppressing silent information regulator 1. Am. J. Physiol. Metab. 299, E110–E116.

Zhao, Y., Li, Y., Luo, P., Gao, Y., Yang, J., Lao, K.-H., Wang, G., Cockerill, G., Hu, Y., Xu, Q., Li, T., Zeng, L., 2016. XBP1 splicing triggers miR-150 transfer from smooth muscle cells to endothelial cells via extracellular vesicles. Sci. Rep. 6, 28627.

Zhao, Y., Srivastava, D., 2007. A developmental view of microRNA function.

Trends Biochem. Sci. 32, 189–197.

Zheng, B., Yin, W.-N., Suzuki, T., Zhang, X.-H., Zhang, Y., Song, L.-L., Jin, L.-S., Zhan, H., Zhang, H., Li, J.-S., Wen, J.-K., 2017. Exosome-Mediated miR-155 Transfer from Smooth Muscle Cells to Endothelial Cells Induces Endothelial Injury and Promotes Atherosclerosis. Mol. Ther. 25, 1279–1294.

Zheng, H., Yu, Z., Wang, H., Liu, H., Chen, X., 2022. MiR-125b-5p ameliorates hypoxia/reoxygenation-induced endothelial cell dysfunction and attenuates reduced uterine perfusion pressure-induced hypertension in pregnant rats via targeting BMF. Hypertens. Pregnancy 41, 79–88.

Zhong, Z., Hou, J., Zhang, Q., Zhong, W., Li, B., Li, C., Liu, Z., Yang, M., Zhao, P., 2018. Circulating microRNA expression profiling and bioinformatics analysis of dysregulated microRNAs of patients with coronary artery disease. Medicine (Baltimore). 97, e11428.

Zhou, J., Li, Y.-S., Nguyen, P., Wang, K.-C., Weiss, A., Kuo, Y.-C., Chiu, J.-J., Shyy, J.Y., Chien, S., 2013. Regulation of vascular smooth muscle cell turnover by endothelial cell-secreted microRNA-126: role of shear stress. Circ. Res. 113, 40–51.

Zhou, X., Li, D., Yan, W., Li, W., 2008. Pravastatin prevents aortic atherosclerosis via modulation of signal transduction and activation of transcription 3 (STAT3) to attenuate interleukin-6 (IL-6) action in ApoE knockout mice. Int. J. Mol. Sci. 9, 2253–2264.

Zhu, J., Angelov, S., Alp Yildirim, I., Wei, H., Hu, J.H., Majesky, M.W., Brozovich, F. V, Kim, F., Dichek, D.A., 2021. Loss of Transforming Growth Factor Beta Signaling in Aortic Smooth Muscle Cells Causes Endothelial Dysfunction and Aortic Hypercontractility. Arterioscler. Thromb. Vasc. Biol. 41, 1956–1971.